Solid-state inorganic phosphors for luminescence thermometry

ABBI LOUISE MULLINS

How to cite:

MULLINS, ABBI LOUISE (2024) Solid-state inorganic phosphors for luminescence thermometry. Doctoral thesis, Durham University.

Abstract – Solid-state inorganic phosphors for luminescence thermometry

Abbi Mullins

Through the link between emission quenching and temperature, luminescence thermometry has emerged as a remote, semi-contact method for temperature sensing. This thesis investigates through variables including the host material choice, and the luminescent ion's identity and concentration, how solid-state thermometers can be designed for specific purposes such as for biological use, with high sensitivity and temperature resolution.

Chapter 1 reviews phosphor constituents, theory of luminescence, method of luminescence thermometry, and current luminescence thermometers using different host materials.

Chapter 2 gives an overview on all methods used in the synthesis and characterisation of the host material's structure, and the optical properties of the introduced activator ions.

Chapter 3 investigates the $LaGa_{1-x}O_3{:}Cr^{3+}_x$ phosphor series (x = 0.0, 0.2, 0.5, 1.0, 2.0, 4.0 mol%). Room-temperature luminescence measurement showed $LaGa_{0.99}O_3{:}Cr_{0.01}$ with the highest quantum yield of the series. Investigation of $LaGa_{0.99}O_3{:}Cr_{0.01}$ by variable-temperature photoluminescence confirmed its application as a luminescence thermometer with a relative sensitivity of 2.5% K^{-1} and a temperature resolution of 0.04 K at 300 K.

Chapter 4 explores the $La_{1-x}Ga_{0.99}O_3{:}Cr^{3+}_{0.01}, Nd^{3+}_x$ series (where x = 0.5, 1.0, 2.0 mol%). Emission from both Cr^{3+} and Nd^{3+} using a single excitation wavelength was confirmed. Variable-temperature emission of the materials presented $La_{0.98}Ga_{0.99}O_3{:}Cr^{3+}_{0.01}, Nd^{3+}_{0.02}$ as the best candidate for luminescence thermometry, with a relative sensitivity of 2.0% K^{-1} and a temperature resolution of 0.05 K at 300 K.

Chapter 5 discusses the $A_5(V_{0.97}O_4)_3Cl{:}\ Mn^{5+}_{0.03}$ materials (where A = Sr^{2+}, Ba^{2+}). Room-temperature luminescence investigations confirmed Mn^{5+} emission within biological window-2 with quantum yields recorded as 47% and 51% respectively. Variable-temperature investigation confirmed both materials as luminescence intensity ratio (LIR), band-shift, and bandwidth thermometers. Multiparametric linear regression (MLR) thermometry of $Sr_5(V_{0.97}O_4)_3Cl{:}\ Mn^{5+}_{0.03}$ gave a relative sensitivity of 3.14% K^{-1} and a temperature resolution of 0.042 K at 308 K.

Chapter 6 concludes with the closing remarks on all discussed work, alongside a perspective on further work that can be continued on the presented, and similar, materials.

Solid-state inorganic phosphors for luminescence thermometry

Abbi Mullins

Ustinov College

Thesis submitted for the degree of

Doctor of Philosophy

29th May 2024

Supervisors:

Prof. Ivana R. Evans

Prof. J. A. Gareth Williams

Department of Chemistry

Durham University

Acknowledgements

Ivana and Gareth – I cannot thank you both enough for your guidance, your compassion, and your unwavering support. Truly I could not wish for better supervisors. At my lowest point, you both gave me some advice: ‘Dyfal donc a dyr y garreg’ (Persistent tapping breaks the stone), and ‘No, not ‘it’s going to get done’, you’re doing it. Active not passive!’ So, I can now say, the stone is broken, and I did it!

To the past and present members of Evans’ group: Josie, Melissa, Chloe, Bettina, Alma, Sam, Ollie, Esther, George, and all the masters students – thank you for the crosswords and all the cups of tea. Special thanks to Peter Rodgers and Artemijs Krimovs, whose master’s work aided in Chapters 4 and 5 of this thesis respectively.

To the past and present members of the JAGW group: Amit, Emma, Rebecca, Chris, Yana, Laura, and Lucy – thank you for your friendship, and for letting me quiz you all on solid-state chemistry (unwillingly).

To Prof John S. O. Evans, for your knowledge and help on your daily wanders through the office. To Gary Oswald for your diffractometer wizardry and chats. To Dr Sam Page for ssNMR data collection and analysis.

To the OMAS group in Vinca, Serbia, particularly Prof. Miroslav Dramićanin, Dr Aleksander Ćirić, Dr Zoran Ristić, and Dr Vesna Đjorđjević: thank you for your hospitality, friendship, and expertise. Hvala vam!

To my family: for being my safety net, and my biggest supporters. To the Hartlepool Caledonians hockey club: for keeping me sane. To Tom Smith(7): From Newcastle University undergrad to PhD thesis hand in, we finally made it!

To Charlie: For keeping me grounded, loving me, and for always just being you.

Dedication

From applying to finishing my PhD, family members I love have passed away. They gave me happiness, encouragement, confidence, and shaped who I am today.

So, to my grandmar and grandar, Martin and Betty; my aunty, Alison; and my cousin, Kieron, I dedicate this to you.

“I believe we’ve reached the end of our journey. All that remains is to collapse the innumerable possibilities before us. Are you ready to learn what comes next?

It’s tempting to linger in this moment, while every possibility still exists. But unless they are collapsed by an observer, they will never be more than possibilities”.

– Solanum, Outer Wilds

Declaration

The work presented in this thesis is entirely the work of the author, except where help or collaboration is acknowledged from a named person, or a reference provided to a published source.

The research presented within was performed in the Department of Chemistry, Durham University, between October 2020 and May 2024. The results of this research have not been submitted for a degree in this or any other university. This thesis conforms to the word limit detailed in the Degree Regulation of the university.

Statement of copyright

List of abbreviations

T.M – transition metal ion(s)

Ln – lanthanide ion(s)

LIR – Luminescence intensity ratio

NIR – Near infrared

BW – Biological window(s)

FRET - Förster resonance energy transfer

QY – Quantum yield

UV – Ultraviolet

T.S - Tanabe-Sugano

ΔE – Energy gap (between two states)

S_a – Absolute sensitivity

S_r – Relative sensitivity

δT – Temperature resolution

FWHM – Full width, half maximum

CCD – Charge-coupled devices

PMT – Photomultiplier tube

YAG - $Y_3Al_5O_{12}$

UC – Upconversion

MOX - Metal oxyhalide

SC-XRD – Single crystal x-ray diffraction

PXRD – Powder x-ray diffraction

GOF – Goodness-of-fit

QY – Quantum yield

PLQY or Φ_{int} – intrinsic photoluminescent quantum yield

Φ_{ovl} – Overall photoluminescence quantum yield

V.T. – Variable-temperature

o.d. – Outer diameter

LED – Light emitting diode

DRS – Diffuse reflective spectroscopy

ssNMR – Solid-state Nuclear magnetic resonance

NMR – Nuclear magnetic resonance

MAS – Magic angle spinning

TEM – Transmission electron microscopy

EDX – Energy-dispersive x-ray spectroscopy

ICSD – Inorganic crystal structure database

WLED – White light emitting diode

MLR – Multi-linear regression

TGA-MS – Thermogravimetric analysis-mass spectrometry

Contents

1. Literature review

Luminescence thermometry is a temperature-sensing technique based on the emission of light from a material which is monitored for thermal variations allowing for temperature to be measured in real time.[1] The semi-contact nature of this technique enables temperature measurement in many extreme, hard-to-reach environments including biological, nano-scale, fast-moving, and flowing systems if the phosphor itself is optimised for these domains.[2–4] An emissive ion is required within the host material. The emissive ion of the phosphor is critical in determining which region of the electromagnetic spectrum the phosphor will absorb and emit, influencing its usage, as is the host material itself. The work within this thesis tackles the factors that influence aspects of the luminescence and thermometric performance when designing a phosphor.

In this chapter, the following topics are explored:

- The constituent parts of a phosphor, and what aspect of luminescence each part influences.
- A brief summary of photoluminescence and its selection rules, and how transition metal (TM) and lanthanide (Ln) ions differ chemically and spectroscopically from each other in solid host materials.
- A general overview of the concept of luminescence quenching and how it can be exploited in luminescence thermometry, including the readout methods most commonly used for temperature sensing and their fundamental equations.
- A review of some classes of luminescence thermometers with different host materials – oxides, halides, and oxyhalides, allowing for a comparison of how different host materials affect the dopants and the sensitivities and temperature resolutions of luminescence thermometers.

1.1. What is a phosphor?

Phosphors are inorganic materials that are able to convert different forms of energy into typically visible electromagnetic radiation - light.[5] A solid-state phosphor consists of a host material (represented by the rectangle in Figures 1.1a and 1.1c) into which small amounts of luminescent ions are introduced (denoted as ‘A’ and ‘S’ in Figures 1.1a and 1.1c). These luminescent ions can absorb and emit specific wavelengths of light. The most common emission process is downshifting photoluminescence by which the absorption of high energy electromagnetic radiation, generally by the luminescent centre, promotes electrons to higher-lying excited states (A_2^* in Figure 1.1b and 1.1d). The excited electron then undergoes non-radiatively decay to the lowest-lying excited state (A_1^* in Figure 1.1b and 1.1d) from which radiative emission of a lower energy photon can be observed.[6]

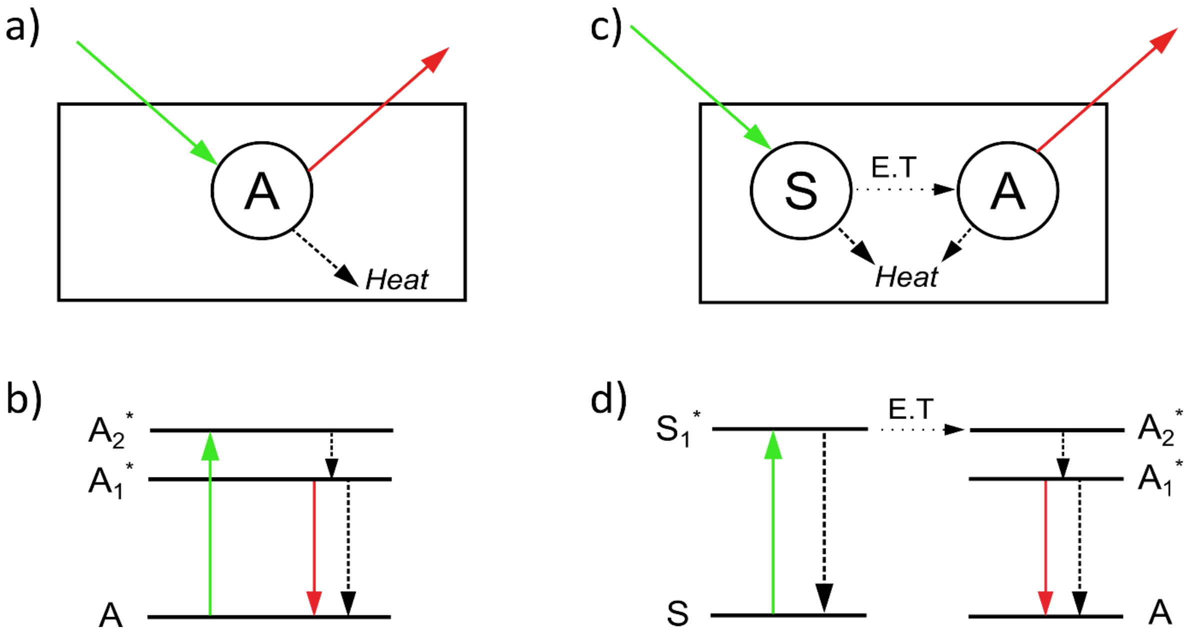

Figure 1.1: a) A simplified schematic of phosphor doped with an activator, A; b) A Jablonski diagram of the single activator system; c) A phosphor doped with a sensitiser, S, and an activator, A; d) A Jablonski diagram for the sensitiser-activator phosphor system. Radiative and non-radiative decay are denoted by the solid and dashed lines respectively. Excited states are labelled with ‘’. E.T indicates energy transfer. Reproduced with permission from Springer Nature.*[5]

The luminescent ions that purposefully substitute cations of the host material are commonly referred to as *activators*. An activator, however, may not emit intensely when excited, or fail to absorb strongly at a specific excitation wavelength. Additional doped ions termed *sensitisers* can also be incorporated into the host to provide an alternative pathway to excitation by absorbing wavelengths of light unavailable to the activator or absorbing more strongly. The sensitiser ions can then transfer the energy from their excited state to the activator ions, allowing emission from the activator without direct excitation (Figures 1.1c and 1.1d). Sensitisers can aid in increasing the efficiency of the phosphor and its net brightness through increasing the quantum yield of the phosphor. The energy transfer efficiency between the sensitiser and activator is, however, strongly dependent on the distance between these two ions. Through space, energy transfer falls off with $1/r^6$, so the ions must be in close proximity within the host matrix to increase the efficency.[7]

By considering these two factors – the host material and the activator ions – a phosphors spectroscopic properties can be optimised for its intended application in areas such as solid-state lighting, anti-counterfeiting, lasing, scintillation, and more recently luminescence thermometry.[8–13]

1.1.1. Choice of host

Changing the structure or chemistry of a host material will affect the properties of the host and influence the optical properties of activator ions. The structure-property relationship allows for tuning and optimisation of a host and activator for its intended purpose.

The crystal structure of the material determines the spatial connectivity of all ions, which affects variables such as the site symmetry of ions, and the bond lengths and bond angles of dopants, influencing the dopant's spectroscopic properties.

The number and symmetry of the sites which an activator ion occupies in a host material can greatly affect emission intensities of certain transitions. The site symmetry affects the ion's orbital symmetry which can relax selection rules (detailed in Section 1.2.2.1) for specific luminescence transitions and change the emission intensity. An example of this is Eu^{3+}-doped phosphors, where the Eu^{3+} ion acts as site-symmetry probe. Red emission is observed when Eu^{3+} ions are on a non-centrosymmetric site, but orange emission is dominant when the Eu^{3+} is on a centrosymmetric site.[14] Additionally, the site symmetry can split degenerate orbitals, and increase the number of emissions such as for Cr^{3+} where a lowering of symmetry leads to two distinct Cr^{3+} emissions bands, termed R-lines, from the splitting of the degenerate ^2E state.[15]

The environment that the phosphor host will be used in must be considered. Different stabilities of the host material such as thermal, photochemical, and biological must be checked to ensure that the host doesn't degrade in its expected operating environments. For example, in the body there should be no leaching of ions, it should not hydrolyse, nor degrade at physiological pH, and it should not be cytotoxic. Similarly, if the material is expected to operate at high temperatures, it should not melt across the required operating temperature range.

Each host material has distinct electronic characteristics that affect activator ions - covalency and the crystal field strength determined by the anions and cations present in the environment around the activator. These two factors will be further discussed in Section 1.2.4.[5] The ions present as ligands in the host material greatly affect the phonon – lattice vibration – energy of the host material, which determine the rates of non-radiative decay, and increase with temperature. Optimisation of a hosts phonon energy for specific purposes such as upconversion luminescence thermometry is discussed further in Section 1.4.

There will often be several possible synthetic routes to host materials, involving different reagents or instruments. Depending on the synthetic route, the same material can be produced as a single crystal, agglomerated crystallites (particles) or ceramics. For photoluminescence, the form of the product affects how light exits the material. For example, a study of yttrium aluminium garnet (YAG) doped with Ce^{3+}, a common yellow phosphor, has shown that whilst a single crystal shows higher thermal stability than its pulverised powdered form, it gave a lower quantum yield due to internal reflection of emitted light.[16] Similarly, a study of the effect of the crystallinity of $LiNbO_3$:Yb^{3+}, Tm^{3+} luminescence thermometers demonstrated that whilst the single crystal thermometer gave a higher absolute sensitivity value, the polycrystalline sample gave a generally higher relative sensitivity (figures of merit for thermometry are detailed in Section 1.3.2.).[17]

1.1.2. Choice of activator

The luminescence emitted from the host material can be classed as either extrinsic or intrinsic, according to the host and dopant ions.[1] Extrinsic luminescence is the electronic transitions of purposefully doped activator ions. The extrinsic luminescent centres are localised, and can be transition metal (TM), post-TM ion such as Bi^{3+}, and Ln^{3+} ions. Intrinsic luminescence, on the other hand, is due to electronic transitions within the host material itself. For example, $CaWO_4$ lamps use the WO_4^{2-} moieties to absorb UV energy, thus being an activator with a concentration on 100%.[18]

When choosing an activator ion, the wavelength of light required for application should be considered. For example, activator ions selected for biological applications should ideally have excitation and emission within at least one of the three near-infrared (NIR) ‘biological windows (BW)’ where tissue penetration is deepest due to poor absorption of light by the body’s fats, water, blood, and melanin.[19] The three BW are: BW-1 between 650 to 950 nm, BW-2 between 1000 nm to 1350 nm, BW-3 between 1550 nm to 1850 nm.

When using both sensitiser and activator ions, attention must be paid to the spectral overlap of the sensitiser emission with the activator’s excitation. The overlap between the donor (sensitiser) emission spectrum and the acceptor (activator) excitation spectrum can be evaluated with the equation:

$$J(\lambda) = \int_0^\infty F_D(\lambda)\varepsilon_A(\lambda)\lambda^4 \, d\lambda \tag{1.1}$$

where $J(\lambda)$ is the overlap integral, F_D is the normalised donor emission spectrum, ε_A is the molar absorption coefficient of the acceptor ion, and λ is the wavelength (nm).

Poor overlap causes lower efficiency of Förster resonance energy transfer (FRET), and lower intensity of the desired emission. The distance between activator and sensitiser ions greatly affects efficiency of energy transfer, as mentioned in Section 1.1. The link between the overlap integral and the FRET efficiency is given through the R_0 term, the Förster distance – the distance between the donor and acceptor ions where FRET is 50% efficient:

$$(R_0)^6 \propto \kappa^2 \, \Phi_D \, J(\lambda) \, n^{-4} \tag{1.2}$$

where κ^2 is the directional relationship of the transition dipoles, $\Phi_D$is the quantum yield of the donor, $J(\lambda)$ is the overlap integral of the donor emission spectrum and the acceptors excitation spectrum, and n is the refractive index of the medium.

The FRET equation is given as:

$$E = \frac{1}{1 + \left(\frac{r}{R_0}\right)^6} \tag{1.3}$$

$$E = \frac{k_{ET}}{k_f + k_{ET} + \sum k_i} \tag{1.4}$$

where E is the efficiency of FRET, r is the donor-acceptor ion distance, k_{ET} is the rate of FRET between the donor and acceptor ions, k_f is the rate of radiative decay, and k_i is the rate of non-radiative decay such as internal conversion and intersystem crossing).

The concentration of the activator ion affects the quantum yield of the sample (explored more thoroughly in Section 2.3.1.2). At concentrations greater than optimal, the emission intensity from an activator ion decreases as decreasing distance between activator ions in the host structure allows for energy transfer between neighbouring ions. The concentration quenching by non-radiative energy transfer due to resonance between activator ions can lower emission intensity as the transferred energy can reach defect sites, quenching emission.[18]

1.2. Fundamentals of luminescence

1.2.1. What is luminescence?

Luminescence is the radiative emission of energy from a material. There are a number of mechanisms for the excitation of a material such as through a chemical reaction (chemiluminescence), friction (triboluminescence), or electric fields (electroluminescence). As mentioned in Section 1.1 photoluminescence is the mechanism of electromagnetic radiation absorption in the UV, visible, or near IR ranges. The cause of the luminescence is transitions between the electronic states of an activator ion. As written in Section 1.1.2, properties such as the identity of the activator ion, its oxidation state, the ligands, and the site symmetry influence the energy of these electronic transitions and thus the wavelengths of absorbed and emitted light. Luminescence can be distinguished into fluorescence and phosphorescence where during a transition, fluorescence has no change in the spin multiplicity of the electron ($\Delta S = 0$), and phosphorescence has a change in the multiplicity ($\Delta S \neq 0$). Fluorescence maintains the same electron spin, whilst phosphorescence involves a change in electron spin. Changing spin is a violation of the spin selection rule (Section 1.2.2.1.1) and gives rise to the characteristic long lifetimes of the phosphorescence excited state compared to fluorescence.

1.2.2. Term symbols and Russell-Saunders coupling

Term symbols denote the spectroscopically distinguishable electronic states of atoms and ions with general form:

$$^{(2S+1)}L_J \tag{1.5}$$

where S is the total spin angular momentum, L is the total orbital angular momentum, and J is the total angular momentum. Transitions between electronic states can be evaluated by their term symbols allowing for at-a-glance assessment of the probability of a transition.

Russell-Saunders coupling is a method to derive the term symbols of states – terms are groups of degenerate microstates with different magnetic quantum number, m_l, and spin quantum number, m_s. The Russell-Saunder coupling scheme requires the coupling of spin angular momenta of electrons, orbital angular momenta, and finally the coupling of spin and orbit angular momenta. The spin-orbit term is small for 1st row TM ions but becomes important for 2nd and 3rd row TM and for the lanthanides and actinides.[20]

Hund's rules are used to predict the order of energies of the different terms.[20] For the ground state, the approach is as follows:

- The ground state must have the highest spin multiplicity ($2S+1$)
- If two or more terms have the same highest spin multiplicity, then the term with the largest angular momentum (L) has the lowest energy; for example, a ^{3}F term will be lower in energy than a ^{3}P term.
- For <1/2 filled orbitals, the energy level with the lowest J value lies lowest in energy ($S-L$). Conversely, for >1/2 filled orbitals, the energy level with the largest J value lies lowest in energy ($S+L$).

1.2.2.1. Selection rules

Selection rules govern the probability and therefore the intensity of electronic transitions. When terms such as allowed and forbidden are used, they should not be regarded as absolute rules and can be partially lifted. A forbidden transition can still show weak intensity due to the relaxing of these selection rules through specific conditions.

The spin selection rule, $\Delta S = 0$, states that the change of an electron's total spin quantum number S, and therefore its spin multiplicity during a transition, is forbidden.[21] The total wavefunction can be broken down into vibrational, rotational, and electronic components through the Born-Oppenheimer approximation. The electronic component of the wavefunction can be further factorised into orbital and spin components. Should the spin wavefunction component change during a transition, the integral of the wavefunction's spin component will equal zero, causing the total wavefunction to equal zero, therefore a transition will not be observed and classed as forbidden.

Breaking of spin selection rules by spin-orbit coupling allows for low intensity spin forbidden bands to appear. The spin orbit coupling increases with Z^4 (where Z is the effective atomic number) and so becomes more significant in the presence of heavy atoms, such as 2nd and 3rd row TM and the f-block elements.

The parity selection rule, also known as the Laporte selection rule, states that a change in parity, $\Delta l = \pm 1$, is required for a transition to be allowed. Both s- and d-orbitals possess centres of symmetry thus their wavefunctions keep the same sign with respect to inversion, and are classed as '*gerade*'. The p- and f-orbitals' wavefunction sign changes due to the orbitals' being asymmetric, and are classed as '*ungerade*'.[22] For a parity allowed transition, the transition must be from a symmetric to an asymmetric orbital, or vice versa. Formally, d-d and f-f transitions are forbidden due to the lack of orbital symmetry change during a transition, but s-p, p-d, and d-f transitions are allowed.

Breaking the parity selection rule is easier to achieve than that of the spin selection rule, particularly for transition metals, due to their stronger valence d-orbital overlap with ligand p-orbitals. For a centrosymmetric site such as octahedral, coupling of odd-symmetry vibrational states to the electronic transition relaxes the Laporte selection rule. As vibrations occur on a longer timescale than absorption of a photon (10^{-15} s^{-1} vs 10^{-18} s^{-1}), the octahedral site symmetry is temporarily lowered as the vibration occurs with a simultaneous absorption of a photon, partially allowing the d-d transition. Additionally, hybridisation of the d-orbitals of a TM on a tetrahedral site with some of the p-orbitals of a ligand due to their shared symmetry also relaxes the Laporte selection rule, which enhances the extinction coefficient of tetrahedral complexes when compared to octahedral complexes.

1.2.3. Lanthanide luminescence

The lanthanides (Ln) are a group of 15 metallic elements from lanthanum to lutetium with electron configurations [Xe] $5s^2$ $4f^n$ (n = 0-14). Of the 15 Ln^{3+} ions, only La^{3+} and Lu^{3+} show no luminescence.

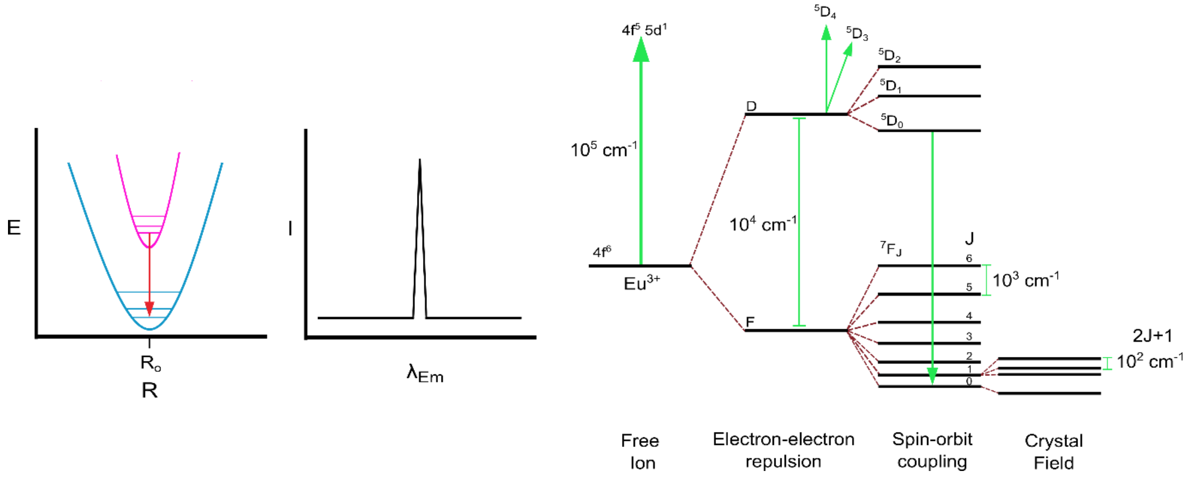

Figure 1.2: a) A configuration coordinate diagram showing the lack of bond geometry change between the excited state (pink parabola) and ground state (blue parabola) with a representative emission spectrum showing the narrow emission peak; b) Illustration of the splitting of the Eu^{3+} term symbol through S.O coupling and the crystal field. Reprinted from Luminescence thermometry, 1st edition, Author(s), chapter 6, Page No. 122, Copyright (2018), with permission from Elsevier.[1]

The core-like nature of the f-orbitals of the Ln^{3+} ions give rise to narrow, highly distinguishable, element-characteristic f-f intra-orbital excitation and emission transitions. The narrow transition peak widths are a consequence of the Ln^{3+} f-orbitals interacting minimally with the ligand orbitals. Figure 1.2a, a configurational coordinate diagram, depicts a representative ground (blue parabola) and higher energy excited state (pink parabola) of a Ln^{3+} ion with the parabola minimum at R_0, the equilibrium bond length. There is a lack of geometric change between the ground and excited state of the Ln^{3+} ion – $\Delta R \approx 0$. This lack of variation in the Ln-ligand length, R, ensures that there is little change in the ligand field strength, and leads to narrow peaks. As the electron transition is between two terms, the parity rule holds for these transitions as well as $S \neq 0$, thus the intensity of Ln^{3+} transitions is very weak. As shown by Figure 1.2b, orbitals are split by electronic repulsion first (~10^4 cm^{-1}), secondly by the spin-orbit coupling (10^3 cm^{-1}), then the crystal field (~10^2 cm^{-1}). The Dieke diagram, an overview of the energy levels of all Ln^{3+} doped into LaF_3, shows relative energy levels of the electronic states of the same Ln^{3+} ion only change by ~100's cm^{-1}. Thus, in different solid hosts, in solution, and in gaseous states, the positions of the excitation and emission peaks are near-identical.[23] The small molar extinction coefficients of the lanthanides means that a high-power excitation source such as a laser, or the use of a sensitising ion or antenna molecule, is required if their excited states are to be populated efficiently.[24]

The narrow bands of the Ln^{3+} ions have been useful for many applications such as phosphors for lighting (Y_2O_3:Eu^{3+}) due to the colour purity of the emission.[25] Lanthanide ions such as Nd^{3+} and Er^{3+} have been especially studied into for medical and research laser dopants due to their states with long wavelengths, and narrow peakwidths.[26,27] Ln^{3+} ions have been used as activator ions for luminescence thermometry, particularly for ratiometric sensing, which will be discussed in Section 1.3.3.1.

1.2.4. Transition metal luminescence

In contrast to the Ln ions, TM ion excitation and emission spectra are highly variable, showing many broad emission bands whose energies depend highly on the identity of the TM metal, its oxidation state, and the ligands it is bound to. The diffuse nature of d-orbitals allows for strong overlap with ligand orbitals. Changes to TM-ligand bond length, R, and therefore the crystal field strength, such as through vibrations that vary the length of bonds during the transition of an electron, cause broad absorption and emission bands to arise (Figure 1.3).

However, for spin-forbidden transitions, there is sometimes a change in spin of the electron without a change in orbital population. Such transitions are relatively insensitive to bond vibrations, leading to narrow emission peaks. An example of a spin-forbidden transition is the case of ^{2}E state of Cr^{3+}, compared to the broad $^4T_2$ emission band (Figure 1.4).

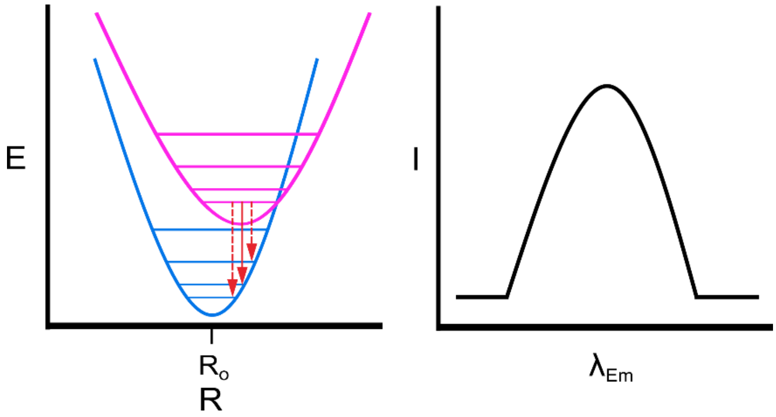

Figure 1.3: A combination of a configurational coordinate diagram showing how an excited state distortion relative to the ground state causes a broad emission.

Due to the strong interaction between the TM d-orbitals and the ligand p-orbitals (as well as the smaller Z value of the 1st row TM), the crystal field splits the d-orbitals on the order of 10^3–10^4 cm^{-1}. This energy gap, between the doubly-degenerate, higher-lying E_g orbitals (d_{z^2} and $d_{x^2-y^2}$), and triply-degenerate, lower-lying T_{2g} orbitals (d_{xy}, d_{zy}, and d_{xz}) of a TM ion in an octahedral environment is referred to as the crystal field strength, Δ_O. The magnitude of Δ_O is determined by the identity of the ion, the ion's oxidation state, and the identity of the ligands. For a given metal ion in a given oxidation state, ligands can be ranked according to the value of Δ_O leading to the spectrochemical series. Ligands are categorised within a range known as the spectrochemical series which determines the field-strength the ligand. Ligands such as CO, which is a good π acceptor, cause a larger Δ_O whilst ligands such as Br^- and I^-, which are π donors, cause a smaller Δ_O, changing the energy of specific terms and consequently the wavelength of absorption and emission bands.

Tanabe-Sugano (T.S) diagrams are used in the interpretation of TM spectra, allowing parameters such as the crystal field strength and Racah parameters to be estimated from the energy ratio of specific transitions.[28–30] Each diagram is unique to the number of d-electrons of the TM metal, and applicable to ions in either octahedral (d^n) or tetrahedral (d^{1-n}) environments. As seen in Figure 1.4, the y-axis gives the energy of a transition, E, over the electron-repulsion B Racah parameter (E/B), whilst the x-axis is the crystal field over the B parameter (Δ/B), allowing for a diagram that can be used for varying B parameter value caused by both different ligand and TM metal identities. The free ion terms appear on the y-axis where the crystal field is zero, and as the crystal field increases across the x-axis, the energies and splitting of the free ions' terms change.

Lines drawn perpendicular to the ground state (which is set as the x-axis for T.S diagrams) indicate that bond vibrations influence the crystal field strength. For the states represented by perpendicular lines, the energy of a given photon absorption and emission will occur at different energies as the bond length, and therefore the crystal field strength, changes during a vibration, giving broad absorption and emission bands (Figure 1.4, red line). Conversely, lines that are near-parallel to the y-axis denote states where bond vibrations do not influence the crystal field value. Thus, bond vibrations do not affect the energy of the state, giving narrow lines similar to Ln^{3+} transitions – such as some spin-forbidden transitions like the $^2E \rightarrow {}^4T_2$ (Figure 1.4, green line).

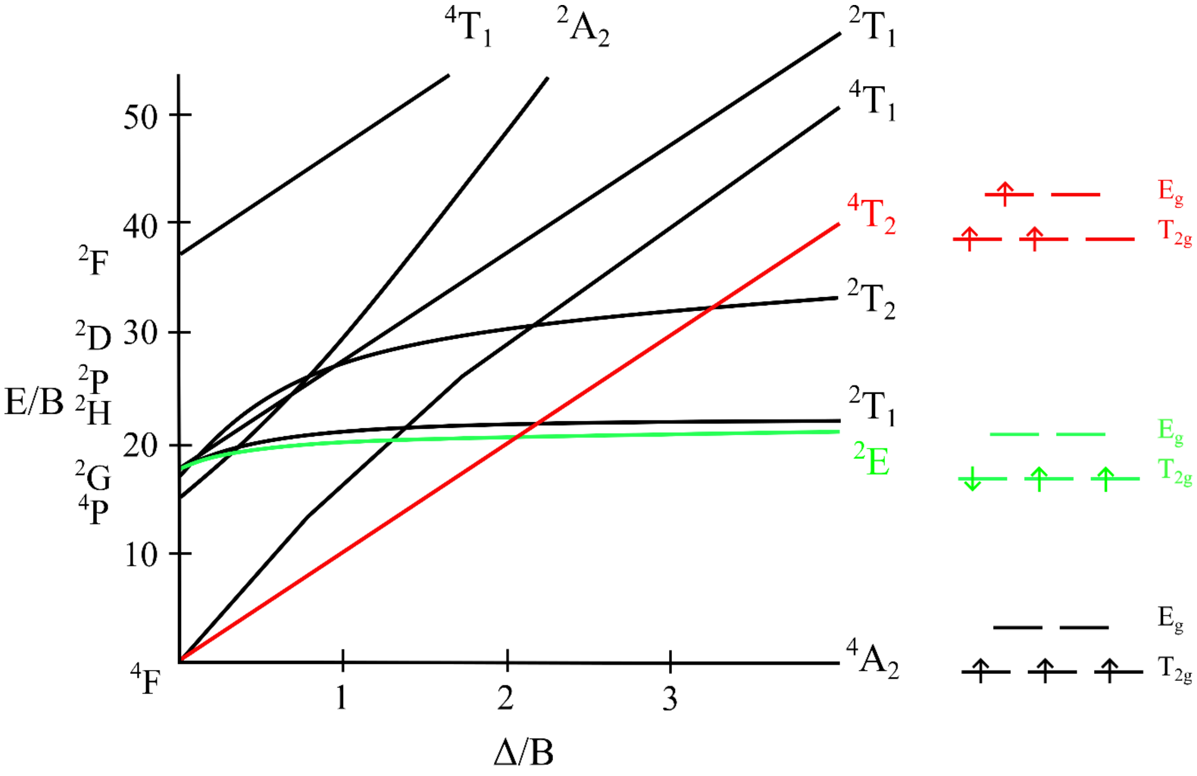

Figure 1.4: Tanabe-Sugano diagram for a d^3 ion in an octahedral environment. The right-hand side displays the electron configuration of the $^4T_2$, ^2E and $^4A_2$ states, showing how a change in orbital from the ground $^4A_2$ state affects the energy of the transition as the crystal field changes.[30]

Rather than the crystal field, it is the covalency of the TM-ligand bond (a consequence of the host material choice) that influences the energy of spin-forbidden transitions due to increasing covalency affecting the *B* and *C* Racah repulsion parameters. Increasing covalency due to the identities of the TM ion and of the ligand allows for the d-orbital electrons to diffuse into the ligand bond effectively 'expanding' the size of the d-orbitals, decreasing electron-electron repulsion and lowering the *B* parameter from its free-ion value. The nephelauxetic effect, β, or cloud-expanding effect is measured as the ratio of the *B* parameters of a complex over the free ion's *B* parameter and will be a value <1, with a lower value indicating a more covalent bond.

1.3. Fundamentals of luminescence thermometry

Temperature is an important variable for many branches of industry, medicine, research, agriculture, and in domestic life. Due to the prevalence of temperature, more ways of being able to measure it accurately and under different conditions are continuously required. Luminescence thermometry uses changes in a material's luminescence as the readout to indicate temperature change. Luminescence thermometry is a 'semi-contact' or 'remote detection' method. The phosphor must have contact with the surface or be within the medium being sampled thus still being invasive albeit minimally due to phosphor size, but detection of luminescence is remote.[31] This is in contrast to many conventional contact thermometry methods still employed today such as liquid-in-glass, thermistor, and thermocouple thermometers whose larger sizes are invasive.[1] The submicron size of phosphor particles along with remote detection allows for a greater number of environments to be accessible to luminescence thermometry methods such as within nano-/micro-electronic devices or at a cellular level.[32,33]

1.3.1 Temperature quenching of luminescence

The technique of luminescence thermometry is underpinned by the phenomenon of temperature quenching of luminescence.[1] Quenching is the term given to pathways that induce non-radiative decay within a luminescent material consequently reducing its luminescence intensity. Non-radiative pathways include energy transfer to neighbouring ions or loss of energy through phonons – vibrations – of the host structure. The intensity of luminescence, $I(T)$, from a material is temperature-dependent since the rate of non-radiative decay increases as temperature increases. Generally, at higher temperatures as non-radiative decay increases, luminescence emission intensity decreases.

$$I(T) = C \cdot k_R \cdot \tau(T) = C \cdot \eta(T) = C \cdot \frac{k_R}{k_R + k_{NR}(T)} \tag{1.6}$$

where *C* is a constant of temperature-invariant factors that in principle do not change with temperature variations such as the material, detector specific set-up conditions, and concentration and absorption coefficients of the luminescent species. k_R is the rate of radiative decay, k_{NR} is the rate of non-radiative decay, τ is the lifetime of the excited state, and η is the efficiency of emission of the luminescent material. Whilst loss of luminescence intensity can be seen as a hindrance at increasing temperatures for applications such as lighting, quenching can be used as a temperature indication. In the case of thermometry, it allows for the tracking of luminescence intensity with changing temperature.

1.3.1.1 Mott-Seitz theory

The link between quenching and the temperature-dependent increase in non-radiative decay can be expressed by Mott-Seitz theory. This theory shows the pathway of non-radiative decay using a configurational coordinate diagram (Figure 1.5) of the ground state and of the excited state where there is a large offset in the equilibrium geometries between the ground and the excited state respectively ($R_0 \neq R_{exc}$).[34–36] The excited state electron population can be deactivated non-radiatively to the ground state by thermal assistance as temperature increases, from the excited state minimum to the intersection point of the two parabolas, *S*. The rate of non-radiative decay from the excited state through S is determined by a Boltzmann distribution-like relationship:

$$k_{NR}(T) = A \cdot \exp(-\Delta E / k_B T) \tag{1.7}$$

where ΔE is the difference in energy between the excited state parabola minimum and the intersection point, *S*. *A* is a frequency constant weakly dependent on temperature.

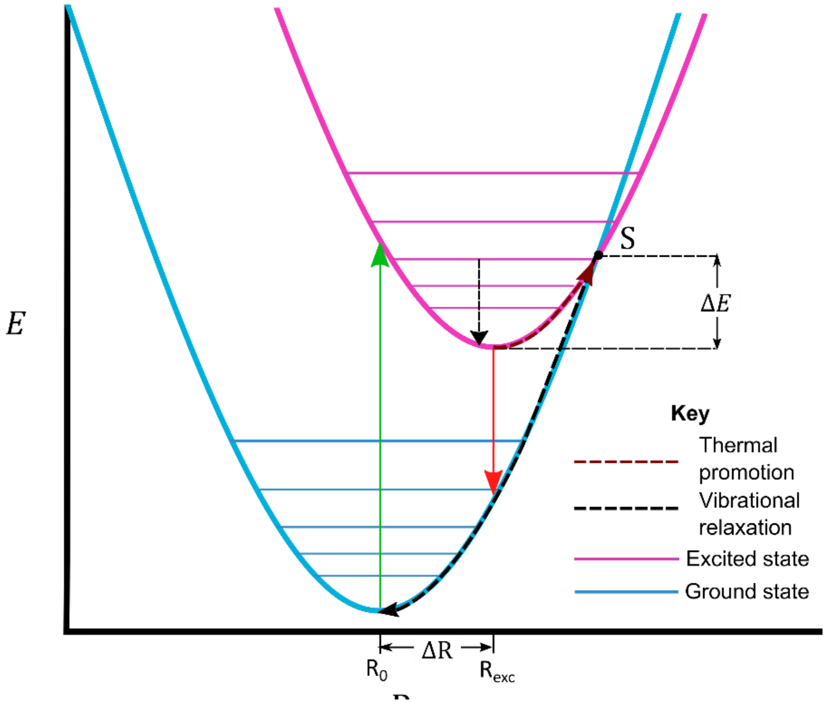

Figure 1.5: A configurational coordinate diagram of the ground and excited state of a luminescent centre where the excited state and ground state have different geometries. The intersection point, S, allows for thermal deactivation to the ground state.[37] Reprinted from Luminescence thermometry, 1st edition, Author(s), chapter 3, Page No. 42, Copyright (2018), with permission from Elsevier.[1]

As ΔE increases, the rate of non-radiative decay decreases. Conversely, increasing the temperature of the material will increase the rate of decay through the intersection point, *S*. The increasing rate of decay decreases the emission intensity. This model of thermally-induced non-radiative decay is applicable to broad activator ions transitions such as from spin-allowed d-block ions and 5f-4d lanthanide ions due to their strong electron-phonon coupling. For the Mott-Seitz model, the expressions for temperature dependence of emission intensity and lifetime can be written as follows:

$$I(T) = C \cdot \frac{1}{1 + \frac{A}{k_R} \cdot \exp\left({}^{-\Delta E}/_{k_B T} \right)} \tag{1.8}$$

$$\tau(T) = C \cdot \frac{1}{k_R + A \cdot \exp\left({}^{-\Delta E}/_{k_B T} \right)} \tag{1.9}$$

1.3.1.2 Multiphonon relaxation

Spin-forbidden TM transitions, and f-orbital transitions of Ln^{3+} ions, both undergo an alternative quenching pathway termed multiphonon relaxation. Figure 1.6 shows a configuration coordinate diagram of the ground state and excited state, with no change to their equilibrium bond position, and thus no intersection point, *S*, as opposed to Figure 1.5.

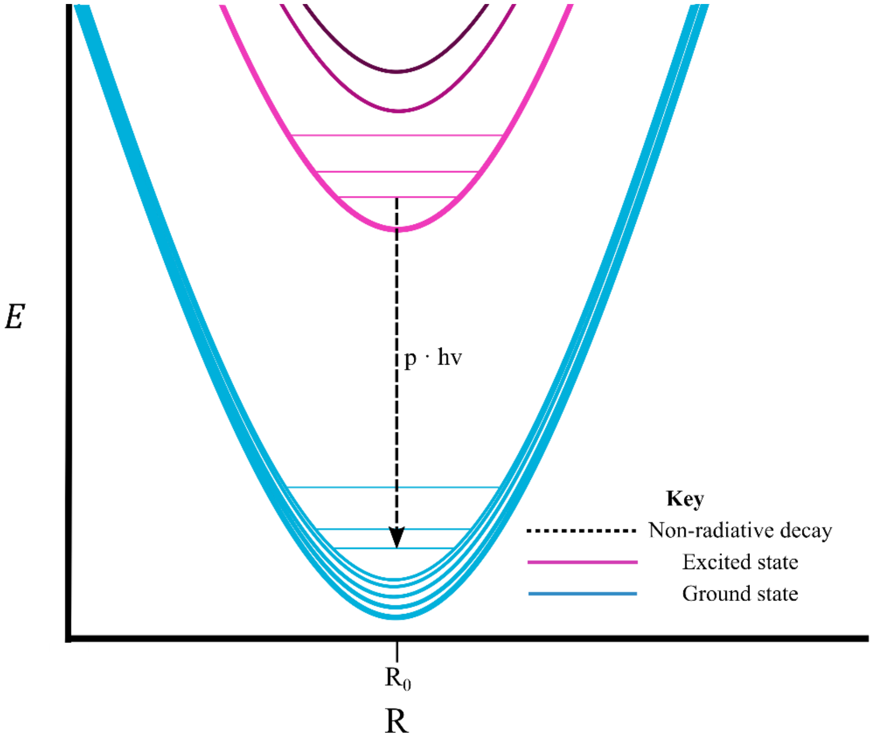

Figure 1.6: Configurational coordinate diagrams of the non-radiative pathway for multiphonon relaxation.[37] *Where p is the number of host material phonons of energy, hν, bridging the energy gap between the excited state and the ground state. Reprinted from Luminescence thermometry, 1st edition, Author(s), chapter 3, Page No. 43, Copyright (2018), with permission from Elsevier.*[1]

Multiphonon relaxation is governed by the following equation:

$$k_{NR}(T) = k_{NR}(0) \cdot \left[\frac{\exp\left(\frac{hv}{k_B T}\right)}{\exp\left(\frac{hv}{k_B T}\right) - 1}\right]^{\frac{\Delta E}{hv}} \tag{1.10}$$

where ΔE is the energy difference between excited level and the next level, hv is the dominant phonon energy of the host, and $k_{NR}(0)$ is the value of non-radiative decay at 0 K, which is dependent on electron-lattice coupling strength. The $\Delta E/hv$ variable denotes the number of phonons required to be emitted for relaxation to the ground state. The higher the number of phonons required, the lower the probability of the process occurring. For example, Eu^{3+}-doped $GdVO_4$ requires 14 phonons of the V–O tetrahedral bond vibration (884 cm^{-1}) to relax from the $^5D_0$ state to the $^7F_6$ state, an energy gap of ~12,500 cm^{-1}.[37,38] The dependence on phonon energy allows for tuning of the hosts phonon energy through structural and chemical changes. Changes to the hosts phonon energy affects the number of phonons required for multiphonon relaxation and therefore the probability of non-radiative emission occurring. This is commonly exploited in upconversion luminescence and will be covered in Sections 1.4.1.2 and 1.4.1.3.

Both the Mott-Seitz model and the multiphonon relaxation model – due to being dependent upon two coupled excited-state energy levels of a single dopant and are therefore ratiometric – can use Boltzmann's distribution as a calibration model when at thermal equilibrium. This is due to both models being extremes of each other, in terms of geometry distortion between the coupled excited states.[31,39] Both the Mott-Seitz and the multiphonon relaxation models of non-radiative decay are the basis of many singly emitting luminescence intensity ratio (*LIR*) thermometers, a topic that will be expanded upon in Section 1.3.3.1.

1.3.2 Luminescence thermometry: Figures of merit

For a luminescence thermometry measuring system the temperature is not provided as a direct value. Instead, an indication (Q) is observed such as a change in emission intensity or a ratio of emission intensities, the energy of an emission intensity maximum, a peaks width, or the decrease of an excited state's lifetime. Such indications must show a change with temperature.

Figures of merit have been devised to quantify parameters such as sensitivity, resolution, and reproducibility from the chosen indication in the field of thermometry. When the measurand is denoted Q, the absolute sensitivity, S_a is given by the change in the indication over the change in temperature:

$$S_a = \frac{\partial Q}{\partial T} \tag{1.11}$$

Absolute sensitivity depends on the indicator of the given thermometer (e.g. lifetime, intensity, peak wavelength maximum, or peak FWHM) and therefore cannot be used to compare thermometers that use different indicators.[40] Instead, relative sensitivity, S_r, is the most common figure quoted when comparing thermometric performances between different thermometers. The equation below gives a general approach to relative sensitivity.[41]

$$S_r = \frac{1}{Q}\left|\frac{\partial Q}{\partial T}\right| \tag{1.12}$$

The higher the sensitivity of the thermometer, the smaller the increments of temperature that can be determined from the indicator's changes. Both absolute and relative sensitivities must be reported with the temperature used to calculate the sensitivity. As temperature increases, emission intensity decreases due to increased non-radiative decay and both the absolute and relative sensitivities will decrease.[1]

The temperature resolution, δT, refers to the smallest temperature change that shows that a perceptible change to the indicator used:

$$\delta T = \frac{1}{S_r}\frac{\delta Q}{Q} = \frac{\sigma_r}{S_r} \tag{1.13}$$

where σ_r is the uncertainty. The lowering of noise through averaging many spectra recorded at the same temperature or through high-intensity of emission is paramount to low uncertainty values.[42] The type of detector influences the second term of this equation, potentially limiting $\delta Q/Q$. Detectors such as charge-coupled devices (CCD) and photomultiplier tubes (PMT) can give $\delta Q/Q$ = 0.03% and 0.05% respectively, with $\delta T <$ 0.003K a much higher resolution than techniques like non-contact infrared cameras (1.0 K).[43]

Spatial resolution, δx_{min}, refers to the minimum distance between points of measurement that can be resolved at a temperature difference greater than the temperature resolution:

$$\delta x_{min} = \frac{\delta T}{|dT/dx|} \tag{1.14}$$

where δx is the spatial measurement.

Temporal resolution, δt_{min}, refers to the minimum time period between measurements capable of being resolved at a temperature greater than the temperature resolution:

$$\delta t_{min} = \frac{\delta T}{|dT/dt|} \tag{1.15}$$

where δt is the temporal measurement.

Repeatability, R, obtained by cycling the probe between two temperatures and performing a measurement when the probe has achieved thermal equilibrium with the temperature stage:

$$R = 1 - \frac{\max(|\Delta_c - \Delta_i|)}{\Delta_c} \tag{1.16}$$

where Δ_c is the mean thermometric parameter from a calibration curve, and Δ_i is the value of each measurement of the thermometric parameter. Good practice for repeatability measurement is to use the same instrumentation, operator, and location. A minimum of 10 cycles of temperature is required to quantify the repeatability of a probe. Reproducibility of results, distinct from repeatability, using different instruments, operators, and locations is an important parameter that helps give confidence in a probes measurement results despite the time-consuming aspect of its testing. The dynamic temperature range denotes the smallest and largest values of temperature that can be measured by the thermometer.

1.3.3 Luminescence thermometry readout methods

Readouts can be classified as either time-resolved or time-integrated (steady-state) measurements. The former requires a pulsed or intensity modulated excitation source, whilst the latter may employ either pulsed or constant illumination.

1.3.3.1 Luminescence intensity ratio thermometry

1.3.3.1.1 Single-centre luminescence intensity ratio thermometry

One of the simplest steady-state luminescent thermometry readouts is that of the change in a single emission intensity. As temperature increases, the rate of non-radiative decay increases due to the increase in thermal energy either promoting the ion’s excited state to the cross-over point given by Mott-Seitz, *S*, or increasing the probability of phonons to return the excited state to the ground state by multiphonon relaxation at a quicker rate than can be emitted radiatively. Additionally, such an increase in temperature may also cause promotion of the electron via thermal energy to higher energy levels, thus depleting the lowest-energy transition of intensity.

Luminescence intensity ratio, or *LIR*, thermometry is a steady-state readout method that uses the ratio of two different absolute emissions from luminescent centres usually in a single host material. This ratiometric indication method is highly important due to its self-referential nature; it requires no temperature standard and eliminates problems caused by measurement conditions or the efficiency of the delivery or detection of light.

The population of higher energy excited state electrons, N_H, from the lower excited state electron population, N_L, is given by the Boltzmann equation:

$$N_H = N_L \cdot \exp\left({}^{-\Delta E}/_{k_B T}\right) \tag{1.17}$$

where ΔE is the difference in energy between the two excited states, k_B is the Boltzmann constant, and T is the temperature in Kelvin.

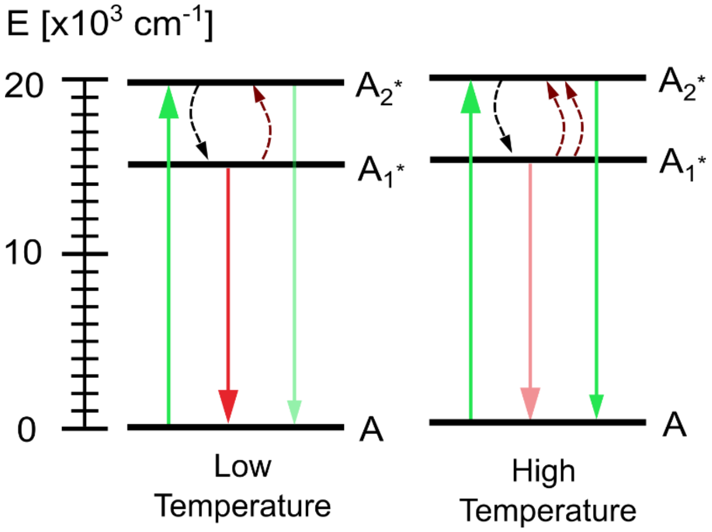

Figure 1.7: A simplified energy level diagram showing two excited states of an activator ion (A_1 and A_2*). The black dashed curved arrow indicates non-radiative decay, whilst the maroon dashed curved arrow indicates the thermal energy at high temperature. Straight solid lines denote radiative transitions.*

The intensity of a given pair of emissions can be used either from a single emission centre, or from two or more distinct emission centres.[44,45] In a single-emission centre thermometer, the ratio of the intensity of two excited state energy levels in thermal equilibrium – close enough in energy (ΔE = 200 to 2000 cm^{-1}) that the higher energy state can be thermally repopulated from the lower energy state at the temperature of interest according to the Boltzmann distribution (Figure 1.7) – are measured. The value of 200 to 2000 cm^{-1} is generally given for the energy difference between two thermally-coupled energy levels. If the energy difference is < 200 cm^{-1}, the emission peaks may be too close to discriminate, whilst if they are > 2000 cm^{-1}, the intensity of the higher lying energy level may be low due to decreased population.[46] This type of ratiometric thermometry is governed by the equation:

$$LIR = \frac{I_2}{I_1} = B\ \exp\left(-\Delta E/_{k_B T}\right) \tag{1.18}$$

$$= C \cdot \frac{\nu_2 A_2 g_2}{\nu_1 A_1 g_1} \exp\left(-\Delta E/_{k_B T}\right) \tag{1.19}$$

where *LIR* is the luminescence intensity ratio and I_2/I_1 is the ratio of the intensities emanating from the higher and lower states respectively. Moreover, $B = \nu_2 A_2 g_2 / \nu_1 A_1 g_1$, where ν is the emission barycentre frequency, A is the radiative transition probability, and g is the degeneracy of the excited state. Ln^{3+} ions are commonly used for single-emission due to the large number of thermally-coupled higher-lying excited states for many Ln^{3+} ions. There are an increasing number of examples of TM-based single-centre *LIR* thermometers, typically with Cr^{3+} or Mn^{4+}.[47]

From each calculated *LIR* point at a given temperature, the linearised *LIR* equation can be fitted.

$$\log(LIR) = \log(B) - \frac{\Delta E}{k_B} \times \frac{1}{T} \tag{1.20}$$

where the slope is equal to $-\Delta E/k_B$, and the y-intercept is equal to log(B). The energy gap, ΔE, is used in the calculation of the figures of merit. For the *LIR* readout scheme specifically, this is done using the following equations, through the use of equation 1.18, with equations 1.21 and 1.22 respectively.

$$S_a = \left|\frac{d(LIR)}{dT}\right| = \frac{\Delta E}{k_B T^2} \times LIR(T) \tag{1.21}$$

$$S_r = \frac{1}{LIR}\left|\frac{d(LIR)}{dT}\right| = \frac{\Delta E}{k_B T^2} \times 100\% \tag{1.22}$$

1.3.3.1.2 Dual-centre luminescence intensity ratio thermometry

Whilst single-centre *LIR* thermometry has dominated literature there is an additional method of LIR that allows for higher relative sensitivities than single-centre *LIR* thermometry. Should the host material permit additional dopants, two different activator ions – two Ln^{3+}, two TM ions, one of each, or even the host material's emission alongside a Ln^{3+} or TM ion – can be used to realise *LIR* thermometry.[45,48–50]

Unlike singly-doped *LIR* thermometry, dual-doped *LIR* relies on one activator ion emission, commonly an Ln^{3+} transition or spin-forbidden transition of a TM ion, being highly temperature-invariant i.e., $k_{nr}(T)$ is constant even at high temperature. The temperature-independent emission intensity is termed the reference intensity, I_{ref}. The remaining activator should be highly temperature-dependent and quench markedly with small increases in temperature. Such an emission is termed the sensing intensity, I_{sens}. The ratio of the easily-quenched emission intensity over the temperature-invariant emission is then determined.

$$LIR(T) = \frac{I_{Sens}}{I_{Ref}} = C \cdot \frac{k_r}{k_r + k_{nr}(T)} = C \cdot \tau(T) \cdot k_r \tag{1.23}$$

where τ(T) is the lifetime of the excited state of the sensing emission. Dual-doped thermometry can be used to circumvent the 200 to 2000 cm^{-1} energy difference commonly used in single- doped *LIR* thermometry, allowing for room temperature S_r values greater than those of Eu^{3+} single-centre *LIR* luminescence thermometry (2.8 % K^{-1} at 300 K due to its ΔE of 1750 cm^{-1}).[36]

1.3.3.2 Band-shift and bandwidth

As a consequence of temperature increasing, the probability of host material phonons increases. Phonons can influence both the energy of a transition – the band-shift – and the width of the peak – the bandwidth, typically given as the full-width-half-maximum (FWHM). Additionally, for TM dopants whose spectroscopic positions are highly perturbed by the crystal field, expansion of the unit cell of the material with temperature will decrease the crystal field, causing peak positions to red-shift. The peaks maximum energy or FWHM is recorded as temperature increases. The fitting for band-shift or bandwidth can be approximated with an exponential function, a polynomial function, or a Voigt function.[51–54] Unlike the readout methods mentioned in this section, band-shift must be given as an S_a value with units of either energy (cm^{-1}) or wavelength (nm), not a S_r value due to the shift from a peak being arbitrary, and thus giving arbitrary S_r values.

1.4. Materials for luminescence thermometry

1.4.1 Chemistry and structure

As mentioned in Section 1.1.1, the host material of a phosphor affects the luminescence of the activator ions, which in turn influences the luminescence thermometry figures of merit.

The following section covers three broad families of materials used as hosts for luminescence thermometry – oxides, halides, and oxyhalides – and how each is used for different types of luminescence thermometry such as downshifting and upconversion thermometry.

1.4.1.1 Oxide materials

Oxide anions are the most common anion used within luminescence thermometry.[55,56] Oxide materials typically show high thermal and chemical stability and are often easily prepared by solid-state or the sol-gel methods (discussed in further detail in Section 2.1). Of importance is the high phonon energy associated with oxide ion lattices (> 500 cm^{-1}). Higher phonon energies are critical for increased probability of multiphonon relaxation for lanthanide and spin-forbidden TM transitions. Increasing the probability of this quenching mechanism decreases intensity of emission, allowing for higher sensitivities to generally be found in oxide materials used for downshifting luminescence thermometry compared to halide and oxyhalide materials.

1.4.1.1.1 Garnet-type hosts

Garnets are materials with the general formula $A^{2+}{}_3B^{3+}{}_2(CO_4{}^{4-})_3$, where A is an 8-coordinate dodecahedral cation site, B is a 6-coordinate octahedral cation site, and C is a 4-coordinate tetrahedral cation site. Commonly the B and C cations are different oxidation states of the same element such as in $Y_3Al_5O_{12}$ (YAG) demonstrated in Figure 1.8.[57]

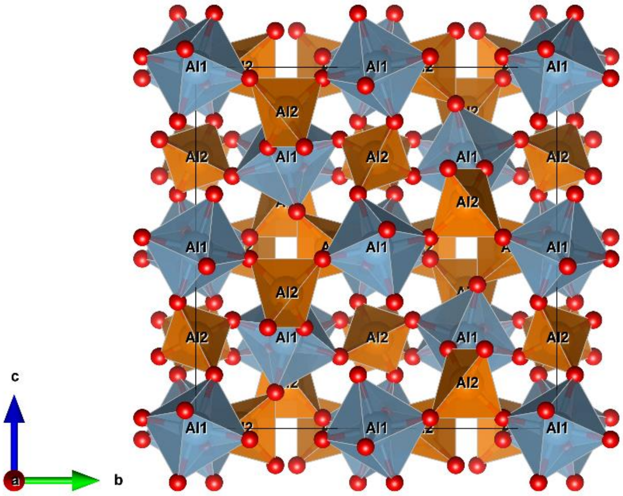

Figure 1.8: A unit cell of cubic Ia-3d YAG showing the 3D network of corner-sharing by O^{2-} (red) ions to Al^{3+} octahedra (grey) and tetrahedra (orange) – dodecahedral Y^{3+} polyhedra have been excluded for clarity. [57]

The structure is made of a network of BO_6 octahedra where each corner is shared with a CO_4 tetrahedron. Each CO_4 tetrahedron shares corners with four BO_6 octahedra (Figure 1.8).[58,59] AO_8 distorted dodecahedra fill the cavities of this network of octahedral and tetrahedra through edge-sharing to both polyhedra. This material predominantly crystallises in space group *Ia-3d*. The appeal of this material as a host is the three unique cation sites for substitution. Various TM and Ln^{3+} ions can be preferentially substituted into these sites, facilitating a wide combination of activator and sensitiser ions to be available for optical applications in the same host material.

Within the area of luminescence thermometry, garnet-type materials, especially YAG, have been used as host matrices.[47] TM and Ln^{3+} combinations for dual-emission LIR thermometry have been explored using YAG as the host material for relative sensitivity optimisation. YAG materials were synthesised with combinations of TM = Mn^{4+} and Cr^{3+}, and Ln^{3+} = Eu^{3+}, Tb^{3}+, Dy^{3+}. The combinations of Ln^{3+} and TM enables different non-radiative deactivation pathways to be used for dual-emission LIR thermometry, with a slow-quenching reference-like emission from the Ln^{3+} ion and a more sensitive, fast-quenching emission to act as the reference signal from the TM ion. For the YAG material doped with Eu^{3+} and Mn^{4+}, the S_r was calculated as 4.81% K^{-1} at ~355 K.[60]

Sensitisation via energy transfer between TM and Ln^{3+} ions was explored with YAG with TM = Cr^{3+}, Cr^{4+} and Ln^{3+} = Nd^{3+}, Er^{3+}; and TM = Cr^{3+}, Mn^{4+},$Ti^{3+,4+}$ with Ln^{3+} = Tb^{3+} and Eu^{3+} doping systems employed.[50,61] The investigations demonstrated how addition of the TM ions – preferentially doped on the octahedral site of the garnet host – can improve the S_r of the luminescence thermometers compared with the non-TM doped luminescence thermometers, through phonon-dependent energy transfer and the antenna effect.

S_r modulation by substitution on different sites of the host garnet material has been investigated.[62–64] Substitution on the A site with Ln^{3+} ions of varying radii such as La^{3+}, Gd^{3+}, and Lu^{3+}, and at the C site with ions such Al^{3+} substituting Ga^{3+}, together with varying the concentration of the Cr^{3+} activator, allowed for a systematic variation in the Cr–O bond length. The Cr–O bond length variation subsequently changes the crystal field strength experienced by the Cr^{3+} ions. The change in the crystal field affects both single-emission *LIR* and Cr^{3+}, Nd^{3+} dual-emission *LIR* S_r values.

A YAG host doped with Cr^{3+} on the octahedral site, and three rare earth ions – Ho^{3+}, Er^{3+}, and Yb^{3+} – at the dodecahedral site was synthesised to allow for all three BW to be covered using a single phosphor.[65] For each BW, a different combination of the dopants and three distinct modes were employed for temperature sensing using LIR. Excitation was achieved via upconversion using Yb^{3+} as the sensitiser of the Ln^{3+} ions, and Cr^{3+} could be excited by energy transfer from the Ln^{3+} ions. The LIR ratio of Cr^{3+} with Ho^{3+} or Er^{3+} emissions covered BW-1; BW-2 used the Ho^{3+} and Er^{3+} emissions for LIR thermometry, and BW-3 used the thermally-coupled Stark splitting – splitting caused by the crystal field – of the Er^{3+} $^4I_{13/2}$ to $^4I_{15/2}$ emission. Whilst this thermometer gave S_r values of 0.3-0.5% K^{-1} at 313 K across the three LIR modes spanning 500 to 1700 nm, it had a poor temperature resolution of 2.2 K.

YAG:0.8, 1.0, 1.5% Tm^{3+} and YAG:0.8% Dy^{3+} were demonstrated to show large changes in lifetime of emission at temperatures up to 1500°C and 1600°C respectively, with correction for increased blackbody radiation up to 1600°C.[66] It was postulated that with an improvement in equipment, YAG:Dy^{3+} could possibly be further heated ≥1800°C. This would allow for lifetime thermometry to be realised in extreme high temperature environments such as car engines and industrial operations.

From the examples given, garnet hosts have been shown that, depending on the dopant, they can give high S_r values up to ~5% K^{-1} and the ability to obtain temperature readings up to 1600°C. With their crystallographic flexibility, thermal stability, and widely researched history as a phosphor, garnet hosts continue to be a common host in luminescence thermometry research.

1.4.1.1.2 Spinel-type hosts

Materials with the spinel structure commonly crystalises in space group *Fd-3m* with general formula $A^{2+}B^{3+}{}_2X_4$, where A^{2+} are tetrahedral divalent ions, B^{3+} are octahedral trivalent ions, and X can be anions such as oxide, sulphide, and nitride.[67]

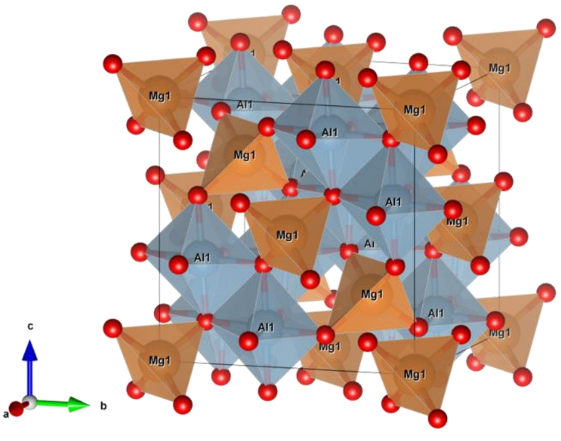

Figure 1.9: A unit cell of cubic Fd-3m $MgAl_2O_4$ showing Mg^{2+} tetrahedra (orange) corner-sharing through O^{2-} ions (red) to Al^{3+} octahedra (grey).[68]

The structure is comprised of an edge-sharing octahedral network with corner-sharing tetrahedra, where octahedra outnumber tetrahedra 2:1.[68] A spinel is classed as normal if all octahedral sites be occupied by B ions – $A(B_2)X_4$; however, if the octahedral sites are equally occupied by both A and B ions – $M(AB)X_4$ – then the spinel is termed inverse spinel.[69]

Inverse or partially inverse spinel-type materials have shown increased emission intensities, thus brighter phosphors, and shorter lifetimes of doped activator ions than normal spinel hosts due to the lower symmetry site of the activator caused by disorder in its environment.[69] In the case of the solid solution of $Mg_{1-x}Zn_xAl_2O_4:Cr_{0.01}$ (where $x = 0, 0.25, 0.5, 0.75, 1.0$), as the Mg^{2+} concentration increased the ^2E lifetime decreased compared to the $ZnAl_2O_4:Cr$ normal spinel ^2E lifetime. This was due to the Al^{3+} ions $\bar{3}m$ site symmetry decreasing as the Mg^{2+} ion occupied both tetrahedral and octahedral sites around the Cr^{3+} ion, removing its centre of inversion and lifting the parity selection rules, increase the probability of the $^2E \rightarrow {}^4A_2$ transition.

$MgAl_2O_4:Cr^{3+}$ was investigated for *LIR* luminescence thermometry of the overlapping $^4T_2$ and ^2E emission intensities caused by the strong crystal field of the host material. The spinel phosphor, after deconvolution of the emission bands, gave a high S_r of 3.5% K^{-1} at 300 K, with a temperature resolution of 0.3 K at 310 K.[70]

$ZnGa_{2-x}Ge_xO_4:Cr^{3+}$ was investigated as a multifunctional phosphor for *LIR* thermometry and bioimaging.[71] S_r was found to be 4.7% K^{-1} at physiological temperatures.

$MgGa_2O_4:Bi^{3+}$, a partially inverted spinel, was investigated for anti-counterfeiting and *LIR* thermometry.[72] Due to the inverse spinel host, Bi^{3+} could occupy two distinct sites – a tetrahedral site and an octahedral site – allowing for Bi^{3+} emission at 430 nm and 709 nm respectively, alongside emission at 500 nm from the host spinel. LIR thermometry was investigated with two different LIR measurements for I_{430}/I_{500} and I_{430}/I_{709} between 283 K and 393 K. S_r values of 2.18% K^{-1} for I_{430}/I_{500} and 2.98% K^{-1} at 283 K for I_{430}/I_{709} were achieved.

$ZnGa_2O_4:Cr^{3+}$ has been investigated for single-centre *LIR* luminescence thermometry of the ^2E and $^4T_2$ emissions of Cr^{3+}. The emission spectra were deconvoluted to allow for the broad $^4T_2$ emission and the narrow ^2E emission to be discriminated. A S_r of 2.8% K^{-1} at 310 K with a temperature resolution of 1 K at 300 K was achieved.[73]

Kniec *et al.* investigated the systematic modification of the A and B cations and their influence on the TM emissions using $MgAl_2O_4$, $MgGa_2O_4$, $CaAl_2O_4$, and $CaGa_2O_4$ hosts (space groups *Fd-3m*, *Fd-3m*, $P2_1/n$, and $Pna2_1$, respectively) with Fe^{3+}, and Fe^{3+}, Tb^{3+} dopants.[74] Changing the cation size at both the A and B sites caused the Fe–O bond length to vary, influencing the crystal field strength. Lowering of point group symmetry of the Fe^{3+} due to occupation of the tetrahedral site compared to the octahedral site was demonstrated by the broader emission bands and the reduction in $T_{1/2}$ – temperature where emission drops to 50% of its initial intensity – of the emissions, and shorter Fe^{3+} lifetimes for the Ca-spinel materials compared to the Mg-spinel materials. Maximum S_r values of 2.17% K^{-1} for $CaGa_2O_4$:Fe^{3+}, and 2.58% K^{-1} at 283 K for $CaAl_2O_4$:Fe^{3+}, Tb^{3+} were found.

All the spinel phosphors mentioned show high S_r values (>1% K^{-1}) of between 2-5% K^{-1} across a temperature range of 283 to 393 K, when doped with transition metal and post-transition metal ions. Spinel-type materials are a highly attractive phosphor hosts for luminescence thermometry due to the large S_r values demonstrated by using these materials, their high melting points, ability to influence TM optical properties based on the doping site symmetry, and capability to be multi-functional materials.

1.4.1.2 Halide materials

Halide host materials, particularly fluoride, are used predominantly within upconversion (UC) luminescence thermometers for biological applications. UC luminescence is the process by which two or more low-energy photons are used to excite a higher-lying state, allowing the emission of a higher energy photon for application such as thermometry. For high efficiency UC luminescence, excited states should be long-lived and there should be a low non-radiative decay rate. The generally low phonon energy of halide hosts reduces the non-radiative decay rate as temperature increases compared to higher energy phonons typically found in oxides (shown by Figure 1.10b). The larger number of low energy phonons, *p*, required to bridge the 5000 cm^{-1} energy gap decreases the probability of non-radiative decay from the A_2^* state to the lower A_1^* state, increasing the intensity of the A_2^* emission. In comparison, as the higher energy phonon can bridge the energy gap with a lower number of phonons, non-radiative decay is more likely, and thus the emission from the A_2^* state decreases, and the emission of the A_1^* state increases. The lower phonon energy allows for more efficient excited-state energy transfer to the appropriate activator ion from a sensitiser (most commonly Yb^{3+}, denoted *S* in Figure 1.10a using pathway 2), or for an excited activator ion, *A*, to remain in an excited state long enough to receive a second NIR photon. Hence, the low phonon energy of the halides keeps up-conversion efficiency high (pathway 1 in Figure 1.10a).[75–77] Halide materials have demonstrated UC *LIR* thermometry using lanthanide ions such as Er^{3+}, Pr^{3+}, Ho^{3+}, Tm^{3+} along with Yb^{3+} as a sensitiser ion absorbing 980 nm photons.

Generally, fluorides and chlorides hosts are used as UC phosphor hosts due to heavier halides such as bromides and iodides being hygroscopic, despite their attractively lower phonon energies. Synthesis of halide materials can require the use of toxic reagents such as trifluoroacetic acid for reagent conversion from oxides to trifluoroacetate form, or NH_4F as the fluoride ion reagent, whilst oxide hosts can typically be made through methods such as the solid-state synthesis of sesquioxide reagents.[78,79] Nanoparticles of the host are commonly synthesised to be tens of nanometres in size for use in biological media, however this form can further decrease the already low quantum yields of fluoride-host UC phosphors caused by surface defects that quench luminescence.[80]

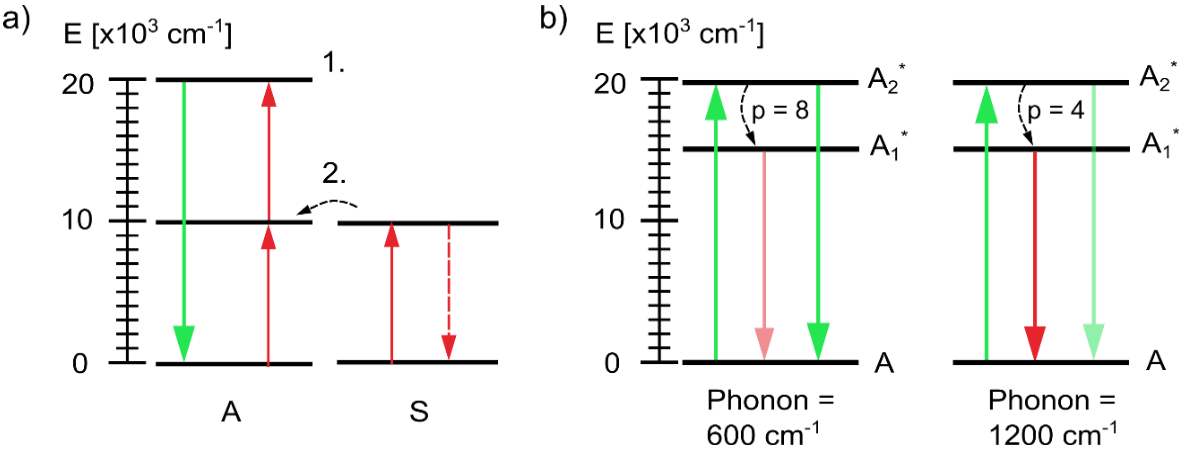

Figure 1.10: Simplified energy level diagram where solid arrows denote high energy radiative absorption and emission; red solid lines indicate low energy absorption and emission; black dashed curves represent nonradiative decay. a) A simplified schematic of UC luminescence with pathway 1 showing absorption of two NIR photons to emit a single visible light photon, and pathway 2 showing how a sensitiser ion, S, can absorb a NIR photon and transfer the energy from its excited state to the activator, A; b) A demonstration of different phonon energies on the non-radiative decay of excited states and the effect on the emission intensity. P denotes the number of phonons of the given energy required to bridge the 5000 cm^{-1} energy gap between A_1^* and A_2^* Permissions granted for reproduction of figures from John Wiley and Sons.[75]

1.4.1.2.1 Tysonite-type hosts

The tysonite-type materials with general formula MF_3 typically crystallise in the space group *P3-c1* – where each M cation is coordinated to 9 F^- anions in corner- and edge-sharing trigonal pyramids (Figure 1.11).[81] These materials have are used as optical materials such as glasses, due to their low phonon energies and low refractive index.[82] Due to this, MF_3 materials, particularly LaF_3 and YF_3, have been explored as UC luminescence thermometers.

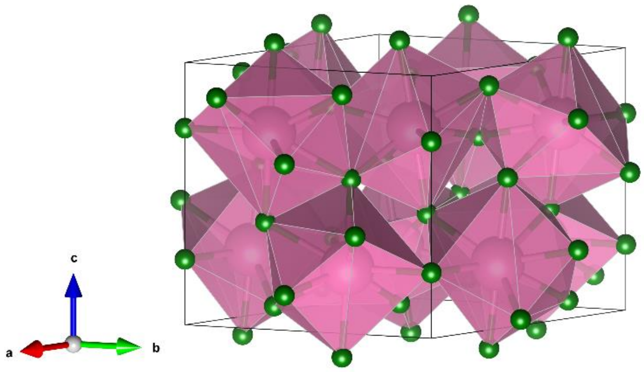

Figure 1.11: Unit cell of trigonal P3-c1 LaF_3 with La^{3+} polyhedra (pink) corner- and edge-sharing through fluoride ions (green).[81]

LaF_3:Yb^{3+}, Er^{3+} was investigated for *LIR* luminescence thermometry using the thermally coupled Er^{3+} transitions of $^2H_{11/2} \rightarrow {}^4I_{15/2}$, and $^4S_{3/2} \rightarrow {}^4I_{15/2}$.[83] S_r was calculated as 0.16% K^{-1} at 386 K.

LaF_3:Tm^{3+} was investigated for downshifting luminescence thermometry with NIR excitation at 690 nm, and emission > 1100 nm.[84] LaF_3 was able to demonstrate the $^5H_5 \rightarrow {}^5H_6$ transition of Tm^{3+}, unlike a similar $NaNbO_3$ system with the same dopants, which was concluded to be due to the lower phonon energy of the LaF_3 host (<400 cm^{-1}) compared to $NaNbO_3$ (~650 cm^{-1}).[85] S_r was calculated as 1.90% K^{-1} at 297 K when Tm^{3+} concentration was 1.0 mol%.

Orthorhombic β-YF_3:Yb^{3+}, Er^{3+} was investigated for three UC *LIR* thermometry readouts using two ratios of the Er^{3+} ion's emission in the visible wavelength range ($^2H_{11/2} \rightarrow {}^4I_{15/2}/{}^4S_{3/2} \rightarrow {}^4I_{15/2}$, and $^4F_{7/2} \rightarrow {}^4I_{15/2}/{}^4S_{3/2} \rightarrow {}^4I_{15/2}$), and a ratio of the Er^{3+} ions emission in BW-1 ($^2H_{11/2} \rightarrow {}^4I_{13/2}/{}^4S_{3/2} \rightarrow {}^4I_{13/2}$).[86] YF_3 was specifically chosen as the host material owing to its low phonon energy of ~ 500 cm^{-1}. S_r values were calculated as 1.06% K^{-1}, 2.03% K^{-1}, and 0.98% K^{-1} for the three *LIR* ratios mentioned, with temperature resolutions of 0.3, 0.7, and 1.8 K respectively.

1.4.1.2.2 Alkali metal tetrafluoride hosts

Alkali metal tetrafluorides, AMF_4, have been used as UC phosphors for display, bioimaging and luminescence thermometry, mainly in the form of nanoparticles for biological applications. AMF_4 materials with A = Li^+, Na^+, and M = Ln^{3+}, Y^{3+}, and Bi^{3+} in varying morphologies such as spherical dots, cubes, and rods have been synthesised and characterised.[87]

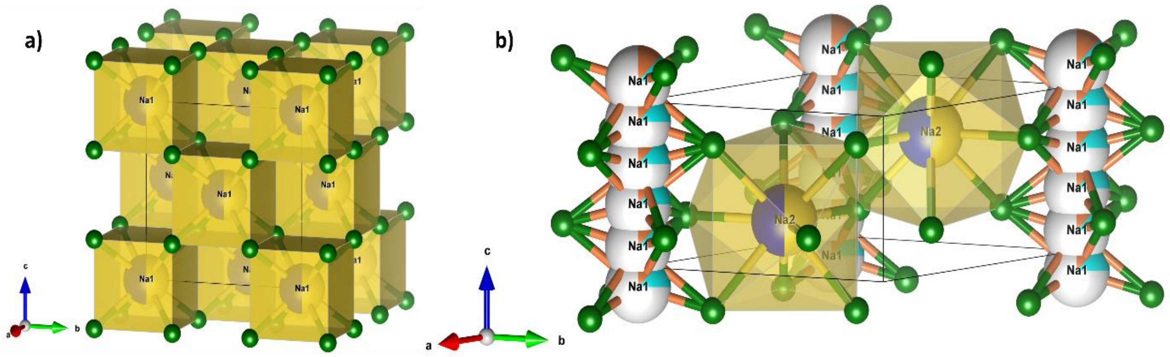

Figure 1.12: a) Unit cell of cubic Fm-3m α-$NaYF_4$, with Na1 and Y1 having 0.5 occupancy of the same site in the cubic polyhedra, b) Unit cell of hexagonal $P6_3/m$ β-$NaYF_4$ with two unique sites for Na and Y, the white spheres indicate disorder (a column of Na1/Y1 has been excluded for clarity).[90-91]

$NaYF_4$ in particular has been a highly researched material for UC due to its low phonon energy. It has been found that the polymorphism of the material significantly affects the UC luminescence intensity, as hexagonal β-$NaYF_4$ demonstrates a luminescence intensity that is an order of magnitude higher than that of cubic α-$NaYF_4$ when both are doped with Yb^{3+} and Er^{3+}. Increased UC efficiency for the hexagonal structure compared to the cubic was due to there being two unique sites for Er^{3+} and Yb^{3+} to occupy, allowing an increase in the number of $Yb^{3+} \rightarrow Er^{3+}$ processes. Additionally, the two sites in β-$NaYF_4$ have a lower site symmetry than in α-$NaYF_4$, and a shorter distance between the sensitiser and activator, further increasing the UC efficiency (Figure 1.12).[88–91]

α-$NaYF_4$:Er^{3+}, Yb^{3+} was one the earliest examples of UC thermometry demonstrating temperature sensing with HeLa cells.[92] While no S_r value was directly given, this investigation showed that the UC nanoparticles could be taken up by cells, and internal temperature through the biological matter could be measured.

Cheng *et al*. investigated UC nanoparticles of Yb^{3+}, Ho^{3+}, Tm^{3+}-doped β-$NaYF_4$ for *LIR* thermometry.[93] *LIR* of both thermally coupled (200 to 2000 cm^{-1}) and non-thermally coupled (> 2000 cm^{-1}) energy levels were explored and a maximum S_r of 1.80% K^{-1} at 345 K with a minimum temperature resolution of 0.017 K was calculated from the $^3F_3 \rightarrow {}^3H_6$ transition of Tm^{3+} with the $^5F_3 \rightarrow {}^5I_8$ transition of Ho^{3+}. Other combinations of the Tm^{3+} and Ho^{3+} emissions gave S_r values of between 0.4 and 1.0% K^{-1}.

$LiYF_4:Er^{3+}$ was recently shown to demonstrate cryogenic thermometry using the crystal field-split multiplet transitions of the $^4I_{13/2} \rightarrow {}^4I_{15/2}$, and $^4I_{11/2} \rightarrow {}^4I_{15/2}$ states for *LIR* readout method between 2.5 and 50 K.[94] Two different *LIR* values with ΔE of 4.0 cm^{-1} and 40.3 cm^{-1} were investigated from the $^4I_{13/2} \rightarrow {}^4I_{15/2}$ transition and gave S_r values of 70% K^{-1} at 3 K and 6.9% K^{-1} at 30 K. An S_r of 18.5% K^{-1} was calculated from a ΔE of 15.0 cm^{-1} from the $^4I_{11/2} \rightarrow {}^4I_{15/2}$ transition.

1.4.1.3 Oxyhalide host materials

Unlike oxides and halides, oxyhalide materials have not been as thoroughly researched as luminescence thermometry host materials.[95] However, oxyhalide materials demonstrate high chemical and thermal stabilities like oxide hosts, with a lower maximum phonon energy akin to that of halides. Phonon energy can be linked to the electronegativity of the anion, as the more covalent oxide anion presents a higher phonon energy than the highly ionic fluoride anion, and mixed oxide-fluoride anions in oxyhalide materials.[96] The combination of oxide and halide material benefits allows for a host material able to perform well for both downshifting and UC luminescence thermometry. A small number of articles have been published comparing the oxyfluoride hosts to their purely oxide and purely fluoride counterparts.[96,97]

1.4.1.3.1 Metal oxyhalide hosts

Metal oxyhalide, MOX, materials with M = Y^{3+}, La^{3+}-Nd^{3+}, Sm^{3+}-Lu^{3+}, Bi^{3+}, and X = F^-, Cl^-, Br^-, I^- are a class of phosphor that have been researched for sensing and imaging in biological media, solar cells, and less commonly for both UC and downshifting luminescence thermometry. Depending on the synthetic route, pH, fluorinating reagent, the M cation identity, and the X anion identity, the materials show a range of morphologies such as rods, spheres, bundles, and spindles; and a large variety of structure types.[95,98–100]

Liu *et al*. synthesised tetragonal $BiOF:Yb^{3+}$, Ho^{3+} for upconverting thermometry, as an analogue to BiF_3 to investigate how an oxyfluoride host material compares to a purely fluoride host.[97] It was found that the BiF_3 host has a greater UC luminescence intensity in comparison to BiOF due to phonon energies of purely F compared to O-F (~350cm^{-1} compared to ≤550cm^{-1}).[97] S_r was calculated for LIR of the $^5F_4$, $^5S_2 \rightarrow {}^5I_8$ and $^5F_5 \rightarrow {}^5I_8$

transitions, and the $^5S_2 \rightarrow {}^5I_7$ and $^5F_5 \rightarrow {}^5I_8$ transitions as 5.06 % K^{-1} and 5.41 % K^{-1} at 300 K respectively for BiF_3, compared to the BiOF host with 0.20% K^{-1} and 0.27% K^{-1} respectively. Thus, the lower phonon energy of the purely fluoride host produced a higher relative sensitivity due to increasing the upconversion efficiency.

Jakka *et al*. investigated YOF:Yb^{3+}, Ho^{3+} for UC luminescence thermometry using the *LIR* of multiple Ho^{3+} transitions. A maximum S_r of 0.81% K^{-1} at 100 K was calculated for the *LIR* of the Ho^{3+} $^5F_4 + {}^5S_2 \rightarrow {}^5I_7$ emission at 755 nm and the combined $^5F_5 \rightarrow {}^5I_8$ and $^5F_3 \rightarrow {}^5I_7$ emission at 655 nm, with an S_r of 0.32% K^{-1} at 300 K. [101]

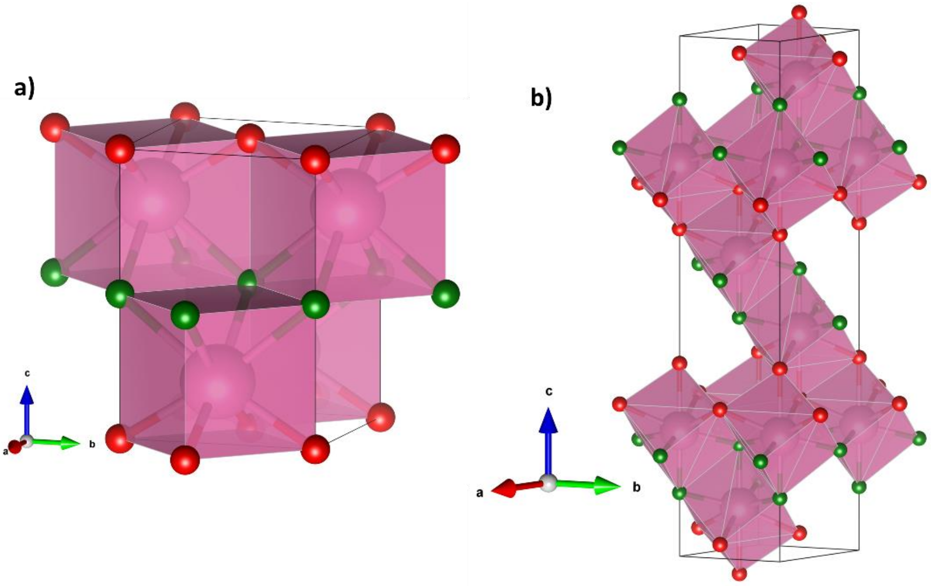

Figure 1.13: a) Unit cell of LaOF in trigonal space group R-3mH; b) Unit cell of LaOF in tetragonal space group P4/nmm. La^{3+} ions are represented as pink polyhedra coordinated by oxide (red) and fluoride (green) ion.[99-100]

Suo *et al*. studied the effect of oxide, oxyfluoride, and fluoride host materials on the S_r of a UC luminescent thermometer.[96] It was found that the phonon energy of the host materials increased from YF_3 (~350 cm^{-1}) to YOF (~480 cm^{-1}) to Y_2O_3 (~600 cm^{-1}) which impacted the intensity of emission from the higher-lying $^2H_{11/2}$, $^4S_{3/2} \rightarrow {}^4I_{15/2}$ state as lower phonon energies of the halide and oxyhalide materials increased the intensity of this green emission, compared to the oxide which gave a more red-orange colour due to increased emission from the lower-lying $^4F_{9/2} \rightarrow {}^4I_{15/2}$. Comparing the S_a values at 490 K across the YF_3, YOF and Y_2O_3 materials, the S_a increased from 0.0027×10^{-4} K^{-1} to 0.0060×10^{-4} K^{-1} to 0.0085×10^{-4} K^{-1}. It was thought that the increased covalency of the oxygen compared to the fluorine increases the S_a, as it increases the B coefficient of the *LIR* equation (Equation 1.18).

LaOF:Pr^{3+} nanorods were shown to demonstrate *LIR* thermometry using the f-f transitions of the Pr^{3+} ion.[102] It was found that increasing the calcination temperature from 500 to 700°C causes LaOF:Pr^{3+} to undergo a phase transition from tetragonal to trigonal (Figure 1.13). The phase transition changed the Pr^{3+} site symmetry from *4mm* to *3m*, enhancing the emission intensity of the Pr^{3+} in the trigonal LaOF material. *LIR* thermometry of the NIR emissions of the $^3P_0 \rightarrow {}^1G_4$ transition and the $^1G_4 \rightarrow {}^3H_5$ transition gave an S_r of 0.8% K^{-1} at 303 K with a temperature resolution of 0.17 K.

LaOF:Yb^{3+}, Er^{3+} nanoparticles were investigated using the Er^{3+} $^4I_{13/2} \rightarrow {}^4I_{15/2}$ transition's Stark levels for UC *LIR* luminescence thermometry with three individual readouts.[103] S_r values of 0.54% K^{-1}, 0.72% K^{-1}, and 0.29% K^{-1} at 303 K for *LIR* ratios using the emissions I_{1490}/I_{1531}, I_{1490}/I_{1563}, and I_{1563}/I_{1531} respectively.

LaOCl:Nd^{3+} core-shell nanoparticles were investigated as a downshifting *LIR* luminescence thermometer due to their low phonon energy (~430 cm^{-1}), highly monodispersed 10 nm particle size, and unique crystal-field splitting of the probed $^4F_{3/2} \rightarrow {}^4I_{11/2}$.[104] The *LIR* S_r calculated from two Stark emissions from the $^4F_{3/2}$ state was 0.26% K^{-1} at 290 K.

Whilst not excelling in either downshifting or UC luminescence thermometry, MOX host materials instead showcase tunability in their phonon energies, able to give moderate S_r values using either downshifting or UC luminescence pathways for successfully demonstrated luminescence thermometry.

1.5. Scope of this PhD work

The work within this thesis focuses on the structure-property relationship of phosphors containing activator ions that emit within BW-1 and BW-2 to allow for potential applications in temperature sensing.

Chapter 2 presents overviews of the main synthetic methods used to produce phosphors, and of the theory behind methods of structural and luminescence characterisation of materials investigated in following chapters.

Chapter 3 introduces the orthorhombic perovskite $LaGaO_3$ as a host material for luminescence thermometry. A series of $LaGa_{1-x}O_3$:$Cr^{3+}{}_x$ phosphors (x = 0.0, 0.2, 0.5, 1.0, 2.0, 4.0 mol%) were synthesised and characterised and their room-temperature photophysical properties were studied. Quantum yield measurements established the 1.0 mol% Cr^{3+} to be the best emitting sample and variable-temperature emission was undertaken to ascertain thermometric parameters of the ^{2}E and $^4T_2$ emission bands. The S_r of the 1.0 mol% Cr^{3+} $LaGaO_3$ sample was found to be 2.5% K^{-1} at 300 K, the highest for a $LaGaO_3$ host material.

Chapter 4 builds upon the previous chapter's perovskite $LaGaO_3$: 1.0% Cr^{3+} material and introduces dual-centre *LIR* luminescence thermometry achieved with doping Nd^{3+} as a BW-1 and BW-2 emitting centre. We find that upon higher levels of Nd^{3+} doping the emission intensity of 2.0% Nd^{3+} aids in the high temperature resolution of the phosphor. Investigation via excitation measurements show both Cr^{3+}-to-Nd^{3+} and Nd^{3+}-to-Cr^{3+} energy transfer, with efficiencies up to 40%. An S_r of 2.0% K^{-1} was achieved at 300 K with a temperature resolution of 0.04 K.

Chapter 5 focuses on oxyhalide apatite materials $A_5(V_{0.97}O_4)_3Cl$: $Mn^{5+}_{0.03}$ (where A = Sr^{2+}, Ba^{2+}) as potential luminescence thermometry materials, due to the apatite structure's crystallographic flexibility, with two A cation doping sites and isolated cation tetrahedra. Multiple temperature readouts – LIR, band-shift, and bandwidth – are reported for both materials, with multilinear parametric regression (MLR) being explored for the Sr^{2+} material. $Sr_5(V_{0.97}O_4)_3Cl$: $Mn^{5+}_{0.03}$ demonstrated a MLR S_r of 3.14% K^{-1} at 308 K, and a temperature resolution of 0.042 K.

Chapter 6 draws conclusions for all aforementioned chapters and provides a number of ideas for future work for luminescence thermometry investigations on related materials.

1.5.1 Publications

Work from Chapters 3 and 4 has been published in the following articles:

Abbi L. Mullins, *Aleksandar Ciric, Zoran Ristic , J.A. Gareth Williams, Ivana Radosavljevic Evans, Miroslav D. Dramicanin*, '**Double-deconvolution method for the separation of thermalised emissions from chromium-doped lanthanum gallate and its potential in luminescence-based thermometry**', *Journal of luminescence*, 2022, 246.

Abbi L. Mullins, *Aleksandar Ciric, Ivana Zekovic, J. A. Gareth Williams, Miroslav D. Dramicanin, and Ivana Radosavljevic Evans*, **'Dual-emission luminescence thermometry using $LaGaO_3$:Cr^{3+},Nd^{3+} phosphors'**, *Journal of Materials Chemistry C*, 2022.

Work from Chapter 5 has been submitted for consideration to Nature Communications.

1.6. References

1 M. Dramicanin, *Luminescence Thermometry: Methods, Materials, and Applications*, Elsevier Science & Technology, Duxford, United Kingdom, 2018.

2 P. Rodríguez-Sevilla, R. Marin, E. Ximendes, B. del Rosal, A. Benayas and D. Jaque, *Front. Chem.*, 2022, **10**, 1–9.

3 R. G. Geitenbeek, J. C. Vollenbroek, H. M. H. Weijgertze, C. B. M. Tregouet, A.-E. Nieuwelink, C. L. Kennedy, B. M. Weckhuysen, D. Lohse, A. van Blaaderen, A. van den Berg, M. Odijk and A. Meijerink, *Lab. Chip*, 2019, **19**, 1236–1246.

4 T. P. van Swieten, T. van Omme, D. J. van den Heuvel, S. J. W. Vonk, R. G. Spruit, F. Meirer, H. H. P. Garza, B. M. Weckhuysen, A. Meijerink, F. T. Rabouw and R. G. Geitenbeek, *ACS Appl. Nano Mater.*, 2021, **4**, 4208–4215.

5 G. Blasse and B. C. Grabmaier, *Luminescent Materials*, Springer-Verlag, 1994.

6 K.-L. Wong, J.-C. G. Bünzli and P. A. Tanner, *J. Lumin.*, 2020, **224**, 117256.

7 J. Lakowicz, *Principles of Fluorescence Spectroscopy*, Springer, 3rd edn., 2006.

8 S. W. Allison, *Meas. Sci. Technol.*, 2019, **30**, 072001.

9 V. B. Mykhaylyk, M. Rudko, H. Kraus, V. Kapustianyk, V. Kolomiets, N. Vitoratou, Y. Chornodolskyy, A. S. Voloshinovskii and L. Vasylechko, *J. Mater. Chem. C*, 2023, **11**, 656–665.

10 Z. Ma, H. Liu, S. Xie, Q. Zeng, Y. Guo and D. Wen, *Dalton Trans.*, 2023, **52**, 1650–1656.

11 L. D. Merkle, Y. Guyot and B. H. T. Chai, *J. Appl. Phys.*, 1995, **77**, 474–480.

12 M. M. Rodríguez-García, J. A. Gareth Williams and I. Radosavljevic Evans, *J. Mater. Chem. C*, 2019, **7**, 7779–7787.

13 A. A. Ansari, A. K. Parchur, M. K. Nazeeruddin and M. M. Tavakoli, *Coord. Chem. Rev.*, 2021, **444**, 214040.

14 K. Binnemans, *Coord. Chem. Rev.*, 2015, **295**, 1–45.

15 D. L. Wood, G. F. Imbusch, R. M. Macfarlane, P. Kisliuk and D. M. Larkin, *J. Chem. Phys.*, 1968, **48**, 5255–5263.

16 K. W. Park, S. G. Lim, G. Deressa, J. S. Kim, T. W. Kang, H. L. Choi, Y. M. Yu, Y. S. Kim, J. G. Ryu, S. H. Lee and T. H. Kim, *J. Lumin.*, 2015, **168**, 334–338.

17 L. Xing, W. Yang, D. Ma and R. Wang, *Sens. Actuators B Chem.*, 2015, **221**, 458–462.

18 W. M. Yen, S. Shionoya and H. Yamamoto, Eds., *Phosphor handbook*, CRC Press/Taylor and Francis, Boca Raton, FL, 2nd ed., 2007.

19 A. N. Bashkatov, E. A. Genina, V. I. Kochubey and V. V. Tuchin, *J. Phys. Appl. Phys.*, 2005, **38**, 2543–2555.

20 C. J. Jones, *d- and f-block chemistry*, RSC, 2001.

21 C. E. Wayne and R. P. Wayne, *Photochemistry*, Oxford University Press, Oxford, 1st edn., 1996.

22 M. J. Winter, *d-block chemistry*, Oxford University Press, Oxford, 2nd edn., 2015.

23 J.-C. G. Bünzli and S. V. Eliseeva, *Chem. Sci.*, 2013, **4**, 1939–1949.

24 J.-C. G. Bünzli and S. V. Eliseeva, in *Lanthanide Luminescence*, eds. P. Hänninen and H. Härmä, Springer Berlin Heidelberg, Berlin, Heidelberg, 2010, vol. 7, pp. 1–45.

25 S. Ray, P. Pramanik, A. Singha and A. Roy, *J. Appl. Phys.*, 2005, **97**, 094312.

26 M. Skorczakowski, J. Swiderski, W. Pichola, P. Nyga, A. Zajac, M. Maciejewska, L. Galecki, J. Kasprzak, S. Gross, A. Heinrich and T. Bragagna, *Laser Phys. Lett.*, 2010, **7**, 498.

27 R. Birang, J. Poursamimi, N. Gutknecht, F. Lampert and M. Mir, *Lasers Med. Sci.*, 2007, **22**, 21–24.

28 Y. Tanabe and S. Sugano, *J. Phys. Soc. Jpn.*, 1954, **9**, 753–766.

29 Y. Tanabe and S. Sugano, *J. Phys. Soc. Jpn.*, 1954, **9**, 766–779.

30 Tanabe-Sugano Diagrams, https://chem.libretexts.org/Bookshelves/Inorganic_Chemistry/Supplemental_Modules_and_Websites_(Inorganic_Chemistry)/Crystal_Field_Theory/Tanabe-Sugano_Diagrams, (accessed 30 June 2021).

31 C. D. S. Brites, R. Marin, M. Suta, A. N. Carneiro Neto, E. Ximendes, D. Jaque and L. D. Carlos, *Adv. Mater.*, 2023, **35**, 2302749.

32 C. Brites, P. Pereira, N. João, A. Millán, V. Amaral, F. Palacio and L. Carlos, *Front. Chem.*, 2013, **1**, 1–6.

33 K. Okabe, N. Inada, C. Gota, Y. Harada, T. Funatsu and S. Uchiyama, *Nat. Commun.*, 2012, **3**, 705.

34 R. W. Gurney and N. F. Mott, *Trans. Faraday Soc.*, 1939, **35**, 69–73.

35 F. Seitz, *Trans. Faraday Soc.*, 1939, **35**, 74–85.

36 M. D. Dramićanin, *Methods Appl. Fluoresc.*, 2016, **4**, 042001.

37 L. A. Riseberg and H. W. Moos, *Phys. Rev.*, 1968, **174**, 429–438.

38 Yu. K. Voron’ko, A. A. Sobol’, V. E. Shukshin, A. I. Zagumennyĭ, Yu. D. Zavartsev and S. A. Kutovoĭ, *Phys. Solid State*, 2009, **51**, 1886–1893.

39 C. W. Struck and W. H. Fonger, *J. Lumin.*, 1975, **10**, 1–30.

40 P. V. dos Santos, M. T. de Araujo, A. S. Gouveia-Neto, J. A. Medeiros Neto and A. S. B. Sombra, *Appl. Phys. Lett.*, 1998, **73**, 578–580.

41 S. F. Collins, G. W. Baxter, S. A. Wade, T. Sun, K. T. V. Grattan, Z. Y. Zhang and A. W. Palmer, *J. Appl. Phys.*, 1998, **84**, 4649–4654.

42 T. P. van Swieten, A. Meijerink and F. T. Rabouw, *ACS Photonics*, 2022, **9**, 1366–1374.

43 C. D. S. Brites, A. Millan and L. D. Carlos, in *Handbook on the Physics and Chemistry of Rare Earths*, Elsevier, 2016, vol. 49, pp. 339–427.

44 A. L. Mullins, A. Ćirić, Z. Ristić, J. A. G. Williams, I. R. Evans and M. D. Dramićanin, *J. Lumin.*, 2022, **246**, 118847.

45 A. L. Mullins, A. Ćirić, I. Zeković, J. A. G. Williams, M. D. Dramićanin and I. R. Evans, *J. Mater. Chem. C*, 2022, **10**, 10396–10403.

46 C. Wang, Y. Jin, R. Zhang, Q. Yao and Y. Hu, *J. Alloys Compd.*, 2022, **894**, 162494.

47 L. Marciniak, K. Kniec, K. Elżbieciak-Piecka, K. Trejgis, J. Stefanska and M. Dramićanin, *Coord. Chem. Rev.*, 2022, **469**, 214671.

48 A. Ćirić, J. Periša, M. Medić, S. Kuzman, Z. Ristić, Ž. Antić and M. D. Dramićanin, *Ceram. Int.*, 2021, **47**, 31915–31919.

49 J. Drabik, B. Cichy and L. Marciniak, *J. Phys. Chem. C*, 2018, **122**, 14928–14936.

50 W. Piotrowski, L. Dalipi, R. Szukiewicz, B. Fond, M. Dramicanin and L. Marciniak, *J. Mater. Chem. C*, 2021, **9**, 12671–12680.

51 J. Periša, Z. Ristić, W. Piotrowski, Ž. Antić, L. Marciniak and M. D. Dramićanin, *RSC Adv.*, 2021, **11**, 15933–15942.

52 A. Ćirić, S. Stojadinović, Z. Ristić, I. Zeković, S. Kuzman, Ž. Antić and M. D. Dramićanin, *Adv. Mater. Technol.*, 2021, **6**, 2001201.

53 A. Ćirić, S. Stojadinović and M. D. Dramićanin, *Sens. Actuators Phys.*, 2019, **295**, 450–455.

54 T. A. Alrebdi, A. N. Alodhayb, Z. Ristić and M. D. Dramićanin, *Sensors*, 2023, **23**, 3839.

55 F. Jahanbazi and Y. Mao, *J. Mater. Chem. C*, 2021, **9**, 16410–16439.

56 M. D. Dramićanin, *J. Appl. Phys.*, 2020, **128**, 040902.

57 A. Speghini, F. Piccinelli and M. Bettinelli, *Opt. Mater.*, 2011, **33**, 247–257.

58 A. F. Wells, *Structural Inorganic Chemistry*, Oxford University Press, Oxford, 5th edn., 1984.

59 A. Emiraliev, A. Kocharov, R. Bakradze, U. Karimov and Z. Ahmetzhanov, *Kristallografiya*, 1976, **21**, 211–213.

60 D. Chen, S. Liu, Y. Zhou, Z. Wan, P. Huang and Z. Ji, *J. Mater. Chem. C*, 2016, **4**, 9044–9051.

61 W. Piotrowski, K. Kniec and L. Marciniak, *J. Alloys Compd.*, 2021, **870**, 159386.

62 K. Elzbieciak and L. Marciniak, *Front. Chem.*, 2018, **6**, 1–8.

63 K. Elzbieciak, A. Bednarkiewicz and L. Marciniak, *Sens. Actuators B Chem.*, 2018, 96–102.

64 K. Elzbieciak-Piecka, C. Matuszewska and L. Marciniak, *New J. Chem.*, 2019, **43**, 12614–12622.

65 Z. Wang, M. Jia, M. Zhang, X. Jin, H. Xu and Z. Fu, *Inorg. Chem.*, 2021, **60**, 14944–14951.

66 M. R. Cates, S. W. Allison, S. L. Jaiswal and D. L. Beshears, *YAG:Dy and YAG:Tm Fluorescence Above 1400 C.*, Oak Ridge National Laboratory, 2003.

67 Y. Wang, W.-B. Chen, F.-Y. Liu, D.-W. Yang, Y. Tian, C.-G. Ma, M. D. Dramićanin and M. G. Brik, *Results Phys.*, 2019, **13**, 102180.

68 T. Yamanaka and Y. Takéuchi, *Z. Für Krist. - Cryst. Mater.*, 1983, **165**, 65–78.

69 Ž. Antić, V. Đorđević, Z. Ristić, A. M. Srivastava, W. W. Beers, M. D. Dramićanin and M. G. Brik, *J. Lumin.*, 2023, 120190.

70 A. Ćirić, Z. Ristić, J. Periša, Ž. Antić and M. D. Dramićanin, *Ceram. Int.*, 2021, **47**, 27151–27156.

71 J. Yang, Y. Liu, Y. Zhao, Z. Gong, M. Zhang, D. Yan, H. Zhu, C. Liu, C. Xu and H. Zhang, *Chem. Mater.*, 2017, **29**, 8119–8131.

72 P. Liu, Y. Zhang, B. Li, L. Han and Y. Xu, *Chem. Eng. J.*, 2022, **437**, 135389.

73 J. Ueda, M. Back, M. G. Brik, Y. Zhuang, M. Grinberg and S. Tanabe, *Opt. Mater.*, 2018, **85**, 510–516.

74 K. Kniec, W. Piotrowski, K. Ledwa, L. D. Carlos and L. Marciniak, *J. Mater. Chem. C*, 2021, **9**, 517–527.

75 R. Naccache, Q. Yu and J. A. Capobianco, *Adv. Opt. Mater.*, 2015, **3**, 482–509.

76 F. E. Auzel, *Proc. IEEE*, 1973, **61**, 758–786.

77 J. L. Sommerdijk and A. Bril, *Philips tech. Rev.*, 1974, **34**, 24–32.

78 R. Naccache, F. Vetrone, V. Mahalingam, L. A. Cuccia and J. A. Capobianco, *Chem. Mater.*, 2009, **21**, 717–723.

79 P. Lei, R. An, S. Yao, Q. Wang, L. Dong, X. Xu, K. Du, J. Feng and H. Zhang, *Adv. Mater.*, 2017, **29**, 1700505.

80 A. Gulzar, J. Xu, P. Yang, F. He and L. Xu, *Nanoscale*, 2017, **9**, 12248–12282.

81 M. Mansmann, *Z. Für Krist.*, 1965, **122**, 375–398.

82 I. Cozmuta, S. Cozic, M. Poulain, S. Poulain and J. R. L. Martini, in *Optical Components and Materials XVII*, SPIE, 2020, pp. 133–147.

83 X. Cheng, X. Ma, H. Zhang, Y. Ren and K. Zhu, *Phys. B Condens. Matter*, 2017, **521**, 270–274.

84 E. C. Ximendes, A. F. Pereira, U. Rocha, W. F. Silva, D. Jaque and C. Jacinto, *Nanoscale*, 2019, **11**, 8864–8869.

85 K. U. Kumar, N. Vijaya, J. Oliva, C. Jacinto, E. de La Rosa and C. K. Jayasankar, *Mater. Express*, 2012, **2**, 294–302.

86 A. Ćirić, J. Aleksić, T. Barudžija, Ž. Antić, V. Đorđević, M. Medić, J. Periša, I. Zeković, M. Mitrić and M. D. Dramićanin, *Nanomaterials*, 2020, **10**, 627.

87 J. Ren, G. Jia, Y. Guo, A. Wang and S. Xu, *J. Phys. Chem. C*, 2016, **120**, 1342–1351.

88 A. Aebischer, M. Hostettler, J. Hauser, K. Krämer, T. Weber, H. U. Güdel and H.-B. Bürgi, *Angew. Chem. Int. Ed.*, 2006, **45**, 2802–2806.

89 K. W. Krämer, D. Biner, G. Frei, H. U. Güdel, M. P. Hehlen and S. R. Lüthi, *Chem. Mater.*, 2004, **16**, 1244–1251.

90 D. M. Roy and R. Roy, *J. Electrochem. Soc.*, 1964, **111**, 421–428.

91 S. Ling, X. Qin, C. Chen, K. Meng, Y. Yan, J. Ming, S. Liao, Y. Huang and L. Hou, *J. Alloys Compd.*, 2023, **940**, 168923.

92 F. Vetrone, R. Naccache, A. Zamarrón, A. Juarranz de la Fuente, F. Sanz-Rodríguez, L. Martinez Maestro, E. Martín Rodriguez, D. Jaque, J. García Solé and J. A. Capobianco, *ACS Nano*, 2010, **4**, 3254–3258.

93 Z. Cheng, M. Meng, J. Wang, Z. Li, J. He, H. Liang, X. Qiao, Y. Liu and J. Ou, *Nanoscale*, 2023, **15**, 11179–11189.

94 K. N. Boldyrev, M. Diab, S. A. Klimin and M. N. Popova, *J. Lumin.*, 2024, 120591.

95 M. Udayakantha, P. Schofield, G. R. Waetzig and S. Banerjee, *J. Solid State Chem.*, 2019, **270**, 569–592.

96 H. Suo, C. Guo, J. Zheng, B. Zhou, C. Ma, X. Zhao, T. Li, P. Guo and E. M. Goldys, *ACS Appl. Mater. Interfaces*, 2016, **8**, 30312–30319.

97 R. Liu, Y. Pan, J. Zhang, X. Zhuang, Y. Wang, X. Zhou, S. Du, H. Li and W. Li, *J. Lumin.*, 2023, **258**, 119791.

98 Y. Zhang, X. Li, Z. Hou and J. Lin, *Nanoscale*, 2014, **6**, 6763–6771.

99 K. Hibino, M. Tanaka, S. Kozakai, K. Fujii, T. Ishihara, J. R. Hester and M. Yashima, *ACS Appl. Energy Mater.*, 2021, **4**, 8891–8900.

100 J. Dabachi, M. Body, J. Dittmer, F. Fayon and C. Legein, *Dalton Trans.*, 2015, **44**, 20675–20684.

101 S. K. Jakka, M. J. Soares, M. P. F. Graça, A. J. Neves, P. C. Nagajyothi and P. K, *Opt. Mater.*, 2022, **129**, 112442.

102 S. Tamboli, G. B. Nair, Z. Xia, S. J. Dhoble and H. C. Swart, *Ceram. Int.*, 2023, **49**, 23579–23590.

103 G. B. Nair, S. Tamboli, S. J. Dhoble and H. C. Swart, *ACS Appl. Nano Mater.*, 2023, **6**, 15255–15265.

104 C. Renero-Lecuna, A. Herrero, D. Jimenez de Aberasturi, M. Martínez-Flórez, R. Valiente, M. Mychinko, S. Bals and L. M. Liz-Marzán, *J. Phys. Chem. C*, 2021, **125**, 19887–19896.

2. Experimental methods

2.1. Fundamentals of solid-state synthesis

2.1.1 Ceramic method

The ceramic method is the most common solid-state synthetic route for the preparation of inorganic polycrystalline materials. By this method, highly pure solid reagents (most commonly oxides of the required elements) are accurately weighed out in the stoichiometries corresponding to those of elements in the desired product. The resultant mix of reagents is ground thoroughly, either manually using a mortar and pestle – commonly made of inert, non-porous material such as agate – or by a mechanical means such as a ball-mill. Grinding is used to give a homogenous mixture of all the reagents, ensuring uniform dispersion within the sample, and also to decrease the size of reactant grains, which increases the surface area of contact. Increasing the surface area of contact between the reagents is key to the diffusion via mass transport when dwelling at the desired high temperature. Reactions occur at the grain boundaries, forming product. However, product formation hinders diffusion of unreacted reagent, slowing down the reaction.[1]

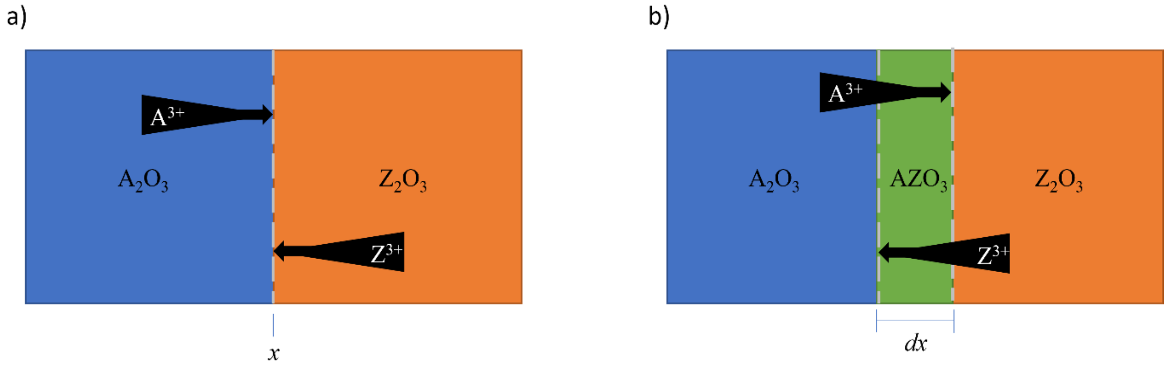

Figure 2.1: Two different reactant grains meeting at a grain boundary: a) shows the concentration gradients between the two reagents; b) shows how the product is formed at the grain boundary, and ions must now diffuse through this product to react at the interface.

As Figure 2.1 shows, when two grains of different reagents meet, their interface forms a grain boundary. The concentration of A^{3+} is high in the blue region on the left, and low on the right, and vice versa for the Z^{3+} in the orange. Diffusion is driven by the concentration gradient of the ions according to Fick's 1st law of diffusion (Equation 2.1).

$$J = D\left(\frac{dc}{dx}\right) \tag{2.1}$$

where J is the diffusion flux, a measure of the flow of substance through an area over a given time; D is the diffusion coefficient; c is the concentration of the diffusing species; and x is the pathlength travelled.

The diffusion coefficient D is proportional to the temperature T through the Einstein equation (Equation 2.2).

$$D = \mu k_B T \tag{2.2}$$

where μ is the particle's mobility and k_B is the Boltzmann constant.[2]

After grinding, the powder can be pressed into pellets or rods by mechanical or pneumatic pressure using pellet presses. The pressing of the powder brings more particle grain boundaries of different reagents into contact, thus increasing the rate of diffusion. Grinding, pressing, and heating can be carried out multiple times during a single synthesis to ensure that the unreacted reagents are redistributed through the sample and are able to undergo further reaction with other unreacted material to give the intended phase-pure product.

High temperatures from 500 to 2000°C are typically required for ceramic synthesis.[1] This generally leads to the formation of the most thermodynamically stable phase. Tammann's rule of metallurgy can be employed where, for a high rate of diffusion to occur without the material melting, a temperature of two-thirds the lowest reagent melting point is employed.[3] The sample must be contained in the furnace within a crucible or boat vessel. These vessels are required to withstand the high temperatures required for long synthesis, whilst also being inert to the reagents and product sample themselves. Crucibles are commonly made of porcelain, steel, platinum, or alumina.[1]

Variable parameters including dwell time, heating and cooling ramp rate, and dwell temperature are controlled to promote formation of the desired product phase. Morphology of particles is hard to control when using the conventional solid-state method, as multiple heatings can cause agglomeration, making production of nano-sized particles difficult.

2.1.2 Sol-Gel method

As an alternative synthetic route, the sol-gel method uses a liquid colloidal suspension (or sol form) of the required precursors that is concentrated further to form a gel structure, before being calcinated to the final powdered ceramic product.

Sol-gel synthesis can improve the homogeneity of starting material. The solvation of the metal ions in sol-gel synthesis enables atomic level intimate mixing. In contrast, solid-state synthesis makes use of ground powdered reagents and is limited by the particle size that can be achieved through grinding. Intimate mixing can suppress the formation of impurities by decreasing the segregation of dissolved starting materials. Additionally, this thorough mixing enables the synthesis to be conducted at lower temperatures than their solid-state counterparts, reducing the loss of volatile reagents. The colloidal sol suspension contains uniformly sized particles between 1 and 100 nm in diameter. The pH of the liquid suspension is critical in maintaining the non-aggregated nature of the colloids, and to enhance cation binding to chelating agents such as citrate. The gel stage is achieved by either heating the colloidal sol or by ageing the suspension, which polymerises the dispersed colloidal particles into a matrix in which solvent molecules are trapped. The form adopted by the gel can differ significantly according to slight changes to the synthetic route, from spongy and porous to a viscous resin-like liquid. For example, pH changes affect the gel morphology, influencing the final product's structure, and particle size.[4] The final product is formed by calcination in a furnace to remove the unwanted solvent from within the gel matrix by boiling off as gases. This also allows crystallisation to occur, and oxides to form from alkoxide and carbonate gels.

2.1.2.1 Small-molecule method

The small-molecule sol-gel route differs from the general sol-gel synthesis due to the addition of low-molecular-weight chelating agents.[5] The choice of chelating agent influences both the structure and the hydrolysis equilibria of metal species present in the sol. The citrate sol-gel method is widely employed. Usually, nitrates of the required metal ions are employed due not only to their high solubility in water, but also to their volatility when pyrolysed. The nitrate also acts as an oxidiser to help decompose the bound citrate as CO_2 and CO in a subsequent self-propagation combustion step at approximately 200°C.[6]

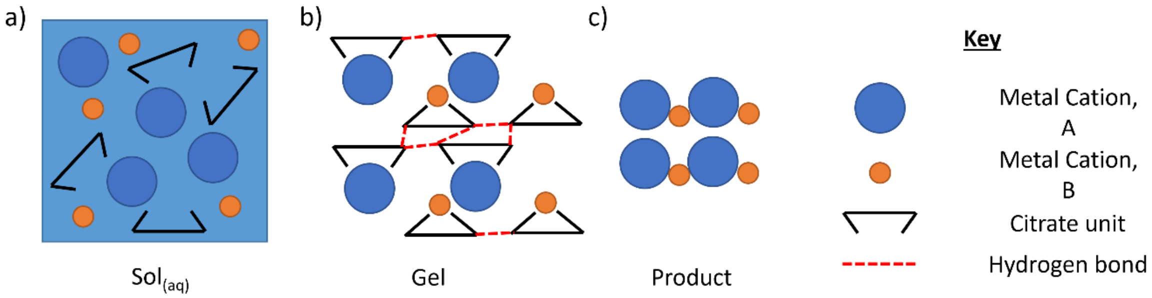

Figure 2.2 a) Intimately mixed aqueous metal ions with citrate; b) dehydrated gel with citrate-bound metal ions held together via hydrogen bonds between citrate -COOH groups in a 3D network; c) ceramic product post sintering of organic citrate unit.

Citric acid – a weakly triprotic organic molecule – is added as one such chelating agent. Bases such as ammonium hydroxide are added to modify the sol's pH. This is a common method in mixed metal-oxide synthesis. Each metal ion is chelated by a citrate ion, and a 3D templated network of citrate-bound reactants is formed (the gel) via hydrogen bonds between adjacent citrate -COOH groups.[7] Variation of the molar ratio of metal cations to citrate is an important factor in the control of impurities.[8] Figure 2.2 offers a diagram of the small-molecule sol-gel process employing citrate as the binding unit.

2.2. Fundamentals of X-ray diffraction (XRD)

2.2.1 The theory of X-ray diffraction

Diffraction is a phenomenon whereby a propagating wave bends around obstacles or passes through openings with widths comparable to the wavelength, by coherent, elastic scattering. Electromagnetic radiation, such as visible light or X-rays, are periodic waves with characteristics such as a phase, amplitude, and a wavelength. Separate waves can interact via superposition constructively by enhancing their amplitude, or destructively thereby diminishing or completely cancelling their amplitude.

The periodic, ordered arrangement of atoms in a crystalline substance act as a diffraction grating to X-rays. This is due to the order of magnitude of interatomic distances being similar to that of the wavelength of X-rays (~0.5 - 2.5 Å). It allows for information about the 3D arrangement of atoms within crystalline solids to be obtained from the coherent scattering of X-rays by atoms.

2.2.1.1 Peak positions

For simplicity, we can visualise the process of diffraction from crystalline solids as a set of parallel, incident beams of X-rays being reflected by parallel planes of atoms with the interplanar spacing, d_{hkl} where *h*, *k*, and *l* are Miller indices – notation for imaginary planes of atoms. Incident waves of X-rays, S_O, interact with the electron cloud of the atoms within the solid. Interaction between the incident X-ray's electric field and the electron cloud causes elastic scattering of X-ray radiation, *S*.

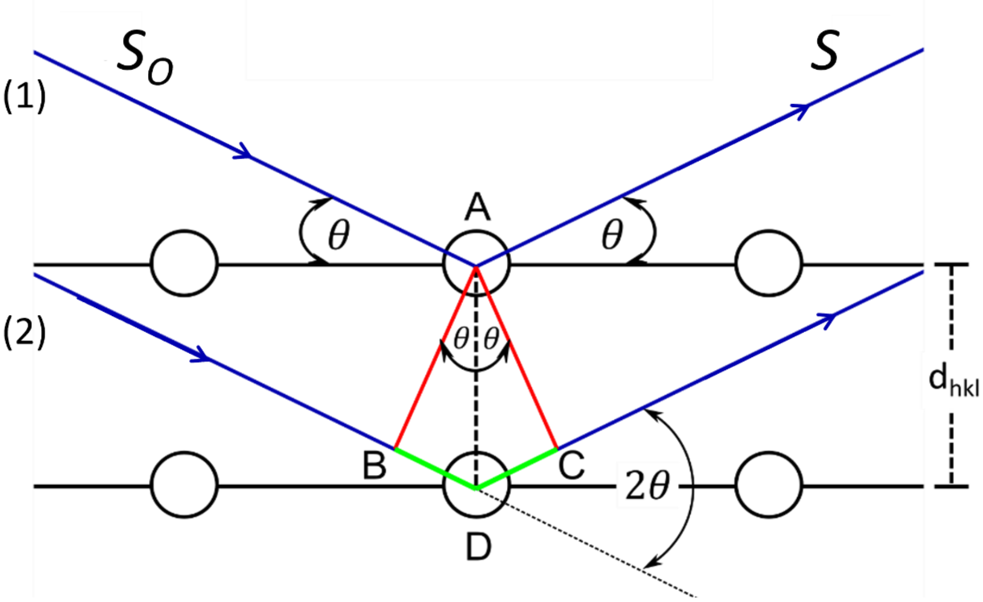

Figure 2.3: Bragg's Law – An incident wavefront of X-rays, S_o, is reflected at angle θ, by parallel planes of atoms with spacing, d_{hkl}. The pathlength difference between layers of atoms, Δ, is shown in green.

As shown in Figure 2.3, for the mirror-like reflection to occur, the angle of incidence must equal the angle of reflection, θ. For constructive interference of the reflected X-rays to occur, the difference in pathlength between waves 1 and 2, *BD* + *DC* (denoted in green in Figure 2.3), between the incident and the reflected X-rays must equal an integer multiple of the X-ray wavelengths, λ.

This relationship between constructive interference and pathlength leads through Equations 2.3 and 2.4 to the Bragg's Law (Equation 2.5):[9]

$$Path\ difference = BD + DC = n\lambda \tag{2.3}$$

$$d_{hkl}sin\theta + d_{hkl}sin\theta = BD + DC = n\lambda \tag{2.4}$$

$$2d_{hkl}sin\theta = n\lambda \tag{2.5}$$

where n is an integer multiple of the X-ray wavelength.

For each crystal system there is a unique relation between the d-spacing and the unit cell parameters a, b, c, which denote unit cell lengths; and α, β, γ which denote unit cell angles. For example, for the orthorhombic crystal system, the equation is:

$$\frac{1}{(d_{hkl})^2} = \frac{h^2}{a^2} + \frac{k^2}{b^2} + \frac{l^2}{c^2} \qquad (2.6)$$

Using Equations 2.5 and 2.6, alongside a fixed wavelength, the peak positions for known unit cell parameters can be predicted. Conversely, parameters of an unknown unit cell can be calculated from the peak positions of experimental data, which is termed 'diffraction pattern indexing'.

2.2.1.2 Peak intensities

While Bragg's Law gives the relationship between peak positions and the unit cell parameters of a crystalline sample, the intensities of the individual *hkl* reflections contain information about the atomic positions and the identity of the atoms present within a unit cell. The structure factor is the collective scattering of all atoms in the unit cell, and characteristic for each individual *hkl* reflection. The structure factor is defined as the following summation over every atom, N, within the unit cell:

$$F_{hkl} = \sum_{1}^{N} f_n \times e^{[2\pi i(hx_n + ky_n + lz_n)]} \times t_n \times occ_n \qquad (2.7)$$

where t_n is the Debye-Waller factor, a term that contains the atomic displacement factor, B_n, which is affected by temperature.[10] f_n is the atomic scattering factor for individual atom, n. The exponential term contains atomic fractional coordinates x_n, y_n, and z_n. The peak intensities, I_{hkl}, are proportional to $|F_{hkl}|^2$, the square of the modulus of the structure factor.

$$I_{hkl} = |F_{hkl}|^2 \times k \times LP \times m \times a \times y \qquad (2.8)$$

The dependence is proportional, and not equality, as the intensities are also dependent on a scalar to the calculated pattern used to fit the observed data (k), the absorption of X-rays by the sample (a), peak multiplicity (m), Lorentz-polarisation factor (LP), and other sample and instrumental parameters (y).[10]

2.2.3. Powder X-ray diffraction

Should a crystal of sufficient size or quality for single-crystal X-ray diffraction (SC-XRD) be unobtainable then powder X-ray diffraction (PXRD) can be used to probe polycrystalline sample structures. PXRD is used as a qualitative method to investigate materials under working conditions such as high or low temperatures. Additionally, PXRD allows for a mixture of phases to be identified and quantitatively measured, a highly important use for monitoring reactions and within industrial and scientific settings.

2.2.3.1 Contents of a powder pattern

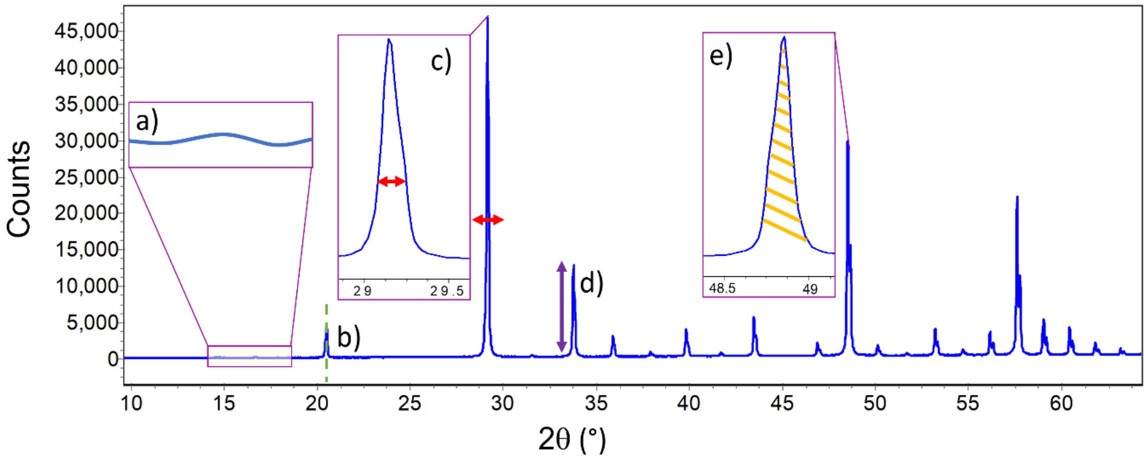

Figure 2.4: A representative diffraction pattern illustrating a) background, b) peak position, c) peak width, d) peak intensity, e) peak area.[9] *the blue line indicates experimental data.*

The output of a powder X-ray diffraction experiment is a diffraction pattern. Different types of information can be gained from individual components of the diffraction pattern (Figure 2.4) including:[10–12]

- *Background*: Short range order, local structure.
- *Peak position*: Unit cell parameters (a, b, c, α, β, γ).
- *Peak intensity*: Atom type; atomic positions, space group.
- *Peak area*: Phase wt% in a multiphase mixture.
- *Peak width and profile*: Crystallite size, strain within a crystal, stacking faults, and instrument broadening.

2.2.4 Rietveld refinement

The Rietveld method uses whole-pattern fitting to perform structure refinement.[13] The peak positions are calculated from lattice parameters using Equation 2.5 and the appropriate d-spacing equation for the desired crystal system. Equation 2.8, along with the appropriate space group and atomic fractional co-ordinates, generates the calculated peak intensities. This calculated pattern of peaks and intensities can then be fitted using an iterative non-linear least-squares refinement method to an experimentally observed PXRD pattern.

The difference, *S*, between calculated, y_{calc}, and observed, y_{obs}, intensities for each step in $2\theta = i$ are minimised by refining parameters until convergence.

$$S = \sum_{i=1}^{N} w_i \left(y_{obs_i} - y_{calc_i}\right)^2 \tag{2.9}$$

where the weighting, w_i, is $1/\sigma_i(y_{i,\,obs})^2$, and σ_i is the standard deviation of each step, i.[14]

The agreement between the experimental and the calculated data is shown as a difference curve; the closer the fit the flatter the curve. A numerical indicator of agreement between the experimental data and calculated data, the weighted R-factor, R_{wp}, is often cited.

$$R_{wp} = \left[\frac{\sum w_i \left(y_{i,obs} - y_{i,calc}\right)^2}{\sum w_i \left(y_{i,obs}\right)^2}\right]^{1/2} \tag{2.10}$$

While a lower R_{wp} value is indicative of a better fit between the observed data and the calculated data, it is not the sole guide. Goodness-of-fit, GOF, measures the quality of a Rietveld refinement, using a ratio, χ, of factors including the weighted R-factor (Equation 2.8), and the expected R-factor, R_{exp}.

$$R_{exp} = \left[\frac{N - P}{\sum_{i=1}^{N} w_i \left(y_{i,obs}\right)^2}\right]^{1/2} \tag{2.11}$$

$$GoF = \frac{R_{wp}}{R_{exp}} = \sqrt{\frac{\sum_{i=1}^{N} w_i \left(y_{i,obs} - y_{i,calc}\right)^2}{N - P}} \tag{2.12}$$

where *N* is the number of data points, and *P* is the number of parameters.

2.2.5 PXRD instrumentation

In the studies described in this thesis, PXRD data were collected using one of two Bruker AXS d8 Advance diffractometers (denoted d7 and d9) operating in Bragg-Brentano mode. The Bragg-Brentano configuration of the diffractometer is shown in Figure 2.5. This set-up includes a source of X-rays, the mounted sample to be analysed, and a Lynx-Eye detector. The X-ray tube was operated at 40 kV and 40 mA. The X-ray source was a sealed X-ray tube producing Cu-$K_{\alpha1,2}$ radiation (1.5404 Å, and 1.5443 Å respectively) by bombarding a copper target with electrons generated from a tungsten filament. Cu-K_{β} radiation was selectively removed via a Ni filter. Soller slits are employed to limit divergence of the X-ray beam. The divergent slits not only block incident X-rays with too great a divergence but also increase the resolution of the instrument, allowing sharper peaks to be resolved from narrower slits. The sample – finely sieved powder on petroleum jelly – was mounted on a silicon wafer embedded in a plastic slide. The slide is placed on a fixed sample stage and held centrally at a calibrated height (set by an alumina standard), whilst the X-ray tube and detector are rotated through a user-set range of angles around the goniometer circle. The X-ray source-to-sample distance is set equal to that of the sample-to-detector distance.

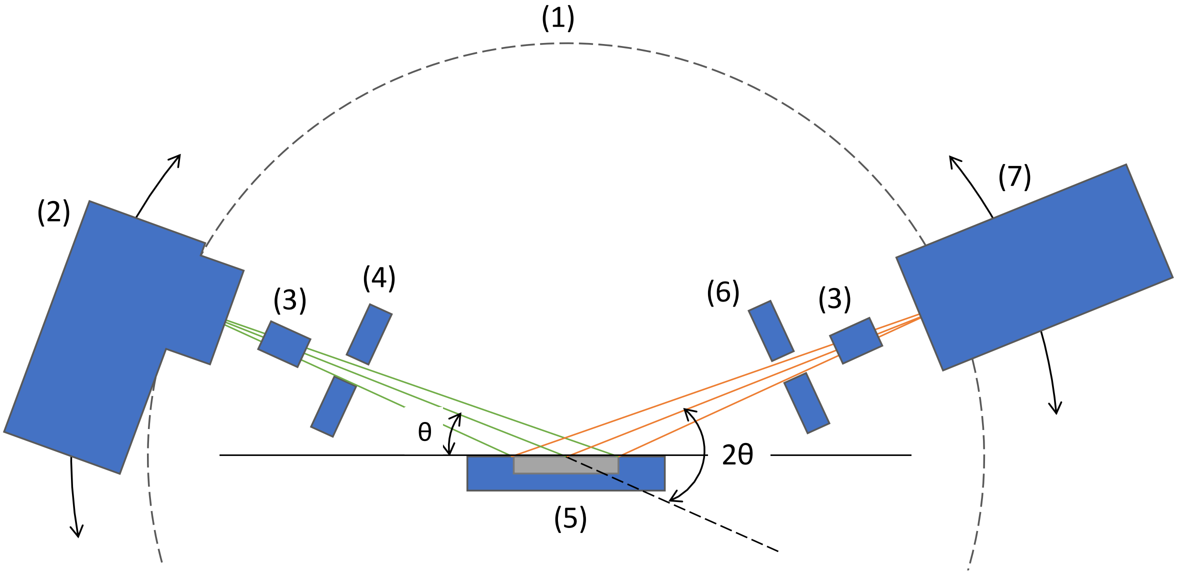

Figure 2.5: Schematic of laboratory PXRD instrument in Bragg-Brentano mode with components: 1) Goniometer circle, 2) X-ray tube, 3) soller silts, 4) divergence slits, 5) sample holder, 6) receiving slits, and 7) detector.

Routine PXRD patterns for monitoring the progress of syntheses at room temperature were recorded in the range of 10.0° < 2θ < 90.0°, with a step size of 0.02°, and a step time of 0.5 s/step – averaging 33 minutes of data acquisition. For detailed structural investigation, 10-

hour data acquisitions were undertaken, in 2θ range of 10.0° < 2θ < 120.0°, with a step size of 0.02°, and a step time of 6.5 s/step. Variable-temperature diffraction data at high (above room temperature) temperatures were collected using an Anton Parr HTK1200 furnace modification. High-temperature diffraction was performed with heating at a rate of 2°C per 10 seconds. Each high-temperature PXRD pattern was recorded with the same collection settings as routine measurements. Multiple PXRD patterns were recorded at equal temperature intervals along a set heating and cooling temperature regime. Variable-temperature patterns were acquired at a fixed temperature, not whilst the temperature was ramping. Sample powder was loaded into the furnace module by sieving it onto vacuum grease on a silica slide.

All diffraction data were analysed in the software package TOPAS.[15] Search-match routines were undertaken using the DIFFRAC EVA software.[16]

2.3. The measurement of luminescence properties

2.3.1 Room-temperature luminescence measurements

2.3.1.1 Emission and excitation

Emission spectra are acquired by selecting a single excitation wavelength to excite the sample to be measured. The intensity of a range of wavelengths of emission is monitored at set increments via the detector. The emission spectrum is plotted as the intensity of emission vs the wavelength. Conversely, excitation spectra are measured by selecting a single wavelength at which the intensity of emission is monitored as a function of the excitation wavelength. The intensity at the selected emission wavelength is recorded for each individual excitation wavelength along a set range, producing an excitation spectrum of intensity vs excitation wavelength.

2.3.1.2 Quantum yield

The intrinsic photoluminescent quantum yield (PLQY or Φ_{int}) denotes the ratio of the number of photons emitted from a material to the number of absorbed photons. Materials with the highest quantum yields are the brightest emitting due to their efficiency of radiative emission and minimalised non-radiative pathways. The intrinsic quantum yield is related to the rate constants of radiative (k_r) and non-radiative (k_{nr}) decay through Equation 2.11.[17]

$$\Phi_{Int}(\lambda) = \frac{k_r}{k_r + \sum k_{nr}} \tag{2.11}$$

Equation 2.11 only holds if the state from which emission occurs is populated directly by the absorbed light (emitting excited energy level denoted *E** in Figure 2.6) to as shown by the inner hashed circle of Figure 2.6. Internal conversion, another source of non-radiative decay, from a higher lying excited state (higher lying excited energy level *A** in Figure 2.6) to the lowest lying excited state can be included for intrinsic QY if the internal conversion is far greater than that of the rate of emission, k_r. If the higher excited state emits or is involved in energy transfer, then it must be counted as part of the overall quantum yield as opposed to Φ_{int} only.

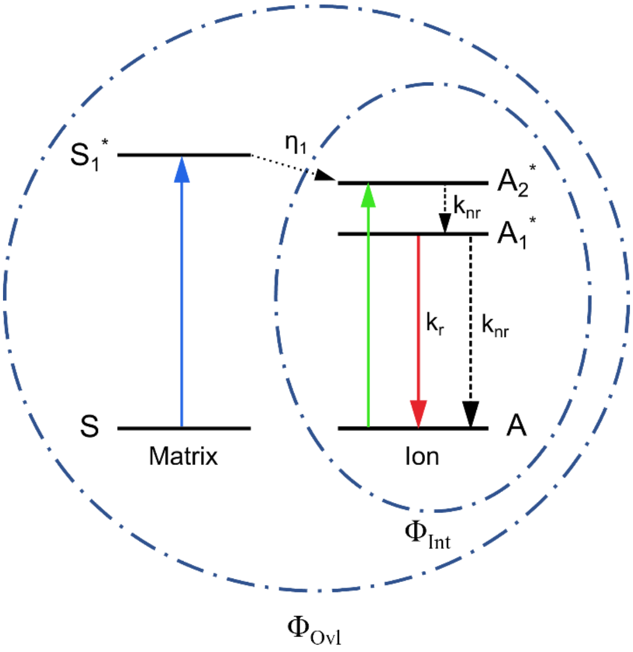

Figure 2.6: A simplified diagram of the energy levels of an activator ion and host matrix. The inner dashed circle shows all processes that occur for intrinsic QY with emitting state E and higher lying acceptor state A. The larger outer dashed line includes the matrix's energy transfer to the activator ion allowing an overall QY to be calculated.

The overall photoluminescence quantum yield, Φ_{ovl}, takes into account that when the system is excited into a state that is *not* the emitting excited state, the efficiency with which the emissive state is formed from the initially generated excited state must be taken into account. This is the case, for example, for the population of a triplet from a singlet in many organic molecules, or when the excited state of an emissive lanthanide ion is populated by energy transfer from a sensitiser ion, the matrix, or from an antenna.[18] Consider an activator ion within a matrix as in Figure 2.6. The intrinsic QY would be classed as the ratio of the number of photons emitted by the activator's *E** state compared to the number absorbed by the activator ion itself, shown by the inner dashed circle. However, the matrix could absorb higher energy photons and transfer the energy to the activator – shown as a black dashed line, allowing the activator to emit radiatively after the energy has been transferred in a separate step, with η_1 being an energy transfer efficiency.

The overall QY is then the activator ion's intrinsic QY and any additional energy transfer efficiencies from the matrix to the activator ion:

$$\Phi_{Ovl} = \Phi_{Int} \times \eta_1 \tag{2.12}$$

The value of overall QY will be equal to or lower than that of the intrinsic QY as the energy transfer efficiency cannot exceed 100%.

The overall QY of solutions (Φ_S) can be determined via relative means by comparison against a standard reference with a known QY using Equation 2.13.

$$\Phi_S = \Phi_R \left(\frac{I_S}{I_R}\right)\left(\frac{1-10^{-A_R}}{1-10^{-A_S}}\right)\left(\frac{n_S}{n_R}\right)^2 \tag{2.13}$$

where *S* and *R* denote sample and reference respectively; Φ_R is the known quantum yield of the reference; *I* is the integrated intensity of the emission spectrum; *A* is the absorbance at a specific excitation wavelength; and *n* is the refractive index of the solvent. The relative QY technique works under the assumption that a sample and a reference with equal absorbance at the same wavelength of excitation will absorb the same number of photons.[19] Whilst possible to prepare both the sample and the reference to have identical absorbances, the second bracketed term in Equation 2.13 accounts for any differences between the reference and the sample's absorbance. The emission spectra of both solutions can then be recorded and the ratio of their integrated emissions – the first bracket of Equation 2.13 – can be used to determine the quantum yield value of the unknown samples by scaling it to the reference solution's quantum yield. The third bracket of Equation 2.13 accounts for cases where the solvent for the sample and the reference differs and different refractive index values must be included. It is important to note that for meaningful comparison, all spectra for both the reference and the unknown sample must be measured under identical parameters such as excitation wavelength and integration time. One key limitation of the relative QY calculation method is the need to match the reference standard's emission range to that of the unknown samples. Additionally, the relative method is not suitable for determining the QY of scattering solids, limiting its usage to the solution state.[20]

Alternatively, QY can be obtained absolutely through actinometry, whereby photons absorbed and emitted by a sample are accurately counted.[21] Integrating spheres can be used as absolute QY set-ups due to their ability to reflect transmitted, scattered, and emitted photons for detection.[22] The key concept behind the integrating sphere QY method is that the number of photons absorbed by the sample can be determined using the reduction in the intensity of the scattered excitation light of the blank holder compared to a holder with sample. Absolute QY measurements using an integrating sphere are advantageous as they allow measurements of solid samples, and they are not limited by the need for a standard that closely matches the sample. The instrumentation and procedures used to measure the QY of samples using an integrating sphere are given in Section 2.3.1.4.

2.3.1.3 Lifetime

The lifetime of the excited state indicates how long the luminescent centre's excited state interacts with its environment before returning to the ground state. Spontaneous emission is usually a kinetically first order process: it depends only on the rate constant, *k*, and the concentration of the excited state, $[A^*]$ as given in the differential first order rate law below, and its integrated solution.

$$\frac{d[A^*]}{dt} = -k[A^*] \tag{2.14}$$

$$[A^*]_t = [A^*]_0 \exp -kt = [A^*]_0 \exp {}^{-t}/_{\tau} \tag{2.15}$$

where $[A^*]_t$ is the concentration of the excited state at time, *t*; $[A^*]_0$ is the concentration at time zero after the excited state has been formed; τ is the luminescence lifetime; and *t* is the time after the excitation event such as a laser pulse. τ is taken as the reciprocal of the 1st order rate constant. Measurements of lifetime use emission intensity, I, in place of excited state concentration. This modifies Equation 2.15 into Equation 2.16, below.

$$I(t) = I_0 \exp {}^{-t}/_{\tau} \tag{2.16}$$

A lifetime experiment measures the intensity of emission as function of time using a pulsed excitation source. The experimental data points are then fitted to a decay function such as Equation 2.16 to estimate the lifetime. A typical lifetime plot shows the decay in intensity as a function of time. Discussion of instrumentation and fitting parameters used in this work are given in Section 2.3.1.4. The lifetime is determined by the sum of the rate of radiative decay, k_r, and the sum of the rates of non-radiative decay, k_{nr} of the emissive state (such as energy transfer and thermal quenching) through Equation 2.17:

$$\tau = \frac{1}{k_r + \sum k_{nr}} \tag{2.17}$$

The natural, or intrinsic, lifetime of the excited state, τ_n, is the lifetime in the absence of any non-radiative decay pathways and is the reciprocal of the radiative rate of decay:

$$\tau_n = \frac{1}{k_r} \tag{2.18}$$

τ_n is often considered as temperature-invariant. The natural lifetime cannot be estimated directly but can be estimated from the quantum yield, Φ, and the measured lifetime, τ, through the combination of Equations 2.12 and 2.17:

$$\tau_n = \frac{\tau}{\Phi} \tag{2.19}$$

Additionally, the lifetime of transitions also differs markedly depending on if they are spin allowed or spin forbidden. Spin-allowed transitions require no change in spin ($\Delta S = 0$). They typically have lifetimes of in the range from around 1 ns to tens of ns, although they may sometimes be strongly forbidden for other reasons (e.g. symmetry restrictions, Section 1.2.2.1). The $\Delta S \neq 0$ nature of spin-forbidden transitions is the key factor in their normally longer lifetimes compared to allowed transitions, such that phosphorescence lifetimes typically range from milliseconds to seconds.

2.3.1.4 Instrumentation

Room-temperature excitation and emission spectra were recorded on a Horiba Fluorolog-3 consisting of a white light source, excitation and emission monochromators, a sample chamber, and detector as shown in a simplified diagram and corresponding image of the instrumentation (Figure 2.7a and b).

A 450 W xenon lamp was used as a white light emitter, with separate diffraction grating monochromators for excitation and emission wavelength selection. Monochromator choice affects dispersion of light, efficiency, and stray light levels. The excitation monochromator grooves and blaze wavelength settings were 1200 mm and 500 nm respectively. The S-side emission monochromator grooves and blaze wavelength were 1200 mm and 330 nm respectively. NIR T-side emission monochromators grooves and blaze wavelength were 600 mm and 1000 nm respectively.

Excitation and emission slits were used to vary the intensity of incoming excitation light and of the collected emission light. Emission slits of 1 nm allowed for higher resolution emission spectra to be obtained but at the expense of signal intensity. High resolution spectra are important for some transition metal and lanthanide ion emission profiles containing vibrational peaks, symmetry-split peaks, Stark splitting, and crystal field splitting of J levels of Ln^{3+} ions. Samples for excitation and emission analysis were contained within quartz capillaries held by a custom 3D printed housing sitting in the cuvette holder within the sample cavity (Figure 2.7c).

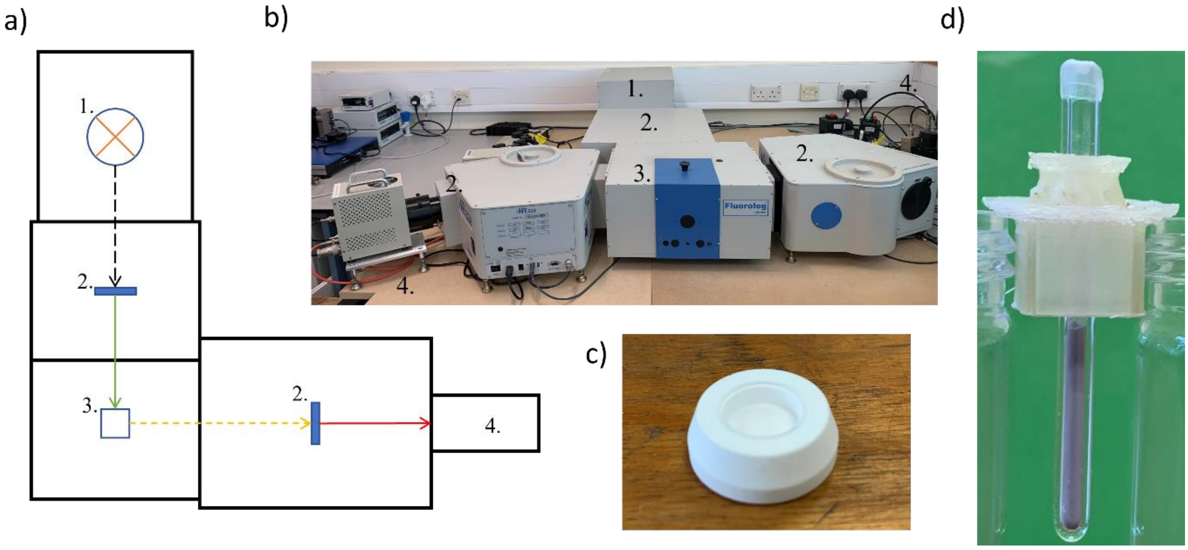

Figure 2.7: a) Diagram of a simplified spectrofluorimeter showing how light is detected: 1) white light source, 2) monochromators, 3) sample, 4) detector. Dashed arrows indicate polychromatic light, whilst unbroken arrows indicate monochromatic light post monochromators. b) An image of the Fluorolog-3 with corresponding numbering to a), c) a spectralon® holder, and d) a 3D-printed capillary holder and capillary.

Emitted light was detected in the range 250 to 1000 nm at right angles to the sample cavity with a Horiba Scientific Synapse charge-coupled device (CCD) or a Hamamatsu R928P photomultiplier tube (PMT) detector in the range 250 to 850 nm. NIR light was detected at the same geometry with a Hamamatsu NIR PMT module detector with an operational range of 950-1700 nm.

For particular wavelengths of emission and excitation monitoring, it was required that a long pass filter be used to remove harmonic peaks. Filters used included a 400 nm, a 495 nm, and an 850 nm set from Thorlab. All emission and excitation spectra were corrected for the wavelength of the detector using a correction curve supplied by the manufacturer. Excitation spectra were corrected for the xenon lamp intensities using a rhodamine internal standard.

The quantum yields of the phosphors were measured using a Horiba Quanta-Phi F3029 integrating sphere connected to the fluorimeter by fibre optic cables. Sample holders were coated in high reflectance (>99% between 450 – 1500 nm) Spectralon®, allowing for the majority of scattered light to be reflected rather than absorbed by the sphere for analysis.[23] Quartz cover slips were used to enclose the powered samples in the Spectralon holders to minimise the possibility of contamination of the sphere (Figure 2.7c). The procedure for QY acquisition was as follows:

- A blank sample holder was placed into the integrating sphere and an emission profile was taken to account for any absorption by the Spectralon holder.
- An emission profile of the excitation wavelength was also taken with the use of a neutral density filter (ND = 2) to attenuate the scattered light intensity reaching the detector.
- The above emission spectra were taken again in the same wavelength ranges but now with the sample in the Spectralon holder.
- These excitation and emission spectra (four in total: two with blank holders, two with sample in holders) were used in quantum yield calculations using the FluorEssence™ software, in a manufacturer's spreadsheet, and alongside by-hand calculations to check the calculated instrument's software values. The equation used by all three methods is as follows:

$$\Phi = \frac{(E_c - E_a)}{(L_a - L_c)} \tag{2.20}$$

where Φ is the QY (%), E_c is the integrated luminescence of the sample's emission, E_a is the integrated luminescence of the blank sample holder's emission, L_c is the integrated blank holder's excitation profile, and L_a is the integrated sample's excitation profile. The use of the neutral density filter to attenuate the excitation light is taken into account with a scaling factor introduced into the denominator. For example, if a neutral density filter of O.D = 2 is used to record the scattered light, then a factor of 10^2 is required in the denominator; for an O.D = 2.5, the factor is $10^{2.5}$. All emission and excitation intensities were corrected for the detector's varying sensitivity at different wavelengths by a correction factor. It should be noted that this technique has a relative error in measurement (~2%) due to non-zero absorption by the integrating sphere material, and re-absorption of reflected excitation and emission by the sample itself.[24]

Room-temperature lifetime data were acquired using an L-geometry Edinburgh Instruments OB920 following excitation of the samples in 3 mm o.d. quartz capillaries with a microsecond-pulsed xenon flashlamp. Emitted light was detected at right angles using a Hamamatsu R928 detector operating in multichannel scaling mode with a range of 200 – 870 nm. Lifetime data were fitted to mono- or bi-exponential decay functions in Origin 2021 software with the following equations:

$$y = A_1 \exp -t_1/\tau_1 + y_0 \tag{2.21}$$

$$y = A_1 \exp -t_1/\tau_1 + A_2 \exp -t_2/\tau_2 + y_0 \tag{2.22}$$

where A_1 and A_2 are constants, τ_1 and τ_2 are lifetimes, t_1 and t_2 are time after absorption, and y_0 is a dark-offset. When mono exponential decay fitting gave high residual values alongside a poor visual fit, indicating that mono exponential decay fitting was incorrect, bi-exponential decay functions (Equation 2.22) were instead used to fit data. From the bi-exponential lifetimes and their respective constants, an average lifetime could be calculated through Equation 2.23:

$$\tau_{avg} = \frac{(A_1(\tau_1)^2) + (A_2(\tau_2)^2)}{(A_1\tau_{1_1}) + (A_2\tau_2)} \tag{2.23}$$

2.3.2 Variable-temperature luminescence measurements

2.3.2.1 Emission

As explained in Section 3.1, increasing temperature affects the luminescence of a material such as its emission intensity, spectral shape, and lifetime. These changes can be probed using variable-temperature emission measurements, allowing for readouts such as absolute emission intensity, relative emission intensities, bandwidth, and band-shift changes to be calculated, and thermometric figures of merit to be extracted for each readout method.

Variable-temperature (VT) emission measurements were collected on 5 mm (o.d.) hand-pressed pellets of sample starting at RT. Emission spectra were acquired similarly to their room temperature counterparts in Section 2.3.1.1 whereby a single excitation wavelength was used, and a range of emission wavelengths observed. For each individual temperature measurement, 75 emission spectra were acquired. Emission spectra for LIR thermometry were analysed by taking the integrals of the desired emission peaks. From the integrated emissions – termed intensity higher for shorter wavelengths and intensity lower for longer wavelengths – *LIR* values for each temperature were calculated. The LIR values were then fitted to the linearised LIR Boltzmann equation (Equation 1.18 in Section 1.3.3.1.1) and plotted as ln(*LIR*) vs 1/*T*. The y-axis intercept of the linear fit of the *LIR* points gives $\Delta E/k_B$, which can then be used to calculate the absolute and relative sensitivity of the phosphor. Each *LIR* point was the average of the 75 acquired spectra's *LIR* value at that temperature. Averaging allowed for uncertainty in measurement to be calculated at each temperature which was used for temperature resolution calculations.

Band-shift thermometry – where peak wavelength maxima change with temperature – was carried out by plotting $\lambda_{\max}$ against *T*. The changes to $\lambda_{\max}$ were then fitted using a polynomial function. Similarly, for bandwidth thermometry – where peak width changes with temperature – the FWHM of the most intense emission peak was plotted for each temperature, and again fitted to a polynomial function.

2.3.2.2 Instrumentation

VT emission spectra were acquired using a heating stage and a luminescence spectroscopy set-up. The set-up is illustrated in Figure 2.8. Variable temperature emission spectra were using an Ocean Insight NIR-Quest+1.7 benchtop spectrometer with an optical range of 900-1700 nm, entrance slit of 25 μm, and a InGaAs linear array detector. The spectrometer was linked via a bifurcated fibre-optic cable to the sample. A custom-built stage heated by a resistance heater with temperature control was used to heat the samples.[25] Samples were left to equilibrate for 30 seconds upon reaching set temperature. Ocean Insight LSM series high powered LEDs were the excitation source controlled by a single-channel LDC-1 driver and

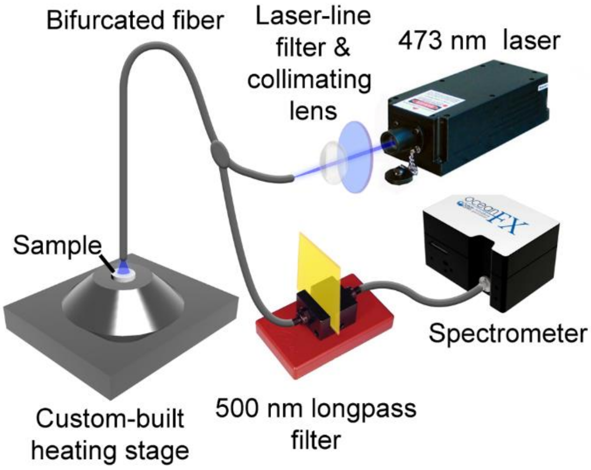

Figure 2.8: Schematic of the experimental set-up used for the acquisition of variable-temperature emission spectra.[24]

control unit for output and waveform. The spectrometer was operated by the software program OceanView via a connected computer.

Variable temperature spectra for Chapters 3 and 4 were collected by Dr Aleksander Ćirić of the OMAS group, Vinča Nuclear Institute, Belgrade, Serbia.

Matlab code was used in order to fit and extract all thermometric parameters of a sample from the variable temperature data. Spectra for each sample were then plotted by pre-written Matlab code created by Dr Zoran Ristić of the OMAS group, Vinča Nuclear Institute, Belgrade, Serbia.

2.4. Ancillary techniques

2.4.1 Diffuse reflectance spectroscopy and the Kubelka-Munk function

Diffuse reflectance spectroscopy (DRS) records the surface-reflected electromagnetic radiation in the UV-Vis, infrared, and mid-infrared range with respect to either wavenumber or wavelength from a material, allowing for vibrational and optical properties of the material to be analysed.[26] This technique is commonly used for powders in research areas such as paint coatings, where samples are not smooth or perfectly reflective.[27] Light scattering can be broken down into specular reflection (Figure 2.9, green arrows) where the angle of reflected light, θ_R, is equal to the angle of incident light, θ_I, like a mirror; and diffuse reflection (Figure 2.9, red arrows) where the angle of reflection is independent of the angle of incidence.

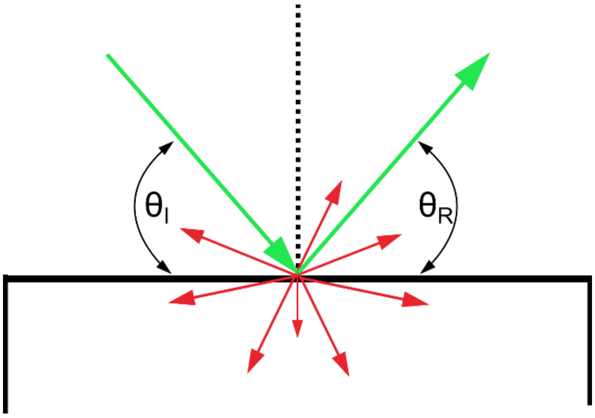

Figure 2.9: A diagram demonstrating two types of reflection when light impinges a surface. The red arrows indicate diffuse scattering of light, whilst the green arrows indicate the specular reflection of light.

The model by Kubelka and Munk is a two-constants model commonly used to interpret diffuse reflection data. The model calculates that surface reflectance is a ratio of molar absorption, k, and scattering, s, coefficients. Using this model with reflectance data allows for a ‘pseudo-absorption’ spectrum to be found, or for the band gap of a material to be calculated.[28] The sample analysed must be assumed to be ‘infinitely thick’ – no light hitting the sample penetrates to the bottom of the holder which is achieved at a depth of a few millimeters’ – and opaque.

DRS data is transformed to absorption intensity data using the Kubelka-Munk function:

$$F(R_\infty) = \frac{k}{s} = \frac{(1 - R_\infty)^2}{2R_\infty} \tag{2.24}$$

where R_∞ is reflectance of the infinitely thick sample over the reflectance of the reference.

DRS data were collected in chapter 5 by Dr Vesna Đjorđjevic of the OMAs group, Vinča Nuclear institute, Belgrade, Serbia, using a using a Shimadzu UV-2600 spectrophotometer (Shimadzu corporation, Tokyo, Japan) with an integrating sphere, using $BaSO_4$ as an optically inert reference over the 220–1350 nm wavelength range.

2.4.2 Solid-state nuclear magnetic resonance

Solid-state NMR (ssNMR) is a spectroscopic technique for probing the local environment of crystalline materials using radiofrequency radiation. ssNMR allows for differentiation between crystallographically distinct nuclei in a crystal structure.

Nuclei with a spin angular momentum vector, I, of integer or half-integer value > 0 when placed in a magnetic field, B_o, will lose degeneracy of their nuclear spin levels. The loss of degeneracy results in $2I+1$ nuclear spin energy levels between $+I$ to $-I$ with equal energy spacing:

$$\omega_0 = \Delta E = -\gamma \hbar B_0 \tag{2.25}$$

where ω_0 is the Larmor frequency, γ is the gyromagnetic ratio of the nuclei, and $\hbar$ is the reduced Planck’s constant. The energy of the splitting is governed by the Zeeman equation (Equation 2.25) which is influenced by the identity of the nuclei and the magnet’s strength. The energy spacing between nuclear spin levels is additionally affected by shielding of the nuclei by its electrons, and by other nuclei in the local environment. Due to the lack of ‘molecular tumbling’ and the large variety of crystallite orientations in a sample, the orientation dependence of interactions such as chemical shift anisotropy, dipolar interactions, and quadrupolar interaction dominate in crystalline samples. This causes broadening of the ssNMR spectrum as each individually orientated crystallite has a unique line shift. To remove this broadening from a crystalline sample’s NMR spectrum, magic-angle spinning (MAS) can be employed. The randomly oriented crystalline sample is contained in a rigid rotor and held at an angle, θ, of 54.74° to the spectrometer's magnetic field and spun rapidly.[29,30] This specific angle is required to minimise the anisotropic interactions as each interaction contains the orientation dependence term:[31]

$$3\cos^2(\theta) - 1 \tag{2.26}$$

ssNMR magic angle spinning measurements were conducted using a Bruker advance III HD spectrometer. All ssNMR sample data were gathered by Dr Samuel Page of Durham University ssNMR service.

2.4.3 TEM and chemical mapping via EDX

Transmission electron microscopy (TEM) is a technique allowing for observations of the structure, ordering, and boundaries of micro- and nano- sized materials via interaction with an electron beam. Electron microscopy exploit that electrons have both wave-particle duality, thus having a wavelength that can be calculated by the following equation as the electron is accelerated through a potential difference:[32]

$$\lambda = \frac{h}{\left(2em_eU + \frac{e^2U^2}{e^2}\right)^{1/2}} = \left(\frac{1.5}{(U + 10^{-6}U^2)}\right)^{1/2} nm \tag{2.27}$$

where h is Planck's constant, e is elementary charge, m_e is the mass of an electron, and U is a potential.

And, as they are charge particles, can be focused by electrostatic lenses. The higher the potential, the faster the electron, and the shorter the wavelength. Thus, the high resolution of electron microscopes compared to optical microscopes is due to the smaller wavelength accessible to the electrons than visible light.

Energy dispersive x-ray (EDX) analysis is both a qualitative and quantitative analytical method. The electron beam ejects inner electrons out of the atoms core orbitals forming an electron hole. This allows for a higher energy, outer electron to relax to fill this vacancy, releasing a photon of X-ray radiation equal to the energy difference between the higher outer electron and the lower lying core electron hole. This radiation is detected and converted to a voltage which is characteristic of the element and the specific energy gap of the inner/outer electrons i.e. K_α or K_β radiation for a given element.

TEM imaging, bright and dark field imaging, and chemical mapping via EDX were undertaken using a JEOL 2100F FEG transmission electron microscope with a single tilt holder. Sample powder was placed into a glass vial with isopropanol, homogenised using an ultrasound bath (10-minute cycle) and a single drop of suspended sample placed onto a lacey carbon film 200 copper mesh disk (Agar scientific). TEM imaging was captured via a Gatan Orius CCD camera. Chemical mapping was done using an Oxford INCAx-sight Si(Li) detector for EDX. TEM training was given by Dr Leon Bowen of the Durham University Physics department.

2.5. References:

1 L. E. Smart and E. A. Moore, *Solid State Chemistry: An Introduction*, CRC Press, 5th edn., 2020.

2 P. M. Woodward, P. Karen, J. S. O. Evans and T. Vogt, *Solid State Materials Chemistry*, Cambridge University Press, Cambridge, 1st edn., 2021.

3 R. Merkle and J. Maier, *Z. Für Anorg. Allg. Chem.*, 2005, **631**, 1163–1166.

4 G. Xu, H. Ma, M. Zhong, J. Zhou, Y. Yue and Z. He, *J. Magn. Magn. Mater.*, 2006, **301**, 383–388.

5 A. E. Danks, S. R. Hall and Z. Schnepp, *Mater. Horiz.*, 2016, **3**, 91–112.

6 W. Wen and J.-M. Wu, *RSC Adv*, 2014, **4**, 58090–58100.

7 J. H. Lopes, O. M. V. M. Bueno, I. O. Mazali and C. A. Bertran, *Mater. Sci. Eng. C*, 2019, **97**, 669–678.

8 B. J. Hwang, R. Santhanam and D. G. Liu, *J. Power Sources*, 2001, **101**, 86–89.

9 W. L. Bragg and W. H. Bragg, *Proc. R. Soc. Lond. Ser. Contain. Pap. Math. Phys. Character*, 1913, **89**, 248–277.

10 Robert. E. Dinnebier, A. Leineweber and J. S. O. Evans, *Rietveld Refinement*, De Gruyter, 2019.

11 F. Girgsdies, Peak Profile Analysis in X-ray Powder Diffraction, (accessed 17 November 2022).

12 I. R. Evans, presented in part at the Powder Diffraction and Rietveld Refinement School, Durham University, 2014.

13 H. M. Rietveld, *J. Appl. Crystallogr.*, 1969, **2**, 65–71.

14 R. A. Young, Ed., *The Rietveld Method*, Oxford University Press, New York, NY, 1st edn., 1993.

15 A. A. Coelho, J. Evans, I. Evans, A. Kern and S. Parsons, *Powder Diffr.*, 2011, **26**, S22–S25.

16 DIFFRAC.EVA, https://www.bruker.com/en/products-and-solutions/diffractometers-and-x-ray-microscopes/x-ray-diffractometers/diffrac-suite-software/diffrac-eva.html, (accessed 13 June 2023).

17 J. Lakowicz, *Principles of Fluorescence Spectroscopy*, Springer, 3rd edn., 2006.

18 K.-L. Wong, J.-C. G. Bünzli and P. A. Tanner, *J. Lumin.*, 2020, **224**, 117256.

19 Edinburgh Instruments, Relative Quantum Yield, https://www.edinst.com/blog/relative-quantum-yield/, (accessed 18 August 2023).

20 Edinburgh Instruments, What is Quantum Yield?, https://www.edinst.com/blog/what-is-quantum-yield/, (accessed 23 July 2023).

21 J. N. Demas and B. H. Blumenthal, *J. Res. Natl. Bur. Stand. Sect. Phys. Chem.*, 1976, **80A**, 409.

22 C. Würth, D. Geißler, T. Behnke, M. Kaiser and U. Resch-Genger, *Anal. Bioanal. Chem.*, 2015, **407**, 59–78.

23 G. T. Georgiev and J. J. Butler, *Appl. Opt.*, 2007, **46**, 7892–7899.

24 A. R. Johnson, S.-J. Lee, J. Klein and J. Kanicki, *Rev. Sci. Instrum.*, 2007, **78**, 096101.

25 A. Ćirić, S. Stojadinović and M. D. Dramićanin, *Meas. Sci. Technol.*, 2019, **30**, 045001.

26 J. P. Blitz, in *Modern Techniques in Applied Molecular Spectroscopy*, John Wiley and Sons, 1998.

27 P. Kubelka and F. Munk, 1931, 16.

28 M. L. Myrick, M. N. Simcock, M. Baranowski, H. Brooke, S. L. Morgan and J. N. McCutcheon, *Appl. Spectrosc. Rev.*, 2011, **46**, 140–165.

29 I. J. Lowe, *Phys. Rev. Lett.*, 1959, **2**, 285–287.

30 E. R. Andrew, A. Bradbury and R. G. Eades, *Nature*, 1958, **182**, 1659–1659.

31 D. C. Apperley, R. K. Harris and P. Hodgkinson, *Solid-state NMR: Basic Principles & practice*, Momentum Press, New York, NY, 1st edn., 2012.

32 S. Hovmöller, X. Zou and P. Oleynikov, in *Electron Crystallography*, University Press, Oxford, 2011.

3. Chromium-doped $LaGaO_3$ for *LIR* luminescence thermometry

3.1. Introduction

Lanthanum gallate $LaGaO_3$ is an orthorhombic perovskite-type material that has been investigated for applications such as display screens, X-ray scintillators, solid-oxide fuel cells, and recently luminescence thermometry.[1–7] Perovskite-type oxides are characterised by the general formula ABO_3, with cations A and B found in 12-coordinate and 6-coordinate sites, respectively. Perovskites are formed of corner-sharing BO_6 octahedra with A cations filling the cavities between them. The stability and structural distortion of perovskites can be evaluated by the Goldschmidt's tolerance factor, t (Equation 3.1):[8]

$$t = \frac{r_A + r_O}{\sqrt{2}(r_B + r_O)} \tag{3.1}$$

where r_A, r_B, and r_O are the ionic radii of a 12-coordinate A cation, a 6-coordinate B cation, and a 2-coordinate oxide ion, respectively. A perovskite with the ideal ratio of ionic radii has a Goldschmidt tolerance of $t \sim 1.0$ and cubic symmetry. If the A cations are smaller or the B cations are larger than ideal, the cubic structure distorts to accommodate the bonding requirements. The distortion, with $t < 1$, gives rise to lower symmetry structures including orthorhombic, rhombohedral, hexagonal and tetragonal.[9,10] The Goldschmidt tolerance factor for $LaGaO_3$ calculated using Shannon ionic radii (Table 3.1) is $t = 0.973$; and so, this material adopts a lower symmetry orthorhombic crystal structure in space group *Pnma*.[7,11]

The structure of $LaGaO_3$, with tilted GaO_6 octahedra due to the La^{3+} ion in the central cavity being smaller than ideal, is shown in Figure 3.1 (Inorganic Crystal Structure Database (ICSD) code: 51285).[12] The GaO_6 octahedral tilting causes a shortening of some of the La–O bonds at the expense of others, leading to the structure distorting from cubic to orthorhombic as the coordination of La^{3+} decreases from 12 to 8. This octahedral tilting is described by the Glazer notation $a^+ b^- b^-$.[13,14] In space group *Pnma*, La^{3+} cations are located on a site with a symmetry of *m* (Wyckoff label 4c), whilst Ga^{3+} cations are located within an octahedron of oxide anions, with a site symmetry of $\bar{1}$ (Wyckoff site 4a). Either the La^{3+} or Ga^{3+} ions, or both, can be substituted by luminescent ions of similar radii including several Ln^{3+} ions, leading to optical properties and potential optoelectronic applications. Based on the ionic radii (Table 3.1), it is known that Cr^{3+} can be substituted for Ga^{3+} on the 4a sites in the LaGaO$_3$ structure.

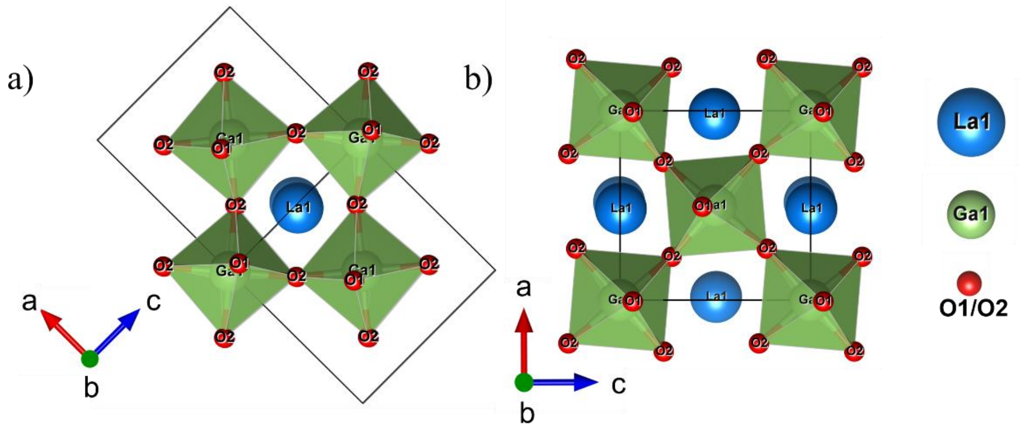

Figure 3.1: Structure of LaGaO$_3$ in the (ac) plane. a) Corner-sharing GaO$_6$ octahedra with La^{3+} cation within the cavity. b) The tilting of the GaO$_6$ octahedra. Black lines indicate the unit cell.[12]

Table 3.1: Crystallographic information for the LaGaO$_3$ host structure and for the dopant of interest, Cr^{3+}.

Ion	Coordination No	Site symmetry	Wyckoff site	Ionic radius[11] (Å)
La1	8	m	4c	1.16
Ga1	6	$\bar{1}$	4a	0.62
O1	2	m	4c	1.35
O2	2	1	8d	1.35
Cr1	6	$\bar{1}$	4a	0.615

Cr^{3+} has been one of the most widely studied transition metal ions for luminescence thermometry. When compared to lanthanide ions, Cr^{3+} demonstrates broader excitation bands, a larger molar absorption coefficient, ε, and a higher sensitivity to the crystal field.[15] The d^3 Cr^{3+} ion in an octahedral environment has a spin-forbidden emission from the ^{2}E state that is almost independent of the crystal field, and sometimes a broad emission from the ^{4}T$_2$ state which is highly dependent on the crystal field. Both Cr^{3+} emissions can be used for *LIR* luminescence thermometry. By manipulating the crystal field strength through modifications of the initial host material composition and structure, and varying the concentration of Cr^{3+} ions, the energy gap, ΔE, between the ^{4}T$_2$ and ^{2}E states can be tuned. Variation in the Cr–O bond length, R, is inversely correlated to the crystal field strength alterations, $Dq/B \approx 1/R^5$, which changes the energy of the ${}^4T_2$ state with respect to the ${}^2E$ state. As the metal-oxygen bond increases in length, the value of Dq/B decreases, lowering the energy of the ${}^4T_2$ state. The ΔE between the two Cr^{3+} emission bands is used in the calculation of luminescence thermometry figures of merit including the absolute and relative sensitivities (Equations 1.21 and 1.22).[16,17]

The aims of the work presented in this chapter were to:

- Synthesise and characterise structure and properties of a series of $LaGaO_3$-based phosphors doped with an increasing concentration of Cr^{3+} ions.
- Record room temperature excitation and emission spectra of the materials prepared to calculate the crystal field strength experienced by the Cr^{3+} ions.
- Measure the quantum yield of each phosphor to determine the optimum concentration of Cr^{3+} ions.
- Perform luminescence thermometry investigations on the selected phosphor.
- Calculate figures of merit for the phosphor as a luminescence thermometer and compare them to current literature.

3.2. Experimental

3.2.1. Synthetic method

Polycrystalline samples of $LaGa_{1-x}O_3:Cr_x$ (x = 0.000, 0.002, 0.005, 0.01, 0.02, 0.04) were synthesised in 2.00 g batches by a conventional solid-state method.[7] Due to its slightly hygroscopic nature, La_2O_3 powder (Aldrich, >99.99%) was pre-heated to 900°C for 10 h to remove bound water. Stoichiometric amounts of the dried La_2O_3, Ga_2O_3 (Aldrich, >99.99%), and Cr_2O_3 (Aldrich, 99.9%) were ground for 30 minutes using an agate mortar and pestle until homogenised. The powders were pressed into two individual 10 mm-diameter pellets at 7 tonnes using a pneumatic pellet press and placed in alumina crucibles. The samples were sintered at either 900°C or 1200°C for 10 h or 20 h intervals with heating and cooling rates of 5°C/min and intermittent grinding (Table 3.2). 900°C was trialled as a sintering temperature to observe if there was a decrease in the impurity phase. Powder X-ray diffraction (PXRD) was used to monitor the phase purity of all samples. All materials were synthesised once.

Table 3.2: Synthetic details for the $LaGa_{1-x}O_3:Cr_x$ *series. The multiple heatings for each row were done on the same material.*

Material	**Synthesis time (h)**	**Synthesis temperature (°C)**
$LaGaO_3$	10, 10, 10, 10	1200, 1200, 1200, 900
$LaGa_{0.998}:Cr_{0.002}$	10, 10, 10, 10	1200, 1200, 1200, 900
$LaGa_{0.995}:Cr_{0.005}$	10, 10, 10	1200, 1200, 1200
$LaGa_{0.99}O_3:Cr_{0.01}$	10, 10, 10, 20, 20	1200, 1200, 1200, 1200, 1200
$LaGa_{0.98}O_3:Cr_{0.02}$	10, 10, 10, 10	1200, 1200, 1200, 900
$LaGa_{0.96}O_3:Cr_{0.04}$	10, 10, 10	1200, 1200, 1200

3.2.2. Powder X-ray diffraction

PXRD measurements were undertaken using a Bruker AXS d8 Advance diffractometer with Lynx Eye detector and CuKα radiation. Routine PXRD data acquisition was between $10° < 2\theta < 90°$ at room temperature, with a step size of 0.02° and a step time of 0.5 s/step. The Rietveld method implemented in TOPAS Academic v7 software was used to analyse all diffraction data.[18,19] Refined parameters included a nine-term polynomial background, sample height displacement, pseudo-Voigt peak shape function terms, unit cell parameters, scale factor, and an overall isotropic atomic displacement parameter.

3.2.3. Room temperature photoluminescence

Room temperature excitation and emission spectra were acquired using a Horiba Jobin-Yvon Fluorolog-3 with a R928 Hamamatsu photomultiplier tube detector and 450W xenon lamp white light source. The selection of excitation and emission wavelengths was achieved using a monochromator grating. A 400 nm long pass filter was used to remove harmonic peaks during the acquisition of excitation spectra. Quantum yield (QY) measurements for each material were performed using a Quanta-Phi F-3029 integrating sphere connected to the sample compartment of the Fluorolog via fibre optic cables. The sample powder was held in a Spectralon holder and covered with a quartz slip to prevent contamination.[20] A neutral density filter was used to attenuate scattered light when scanning over the wavelength of excitation. FluorEssence software was used to calculate the QY from excitation and emission data. Lifetime measurements were undertaken using an Edinburgh Instruments OB920 lifetime spectrometer with the sample contained in a 3 mm outer-diameter quartz capillary and excited by a microsecond pulsed flashlamp. A R928 detector operating in multichannel scaling mode was used to detected emitted light at a right angle to the excitation beam.

3.2.4. Variable-temperature photoluminescence

Variable-temperature emission data were collected between 300 and 600 K using an Ocean Insight FX spectrometer attached to a bifurcated fibre optic cable, with a custom-made heating stage. [21]

The samples were excited using a 473 nm LED with the second harmonic of elastically scattered light at λ_{ex} = 946 nm being removed using a 500 nm long pass filter.

3.3. Results and discussion

3.3.1. Structural characterisation

Six materials with increasing Cr^{3+} concentration were synthesised. PXRD patterns for all $LaGa_{1-x}O_3$:Cr_x materials were fitted using an orthorhombic perovskite structural model, $LaGaO_3$ in space group *Pnma* (ICSD code: 51285), with Cr^{3+} ions placed on Ga^{3+} sites.[12] The Rietveld plots show excellent fits to the experimental data with R_{wp} values around 5% (Figure 3.2).

A small amount of $La_4Ga_2O_9$ impurity was identified in all the samples except $LaGa_{0.99}O_3$:$Cr_{0.01}$ (Table 3.3). $La_4Ga_2O_9$ (ICSD code: 261173) was therefore included as the second phase in the Rietveld analysis of the PXRD data.[22] This impurity has been previously identified in similar Cr^{3+}-doped $LaGaO_3$ phase.[6] From literature it has been reported that both substituted and unsubstituted $LaGaO_3$ materials following different synthetic methods (including chemical vapour synthesis and sol-gel methods) show formation of $La_4Ga_2O_9$.[23,24]

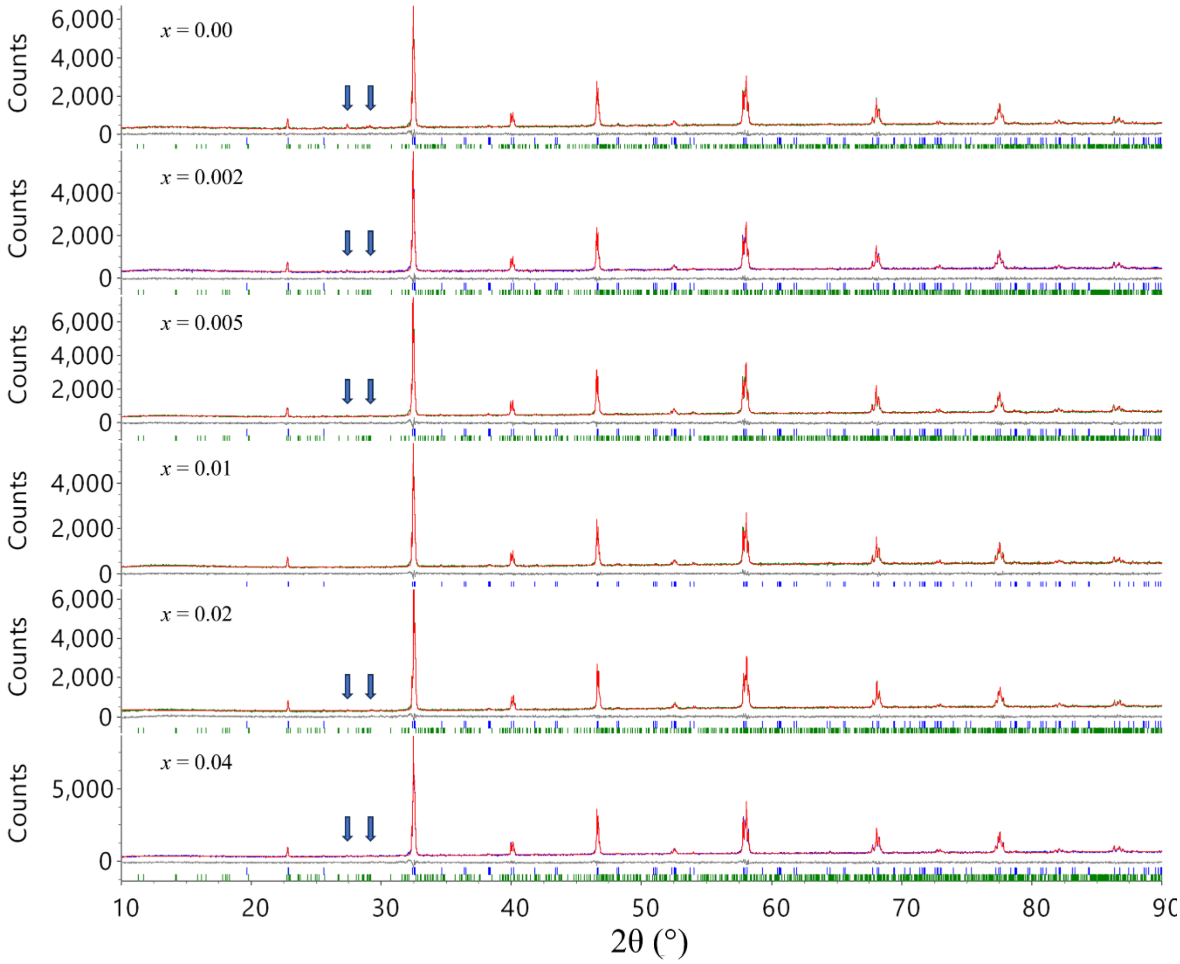

Figure 3.2: Rietveld plots for $LaGa_{1-x}O_3:Cr_x$ *at the x values indicated. Arrows indicate* $La_4Ga_2O_9$ *impurity.*

Unit cell parameters obtained from the refinement and calculated unit cell volumes for each material, are given in Table 3.3. The radii of Ga^{3+} and Cr^{3+} are near identical at 0.62 Å and 0.615 Å respectively, and thus increasing Cr^{3+} concentration to the maximum of 4.0 mol% (x = 0.04) in this investigation will give little change to unit cell parameters and the calculated unit cell volume (Table 3.3). Cr^{3+} is not thought to have substituted into the $La_4Ga_2O_9$ impurity phase, as the structure has only two unique 4-coordinate Ga^{3+} sites and Cr^{3+} does not readily adopt a 4-coordinate geometry.[25] The substitution on the La^{3+} sites is unlikely due to the very different ionic radii (1.16 Å for La^{3+}, and 0.615 Å for Cr^{3+}). A corresponding La^{3+}-poor impurity phase was not seen in the PXRD patterns.

Table 3.3: Unit cell parameters and phase wt% obtained from Rietveld refinement for $LaGa_{1-x}O_3$:Cr_x (x = 0.0, 0.002, 0.005, 0.01, 0.02, 0.04).

Material	**R_{wp} (%)**	**a (Å)**	**b (Å)**	**c (Å)**	**Volume ($Å^3$)**	**$LaGaO_3$ (wt%)**	**$La_4Ga_2O_9$ (wt%)**
$LaGaO_3$	5.136	5.4929(1)	7.7754(1)	5.52499(9)	235.972(8)	91.0(9)	8.9(9)
$LaGa_{0.998}$:$Cr_{0.002}$	5.381	5.4925(1)	7.7747(1)	5.5246(1)	235.922(8)	97.7(5)	2.2(5)
$LaGa_{0.995}$:$Cr_{0.005}$	5.093	5.49268(9)	7.7748(1)	5.52486(9)	235.937(7)	98.0(4)	1.9(4)
$LaGa_{0.99}O_3$:$Cr_{0.01}$	5.424	5.49237(9)	7.7745(1)	5.52456(8)	235.903(7)	100.0	N.D.
$LaGa_{0.98}O_3$:$Cr_{0.02}$	5.644	5.4924(1)	7.7744(1)	5.52468(9)	235.920(8)	97.6(8)	2.3(8)
$LaGa_{0.96}O_3$:$Cr_{0.04}$	4.930	5.4921(7)	7.7743(1)	5.52471(7)	235.897(6)	98.4(3)	1.5(3)

3.3.2. Room temperature photoluminescence

Figure 3.3 shows the emission spectrum of $LaGaO_3$ excited at 250 nm (blue curve).

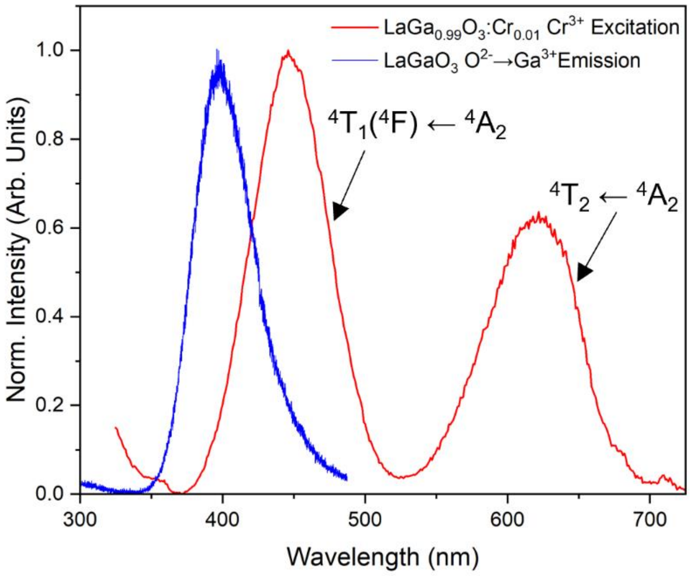

Figure 3.3: Normalised emission spectrum of the $LaGaO_3$ host material (blue) superimposed over the Cr^{3+} excitation spectrum of $LaGa_{0.99}O_3$:$Cr_{0.01}$(red).

The emission spectrum shows a single broad transition centred at 396 nm, in agreement with the literature.[6,26,27] This transition is attributed to the $O^{2-}\rightarrow Ga^{3+}$ charge transfer within the GaO_6 octahedra. The intensity of this charge transfer band is linked to the extent of the delocalisation of the d^{10} Ga^{3+} ions.[28] The reduction of the Ga^{3+} d^{10} electrons delocalisation permits emission to occur that would have been quenched if the electrons were fully delocalised.[28] The delocalisation of the Ga^{3+} d^{10} electrons between neighbouring Ga^{3+} ions is greatly affected by the crystal structure of the host and the distortion of the GaO_6 octahedra. The delocalisation mechanism requires strong overlap of the Ga^{3+} d-orbitals with the 2p orbitals of O^{2-}, which is maximal when the angle Ga–O–Ga is 180°. The bond angles of Ga–O–Ga in orthorhombic $LaGaO_3$ are ~ 160° (Ga–O1–Ga =158.26° and Ga–O2-Ga = 161.33°).[12,29] The deviation from the ideal Ga–O–Ga bond angle of 180° decreases the overlap of the Ga^{3+} 3d orbitals with the O^{2-} 2p orbitals, localising the d^{10} electrons and allowing for luminescence to be observed. The energy of the $O^{2-}\rightarrow Ga^{3+}$ emission is favourable for the host material to transfer absorbed energy to the Cr^{3+} dopant owing to the overlap of the $LaGaO_3$ emission band (Figure 3.3, blue line) with the $^4A_2$ to $^4T_1$ (^4F) excitation peak, which for Cr^{3+}-doped $LaGaO_3$ is maximal at 446 nm (Figure 3.3, red line).

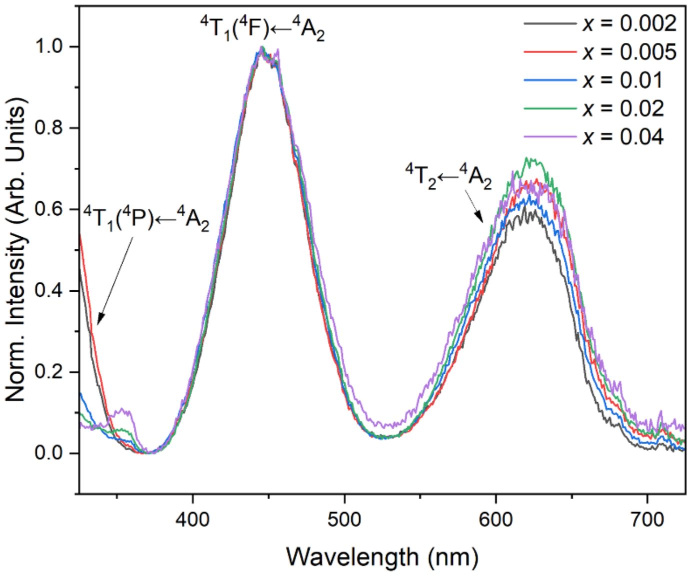

Figure 3.4: Normalised excitation spectra of $LaGa_{1-x}O_3:Cr_x$ (x = 0.002, 0.005, 0.01, 0.02, 0.04) monitored at 748 nm.

The excitation spectra of all the Cr^{3+}-containing materials were monitored in the region of the $^2E\rightarrow{}^4T_2$ transition at λ_{em} = 748 nm (Figure 3.4). The spectra clearly show two excitation peaks, with the onset of a third peak at shorter wavelengths (< 350 nm), as is expected for Cr^{3+} in an octahedral environment. The peak centred at 446 nm (22,400 cm^{-1}) is ascribed to the $^4T_1$ (^4F) ← $^4A_2$ transition, whist the peak centred at 619 nm (16,200 cm^{-1}) is attributed to the $^4T_2$ ← $^4A_2$ transition. The rising edge at < 350 nm is the edge of the $^4T_1$ (^4P) ← $^4A_2$ transition.

Emission spectra were recorded upon excitation at 450 nm (Figure 3.5). All Cr^{3+}-doped materials showed a sharp peak at 729 nm, a second peak at 739 nm, and associated Stokes and anti-Stokes peaks between 700 and 770 nm.[2] The 729 nm (13,700 cm^{-1}) peak arises from the $^2E \rightarrow {}^4A_2$ transition. The band is narrow due to the energy of the transitions being essentially independent of the crystal field and hence in changes in the crystal field with Cr–O bond vibrations. The absence of the $^4T_2 \rightarrow {}^4A_2$ broad emission band at room temperature shows that the Cr^{3+} ions are experiencing a strong crystal field (Dq/B > 2.5). Such a crystal field strength has a high energy $^4T_2 \rightarrow {}^4A_2$ state that can't be thermally populated at room temperature by back energy transfer from the ^2E, and thus the transition is not seen. Further discussion on the crystal field strength of Cr^{3+} in $LaGaO_3$ materials is presented in Section 3.3.3.

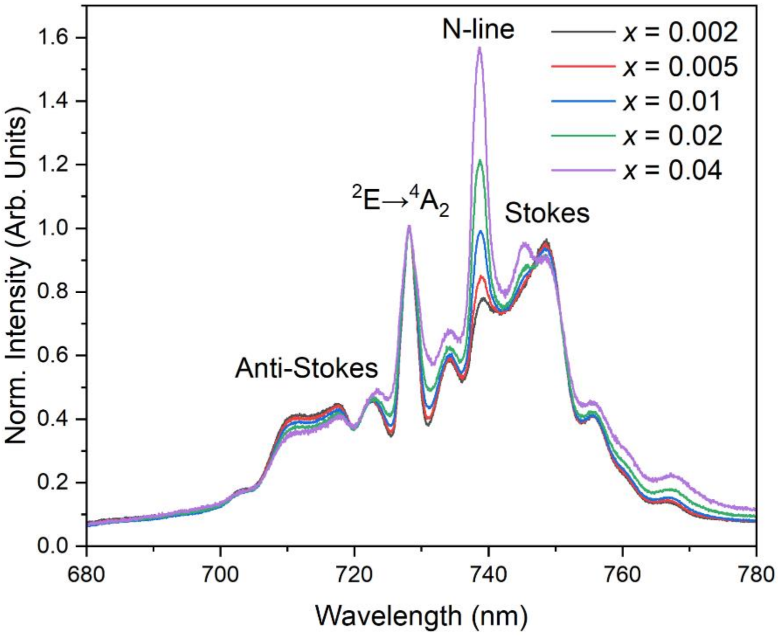

Figure 3.5: Emission spectra of the $LaGa_{1-x}O_3:Cr_x$ (x = 0.002, 0.005, 0.01, 0.02, 0.04) series, normalised to the ^2E transition at 729 nm to highlight the concentration dependence of the N-line transition at 739 nm.

The peak at 739 nm, termed the Cr^{3+} N-Line, originates from Cr^{3+}-Cr^{3+} interactions in the material.[30,31] This is seen more clearly when the emission spectra are normalised to the ^2E transition peak. The N-line appears in the emission spectra of all Cr^{3+}-containing materials. The substituted Cr^{3+} ions occupying neighbouring sites within the structure of the material cause short range exchange-coupled Cr^{3+} pairs.[32] The growth in the N-line intensity with Cr^{3+} concentration relative to the ^2E emission line is due to the higher probability of Cr^{3+} ions being closer together as the Cr^{3+} concentration increases.

3.3.3 Crystal field strength in $LaGaO_3$

By analysing the excitation spectrum – particularly the transition energies – of $LaGa_{0.99}O_3$:$Cr_{0.01}$ (Figure 3.6), the crystal field strength and inter-electronic repulsion parameter were estimated using Equations 3.2 to 3.4. The energies of the $^4T_1(^4F) \leftarrow {}^4A_2$ transition and $^4T_2 \leftarrow {}^4A_2$ transition, 22,000 cm^{-1} and 16,000 cm^{-1} respectively, were used as variables in the following calculations:[16,33]

$$Dq = \frac{E(^4A_2 \rightarrow {}^4T_2)}{10} \tag{3.2}$$

$$\frac{Dq}{B} = \frac{15(x-8)}{(x^2-10x)} \tag{3.3}$$

where x was calculated by:

$$x = \frac{E(^4A_2 \rightarrow {}^4T_1) - E(^4A_2 \rightarrow {}^4T_2)}{Dq} \tag{3.4}$$

The following parameters were calculated for $LaGa_{1-x}O_3$:Cr_x ($x = 0.02$): $Dq/B = 2.60$; $B = 620$ cm^{-1}; and $Dq = 1616$ cm^{-1}.

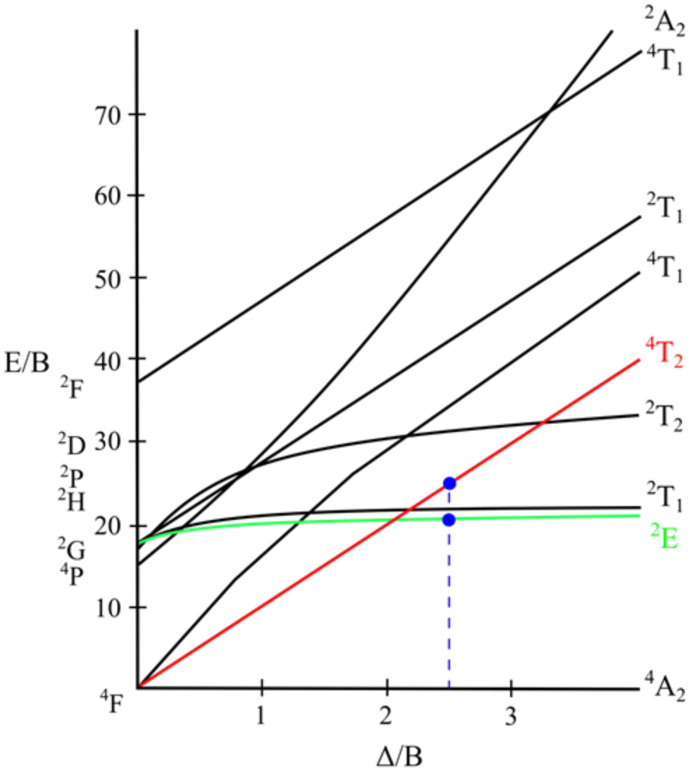

Figure 3.6: Tanabe-Sugano diagram for octahedrally co-ordinated d^3 transition metal ions indicating Dq/B calculated for $LaGa_{1-x}O_3$:Cr_x ($x = 0.02$) of 2.6 (blue dashed line and dots.) C/B = 4.5.[36]

The value of the crystal field strength is determined through the Tanabe-Sugano diagram for d^3 electron configuration in the octahedral crystal field (blue line and dots, Figure 3.6.).[34–36] The value of *Dq/B* obtained for $LaGa_{1-x}O_3:Cr_x$ (x = 0.02) indicates that the Cr^{3+} ions are experiencing a strong-field environment, which is further supported by the emission spectrum only showing the ^2E forbidden transition at room temperature (Figure 3.5). As the crystal field strength increases, the $^4T_2$ state increases in energy in comparison to the spin forbidden ^2E transition, which is near-independent of the crystal field strength. A material which has an "intermediate" field strength ($Dq/B < 2.5$) would show not only the sharp ^2E peak, but also a broad $^4T_2$ emission band as the $^4T_2$ state would be close enough in energy to be populated thermally from the ^2E state at room temperature. The nephelauxetic parameter, *β*, a measure of the degree of covalency of the metal-ligand (M–L) bond, was calculated from the Racah parameter value, *B*, which indicates the extent of electron-electron repulsion within the d-orbitals of the transition metal ion. The value of *B* calculated for $LaGa_{1-x}O_3:Cr_x$ (x = 0.02) sample equalling 620 cm^{-1} differs greatly from that of the *B* value for the free Cr^{3+} ion (918 cm^{-1}).[37] The nephelauxetic parameter, *β*, the ratio of the calculated *B* value to the free Cr^{3+} ion *B* value, was found to be 0.68. A low *β* value is indicative of significant delocalisation of the d-electrons from the d-orbitals of the Cr^{3+} ion into the Cr–O bonds of the surrounding six O^{2-} ligands, and thus to a relatively high degree of bond covalency.

Table 3.4: Dq/B, B parameters of inter-electronic repulsion, and excitation bands of Cr^{3+}-doped $LaGaO_3$ phosphors of different Cr^{3+} concentration, and the synthetic methods used to make them. The orange shaded cells are used to highlight the material reported in this chapter. Cr^{3+} concentration is wrt Ga^{3+} concentration.

Material	**Cr^{3+} conc. (mol%)**	**Synthetic route**	**$^4T_1$ (nm, cm^{-1})**	**$^4T_2$ (nm, cm^{-1})**	**Dq/B**	**B (cm^{-1})**
$LaGaO_3$[2]	0.3	Hydrothermal	446, 22421	615, 16260	2.68	605
$LaGaO_3$[4]	0.3	Solid state	468, 21367	629, 15898	3.03	524
$LaGaO_3$[38]	0.3	Czochralski	394, 25380	582, 19157	3.25	589
$LaGaO_3$[6]	0.5	Hydrothermal	458, 21834	624, 16026	2.87	564
$LaGaO_3$[29]	0.5	Solid state	450, 22222	615, 16260	2.87	564
$LaGaO_3$[39]	1.0	Solid state	446, 22422	619, 16155	2.60	620
$LaGaO_3$[26]	3.0	Polyol	453, 22075	617, 16207	2.84	570
$LaGaO_3$[40]	15	Pechini	450, 22222	613, 16306	2.83	576

A range of lanthanum gallate materials doped with Cr^{3+} at various concentrations have been reported in the literature (Table 3.4). Across all these materials the *Dq/B* does not fall below 2.5, indicating a strong crystal field with only a ^2E emission at room temperature (in all the emission spectra). The three materials with a Cr^{3+} concentration of 0.3 mol% exhibit a large variability in the excitation band positions, leading to different values for their electronic repulsion parameter and *Dq/B*. The materials with 0.5 mol% Cr^{3+} prepared under different conditions have the same *Dq/B* for different excitation band energies. The difference between our material's *Dq/B* value and that of other phosphors from the literature may be due to slightly different λ_{max} for excitation bands as energy is approximated. The material's local structure such as bond length and bond angle, will affects the degree of delocalisation and energy of the excitation bands. The excitation band positions vary as they are highly dependent on the local crystal field, bond vibrations and therefore temperature. The site symmetry can split the degenerate orbitals and change the band shape. Generally, all $LaGa_{1-x}O_3:Cr_x$ phosphors show a large reduction in the *B* parameter from the free-ion value of 918 cm^{-1}, indicative of highly covalent Cr–O bonds.

Table 3.5: Quantum yields for Cr^{3+}-containing $LaGaO_3$ phosphors. A single measurement of each phosphor was taken. Errors are large (~10%) due to the low quantum yields of the materials.

Material	QY (%)
$LaGa_{0.998}:Cr_{0.002}$	6
$LaGa_{0.995}:Cr_{0.005}$	4
$LaGa_{0.99}O_3:Cr_{0.01}$	8
$LaGa_{0.98}O_3:Cr_{0.02}$	3
$LaGa_{0.96}O_3:Cr_{0.04}$	<1

The photoluminescence quantum yields of all Cr^{3+}-containing samples were obtained using excitation at 450 nm (Table 3.5). $LaGa_{0.99}O_3:Cr_{0.01}$ gave the highest quantum yield. The decrease in the quantum yield for $x > 0.01$ is probably caused by concentration quenching due to resonant energy transfer to neighbouring Cr^{3+} ion, i.e. increasing probability of non-radiative decay processes via energy migration increases at the expense of emission.[41] For this reason, $LaGa_{0.99}O_3:Cr_{0.01}$ was selected for further characterisation and evaluation as a luminescence thermometer.

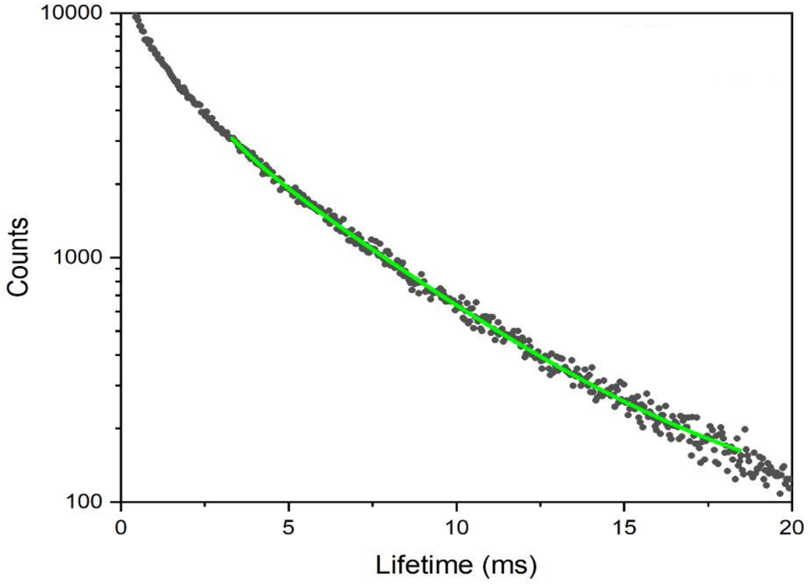

Figure 3.7: The experimental lifetime data for phosphor $LaGaO_3:Cr_{0.01}$ *(black circles) with a best fit to a sum of two exponentials (green curve).*

The lifetime of the ^2E state of the Cr^{3+} was measured by following the decay of the emission at 729 nm with time (Figure 3.7), and the data were fitted using Equation 2.22. The average lifetime value was then calculated using Equation 2.23 as 4.2 ms. The value of 4.2 ms at room temperature is similar to literature values of 4.3 and 3.98 ms for related materials $LaGaO_3:Cr_{0.003}$ and $LaGaO_3:Cr_{0.005}$, respectively.[4,6]

3.3.4. Luminescence thermometry

Variable-temperature emission spectra of $LaGa_{0.99}O_3:Cr_{0.01}$ were collected between 300 and 600 K and analysed using a custom-made MATLAB script. The variable-temperature emission spectrum at 300 K (Figure 3.8b, purple curve) shows the typical room-temperature emission of $LaGa_{0.99}O_3:Cr_{0.01}$ (as seen in Figure 3.5) consisting of the sharp ^2E emission peak, the Cr^{3+}-Cr^{3+} N-line emission, and Stokes and anti-Stokes emissions, similar to the spectrum. As the temperature is increased (Figure 3.8b), a second band appears due to emission from the $^4T_2$ state populated thermally from the ^2E state. The $^4T_2$ emission band increases in intensity until reaching a maximum at 450 K. As the temperature continues to increase, the ^2E and $^4T_2$ emission intensities both decrease due to increasing thermally-activated non-radiative decay. To illustrate the mechanisms of radiative and non-radiative decay in this system, Figure 3.8a shows a coordinate configuration diagram of the ground and excited states of octahedral Cr^{3+} as parabolas and the corresponding excitation and emission wavelengths. The energy difference between the ^2E and $^4T_2$ states, denoted ΔE, is the energy gap between the two coupled states required for *LIR* thermometry. The larger ΔE_{NR} is the energy required for non-radiative decay from the ^2E state to the cross over point of the $^4T_2$ and $^4A_2$ parabola.

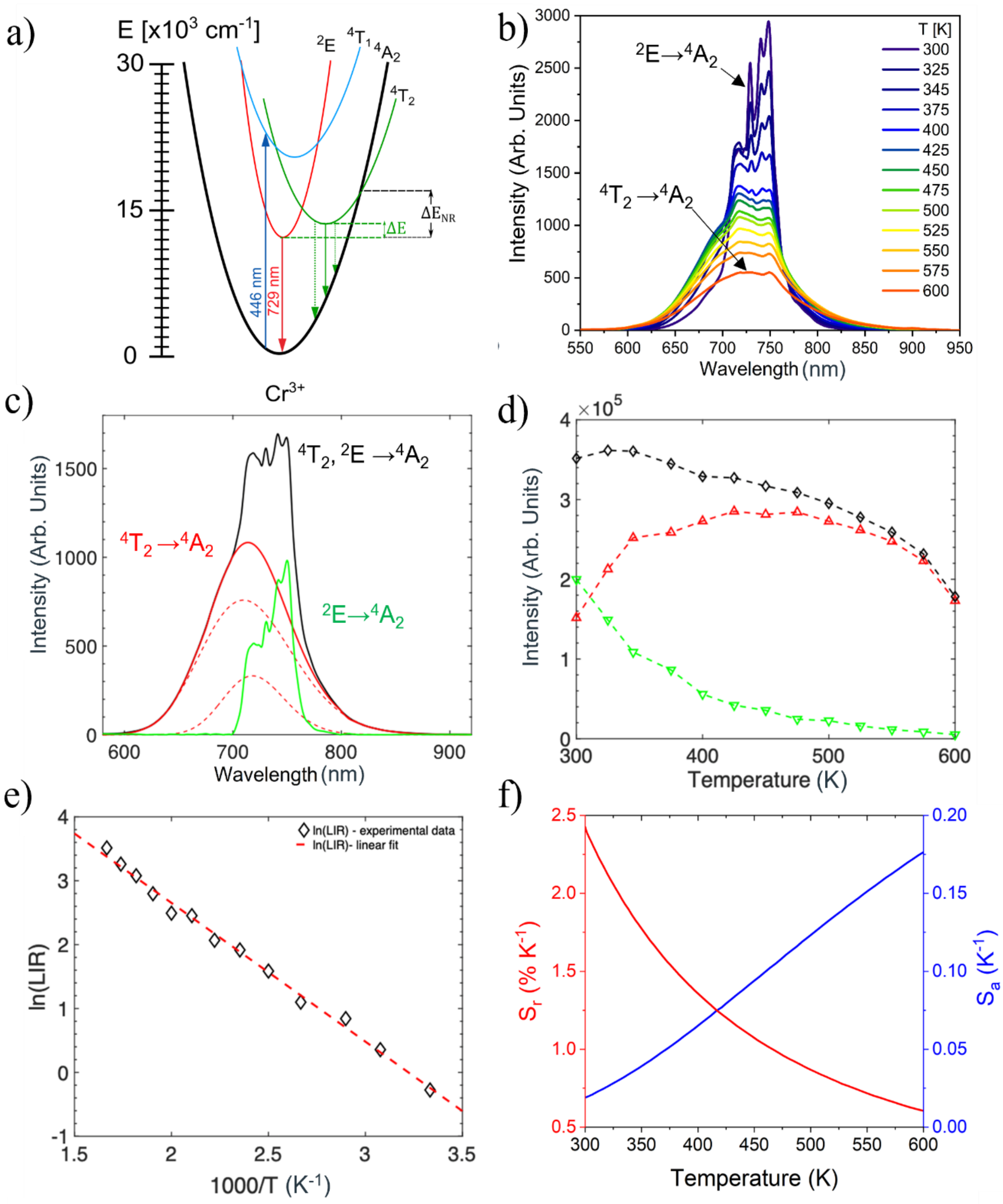

Figure 3.8: a) Coordinate-configurational diagram showing the excitation and emission monitored for LIR thermometry. b) Variable-temperature emission spectra of the x = 0.01 material between 300 and 600 K. c) Deconvoluted Cr^{3+} emission spectrum (solid red $^4T_2 \rightarrow {}^4A_2$ curve, and solid green $^2E \rightarrow {}^4A_2$ curve) at 375 K. d) Intensities of the deconvolved emissions (^2E = green curve, $^4T_2$ = red curve) and of the whole emission spectrum (black curve). e) LIR data points of the deconvolved emissions and linear fit to Equation 1.20. f) Dependence of absolute (blue) and relative (red) sensitivities on temperature.

A notable obstacle to the interpretation of the Cr^{3+} spectra for *LIR* is the large overlap between the broad $^4T_2$ and the narrow ^2E emissions, which affects the calculation of the energy gap and therefore the sensitivity of the thermometer. To circumvent this, the approximate deconvolution method was used to identify and separate the two emissions, allowing them to be individually tracked at each temperature. This allows the *LIR* value to be determined more accurately and sensitivities to be quantified.[42] To demonstrate, in Figure 3.8c, the whole Cr^{3+} emission spectrum at 375 K is given as the black curve. The broader $^4T_2$ emission ranges between 600 and 900 nm. The tails of this $^4T_2$ broad emission between 600 and 650 nm, and 800 to 900 nm, respectively, were fitted to a Jacobian transform of the Gaussian function in the energy scale (converted from wavelength) and subtracted from the original black curve of the whole Cr^{3+} emission (shown as the larger, red-dashed curves in Figure 3.8c). After this, a smaller broad band (smaller, red-dashed curve) between 600 and 700 nm was also fitted and subtracted in Figure 3.8c. This secondary broad emission is due to the distorted GaO_6 octahedra lowering the symmetry of the site that the Cr^{3+} ion occupies, which causes a splitting of the $^4T_2$ state.[43] The two red-dashed curves were summed to give the overall $^4T_2$ deconvolved emission (solid red curve, Figure 3.8c). With both broad bands removed, a set of sharp emissions remained as the ^2E peak, Cr^{3+}-Cr^{3+} N-lines, and both Stokes and anti-Stokes emissions, shown as the green $^2E\rightarrow{}^4A_2$ in Figure 3.8c. Owing to this separation, deconvolved $^4T_2$ and ^2E emission intensities can be monitored with temperature (Figure 3.8d). From the individual emission intensities at each temperature, *LIR* values were calculated using Equation 1.18 and fitted to the linearised Boltzmann equation (Equation 1.20, Figure 3.8e) with $R^2 = 0.994$. The linearised fit gave a ΔE between the ^2E and $^4T_2$ states of 1509 cm^{-1}.

From the calculated ΔE, the absolute and relative sensitivities of the $LaGa_{0.99}O_3{:}Cr_{0.01}$ luminescence thermometer were calculated, using Equations 1.21 and 1.22 respectively. The maximum absolute sensitivity was ~ 0.75 K^{-1} at 600 K and the maximum relative sensitivity was 2.5% K^{-1} at 300 K (Figure 3.8f). To determine the temperature resolution at 300 K, 30 consecutive measurements were performed, and *LIR* values calculated to use in Equations 1.13. Using Equation 1.16 the relative uncertainty, σ_r, of the measuring set-up was 0.13%, giving an excellent temperature resolution of 0.05 K. This high temperature resolution was achieved owing to the high-quality equipment, long spectral acquisition time, and by collecting the spectra at each temperature 100 times and averaging. For a typical experimental set up, the *LIR* relative uncertainty is around 1% and therefore the highest temperature resolution will be ~0.4 K.

3.3.4.1. Discussion of selected Cr^{3+}-containing luminescence thermometers

Comparison of the materials in terms of spectroscopic and thermometric parameters helps to rationalise why $LaGa_{0.99}O_3:Cr_{0.01}$ has a large S_r at 300 K, and what trends in thermometer phosphor structure and chemistry can be used to improve the performance of future materials.

Table 3.6 summarises the key properties of singly Cr^{3+}-doped thermometers that use either the ratio of the ^2E R-lines or of the $^4T_2$ and ^2E emissions as their *LIR*. The thermometers can be broadly split into three categories:

- Those that use the small ΔE of the ^2E R-lines for cryogenic thermometry ($T < 120$ K).
- Those with weak or intermediate crystal field, $Dq/B < 2.5$.
- Those with a strong crystal field, $Dq/B > 2.5$.

Trigonal distortion of the CrO_6 group from the ideal octahedron is the main cause of the degenerate ^2E state splitting into R_1 and R_2 lines. The magnitude of this splitting is small ($\Delta E \sim 30$ cm^{-1} to 200 cm^{-1}) and so it is suited to cryogenic thermometry, as a smaller ΔE lowers the temperature boundary of the thermometer. In the cases of materials with the mullite structure such as $Bi_2Al_4O_9$ and $Bi_2Ga_4O_9$ (Entries 2 and 3), the lone pair of Bi^{3+} $6s^2$ electrons cause the distortion of the CrO_6 octahedra. The distortion-induced splitting results in a ΔE of 130 cm^{-1} to 170 cm^{-1} between the R_1 and R_2 states, larger compared to α-Al_2O_3 (entry 1, $\Delta E = 30$ cm^{-1} to 40 cm^{-1}). In the case of Entry 9 $LaGaO_3$, with a Ga^{3+} site symmetry of $\bar{1}$, R-lines have been reported at low temperature (77 K) and at room temperature with high resolution emission spectra. Generally, the ^2E R-line emissions in Cr^{3+}-doped $LaGaO_3$ are reported as a single line. A single emission is observed due to peak shifting and broadening brought about by increased bond vibrations at room temperature, relative to 77 K, causing the two R-lines to overlap.[38]

Table 3.6: Table of LIR luminescence thermometers based on Cr^{3+} emission. The orange shaded cells are used to denote the material reported in this chapter.

Entry	**Material**	**Cr^{3+} conc (mol%)**	**Cr^{3+} site sym**	***LIR* emissions**	**Dq/B**	**ΔE (cm^{-1})**	**S_r (% K^{-1}) [T/K]**	**Temp Res (K) [T/K]**
1	α-Al_2O_3 [44]	0.5	3	$R_2\rightarrow{}^4A_2/R_1\rightarrow{}^4A_2$	2.81	40	4.8 (20)	0.06 (20)
2	$Bi_2Al_4O_9$ [45]	0.75	2	$R_2\rightarrow{}^4A_2/R_1\rightarrow{}^4A_2$	2.45	~ 130	1.4 (100)	N/A
3	$Bi_2Ga_4O_9$ [46]	0.75	2	$R_2\rightarrow{}^4A_2/R_1\rightarrow{}^4A_2$	2.31	170	2.74 (80)	N/A
4	$Bi_2Ga_4O_9$ [46]	0.75	2	${}^2E\rightarrow{}^4A_2/{}^4T_2\rightarrow{}^4A_2$	2.31	390	0.7 (290)	N/A
5	$Bi_2Al_4O_9$ [45]	0.75	2	${}^2E\rightarrow{}^4A_2/{}^4T_2\rightarrow{}^4A_2$	2.45	726	1.24 (290)	0.2 (290)
6	$CaHfO_3$ [47]	0.0025	$\bar{1}$	${}^2E\rightarrow{}^4A_2/{}^4T_2\rightarrow{}^4A_2$	2.59	21	1.89 (40)	0.045 (40)
7	$YAl_3(BO_3)_4$ [48]	0.1	2	${}^2E\rightarrow{}^4A_2/{}^4T_2\rightarrow{}^4A_2$	2.44	457	2.03 (180)	~1.0 (180)
8	$LaSr_2Ga_{11}O_{20}$ [49]	3.0	2	${}^2E\rightarrow{}^4A_2/{}^4T_2\rightarrow{}^4A_2$	2.05	654	2.6 (190)	0.77 (190)
9	$LaGaO_3$[39]	1.0	$\bar{1}$	${}^2E\rightarrow{}^4A_2/{}^4T_2\rightarrow{}^4A_2$	2.60	1509	2.5 (300)	0.05 (300)
10	$ZnGa_2O_4$ [50]	0.5	$\bar{3}m$	${}^2E\rightarrow{}^4A_2/{}^4T_2\rightarrow{}^4A_2$	2.8	1744	2.8 (310)	1.0 (300)
11	$MgAl_2O_4$ [51]	1.0	$\bar{3}m$	${}^2E\rightarrow{}^4A_2/{}^4T_2\rightarrow{}^4A_2$	2.7	2206	3.5 (300)	0.3 (310)

The intermediate crystal field (Dq/B < 2.5) typically produces a moderate *ΔE* (< 1000 cm^{-1}) between the ^2E and $^4T_2$ states. The moderate *ΔE* allows for a high S_r (S_r < 1% K^{-1}) at temperatures below room temperature (~ 300 K), but not as low cryogenic temperatures; however, as temperature increases emission intensity decreases due to increased rate of non-radiative decay quenching the emission intensities. The choice of host material' containing cations that can be substituted by Cr^{3+}, can greatly affect the value of *ΔE*. For mullite-structured hosts $Bi_2Al_4O_9$ and $Bi_2Ga_4O_9$ (Entries 5 and 4), the *ΔE* values are 726 cm^{-1} and 360 cm^{-1}, with respective S_r at 290 K of 1.24 % K^{-1} and 0.7 % K^{-1}. Whilst they are isovalent, Ga^{3+} has a larger radius than Al^{3+} (0.62 Å vs 0.535 Å) and has a smaller difference in electronegativity than Al^{3+} when compared to O^{2-} (Al–O = 1.83, Cr–O = 1.78, Ga–O = 1.63). This is demonstrated by examining isostructural $Bi_2Al_4O_9$ and $Bi_2Ga_4O_9$, containing Al–O and Ga–O bond lengths of 1.914 Å and 1.993 Å, with *Dq/B* values of 2.46 and 2.3,1 respectively. The strength of the crystal field environment affecting Cr^{3+} ions when Cr^{3+} substitutes Ga^{3+} in a gallate material is typically weaker than when Cr^{3+} replaces Al^{3+} ions in an isostructural host material. The energy of the $^4T_2$ state markedly increases as the Cr–O bond length decreases.[52] The difference in the radii of Al^{3+} and Ga^{3+}, and therefore the bond lengths, changes the crystal field strength affecting Cr^{3+} for these two isostructural materials leading to the difference in the *ΔE.* A series of $YAl_3(BO_3)_4$ thermometers (Entry 7) were investigated to show how increasing Cr^{3+} concentration affected the S_r values. Increasing the Cr^{3+} concentration from 0.1 to 20 mol% lowered the crystal field from *Dq/B* = 2.44 to 2.30, which was attributed to the increase in Cr–O bond length from 1.916 Å to 1.924 Å as larger Cr^{3+} ions substituted the Al^{3+} ions. As a result of the decrease in the crystal field strength, the 0.1 mol% Cr^{3+} material had an S_r of 2.03% K^{-1} at 180 K, whilst that contains 5% Cr^{3+} had an S_r of 0.81% K^{-1}. For Cr^{3+} concentration over 5%, the phosphors gave negative S_r values due to reversed thermal trends. Spectral deconvolution enhanced the S_r values of the 1.0 mol%, 5 mol% and 10 mol% Cr^{3+}-doped thermometers to 1.84% K^{-1} at 179 K, 1.14% K^{-1} at 193 K, and 0.5% K^{-1} across 273 K to 323 K.

An exception of such intermediate field where the *ΔE* is small enough for cryogenic thermometry like R-line *LIR*. $CaHfO_3$ (Entry 6) was selected as a host due to its Cr–O bond length that would fall into the intermediate crystal field range, enabling a small *ΔE* between the ^2E and $^4T_2$ states. Whilst this material showed a *Dq/B* of 2.59, which is a strong crystal field environment, the *C/B* of the field is 5.49, higher than the standard *C/B* = 4.5 used to generate the d^3 Tanabe-Sugano diagram. Such a high *C/B* shows an increase in the energy of the ^2E state, thus lowering the *ΔE* between the ^2E and $^4T_2$ states (Figure 3.9b). The *ΔE* of 21 cm^{-1} then gave a S_r of 1.89 %K^{-1} at 40 K. Conversely, $LaSr_2Ga_{11}O_{20}$ doped with 3.0 mol% Cr^{3+} (Entry 8), gave a *Dq/B* of 2.05, indicating a weak crystal field; however, the emission spectrum showed both the $^4T_2$ and the ^2E emissions indicating an intermediate crystal field. This was due to *C/B* = 3.59, a far lower value than the typical *C/B* of 4.5. If the Tanabe-Sugano diagram is recalculated for *C/B* = 3.59 the *Dq/B* of 2.05 is then close to the intersection of the $^4T_2$ and ^2E states, thus matching the experimental emission data (Figure 3.9a). S_r for Entry 8 was calculated from a *ΔE* of 654 cm^{-1} as 2.6% K^{-1} at 190 K.

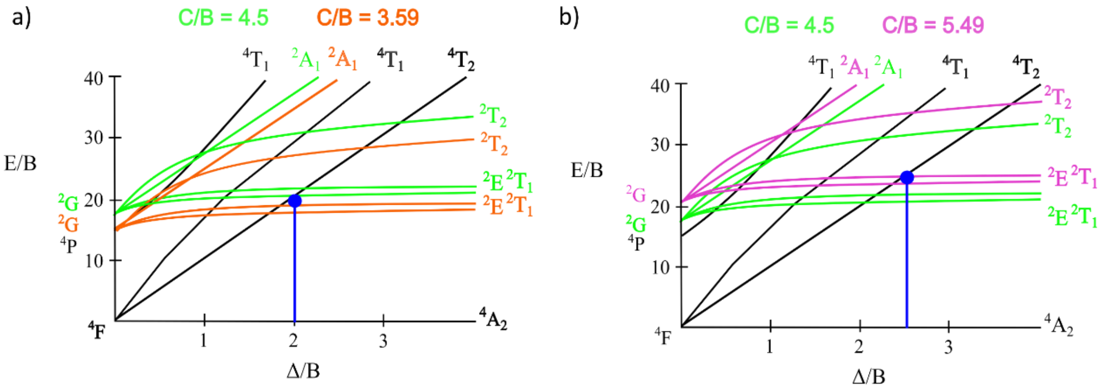

Figure 3.9: Tanabe-Sugano diagrams for d^3 ions in an octahedral coordination showing the change in energy of the ^2G free ions electronic states when C/B differs from that of 4.5. a) Lower C/B value than 4.5, b) Higher value than C/B = 4.5.[36]

The strong crystal field (*Dq/B* > 2.5) produces a large *ΔE* between ^2E and $^4T_2$ state as the $^4T_2$ state increases in energy above the crystal field-invariant ^2E state. A larger *ΔE* increases the temperature boundary of the thermometer and leads to higher S_r values, but is unusable at low temperatures due to the lack of energy to thermalise the excited ions from the lower excited state to the higher-lying excited state. $LaGa_{0.99}O_3:Cr_{0.01}$ (Entry 9) has a high S_r of 2.5% K^{-1} at 300 K due to the large *ΔE* between the $^4T_2$ and the ^2E excited states caused by the strong crystal field experienced by the Cr^{3+} ions in the CrO_6 octahedra. Spinel-structured $ZnGa_2O_4$ (Entry 10) has a smaller S_r value than the isostructural aluminate $MgAl_2O_4$ (Entry 11) at 300 K, of 3.2 % K^{-1} compared to 3.5 % K^{-1}. Contrary to previous isostructural materials such as the mullites, in the $ZnGa_2O_4$ structure the Cr^{3+} is estimated to be experiencing a slightly higher crystal field, than in $MgAl_2O_4$ despite Ga^{3+} having a larger radius than Al^{3+}.

The temperature resolution of the thermometer is dependent on the standard uncertainty in the *LIR* measurements and the relative sensitivity of the thermometer (Equation 1.13). A strongly emitting luminescent centre is a factor for low uncertainty in the measurements (low noise) of the phosphor at a single temperature, and thus an excellent temperature resolution.[53] The temperature resolution is also dependent on the detector sensitivity, the number of measurements recorded, the length of the acquisition time, the thermal stability of the host, and the S_r of the thermometer at the measured temperature. Higher S_r thermometers generally have higher resolution due to this dependence. There is, however, no set standard for the number of measurements to be taken, or the acquisition time and temperature resolution calculations have often not been reported in older research articles. $LaGa_{0.99}O_3:Cr_{0.01}$ has one of the best temperature resolutions of all the compared *LIR* thermometers, with only $CaHfO_3$ and α-Al_2O_3 offering similar temperature resolution. $CaHfO_3$ and α-Al_2O_3 , however, only give attain these temperature resolution values at cryogenic temperatures, unlike $LaGa_{0.99}O_3:Cr_{0.01}$ who achieves 0.05 K resolution at 300 K making it an excellent luminescence thermometer for practical room, and biological, temperature research.

Table 3.7: Comparison table of all $LaGaO_3$ LIR thermometers currently in the literature. The orange shaded cells are used to denote the material reported in this chapter.

Entry	**Dopant**	**Conc (mol%)**	**LIR emissions**	**ΔE (cm^{-1})**	**S_r (% K^{-1}) [T/K]**	**Temp Res (K)**	**Ref**
1	Cr^{3+}	1.0	$^2E\rightarrow^4A_2/^4T_2\rightarrow^4A_2$	1509	2.50 (300)	0.05 (300)	39
2	Cr^{3+}	0.5	$^2E\rightarrow^4A_2/^4T_2\rightarrow^4A_2$	324	2.07 (150)	0.24 (150)	6
3a	Nd^{3+}	3.0	$^4F_{5/2}\rightarrow^4I_{9/2}/^4F_{3/2}\rightarrow^4I_{9/2}$	994	1.59 (300)	1.1 (300)	7
3b	Nd^{3+}	3.0	$^4F_{7/2}\rightarrow^4I_{9/2}/^4F_{3/2}\rightarrow^4I_{9/2}$	1960	1.59 (450)	5.0 (450)	7
4	Er^{3+}, Yb^{3+}	3.0	$^4S_{3/2}\rightarrow^4I_{15/2}/^2H_{11/2}\rightarrow^4I_{15/2}$	720	1.17 (298)	N/A	54
5	Sm^{3+},Mn^{4+}	1.0, 0.1	$G_{5/2} \rightarrow H_{9,7,5/2}/^2E\rightarrow^4A_2$	N/A	2.09 (456)	N/A	55
6a	Nd^{3+}, V^{5+}	0.1, 1.0	$V^{4+}\rightarrow O^{2-}/^4F_{3/2}\rightarrow^4I_{9/2}$	N/A	1.0 (268)	N/A	56
6b	Nd^{3+}, V^{4+}	0.1, 1.0	$^2E\rightarrow^2T_2/^4F_{3/2}\rightarrow^4I_{9/2}$	N/A	0.49 (293)	N/A	56
6c	Nd^{3+}, V^{3+}	0.1, 1.0	$^3T_2\rightarrow^3T_{1g}/^4F_{3/2}\rightarrow^4I_{9/2}$	N/A	1.44 (348)	N/A	56
7a	Nd^{3+}, Er^{3+}	1.0, 1.0	$^4F_{3/2}\rightarrow^4I_{11/2}/^4F_{13/2}\rightarrow^4I_{15/2}$	N/A	0.6 (~480)	N/A	40
7b	Nd^{3+}, Er^{3+}, Cr^{3+}	1.0, 1.0, 15.0	$^4F_{3/2}\rightarrow^4I_{11/2}/^4F_{13/2}\rightarrow^4I_{15/2}$	N/A	0.54 (~250)	N/A	40
8	Cr^{3+}, Nd^{3+}	0.5, 2.0	$^2E\rightarrow^4A_2/^4F_{3/2}\rightarrow^4I_{9/2}$	310	0.49 (303)	N/A	57
9	Cr^{3+}, Nd^{3+}	1.0, 2.0	$^2E,^4T_2\rightarrow^4A_2/^4F_{3/2}\rightarrow^4I_{9/2}$	1170	2.00 (300)	0.04 (300)	58

3.3.4.2. Discussion of selected $LaGaO_3$ based luminescence thermometers

Table 3.7 summarises all the key parameters from all current $LaGaO_3$ thermometer literature at time of writing. Two different types of LIR have been reported:

- Singly doped luminescence thermometry using the emission ratio of a single transition metal or lanthanide ion.
- Dual emission LIR thermometry whereby the ratio of two luminescent centres with different temperature dependencies are used as the readout method.

As detailed in Section 3.3.3 of this chapter, the strong crystal field environment experienced by the Cr^{3+} in $LaGa_{0.99}O_3:Cr_{0.01}$ (Entry 1) causes the large ΔE between the ^2E and $^4T_2$ electronic states and therefore a high S_r at room temperature. For the related material, $LaGa_{0.995}O_3:Cr_{0.005}$ (Entry 2) there is a marked difference in ΔE, it has a lower maximum S_r and lower temperature at which the phosphor achieved that S_r value. The difference in the ΔE may be due to a potentially incorrect assignment of Cr^{3+} emission peaks, lack of deconvolution, and poor fitting of the LIR points to the linearised Boltzmann equation.

$La_{0.97}GaO_3:Nd_{0.03}$ (Entries 3a and 3b) and $La_{0.925}Ga_{0.99}O_3:Er_{0.75},Yb_{1.0}$ (Entry 4) use lanthanide ions as their luminescent centres. The shielded nature of the *4f* orbitals indicates the Ln^{3+} electronic states are barely split by the crystal field, and thus their electronic states are at approximately the same energy in most host materials regardless of the crystal field strength. Figure 3.10 displays a number of Ln^{3+} ion and their energy levels with pertinent transitions for the following discussion.

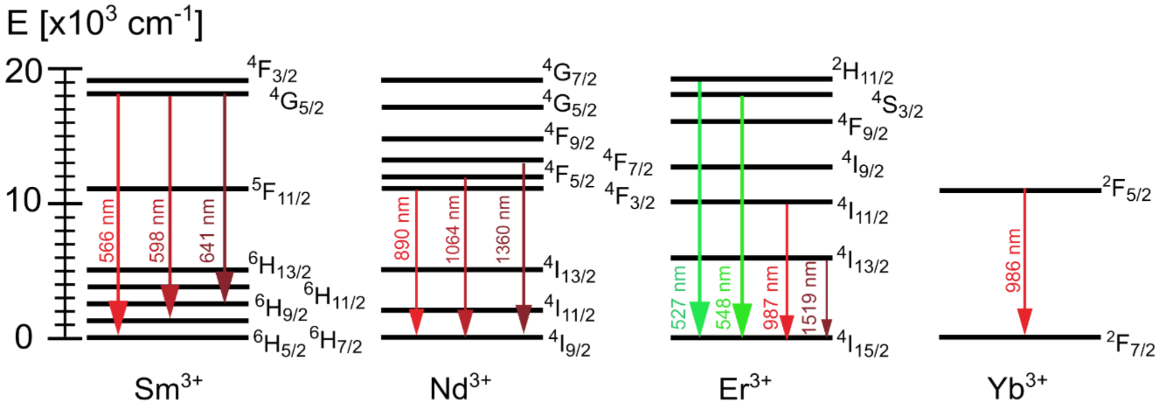

Figure 3.10: Energy level diagrams of Ln^{3+} ions and associated transitions shown by arrows.

Entry 3a used the emissions of the Nd^{3+} $^4F_{5/2}$, $^4F_{3/2} \rightarrow$ $^4I_{9/2}$ states for LIR thermometry. These emissions give a S_r of 1.59 % K^{-1} at 300 K with a ΔE of 994 cm^{-1}. Entry 3b shows the same material also has a higher-lying excited state, $^4F_{7/2} \rightarrow {}^4I_{9/2}$, that can be accessed with thermalisation above 450 K. The ratio of the $^4F_{7/2}$, $^4F_{3/2} \rightarrow {}^4I_{9/2}$ states give a larger ΔE (1960 cm^{-1}) than the aforementioned $^4F_{5/2}$ and $^4F_{3/2}$ thermally coupled states. However, as population of the $^4F_{7/2}$ state is not thermalised until the temperature is above 450 K, the S_r is the same as entry 3a at 1.59 % K^{-1} despite a larger ΔE given that S_r is inversely dependent on T^2 (Equation 1.22). Whilst Entry 4 is doped with two different lanthanide ions, it is not a dual-emitting *LIR* thermometer as no Yb^{3+} emission transitions are used in the *LIR* ratio. The Yb^{3+} ion is used instead as a sensitiser due to its $^2F_{5/2} \leftarrow {}^2F_{7/2}$ excitation at 980 nm which has a large cross section and is commonly used for NIR up-conversion excitation. Er^{3+} is the emitting ion and therefore this phosphor is treated as a singly-doped *LIR* thermometer. The ΔE between the two Er^{3+} emission bands of $^4S_{3/2} \rightarrow {}^4F_{15/2}$ and $^2H_{11/2} \rightarrow {}^4F_{15/2}$ at 527 nm and 548 nm respectively was calculated as 720 cm^{-1}, thus the S_r is 1.16 % K^{-1} at 298 K compared to 1506 cm^{-1} and an S_r of 2.5 %K^{-1} at 300 K for Entry 1. In the cases of Entries 3a and 4, the ΔE of the crystal field invariant Nd^{3+} and Er^{3+} electronic states chosen for *LIR* are smaller than that Entry 1, and thus had a lower S_r. In the case of Entry 3b, the S_r is larger than that of Entry 1 due to the thermalisation to a higher-lying excited state giving a larger ΔE than used in Entry 3a. The $^4F_{7/2} \rightarrow {}^4I_{9/2}$ emission, however, has little intensity below 450 K, therefore despite its larger ΔE, its maximum S_r is both lower than that of Entry 1 and only useable at a higher temperature.

The remaining $LaGaO_3$ thermometers are dual-doped *LIR* thermometers. As laid out in Section 1.3.3.1.2, dual-emission *LIR* thermometers use two different luminescence centres e.g., two Ln^{3+} ions, two TM ions, or one of each. The emission that does not change or changes minimally over the temperature range is used as a reference emission intensity. The remaining emission that quenches in intensity greatly with temperature is used as the sensing emission intensity. Entry 5 uses the 568 nm, 591 nm, and 641 nm emissions of the $G_{5/2} \rightarrow H_{9,7,5/2}$ states of the Sm^{3+} ion alongside the 701 nm ^2E emission of the Mn^{4+} ion for dual-emission *LIR* thermometry. The S_r was calculated as 2.09 % K^{-1} at 456 K. LIR points for the Sm^{3+} and Mn^{4+} emission intensities were calculated with an offset, and as there is a lack of calculated constants given in the publication, ΔE could not be accurately calculated. It follows that due to the similar S_r at a higher temperature, the ΔE of Entry 5 must be higher than that of Entry 1. The larger ΔE requires a higher temperature for thermalisation of the two emitting levels, thus decreasing the S_r to lower than that of Entry 1.

Entries 6a, 6b, and 6c represents three $LaGaO_3$ materials doped with vanadium and neodymium. Through changing the annealing temperature, the crystallite size was modified, changing the emission intensity of the various oxidation states of vanadium present. As annealing temperature increased and the crystallite grew, the intensity of V^{5+} emissions decreased, whilst V^{3+} and V^{4+} intensities increased. Nd^{3+} was co-doped to be used as the reference intensity due to the parity forbidden nature of its transitions causing the emission quenching to be low over the temperature range investigated. Entry 6a, using V^{5+} emission as the reference signal, showed a maximum sensitivity of ~1 % K^{-1} below room temperature. *LIR* using the V^{4+} emission, entry 6b, gave a lower maximum S_r of 0.49 % K^{-1} at 303 K due to the loss of V^{4+} emission intensity as energy transfer between the V^{4+} emission and Nd^{3+} dominated. Entry 6c gave the highest S_r of 1.44 %K^{-1} at 348 K. These S_r values were only achievable through selective annealing temperatures to enhance emission intensity due to increasing crystallite agglomeration with temperature. In comparison to entry 1, all three *LIR* thermometry readouts show a lower S_r, and no temperature resolution was recorded for the phosphors.

Entries 7a and 7b were investigated as a dual-emission Er^{3+}, Nd^{3+} *LIR* thermometers both with and without the addition of a large concentration of Cr^{3+} ions. Cr^{3+} was doped into the material to investigate its role as a sensitiser to Nd^{3+}, as a function of the host material's effects on the crystal field of Cr^{3+} for energy transfer. The maximum S_r of Entry 8 was 0.6% K^{-1} at 480 K (ΔE = 950 cm^{-1}), which then decreased slightly to 0.54% K^{-1} at 250 K (ΔE = 235 cm^{-1}) for Entry 9 when the Cr^{3+} ions were doped into the structure. A change to the thermometers' operating temperature range through Cr^{3+} doping to control the thermal quenching temperature can be highlighted. Both thermometers gave a lower ΔE than Entry 1, but, they show the ability to change the effective temperature range of a phosphor, which can be useful for non-room temperature systems.

Entry 8 used the $^2E \rightarrow {}^4A_2$ emission of the Cr^{3+} ion at 730 nm with the Nd^{3+} ion's $^4F_{3/2} \rightarrow {}^4I_{9/2}$ emission for dual luminescence LIR thermometry. The ΔE was calculated as 310 cm^{-1} resulting in a S_r of 0.49% K^{-1} at 303 K. The integrated emission intensities used for both the sensing and reference emission intensity peaks only spans 1 nm. The small integration used for each emission may have contained an area of intensity that did not quench quickly with increasing temperature, thereby lowering the sensitivity of the phosphor thermometer. This contrasts with Entry 1 where through the use of deconvolution, the whole ^2E and $^4T_2$ emission bands were integrated and used for calculation of the *LIR* points, allowing for the high ΔE to be calculated. A similar material synthesised by solid state method with an increased concentration of Cr^{3+}, and a higher S_r – $La_{0.98}Ga_{0.99}O_3$: $Cr_{0.01}$, $Nd_{0.02}$ (Entry 9) – will be discussed further in Chapter 4.

To summarise the $LaGaO_3$ thermometers: both the number, and the choice, of the dopants for *LIR* are the key to the ΔE, the quenching rate, and therefore to the S_r of the thermometer. Singly doped lanthanide ion *LIR* thermometers suffer from little variation on the crystal field, and (such as with Nd^{3+} doping), require higher temperatures to thermalise thermally coupled states with large ΔE for high S_r. On the other hand, dual-emission *LIR* thermometry depends on the different quenching behaviours of the dopants, with reference emissions with fast quenching giving high S_r values. $LaGa_{0.99}O_3$:$Cr_{0.01}$ prepared in this work exhibits the highest S_r of all $LaGaO_3$ materials in the current literature, alongside one of the highest temperature resolutions. Much of the $LaGaO_3$-based thermometer research either did not state a temperature resolution, or temperature resolutions reported were markedly lower compared to the $LaGaO_3$ material due to low S_r values.

3.4. Conclusion and future work

A series of six $LaGa_{1-x}O_3$:Cr_x (x = 0.002, 0.005, 0.001, 0.02, and 0.04) phosphors were successfully synthesised and characterised by PXRD. Room-temperature excitation spectra showed the distinct $^4T_1(P)$ and $^4T_2$ excitation bands of Cr^{3+} at 446 nm and 619 nm respectively for all Cr^{3+} containing samples. Through calculations using the energy of these excitation bands, the crystal field strength was found to be Dq/B = 2.6, indicating that the Cr^{3+} ions are experiencing a strong crystal field environment. Emission spectra supported this assessment with the sharp, spin-forbidden ^2E peak being the only emission band observed at room temperature. The quantum yields measured showed that $LaGa_{0.99}O_3$:$Cr_{0.01}$was the most promising phosphor for further evaluation, with a *QY* of 8(2)%. Variable-temperature emission spectra were recorded between 300 K and 600 K and the *LIR* values from the ratio of the $^4T_2$ and ^2E transitions as temperature increased were calculated. By deconvolving the two emissions through the approximate deconvolution method, the values of the LIR were achieved without the need of an additional term to the LIR Boltzmann equation. The energy gap of the deconvolved emissions was calculated as 1509 cm^{-1}, and from this the relative sensitivity was found to be 2.5% K^{-1} at 300 K with a high temperature resolution of 0.05 K. When compared to the current literature on $LaGaO_3$ *LIR* thermometers, $LaGa_{0.99}O_3$:$Cr_{0.01}$ shows the largest S_r at 300 K. The high S_r value was attributed to the strong crystal field interaction on the Cr^{3+} leading to a large ΔE compared to the energy gaps between the transitions of the other $LaGaO_3$ thermometers with different doping ions, and singly-doped Cr^{3+} *LIR* thermometers using either the ^{2}E and $^4T_2$ emission ratios or R-lines due to Cr^{3+} ion site symmetry lowering. Due to its high S_r and low uncertainty in temperature measurements, $LaGa_{0.99}O_3$:$Cr_{0.01}$ demonstrated one of the highest temperature resolutions of all compared thermometers at 300 K.

Future work on this material should focus on additional readout methods that have not been fully explored, such as ^{2}E and N-line lifetimes, band-shifts, and bandwidth. At cryogenic temperatures ($T < 120$ K) the ^{2}E R-lines for *LIR* thermometry could also be explored. Additionally, there is the potential for increasing the crystal field of $LaGa_{1-x}O_3$:Cr_x^{3+} by substituting Ga^{3+} by smaller Al^{3+} in high concentrations. Substitution of the Ga^{3+} by isovalent Al^{3+} should decrease the unit cell volume and Cr-O bond length, in turn increasing the crystal field and ΔE, thus increasing the S_r of the thermometer. $LaAlO_3$:Cr^{3+} has been investigated for as a phosphor, with excitation peaks reported at shorter wavelengths than $LaGaO_3$:Cr^{3+}, indicating a higher *Dq/B*.[59] $LaAlO_3$:Cr^{3+} has not yet been investigated as a luminescence thermometer, allowing the possibility for exploration of a similar host to $LaGaO_3$:Cr^{3+}. Furthermore, with an optimal Cr^{3+} concentration identified for $LaGaO_3$ phosphors, co-doping with a second dopant can be investigated. A second luminescent centre would extend the range of wavelengths over which the phosphor can absorb and emit, with emission in the NIR range achieved using lanthanide ions such as Nd^{3+}, Yb^{3+}, or Er^{3+}.[4,60] Such an investigation is presented in Chapter 4, which details the synthesis of materials of composition $La_{1-y}Ga_{0.99}O_3$:$Cr_{0.01}$, Nd_y ($y = 0.005, 0.01, 0.02$) materials, their characterisation, and results for dual emission near-infrared *LIR* thermometry.

3.5. References

1 X. Liu and J. Lin, *J Appl Phys*, 2006, **100**, 124306.

2 B.-M. Liu, R. Zou, S.-Q. Lou, Y.-F. Gao, L. Ma, K.-L. Wong and J. Wang, *Chem. Eng. J.*, 2021, **404**, 127133.

3 T. Ishihara, J. Tabuchi, S. Ishikawa, J. Yan, M. Enoki and H. Matsumoto, *Solid State Ion.*, 2006, **177**, 1949–1953.

4 L. Zhang, L. Dong, B. Shao, S. Zhao and H. You, *Dalton Trans.*, 2019, **48**, 11460–11468.

5 Z. Li, Y. Yan, T. Wang, S. Wang, L. Guo, W. Feng, L. Zhao, Z. Wang, F. Zhao, J. Chen, Z. Zhang, X. Xu and X. Yu, *J. Rare Earths*, 2023, **41**, 1869–1875.

6 A. Mondal and J. Manam, *Ceram. Int.*, 2020, **46**, 23972–23984.

7 M. Back, J. Ueda, J. Xu, D. Murata, M. G. Brik and S. Tanabe, *ACS Appl. Mater. Interfaces*, 2019, **11**, 38937–38945.

8 V. M. Goldschmidt, *Naturwissenschaften*, 1926, **14**, 477–485.

9 S. A. T. Redfern, *J. Phys. Condens. Matter*, 1996, **8**, 8267–8275.

10 P. M. Woodward, P. Karen, J. S. O. Evans and T. Vogt, *Solid State Materials Chemistry*, Cambridge University Press, Cambridge, 1st edn., 2021.

11 R. D. Shannon, *Acta Cryst. A*, 1976, **32**, 751–767.

12 M. Lerch, H. Boysen and T. Hansen, *J. Phys. Chem. Solids*, 2001, **62**, 445–455.

13 A. M. Glazer, *Acta Crystallogr. Sect. B*, 1972, **28**, 3384–3392.

14 P. M. Woodward, *Acta Crystallogr. Sect. B*, 1997, **53**, 44–66.

15 L. Marciniak, K. Kniec, K. Elżbieciak-Piecka, K. Trejgis, J. Stefanska and M. Dramićanin, *Coord. Chem. Rev.*, 2022, **469**, 214671.

16 K. Elzbieciak, A. Bednarkiewicz and L. Marciniak, *Sens. Actuators B Chem.*, 2018, 96–102.

17 K. Elzbieciak and L. Marciniak, *Front. Chem.*, 2018, **6**, 1–8.

18 A. A. Coelho, J. Evans, I. Evans, A. Kern and S. Parsons, *Powder Diffr.*, 2011, **26**, S22–S25.

19 H. M. Rietveld, *J. Appl. Crystallogr.*, 1969, **2**, 65–71.

20 G. T. Georgiev and J. J. Butler, *Appl. Opt.*, 2007, **46**, 7892–7899.

21 A. Ćirić, S. Stojadinović and M. D. Dramićanin, *Meas. Sci. Technol.*, 2019, **30**, 045001.

22 M. Kasunič, A. Meden, S. D. Škapin, D. Suvorov and A. Golobič, *Acta Crystallogr. Sect. B*, 2009, **65**, 558–566.

23 I. Stijepovic, R. Djenadic, V. V. Srdic and M. Winterer, *J. Eur. Ceram. Soc.*, 2015, **35**, 3545–3552.

24 Q. Yang, A. Cao, N. Kang, K. An, Z.-T. Liu and Y. Liu, *Fuel Process. Technol.*, 2018, **179**, 42–52.

25 D. Waroquiers, X. Gonze, G.-M. Rignanese, C. Welker-Nieuwoudt, F. Rosowski, M. Göbel, S. Schenk, P. Degelmann, R. André, R. Glaum and G. Hautier, *Chem. Mater.*, 2017, **29**, 8346–8360.

26 Ch. S. Kamal, T. K. V. Rao, T. Samuel, P. V. S. S. S. N. Reddy, J. B. Jasinski, Y. Ramakrishna, M. C. Rao and K. R. Rao, *RSC Adv.*, 2017, **7**, 44915–44922.

27 N. V. Chezhina, É. V. Bodritskaya, N. A. Zhuk, V. V. Bannikov, I. R. Shein and A. L. Ivanovskiĭ, *Phys. Solid State*, 2008, **50**, 2121–2126.

28 N. Lakshminarasimhan and U. V. Varadaraju, *Mater. Res. Bull.*, 2006, **41**, 724–731.

29 H. Hua, J. Ueda, J. Xu, M. Back and S. Tanabe, *Inorg. Chem.*, 2021, **60**, 19253–19262.

30 W. Mikenda and A. Preisinger, *J. Lumin.*, 1981, **26**, 53–66.

31 J. Derkosch, W. Mikenda and A. Preisinger, *J. Solid State Chem.*, 1977, **22**, 127–133.

32 W. Mikenda and A. Preisinger, *J. Lumin.*, 1981, **26**, 67–83.

33 J. Xu, J. Ueda and S. Tanabe, *J. Am. Ceram. Soc.*, 2017, **100**, 4033–4044.

34 Y. Tanabe and S. Sugano, *J. Phys. Soc. Jpn.*, 1954, **9**, 753–766.

35 Y. Tanabe and S. Sugano, *J. Phys. Soc. Jpn.*, 1954, **9**, 766–779.

36 Tanabe-Sugano Diagrams, https://chem.libretexts.org/Bookshelves/Inorganic_Chemistry/Supplemental_Modules_and_Websites_(Inorganic_Chemistry)/Crystal_Field_Theory/Tanabe-Sugano_Diagrams, (accessed 30 June 2021).

37 M. G. Brik and A. M. Srivastava, *Opt. Mater.*, 2013, **35**, 1251–1256.

38 W. Ryba-Romanowski, S. Golab, G. Dominiak-Dzik, I. Sokolska and M. Berkowski, in *SPIE*, Zakopane, Poland, 1999, vol. 3724.

39 A. L. Mullins, A. Ćirić, Z. Ristić, J. A. G. Williams, I. R. Evans and M. D. Dramićanin, *J. Lumin.*, 2022, **246**, 118847.

40 W. M. Piotrowski, K. Maciejewska and L. Marciniak, *Mater. Today Chem.*, 2023, **30**, 101591.

41 G. Blasse and B. C. Grabmaier, *Luminescent Materials*, Springer-Verlag, 1994.

42 A. Ćirić, Z. Ristić, Ž. Antić and M. D. Dramićanin, *Phys. B Condens. Matter*, 2022, **624**, 413454.

43 W. Ryba-Romanowski, S. Golab, G. Dominiak-Dzik and M. Berkowski, *J. Alloys Compd.*, 1999, **288**, 262–268.

44 A. Ćirić, S. Stojadinović, Z. Ristić, Ž. Antić and M. D. Dramićanin, *Sens. Actuators Phys.*, 2021, **331**, 112987.

45 M. Back, J. Ueda, J. Xu, K. Asami, M. G. Brik and S. Tanabe, *Adv. Opt. Mater.*, 2020, **8**, 2000124.

46 M. Back, E. Trave, J. Ueda and S. Tanabe, *Chem. Mater.*, 2016, **28**, 8347–8356.

47 M. Back, J. Ueda, M. G. Brik and S. Tanabe, *ACS Appl. Mater. Interfaces*, 2020, **12**, 38325–38332.

48 K. Elzbieciak-Piecka and L. Marciniak, *Sci. Rep.*, 2022, **12**, 16364.

49 X. Shan, M. Back, D. Chen, S. Miao, R. Shi and Y. Liang, *J. Mater. Chem. C*, 2023, **11**, 8952–8960.

50 J. Ueda, M. Back, M. G. Brik, Y. Zhuang, M. Grinberg and S. Tanabe, *Opt. Mater.*, 2018, **85**, 510–516.

51 A. Ćirić, Z. Ristić, J. Periša, Ž. Antić and M. D. Dramićanin, *Ceram. Int.*, 2021, **47**, 27151–27156.

52 K. Ogasawara, F. Alluqmani and H. Nagoshi, *ECS J. Solid State Sci. Technol.*, 2016, **5**, R3191–R3196.

53 T. P. van Swieten, A. Meijerink and F. T. Rabouw, *ACS Photonics*, 2022, **9**, 1366–1374.

54 H. Xu, Y. Lian, Z. Lu, I. Kolesnikov, Y. Zhao, K. He, Z. Su, G. Bai and S. Xu, *J. Mater. Chem. C*, 2022, **10**, 10660–10668.

55 Z. Li, X. Yu, T. Wang, S. Wang, L. Guo, Z. Cui, G. Yan, W. Feng, F. Zhao, J. Chen, X. Xu and J. Qiu, *J. Am. Ceram. Soc.*, 2022, **105**, 2804–2812.

56 K. Kniec and L. Marciniak, *Phys. Chem. Chem. Phys.*, 2018, **20**, 21598–21606.

57 H. Xu, G. Bai, K. He, S. Tao, Z. Lu, Y. Zhang and S. Xu, *Mater. Today Phys.*, 2022, **28**, 100872.

58 A. L. Mullins, A. Ćirić, I. Zeković, J. A. G. Williams, M. D. Dramićanin and I. R. Evans, *J. Mater. Chem. C*, 2022, **10**, 10396–10403.

59 Y. Katayama, H. Kobayashi and S. Tanabe, *Appl. Phys. Express*, 2014, **8**, 012102.

60 J. Xu, D. Murata, Y. Katayama, J. Ueda and S. Tanabe, *J. Mater. Chem. B*, 2017, **5**, 6385–6393.

4. Dual-emission luminescence intensity ratio luminescence thermometry using $LaGaO_3:Cr^{3+}, Nd^{3+}$ phosphors

4.1. Introduction

Aiming to improve the properties of the Cr^{3+}-doped $LaGaO_3$-based luminescence thermometers presented in Chapter 3, further work was undertaken by preparing a series of materials doubly-doped with Cr^{3+} and Nd^{3+}. La^{3+} has an ionic radius of 1.160 Å when 8-coordinate.[1] Despite the lanthanide contraction, other Ln^{3+} ions are only slightly smaller, so that it should be possible to substitute some of the La^{3+} by emissive Ln^{3+} ions.[1] The visible and NIR-emissive Nd^{3+} ion has an ionic radius of 1.109 Å when 8-coordinate, and it has been proven to readily substitute La^{3+} in $LaGaO_3$ phosphors.[1–7]

Nd^{3+} has been used as an activator for single-emission *LIR* thermometers, lifetime thermometers, band-shift and bandwidth thermometers, as well as in dual-emission *LIR* thermometers with two unique Ln^{3+}-Ln^{3+} ions and with Ln^{3+}-TM ions.[8–12] Parity-forbidden 4f-4f intra-ionic transitions give rise to narrow excitation and emission peaks, facilitating good discrimination between different emission bands. The narrow peak widths are due to the contracted Ln^{3+} f-orbitals having little overlap with the ligand orbitals. Upon excitation and emission the Stokes shift is small as there is little change to Ln^{3+}-ligand bond lengths between the ground and excited states. A further consequence of the small crystal field is that the ligands only affect the energy of the states slightly ($\sim 10^2$ cm^{-1}); therefore, in most host materials, the emission and excitation wavelengths of a given Ln^{3+} ion are similar. Nd^{3+} has several NIR emissions including the $^4F_{3/2} \rightarrow {}^4I_{9/2}$, $^4I_{11/2}$, and $^4I_{13/2}$ transitions that span biological windows 1 and 2 (BW-1, BW-2), making Nd^{3+} thermometers attractive for medical application.[13] Moreover, the large number of higher energy levels of Nd^{3+} permits multiple excitation wavelengths within the visible and BW-1 regions of the electromagnetic spectrum to be used.

As discussed in Section 1.3.3.1.2, dual-emission *LIR* thermometry uses any combination of two different TM and Ln^{3+} ions, or an activator ion and the emission from the host material.[14] It usually relies on one ion's emission being invariant to quenching as temperature increases, whilst the remaining centre's emission is efficiently quenched in the temperature range investigated.[15] Ln^{3+} excited states are deactivated mostly through multiphonon relaxation and promotion to higher energy states. The Ln^{3+} excited states are usually quenched far more slowly than the spin-allowed TM complexes, which quench through a crossover point of the excited and ground state potential surfaces.

The aims of this work, expanding the best performing Cr^{3+}-doped thermometer ($LaGa_{0.99}O_3:Cr_{0.01}$) presented in Chapter 3, were:

- To synthesise and characterise the structure and properties of a series of $La_{1-x}Ga_{0.99}O_3:Cr_{0.01},Nd_x$ materials with increasing Nd^{3+} concentration ($x = 0.005$, 0.01, 0.02).
- To collect room temperature excitation spectra, and emission spectra showing simultaneous emissions from both the Cr^{3+} and Nd^{3+} ions using a single excitation wavelength.
- To record the Cr^{3+} ^2E emission lifetimes of each material to probe the expected increase in energy transfer from $Cr^{3+} \rightarrow Nd^{3+}$ as Nd^{3+} concentration increased.
- To measure variable-temperature emission spectra of each material.
- To calculate figures of merit and compare the phosphors' effectiveness as luminescence thermometers against current literature.

4.2. Experimental

4.2.1. Synthetic method

Polycrystalline samples of $La_{1-x}Ga_{0.99}O_3:Cr_{0.01},Nd_x$ (where $x = 0.005$, 0.01, 0.02) were synthesised in 2.00 g batches by conventional solid-state methods.[9] Due to its hygroscopic nature, La_2O_3 powder (Aldrich, >99.99%) was pre-heated to 900°C for 10 hours to remove bound water. Stoichiometric masses of the dried La_2O_3, Ga_2O_3 (Aldrich, >99.99%), Cr_2O_3 (Aldrich, 99.9%) and Nd_2O_3 (Aldrich, 99.99%) were ground for 30 minutes in agate mortar and pestles until homogenised. The powders were pressed into two individual 10 mm diameter pellets at 7 tonnes via pneumatic pellet press and placed in alumina crucibles. The samples were sintered at 1200°C in 10 h or 20 h intervals with heating and cooling ramps of 5°C/min. All materials were synthesised once. Table 4.1 summarises the heating regime of each material.

Table 4.1: Synthetic details for the $LaGa_{1-x}O_3$: $Cr_{0.01}$, Nd_x series until a pure phase was determined.

Material	Synthesis time (h)
$La_{0.995}Ga_{0.99}O_3:Cr_{0.01}$, $Nd_{0.005}$	10, 20, 20
$La_{0.99}Ga_{0.99}O_3:Cr_{0.01}$, $Nd_{0.01}$	10, 20, 20
$La_{0.98}Ga_{0.99}O_3:Cr_{0.01}$, $Nd_{0.02}$	10, 20, 20, 20, 20

4.2.2. Powder X-ray diffraction

PXRD measurements for monitoring sample phase purity were undertaken using a Bruker d8 AXS Advance diffractometer with Lynx Eye detector and CuK_α radiation source. Patterns were recorded in the 2θ range between $10° < 2\theta < 80°$, with a step size of 0.02° and a step time of 0.5 s/step. All diffraction data were analysed by the Rietveld method using TOPAS Academic v7 software.[16,17] Refined parameters included a nine-polynomial background, sample height displacement, unit cell parameters, pseudo-Voigt peak shape terms, scale factor, and an overall isotropic atomic displacement parameter.

4.2.3. Room-temperature photoluminescence

Room temperature excitation and emission spectra were acquired using a Horiba Jobin-Yvon Fluorolog-3 with either a R928 Hamamatsu photomultiplier tube detector, or a Horiba Synapse back-illuminated deep depletion CCD detector, and a 450W xenon lamp white light source with monochromator grating for excitation and emission wavelength selection. For monitoring NIR emission $\lambda > 1000$ nm, a Hamamatsu NIR photomultiplier tube was employed. Both 400 nm and 850 nm long pass filters were used to remove harmonic peaks during excitation and emission spectra acquisition. Samples were contained in either 3.0 mm O.D quartz capillaries and held in a custom 3D printed holder, or within Spectralon© cups with quartz cover slips in a Quanta-Phi integrating sphere. FluorEssence software was used to control the spectrometer and acquire excitation and emission data. Lifetime measurements were undertaken using an Edinburgh Instruments OB920 lifetime spectrometer with samples inside 3 mm outer diameter quartz capillary and excited by a microsecond pulsed flashlamp. A R928 detector operating in multichannel scaling mode was used to detect emitted light at a right angle from the excitation source.

4.2.4. Variable-temperature photoluminescence

Variable-temperature emission data were collected between 300 and 625 K using an Ocean Insight FX spectrometer attached to a bifurcated fibre optic cable, with a custom-made heating stage.[18] Material excitation was achieved using a 473 nm high stability laser (150 mW) with reflected light removed using a 500 nm long pass filter.

4.3. Results and discussion

4.3.1. Structural characterisation

$LaGaO_3$ in space group *Pnma* (ICSD code: 51258) was used as the initial structural model and fitted to all PXRD data.[19] Figure 4.1 shows excellent agreement between the experimental PXRD data and structural model, with all three refinements having R_{wp} of ~ 5% (Table 4.1). No extra peaks are seen in the Rietveld plots, suggesting that single-phase products have been obtained. The R_{wp}, unit cell parameters, and calculated unit cell volumes of each material are given in Table 4.2. With the slight difference in ionic radii between La^{3+} and Nd^{3+} (1.160 Å vs 1.109 Å), there was a small decrease in both the unit cell parameters and volume across the investigated doping range.

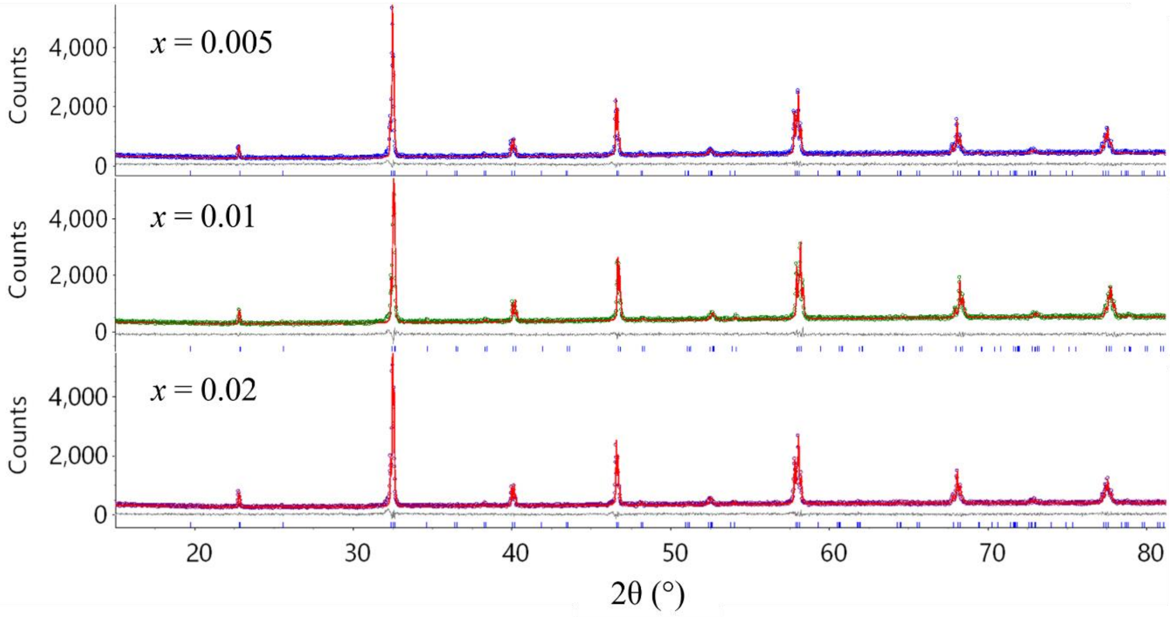

Figure 4.1: Rietveld plots of $La_{1-x}Ga_{0.99}O_3:Cr_{0.01},Nd_x$ (where x = 0.005, 0.01, and 0.02) with $LaGaO_3$ structural model fitted to the experimental data.

Table 4.2: Unit cell parameters obtained from Rietveld refinement for $La_{1-x}Ga_{0.99}O_3:Cr_{0.01}$, Nd_x (where x = 0.005, 0.01, and 0.02)

Material	**R_{wp} (%)**	**a (Å)**	**b (Å)**	**c (Å)**	**Unit Cell volume (Å^3)**
$La_{0.995}Ga_{0.99}O_3:Cr_{0.01}$, $Nd_{0.005}$	5.52	5.4924(1)	7.7747(1)	5.5241(1)	235.895(8)
$La_{0.99}Ga_{0.99}O_3:Cr_{0.01}$, $Nd_{0.01}$	5.35	5.49259(9)	7.7745(1)	5.52399(9)	235.890(7)
$La_{0.98}Ga_{0.99}O_3:Cr_{0.01}$, $Nd_{0.02}$	5.75	5.4923(1)	7.7745(1)	5.5227(1)	235.828(8)

4.3.2. Room temperature photoluminescence

The emission spectra of $La_{0.995}Ga_{0.99}O_3$:$Cr_{0.01}$, $Nd_{0.005}$, $La_{0.99}Ga_{0.99}O_3$:$Cr_{0.01}$, $Nd_{0.01}$, and $La_{0.98}Ga_{0.99}O_3$:$Cr_{0.01}$, $Nd_{0.02}$ were collected upon excitation into the spin-allowed $^4T_2 \leftarrow ^4A_2$ absorption band of Cr^{3+} at 590 nm. The spectra (Figure 4.2) show two distinct sets of peaks: a set between 700 and 750 nm attributed to the spin-forbidden ^2E emission of the Cr^{3+} ion; and a set of narrow peaks in the range 860 nm and 930 nm arising from the $^4F_{3/2} \rightarrow ^4I_{9/2}$ transition of the Nd^{3+} ion. No evidence of emission arising from the spin-allowed $^4T_2 \rightarrow ^4A_2$ transition of Cr^{3+} is observed. This indicated a strong crystal field about the Cr^{3+} such that the $^4T_2$ state lies at a significantly higher energy than the ^2E state, thermally inaccessible at room temperature. The Cr^{3+} band shows not only the spin-forbidden ^2E peak at 729 nm but also the Cr^{3+} concentration-dependent N-line indicative of exchange-coupled Cr^{3+}-Cr^{3+} pairs at 739 nm.[20,21] When normalised to the ^2E peak, the N-lines have approximately equal emission intensities, as expected given the constant Cr^{3+} concentration of 1.0 mol%. Either side of ^2E and N-line emission peaks, Stokes and anti-Stokes sidebands caused by phonons of the host can be observed for all three materials. The intensity of the distinct, line-like Stark splitting of the Nd^{3+} emission centred at 890 nm can be seen to increase with the concentration of Nd^{3+}, relative to the Cr^{3+} emission normalised to the ^2E emission. Additionally, there is a slight increase in the intensity of the emerging $^4F_{5/2} \leftarrow ^4I_{9/2}$ emission at around 800 nm as the Nd^{3+} concentration increases. The $^4F_{5/2}$ state is thermally coupled to the $^4F_{3/2}$ state at room temperature due to the small energy difference between them. The Nd^{3+} emissions may arise, in part, due to direct excitation of the $^4G_{5/2} \leftarrow ^4I_{9/2}$ transition at the excitation wavelength used. Alternatively, energy transfer due to the overlap of the ^2E emission of the Cr^{3+} with the $^4F_{7/2}$, $^4S_{3/2}$, and $^4F_{9/2}$ states of the Nd^{3+} could cause indirect population.

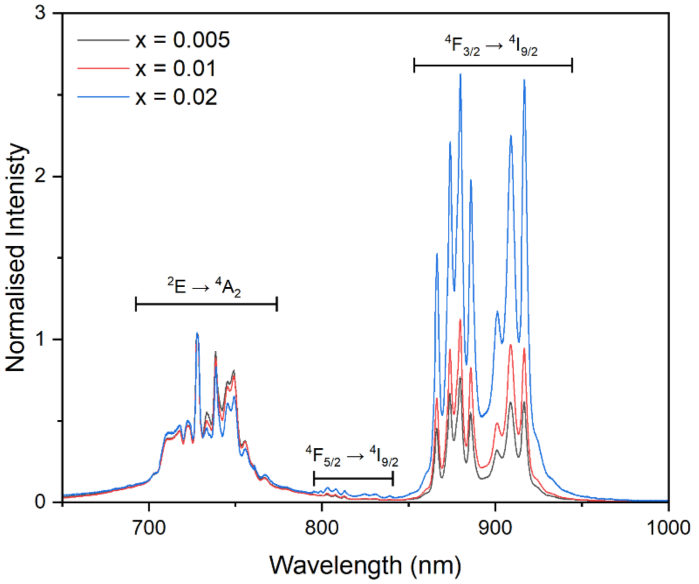

Figure 4.2: Emission spectra of $La_{1-x}Ga_{0.99}O_3$: $Cr_{0.01}$, Nd_x (x = 0.005, 0.01, 0.02) series, normalised to the ^2E Cr^{3+} emission at 729 nm. Excitation wavelength = 590 nm.

Figure 4.3 shows the deeper NIR emissions of by all three materials, with the $^4F_{3/2}\rightarrow{}^4I_{9/2}$ band centred at 1070 nm, and the $^4F_{3/2}\rightarrow{}^4I_{11/2}$ band centred at 1360 nm both observed.

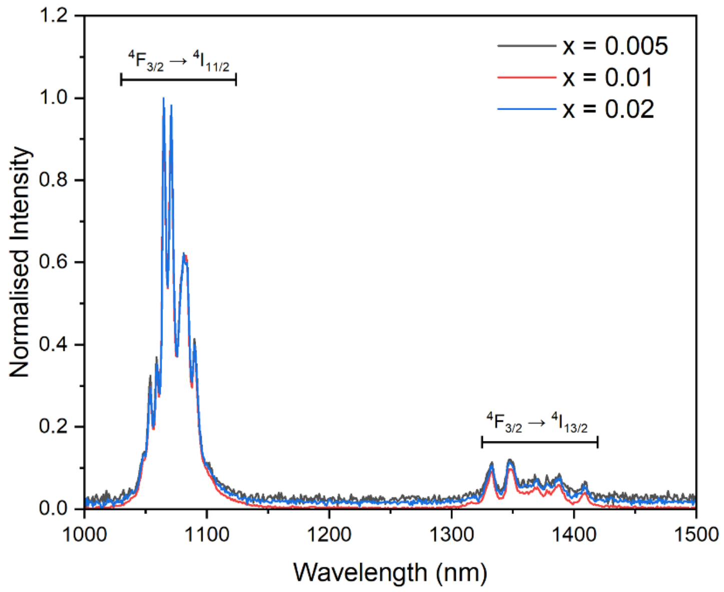

Figure 4.3: NIR emission spectra of Nd^{3+} in the $La_{1-x}Ga_{0.99}O_3$: $Cr_{0.01}$, Nd_x (x = 0.005, 0.01, 0.02) series, normalised to the highest intensity. Excitation wavelength = 590 nm.

Interpretation of the excitation spectra of Cr^{3+} and Nd^{3+} respectively aided in determining if energy transfer had played a significant role. The Cr^{3+} excitation spectra in Figure 4.4 show the expected broad excitation bands of the $^4T_1 \leftarrow {}^4A_2$ and $^4T_2 \leftarrow {}^4A_2$ transitions at 444 nm and 624 nm respectively. Additionally, there is evidence of the characteristic sharp excitation peaks of Nd^{3+} ions superimposed on the Cr^{3+} absorption bands.

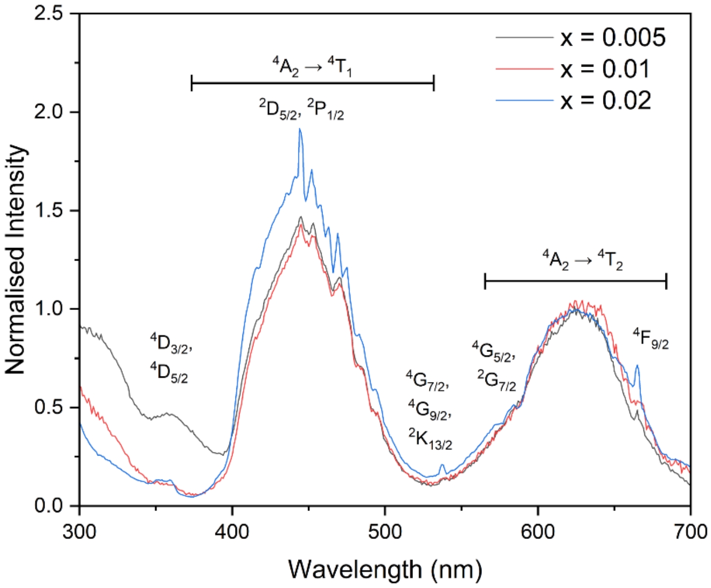

Figure 4.4: Excitation spectra of Cr^{3+} in the $La_{1-x}Ga_{0.99}O_3$: $Cr_{0.01}$, Nd_x (x = 0.005, 0.01, 0.02) series, monitored at 729 nm, normalised to the $^4T_2$ excitation band.

The narrow peaks at 665, 537, 444, and 354 nm matched well with the positions of the $^4F_{9/2}$; $^4G_{5/2}$ and $^2G_{7/2}$; $^4G_{7/2}$, $^4G_{9/2}$, and $^2K_{13/2}$; $^2D_{5/2}$ and $^2P_{1/2}$; and $^4D_{3/2}$ and $^4D_{5/2}$ excited states of Nd^{3+}.[13] The appearance of these Nd^{3+} excitation peaks in all three Cr^{3+} excitation spectra suggested there was a level of $Nd^{3+} \rightarrow Cr^{3+}$ energy transfer occurring.

The Nd^{3+} excitation spectra for all three materials (Figure 4.5) showed typical line-like excitations to the $^4F_{3/2}$ at 880 nm; $^2H_{9/2}$ and $^4F_{5/2}$ at 810 nm; $^4F_{7/2}$ and $^4S_{3/2}$ at 740 nm; $^4F_{9/2}$ at 680 nm; $^4G_{5/2}$ and $^2G_{7/2}$ at 590 nm; $^4G_{7/2}$, $^2G_{9/2}$, and $^2K_{13/2}$ at 520 nm; $^2D_{5/2}$ and $^2P_{1/2}$ at 440 nm; and $^4D_{3/2}$ and $^4D_{5/2}$ states at 350 nm. It's notable that the broad emission bands characteristic of Cr^{3+} excitation centred at 444 nm and 624 nm appear in all three Nd^{3+} excitation spectra. The appearance of the Cr^{3+} excitations when monitoring the Nd^{3+} emission indicates the occurrence of $Cr^{3+}\rightarrow Nd^{3+}$ energy transfer. The decrease in the relative intensity of the Nd^{3+} excitations may be due to the increasing Nd^{3+} content causing quenching via cross-relaxation.

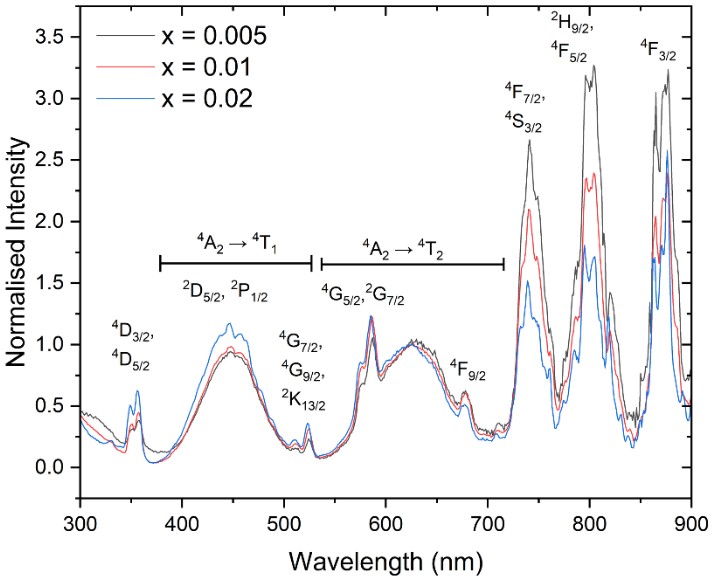

Figure 4.5: Excitation spectra of Nd^{3+} in the $La_{1-x}Ga_{0.99}O_3$: $Cr_{0.01}$, Nd_x (x = 0.005, 0.01, 0.02) series monitored at 1071 nm, normalised to the $^4T_2$ excitation band.

A configuration coordinate diagram showing the relevant relative energy levels of both Cr^{3+} and Nd^{3+} electronic states is given in Figure 4.6. The black and red dashed lines illustrate the $Cr^{3+}\rightarrow Nd^{3+}$ and the $Nd^{3+}\rightarrow Cr^{3+}$ energy transfer respectively, revealed by the excitation spectra.

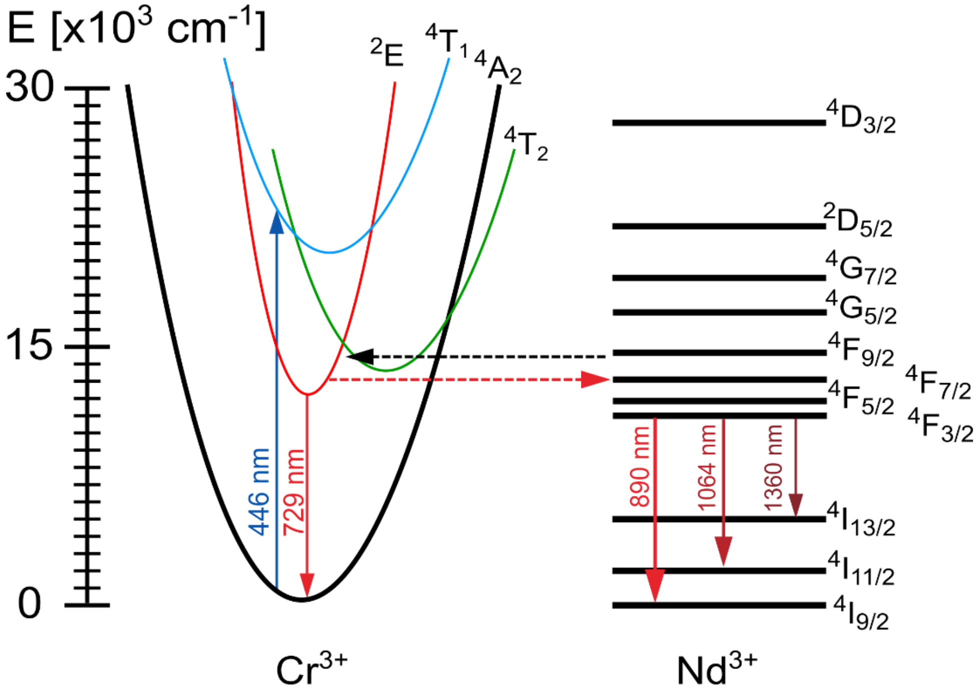

Figure 4.6: Coordinate configuration and energy level diagram of the Cr^{3+} and Nd^{3+} activator system showing the energy transfer between the ions. $Cr^{3+} \rightarrow Nd^{3+}$ is shown as a dashed red arrow, whilst $Nd^{3+} \leftarrow Cr^{3+}$ is denoted as a black dashed arrow.

The lifetimes of the ^2E state of Cr^{3+} at 729 nm for all three Nd^{3+}-doped materials were measured alongside $LaGa_{0.99}O_3$: $Cr_{0.01}$ at room temperature. All data fitted well to bi-exponential decay curves with y-offset (Figure 4.7, Equation 2.22). The average lifetime of the ^2E excited state in each material was calculated using Equation 2.23 (Table 4.3). As the Nd^{3+} concentration increases from x = 0.00 to 0.02, the average lifetime of the ^2E state decreases from 4.2 to 2.6 ms which further supports the conclusion that $Cr^{3+} \rightarrow Nd^{3+}$ energy transfer occurs. The efficiency of the energy transfer, η_{ET}, was calculated using Equation 4.1, where τ_{Cr} is the average lifetime without Nd^{3+} present, and $\tau_{Cr\text{-}Nd}$ is the average lifetime with Nd^{3+} present (Table 4.3).[22]

$$\eta_{ET} = 1 - \frac{\tau_{Cr-Nd}}{\tau_{Cr}} \tag{4.1}$$

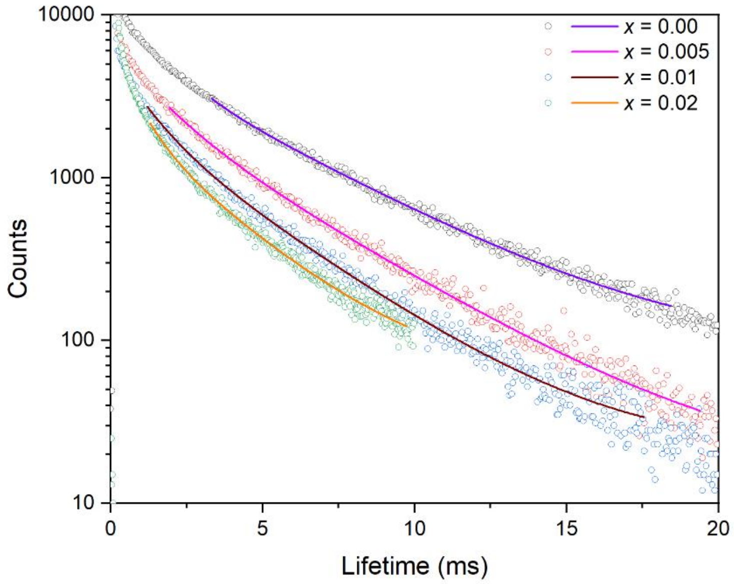

Figure 4.7: Experimental lifetime data (dark circles) and best fits to a sum of two exponentials (solid lines) of $La_{1-x}Ga_{0.99}O_3$: $Cr_{0.01}$, Nd_x *(where x = 0.00, 0.005, 0.01, 0.02).*

Table 4.3: Lifetime calculated from bi-exponential fits, and the efficiency of energy transfer from $Cr^{3+} \rightarrow Nd^{3+}$ *using lifetime data from* $LaGa_{0.99}O_3$:$Cr_{0.01}$ *(Chapter 3).*

Sample	**$LaGa_{0.99}O_3$:$Cr_{0.01}$**	**$La_{0.995}Ga_{0.99}O_3$:$Cr_{0.01}$, $Nd_{0.005}$**	**$La_{0.99}Ga_{0.99}O_3$:$Cr_{0.01}$, $Nd_{0.01}$**	**$La_{0.98}Ga_{0.99}O_3$:$Cr_{0.01}$, $Nd_{0.02}$**
τ (ms)	4.2(2)	3.6(2)	3.0(2)	2.6(2)
η_{ET} (%)	0	14	28	40

A similar decrease in the lifetime of the ^2E emission as Nd^{3+} concentration increases has been reported for an analogous $LaGaO_3$ phosphor doped with lower concentrations of both Cr^{3+} and Nd^{3+} ions.[3] With $LaGaO_3$:$Cr_{0.003}$ having an initial ^2E lifetime of 4.3 ms, as Nd^{3+} concentration increased to $LaGaO_3$:$Cr_{0.003}$, $Nd_{0.01}$ the ^2E lifetime reduced to 2.68 ms.

4.3.3. Luminescence thermometry

Variable-temperature emission spectra of $La_{0.995}Ga_{0.99}O_3$:$Cr_{0.01}$, $Nd_{0.005}$, $La_{0.99}Ga_{0.99}O_3$:$Cr_{0.01}$, $Nd_{0.01}$, and $La_{0.98}Ga_{0.99}O_3$:$Cr_{0.01}$, $Nd_{0.02}$ were collected between 300 K and 625 K in 25 K increments. Of the three materials, it was found that only the one with $x = 0.02$ had a Nd^{3+} emission intensity comparable to that of Cr^{3+} (Figure 4.8a, b, and c), and so all further thermometric evaluation was undertaken on that material.

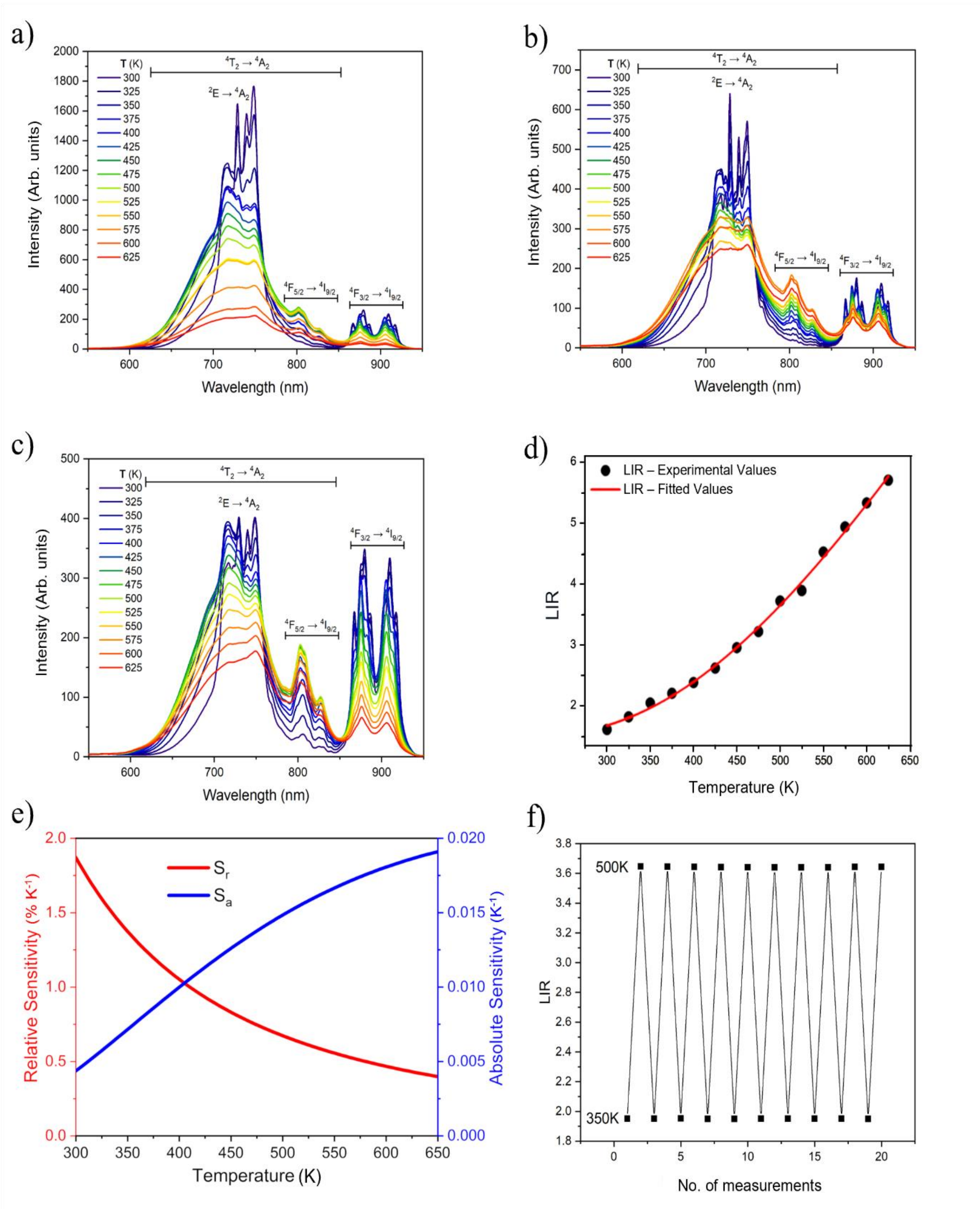

Figure 4.8: Variable-temperature emission spectra, excited at 473nm, of a) $La_{0.995}Ga_{0.99}O_3{:}Cr_{0.01}$, $Nd_{0.005}$, *b)* $La_{0.99}Ga_{0.99}O_3{:}Cr_{0.01}$, $Nd_{0.01}$, *and c)* $La_{0.98}Ga_{0.99}O_3{:}Cr_{0.01}$, $Nd_{0.02}$. *d) Fitted LIR of* $La_{0.98}Ga_{0.99}O_3{:}Cr_{0.01}$, $Nd_{0.02}$. *e) Absolute (blue curve) and relative (red curve) sensitivities of* $La_{0.98}Ga_{0.99}O_3{:}Cr_{0.01}$, $Nd_{0.02}$. *f) Repeatability measurements of* $La_{0.98}Ga_{0.99}O_3{:}Cr_{0.01}$, $Nd_{0.02}$ *cycling between 350 K and 500 K.*

The variable-temperature emission spectra of $La_{0.98}Ga_{0.99}O_3$:$Cr_{0.01}$, $Nd_{0.02}$ (Figure 4.8c) show a weak set of peaks centred at 808 nm, arising from the thermalised $^4F_{5/2} \rightarrow {}^4I_{9/2}$ Nd^{3+} transition. As temperature increases from 300 to 450 K, the Cr^{3+} ^2E emission is quenched due to the thermal activation to the higher lying $^4T_2$ state, causing the broad emission band from the latter to appear. From 450 to 625 K, both Cr^{3+} emission bands quench due to increasing non-radiative decay, probably through the $^4T_2$ intersection with the $^4A_2$ ground state. The Nd^{3+} $^4F_{3/2} \rightarrow {}^4I_{9/2}$ emission, across the observed temperature range, decreased in intensity as higher temperatures allowed for an increase in multiphonon relaxation. Additionally, thermalisation from the lower-lying $^4F_{3/2}$ state to the higher-lying $^4F_{5/2}$ state diminishes the emission intensity of the $^4F_{3/2}$ state.

As the $^4F_{5/2} \rightarrow {}^4I_{9/2}$ emission band centred at 808 nm overlapped with the tail of the $^4T_2 \rightarrow {}^4A_2$ Cr^{3+} emission (Figure 4.8c), it was excluded from the *LIR* analysis. The pure Cr^{3+} emissions at $\lambda < 790$ nm – ^2E, $^4T_2$, N-line, and Stokes/anti-Stokes phonon sidebands, and the pure Nd^{3+} $^4F_{3/2} \rightarrow {}^4F_{9/2}$ emission at $\lambda > 850$ nm were integrated for *LIR* calculations.

Typically, in dual-emission Ln^{3+}-TM thermometers, the Ln^{3+} ion is used as the reference emission due to the slower quenching of luminescence compared to TM ions. However, in the case of $La_{0.98}Ga_{0.99}O_3$:$Cr_{0.01}$, $Nd_{0.02}$, as the total integrated Cr^{3+} emission includes the $^4T_2$ emission that increases in intensity, the overall Cr^{3+} intensity quenches more slowly than that of the Nd^{3+} $^4F_{3/2} \rightarrow {}^4I_{9/2}$ emission. The *LIR* equation (Equation 1.18) was fitted to the integrated intensities at each temperature with $I_H = I(Cr^{3+})$ and $I_L = I(Nd^{3+})$ respectively (Figure 4.8d, $R^2 = 0.997$). The energy gap, ΔE, used in Equation 1.18 in the case of dual-emission *LIR* is between the two activator ions. *B*, the pre-exponential factor, was found to be 63.9(8), whilst ΔE was calculated as 1170 cm^{-1}, a value larger than the ΔE of thermally coupled states in most Ln^{3+} ions except for Eu^{3+} $^5D_1$ and $^5D_0 \rightarrow {}^7F_j$ transitions. The relative sensitivity, S_r, will therefore be high.[23] The absolute sensitivity, S_a, and S_r were calculated using Equations 1.11 and 1.12, and found to be 0.02 K^{-1} at 625 K and 2.0% K^{-1} at 300 K respectively (Figure 4.8e). As predicted, the S_r of $La_{0.98}Ga_{0.99}O_3$: $Cr_{0.01}$, $Nd_{0.02}$ was higher than all Ln^{3+} singly-doped LIR thermometers but Eu^{3+} with its maximum S_r value of 2.8% K^{-1}. The stability of the sensor was tested by cycling 10 times between 350 K and 500 K. The *LIR* values for each temperature were recorded (Figure 4.8f) and the repeatability was calculated for the two temperatures using Equation 1.16. The repeatability was found to be 99.92% at 350 K, and 99.88% at 500 K respectively. The relative uncertainty at 300 and 435 K was estimated from 30 consecutive measurements as 0.07% and 0.09% respectively.

Using the calculated S_r values and relative uncertainty, a temperature resolution of 0.04 K at 300 K was estimated using Equation 1.13. Such a high temperature resolution was attributed to the high intensities of both the Cr^{3+} and Nd^{3+} emission bands, as high intensity reduces the uncertainty in the *LIR* measurement.[24]

4.4. Discussion and comparisons between selected Cr^{3+}, Nd^{3+} thermometers

Table 4.4 summarises the key properties of selected Cr^{3+}, Nd^{3+} dual-doped luminescence thermometers. Comparison of Cr^{3+}, Nd^{3+} dual-emission *LIR* thermometers reported in the literature with the material synthesised in this work, Entry 1, allows exploration of the structural and experimental factors that improve thermometer performance.

Three key factors, discussed below, to produce both high S_r and high temperature resolution dual-emission Cr^{3+}-Nd^{3+} thermometers are:

1. The crystal field strength experienced by the Cr^{3+} ion – Section 4.4.1.
2. The excitation wavelength used to excite the Cr^{3+} and Nd^{3+} ions – Section 4.4.2.
3. The area of integration used for *LIR* calculations – Section 4.4.3.

Table 4.4: Comparison table of all $LaGaO_3$ LIR thermometers currently in the literature. The orange shaded cells are used to denote the material reported in this chapter.

Entry	**Host**	**Dopant conc (Cr mol%, Nd mol%)**	***LIR* emissions**	***λ_{Exc} (nm)***	***Dq/B***	**S_r (% K^{-1}) [T/K]**	**Temp res (K) [T/K]**
1	$LaGaO_3$[25]	1.0, 2.0	${}^2E, {}^4T_2 \rightarrow {}^4A_2$ / ${}^4F_{3/2} \rightarrow {}^4I_{9/2}$	473	2.6	2.0 (300)	0.04 (300)
2	$LaGaO_3$[2]	0.5, 2.0	${}^2E \rightarrow {}^4A_2$/ ${}^4F_{3/2} \rightarrow {}^4I_{9/2}$	460	2.8	0.49 (303)	N/A
3a	$Gd_3Al_5O_{12}$[26]	1.0, 1.0	${}^4T_2 \rightarrow {}^4A_2$ / ${}^4F_{3/2} \rightarrow {}^4I_{9/2}$	450	2.69	1.2 (123)	N/A
3b	$Gd_3Ga_5O_{12}$[26]	1.0, 1.0	${}^4T_2 \rightarrow {}^4A_2$ / ${}^4F_{3/2} \rightarrow {}^4I_{9/2}$	450	2.16	1.9 (123)	N/A
4	$LaScO_3$[27]	1.0, 1.0	${}^2E \rightarrow {}^4A_2$/ ${}^4F_{3/2} \rightarrow {}^4I_{9/2}$	460	2.67	1.3 (400)	N/A
5	$LiLaP_4O_{12}$[28]	1.0, 10.0	${}^4T_2 \rightarrow {}^4A_2$ / ${}^4F_{3/2} \rightarrow {}^4I_{11/2}$	665	< 2	4.89 (323)	N/A
6	$LiLaP_4O_{12}$[29]	1.0, 10.0	${}^4T_2 \rightarrow {}^4A_2$ / ${}^4F_{3/2} \rightarrow {}^4I_{11/2}$	665	N/A	4.9 (323)	0.05 (323)
7a	$Y_3A_5O_{12}$[30]	0.5, 1.0	${}^2E, {}^4T_2 \rightarrow {}^4A_2$ / ${}^4F_{3/2} \rightarrow {}^4I_{9/2}$	590	2.52	3.49 (200)	N/A
7b	$Y_3A_5O_{12}$[30]	0.5, 1.0	${}^2E, {}^4T_2 \rightarrow {}^4A_2$ / ${}^4F_{3/2} \rightarrow {}^4I_{9/2}$	650	2.52	0.58 (200)	N/A
8a	$Y_3A_5O_{12}$[31]	0.5, 2.0	${}^2E \rightarrow {}^4A_2$/ ${}^4F_{3/2} \rightarrow {}^4I_{9/2}$	488	N/A	0.8 (298)	N/A
8b	$Y_3A_5O_{12}$[31]	0.5, 2.0	${}^2E \rightarrow {}^4A_2$/ ${}^4F_{3/2} \rightarrow {}^4I_{9/2}$	514	N/A	1.8 (298)	N/A
8c	$Y_3A_5O_{12}$[31]	0.5, 2.0	${}^2E \rightarrow {}^4A_2$/ ${}^4F_{3/2} \rightarrow {}^4I_{9/2}$	532	N/A	2.5 (298)	N/A
9a	$Y_3A_2Ga_3O_{12}$[32]	12.0, 1.0	${}^4T_2 \rightarrow {}^4A_2$ / ${}^4F_{3/2} \rightarrow {}^4I_{9/2}$	450	3.25	1.17 (423)	N/A
9b	$Y_3A_2Ga_3O_{12}$[32]	12.0, 1.0	${}^4T_2 \rightarrow {}^4A_2$ / ${}^4F_{5/2} \rightarrow {}^4I_{9/2}$	450	3.25	2.16 (225)	N/A
10	GdP_5O_{14}[33]	1.0, 0.5	${}^4T_2 \rightarrow {}^4A_2$ / ${}^4F_{3/2} \rightarrow {}^4I_{11/2}$	460	2.18	0.40 (573)	~ 1 (573)
11	$La_2LuGa_5O_{12}$	0.1, 5.0	${}^4F_{5/2} \rightarrow {}^4I_{9/2}/{}^2E \rightarrow {}^4A_2$	532	1.5	1.47 (123)	N/A

4.4.1. Effects of different crystal field strength experienced by the Cr^{3+} ions

The Nd^{3+} ion is typically used as the reference emission band, because its non-radiative deactivation rate is assumed to be constant across the temperature range explored, whilst the Cr^{3+} emission is used as the sensing emission. The greater the Cr^{3+} emission quenching with increasing temperature, the more sensitive the thermometer. Having a Cr^{3+} ion experiencing a weak crystal field ($Dq/B < 2.1$) has been found to increase the S_r value. When Cr^{3+} ions experience a weak crystal field, generally only a broad emission band is seen at room temperature as the $^4T_2$ state lies at lower energy than the ^2E state (Figure 4.9, dashed green parabola). Conversely, with a strong crystal field the $^4T_2$ state will not be thermalised at room temperature, with no broad emission band observed, because the $^4T_2$ state is at a higher energy than the ^2E state (Figure 4.9, solid green parabola). When temperature increases, the thermal energy promotes deactivation through the intersection between the $^4T_2$ excited state and the $^4A_2$ ground state. There is a smaller energy gap between the intersection of the $^4T_2$ and the bottom of the weak field $^4T_2$ parabola, ΔE_w, than the strong field parabola, ΔE_s. The smaller the energy gap between the bottom of the $^4T_2$ parabola and the intersection point, the higher the rate of non-radiative decay, the greater the magnitude of the emission quenching, and therefore the higher the S_r of the thermometer.

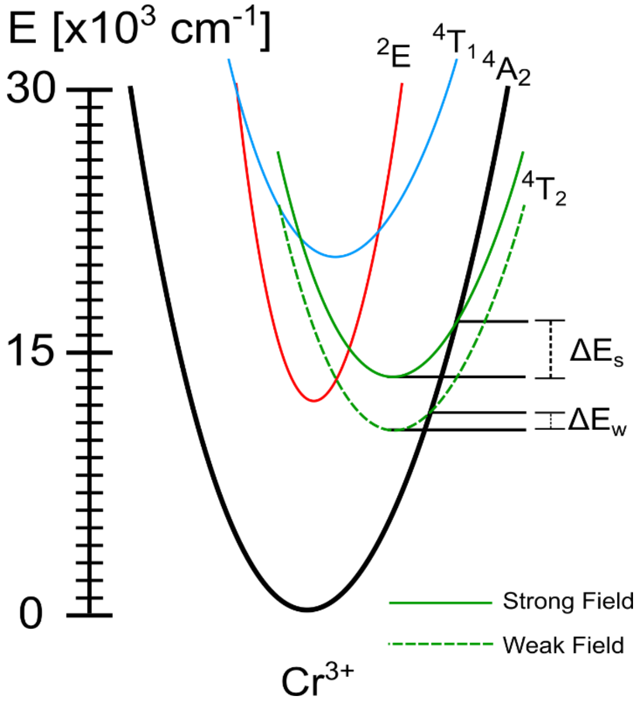

Figure 4.9: Coordinate-configurational diagram of Cr^{3+} showing the change in energy of the $^4T_2$ energy level when experiencing a strong (solid green curve) or weak (dashed green curve).

There are a number of methods to manipulate the crystal field strength of a material. The host material itself can have a structure that generates a weaker crystal field. GdP_5O_{14} (Entry 10) doped with Cr^{3+} and Nd^{3+} was estimated to have a *Dq/B* of 2.18, consistent with the emission showing only the broad $^4T_2$ emission band. It gave a maximal S_r of 0.4% K^{-1} at 573 K. The low S_r of the GdP_5O_{14} phosphor compared to Entry 1 (2.0% K^{-1}), despite a lower *Dq/B,* may be as a result of the inability to use the high intensity $^4F_{3/2}\rightarrow{}^4I_{9/2}$ emission, which overlapped with the Cr^{3+} $^4T_2$ emission, as the Nd^{3+} reference emission. Instead, the lower intensity $^4F_{3/2}\rightarrow{}^4I_{11/2}$ emission was used as the Nd^{3+} emission for *LIR*. The crystal field strength experienced by Cr^{3+} can, therefore, determine which Nd^{3+} emission to use in some cases, as wavelength ranges where Cr^{3+} and Nd^{3+} emission overlap must be excluded unless deconvolution is used to separate the emissions.

As mentioned in Chapter 3, substituting ions of differing radii affects the Cr–O bond lengths, which in turn changes the crystal field strength experienced by the Cr^{3+} ion and thus the Cr^{3+} emission and absorption band positions. To weaken the crystal field strength, ions with larger radii than those of the host cations should be substituted into the structure. A series of six phosphors with the formula $Gd_3Al_{5-x}Ga_xO_{12}$ (where x = 0, 1, 2, 3, 4, 5) demonstrate how substitution of the Al^{3+} by the larger Ga^{3+} ion systematically changes the S_r with decreasing *Dq/B*. The gradual substitution from $GdAl_5O_{12}$ (Entry 3a) to $GdGa_5O_{12}$ (Entry 3b) increases the S_r from 1.2% K^{-1} to 1.9% K^{-1} at 123 K. The increasing S_r value followed the trend of the *Dq/B* falling from 2.69 to 2.16 as Ga^{3+} concentration increased. $GdGa_5O_{12}$ gave approximately the same S_r value as $La_{0.98}Ga_{0.99}O_3$:$Cr_{0.01}$, $Nd_{0.02}$; however, this value was found only at low temperatures (1.9% K^{-1} at 123 K). Whilst materials $La_{3-x}Lu_xGa_5O_{12}$ (x = 0, 3) all have similar *Dq/B* of 2.5-2.6, $La_2LuGa_5O_{12}$ (Entry 11) gave a markedly lower *Dq/B* value of ~1.5. The lower crystal field estimate was supported by its emission spectrum showing only the $^4T_2$ broad emission band, unlike its counterparts that also gave the ^2E sharp emission intensities. Entry 11 gave a S_r of 1.47% K^{-1} at 123 K, both a lower S_r and temperature range than Entry 1.

An isostructural phosphor to Entry 1, $LaScO_3$ (Entry 4) gave a lower value of *Dq/B* than is common for $LaGaO_3$ (2.67 vs 2.8). Despite this lower crystal field strength, such that the $^4T_2$ emission could be seen at room temperature, the material's S_r of 1.3% K^{-1} at 400 K was lower than that of Entry 1.

4.4.2. Effect of excitation wavelength used to excite the Cr^{3+} and Nd^{3+} ions

The choice of the excitation wavelength has been shown to influence the relative sensitivity of Cr^{3+}, Nd^{3+} thermometers. There are two main pathways for excitation for both ions: 1) the excitation is independent for each activator (does not rely on energy transfer from another ion) and direct into an excitation band, and 2) the excitation of one ion is direct, and the other ion is excited through energy transfer. Direct excitation of both ions through a single wavelength generally leads to higher S_r values, as will be discussed below. However, direct excitation of only the Cr^{3+} ion causes a dependence on the energy transfer between the Cr^{3+} ion and the Nd^{3+} ion to facilitate emission from both centres.

Entry 7a and b in Table 4.4 show the same $Y_3Al_5O_{12}$ (YAG)-based phosphor doped with Cr^{3+} and Nd^{3+}, excited using two different wavelengths, 590 nm and 650 nm. Under 590 nm excitation, the dual-emission thermometer gave an S_r of 3.49% K^{-1} at 200 K, whilst an S_r of 0.58% K^{-1} was obtained using 650 nm excitation. When using 590 nm excitation, both the Cr^{3+} $^4T_2 \leftarrow ^4A_2$ and the Nd^{3+} $^4G_{5/2}$, $^2G_{7/2} \leftarrow ^4I_{9/2}$ are simultaneously and directly excited. However, the 650 nm excitation does not excite the Nd^{3+} $^2H_{11/2} \leftarrow ^4I_{9/2}$ transition at the same time as the Cr^{3+} excitation. Energy transfer from the Cr^{3+} is required to excite the Nd^{3+}. The seven-fold difference in the S_r value according to the selected excitation wavelengths highlighted the two distinct excitation pathways, and how the choice of excitation wavelength can affect the S_r. Compared to Entry 1, direct excitation at 590 nm gave a higher S_r, but at lower temperature of 200 K.

Entries 8a-c summarise a YAG host co-doped with Cr^{3+} and Nd^{3+} to investigate the S_r dependence on excitation wavelength. Using three different excitation wavelengths, 488 nm, 514 nm, and 532 nm, S_r values of 0.8% K^{-1}, 1.8% K^{-1}, and 2.5% K^{-1} were achieved at 298 K. Whilst all three wavelengths excited into Nd^{3+} excitation peaks, the 532 nm wavelength excited directly into the $^4G_{7/2}$, $^2G_{9/2}$ state and gave an S_r three times higher than that obtained using 488 nm excitation. Compared to Entry 1, two of the selected wavelengths gave YAG thermometers with equal or higher S_r at a similar temperature.

As mentioned in the introduction section, the crystal field strength affects the position and splitting of Nd^{3+} electronic states by a few hundred wavenumbers. Changes to the *Dq/B* cause variation of the excitation band’s widths that can affects which excitation wavelength to use for individual hosts when trying to excite both Cr^{3+} and Nd^{3+} simultaneously and independently. An example of this is the host materials YAG and $LiLaP_4O_{12}$ both with Cr^{3+}, Nd^{3+} activator ions. A 650 nm excitation wavelength did not directly excite the Nd^{3+} ions doped in the YAG host matrix as the $^2H_{11/2}\leftarrow^4I_{9/2}$ excitation peak was narrower than that of the Nd^{3+} ions in the $LiLaP_4O_{12}$ host which used 665 nm. Instead, the Nd^{3+} in YAG used 590 nm for simultaneous excitation which then gave a 7-fold increase in the S_r compared to the 650 nm excitation wavelength.

Entry 1 used 590 nm for room temperature excitation into the $^4T_2\leftarrow^4A_2$ Cr^{3+} excitation band, alongside the narrow $^4G_{5/2}$, $^2G_{7/2}$ excitation peaks of Nd^{3+} as seen in Figures 4.5 and 4.6. Variable-temperature measurements for luminescence thermometry, however, were performed using an excitation wavelength of 473 nm. Excitation at 473 nm directly excites the Cr^{3+} $^4T_1\leftarrow^4A_2$ excitation band, but it may not directly populate the $^2D_{5/2}$, $^2P_{1/2}$ Nd^{3+} states. The lack of a direct excitation may have limited the S_r value achieved by Entry 1, and thus selection of a more appropriate excitation wavelength such as 590 nm or 665 nm may improve the S_r value of 2.0% K^{-1} at 300 K. Entries 5, 6, 7a, and 8c all give higher S_r values, having been excited directly into both the Cr^{3+} and Nd^{3+} excitation bands using $\lambda_{ex} > 473$ nm.

4.4.3. Effect of the area of integration used for LIR calculations

An additional factor contributing to the different relative sensitivities values of the selected thermometers is the range of emission intensity chosen for integration and used for *LIR* calculations. For the thermometers summarised in Table 4.4, a range from 0.5 to ~150 nm has been used for integration. For Cr^{3+}-doped thermometers, depending on the strength of the crystal field experienced, an integration area containing only the $^4T_2$ could be selected. Small integration ranges permit the selection of an emission's area with large changes in intensity. Selecting a wavelength range that only contains $^4T_2$ emission intensity, over the investigated temperature range, can increase the S_r but this introduces a larger uncertainty in the measurement. Small integration ranges therefore give a lower temperature resolution due to the higher uncertainty. Alternatively, integrating a larger range or the whole emission band allows for a less uncertain measurement, and generally a higher temperature resolution.

For the singly-doped thermometer, $LaGa_{0.99}O_3:Cr_{0.01}$ described in Chapter 3, approximate deconvolution of the overlapped $^4T_2$ and ^2E emissions was implemented and the entire emission peaks were used for *LIR* calculations. The Cr^{3+}-only thermometer gave both an excellent S_r of 2.5% K^{-1} at 300 K, and an excellent temperature resolution of 0.05 K. The data for Entry 1 were not deconvolved as the chosen emissions for LIR didn't overlap, but instead were integrated with a range that spanned the entire Cr^{3+} emission (excluding the overlapping Nd^{3+} $^4F_{5/2}$ thermalised emission with the trailing $^4T_2$ emission) and the entire Nd^{3+} $^4F_{3/2}\rightarrow{}^4I_{9/2}$ emission. Whilst Entry 1 has a lower S_r than $LaGa_{0.99}O_3:Cr_{0.01}$, the dual-doped thermometer has a near identical temperature resolution of 0.04 K. Thus, regardless of if deconvolution was implemented or not, the range of integration influences the temperature resolution as including more emission intensity signal lowers uncertainty.

$La_2LuAl_5O_{12}$ (Entry 11) emission was integrated over only 0.5 nm for both the Cr^{3+} and the Nd^{3+} emissions intensities and gave an S_r of 1.47% K^{-1} at 123 K. Similarly, $Y_3A_2Ga_3O_{12}$ (Entries 9a and 9b) was investigated with only a 0.5 nm integration range for both Cr^{3+} and Nd^{3+} intensity *LIR* measurements using two different Nd^{3+} emissions, with an S_r of 1.17% K^{-1} at 423 K, and 2.16% K^{-1} at 226 K respectively. A YAG phosphor (Entry 7a) was studied using ranges of 630 nm and 715 nm, and 870 nm and 920 nm for Cr^{3+} and Nd^{3+} emission integration respectively. Entry 7a gave an S_r of 3.48% K^{-1} at 200 K. The high Nd^{3+} emission intensity of the YAG phosphor was linked to the high S_r. For the $Gd_3Ga_5O_{12}$ phosphor (Entry 3b) only the Cr^{3+} $^4T_2$ emission band was integrated, as well as the whole $^4F_{3/2}\rightarrow{}^4I_{9/2}$ Nd^{3+} emission, giving an S_r of 1.9% K^{-1} at 123 K. For $LiLaP_4O_{12}$ (Entry 6) a range of 20 nm was selected for the Cr^{3+} integration, with the whole Nd^{3+} emission between 1025 nm and 1075 nm also integrated. The phosphor gave very poor Nd^{3+} emission intensity, except at low temperature. Entry 6 did produce a temperature resolution of 0.05 K at 323 K, comparable to Entry 1 at 300 K. Another $LaGaO_3$ material, Entry 2, had a low S_r value of 0.60% K^{-1} at 303 K, a large difference from Entry 1 at a similar temperature. The lower S_r of Entry 2 may have been due to the integration range used for both emission intensities being only 1 nm and that the more temperature-invariant ^2E emission was integrated for the Cr^{3+} emission. As the ^2E emission quenches slowly, this can affect the S_r value of the thermometer.

In comparison, the $LaGaO_3$ thermometer (Entry 1) has an intermediate value of S_r (2.0% K^{-1} at 300 K) when compared to the selected thermometers in Table 4.4 due to the Cr^{3+} within the CrO_6 octahedra experiencing a strong crystal field. As the whole Cr^{3+} emission intensity was integrated and both the ^2E and $^4T_2$ are thermalised as temperature increases, the overall integral intensity of the Cr^{3+} emission doesn't quench quickly over the temperature range, lowering the S_r value. The integration of the whole Cr^{3+} and Nd^{3+} emissions bands, alongside their high individual intensities played a role in lowering the uncertainties in the temperature measurement and therefore gave an excellent temperature resolution of 0.04 K, the best of the selected thermometers at physiological temperature.

4.5. Conclusion and future work

A series of $LaGaO_3$-based phosphors with compositions $La_{1-x}Ga_{0.99}O_3$:$Cr_{0.01}$, Nd_x (x = 0.005, 0.01, 0.02) were successfully synthesised by conventional solid-state method and structurally characterised by the Rietveld method. Upon excitation into the Cr^{3+} $^4T_2 \leftarrow ^4A_2$ absorption band at 590 nm, both the characteristic Cr^{3+} emissions and the Nd^{3+} emissions could be observed simultaneously. Examination of the excitation spectra monitoring individual Cr^{3+} and Nd^{3+} emissions showed evidence of both $Nd^{3+} \rightarrow Cr^{3+}$ and $Cr^{3+} \rightarrow Nd^{3+}$ energy transfer occurring; the latter was supported by Cr^{3+} lifetime data. Owing to the comparable intensities of the Cr^{3+} and Nd^{3+} emissions in the temperature range probed for thermometry, $La_{0.98}Ga_{0.99}O_3$:$Cr_{0.01}$, $Nd_{0.02}$ was chosen to be evaluated further and found to be an effective *LIR* Boltzmann thermometer. Due to the high intensities of both the Cr^{3+} and Nd^{3+} emissions, the phosphor had high sensitivities (S_r of 2.0% K^{-1} at 300 K, and S_a of 0.20 K^{-1} at 650 K) and low uncertainty in measurement. The combination led to an excellent high temperature resolution of 0.04 K at 300 K. Such a high S_r and temperature resolution at physiological temperature (~310 K), together with the excitation and emission being with BW-1, suggests that $La_{0.98}Ga_{0.99}O_3$:$Cr_{0.01}$, $Nd_{0.02}$ may find an application as a thermometer for biological samples.

Future work on this material should be focused on optimisation of the Nd^{3+} concentration, as up to x = 0.02 there are no signs of concentration quenching of the emission intensity, so increased Nd^{3+} concentration could be explored. Additionally, the use of different excitation wavelengths should be considered, as it has been found for Cr^{3+}-Nd^{3+} systems that excitation directly into excitation bands of both activator ions can enhance the S_r of the thermometer compared to excitation into only the Cr^{3+} ion, which then relies on energy transfer to the Nd^{3+} activator.[28] Future work on the $LaGaO_3$:Cr^{3+}, Nd^{3+} series should investigate the S_r of the phosphors using excitation wavelengths of either 590 nm or 680 nm, where the Cr^{3+} $^4T_2$ excitation band overlaps with either the $^4G_{5/2}$ and $^2G_{7/2}$ peak excitation, or $^4F_{9/2}$ peak of Nd^{3+} respectively. Furthermore, dual-emission *LIR* thermometry could be realised using the longer wavelength NIR $^4F_{3/2} \rightarrow ^4I_{11/2}$ emission band found in the range of BW-2. A potential investigation into using the isostructural host $LaInO_3$ doped with Cr^{3+} and Nd^{3+} ions could be undertaken. With a longer average In–O bond than the Ga–O bond length in $LaGaO_3$, the crystal field experienced by Cr^{3+} when doped into InO_6 octahedra should be weaker than $LaGaO_3$, such that the fast-quenching $^4T_2 \rightarrow ^4A_2$ emission may dominate the Cr^{3+} emission spectrum. The weaker crystal field strength affecting Cr^{3+} in a $LaInO_3$:Cr^{3+},Nd^{3+} should cause the Cr^{3+} emission to quench quicker than Cr^{3+} in $LaGaO_3:Cr^{3+},Nd^{3+}$ over the same temperature range and potentially give a higher relative sensitivity.

4.6 References

1 R. D. Shannon, *Acta Cryst. A*, 1976, **32**, 751–767.

2 H. Xu, G. Bai, K. He, S. Tao, Z. Lu, Y. Zhang and S. Xu, *Mater. Today Phys.*, 2022, **28**, 100872.

3 L. Zhang, L. Dong, B. Shao, S. Zhao and H. You, *Dalton Trans.*, 2019, **48**, 11460–11468.

4 W. M. Piotrowski, K. Maciejewska and L. Marciniak, *Mater. Today Chem.*, 2023, **30**, 101591.

5 Z. Li, X. Yu, T. Wang, S. Wang, L. Guo, Z. Cui, G. Yan, W. Feng, F. Zhao, J. Chen, X. Xu and J. Qiu, *J. Am. Ceram. Soc.*, 2022, **105**, 2804–2812.

6 T. Samuel, Ch. Satya Kamal, K. Sujatha, V. Veeraiah, Y. Ramakrishana and K. R. Rao, *Optik*, 2016, **127**, 10575–10587.

7 J. Xu, D. Murata, B. So, K. Asami, J. Ueda, J. Heo and S. Tanabe, *J. Mater. Chem. C*, 2018, **6**, 11374–11383.

8 I. E. Kolesnikov, A. A. Kalinichev, M. A. Kurochkin, E. V. Golyeva, E. Y. Kolesnikov, A. V. Kurochkin, E. Lähderanta and M. D. Mikhailov, *Sci. Rep.*, 2017, **7**, 18002.

9 M. Back, J. Ueda, J. Xu, D. Murata, M. G. Brik and S. Tanabe, *ACS Appl. Mater. Interfaces*, 2019, **11**, 38937–38945.

10 S. Balabhadra, M. L. Debasu, C. D. S. Brites, L. A. O. Nunes, O. L. Malta, J. Rocha, M. Bettinelli and L. D. Carlos, *Nanoscale*, 2015, **7**, 17261–17267.

11 G. Jiang, X. Wei, S. Zhou, Y. Chen, C. Duan and M. Yin, *J. Lumin.*, 2014, **152**, 156–159.

12 K. Kniec, A. Kochanowska, L. Li, M. Suta and L. Marciniak, *J. Mater. Chem. C*, 2022, **10**, 9278–9286.

13 M. J. Weber and T. E. Varitimos, *J. Appl. Phys.*, 1971, **42**, 4996–5005.

14 A. Ćirić, J. Periša, M. Medić, S. Kuzman, Z. Ristić, Ž. Antić and M. D. Dramićanin, *Ceram. Int.*, 2021, **47**, 31915–31919.

15 M. D. Dramićanin, *J. Appl. Phys.*, 2020, **128**, 040902.

16 A. A. Coelho, J. Evans, I. Evans, A. Kern and S. Parsons, *Powder Diffr.*, 2011, **26**, S22–S25.

17 H. M. Rietveld, *J. Appl. Crystallogr.*, 1969, **2**, 65–71.

18 A. Ćirić, S. Stojadinović and M. D. Dramićanin, *Meas. Sci. Technol.*, 2019, **30**, 045001.

19 M. Lerch, H. Boysen and T. Hansen, *J. Phys. Chem. Solids*, 2001, **62**, 445–455.

20 W. Mikenda and A. Preisinger, *J. Lumin.*, 1981, **26**, 53–66.

21 W. Mikenda and A. Preisinger, *J. Lumin.*, 1981, **26**, 67–83.

22 P. I. Paulose, G. Jose, V. Thomas, N. V. Unnikrishnan and M. K. R. Warrier, *J. Phys. Chem. Solids*, 2003, **64**, 841–846.

23 M. D. Dramićanin, *Methods Appl. Fluoresc.*, 2016, **4**, 042001.

24 T. P. van Swieten, A. Meijerink and F. T. Rabouw, *ACS Photonics*, 2022, **9**, 1366–1374.

25 A. L. Mullins, A. Ćirić, I. Zeković, J. A. G. Williams, M. D. Dramićanin and I. R. Evans, *J. Mater. Chem. C*, 2022, **10**, 10396–10403.

26 K. Elzbieciak, A. Bednarkiewicz and L. Marciniak, *Sens. Actuators B Chem.*, 2018, 96–102.

27 K. Elzbieciak-Piecka, M. Suta and L. Marciniak, *Chem. Eng. J.*, 2021, **421**, 129757.

28 L. Marciniak, A. Bednarkiewicz, D. Kowalska and W. Strek, *J. Mater. Chem. C*, 2016, **4**, 5559–5563.

29 L. Marciniak, A. Bednarkiewicz and W. Strek, *Sens. Actuators B Chem.*, 2017, **238**, 381–386.

30 L. Marciniak, A. Bednarkiewicz, J. Drabik, K. Trejgis and W. Strek, *Phys. Chem. Chem. Phys.*, 2017, **19**, 7343–7351.

31 G. Dantelle, V. Reita, A. Ibanez, G. Ledoux and C. Dujardin, *Phys. B Condens. Matter*, 2022, **628**, 413622.

32 K. Elzbieciak and L. Marciniak, *Front. Chem.*, 2018, **6**, 1–8.

33 K. Maciejewska and L. Marciniak, *Chem. Eng. J.*, 2020, **402**, 126197.

5. Mn^{5+}-activated $A_5(VO_4)_3Cl$ ($A^{2+} = Sr^{2+}, Ba^{2+}$) phosphors for single- and multi-parameter near-infrared luminescence thermometry

5.1. Introduction

Luminescence thermometry, due to its semi-contact nature, is used to measure temperature in extreme environments including biological samples.[1–3] *In vivo* applications typically require that both the excitation and emission fall within the so-called "windows of transparency" of tissues from 650 to 1800 nm. Absorption, autofluorescence and scattering by tissue are reduced in these regions compared to shorter wavelengths,[4] and the 1000–1350 nm range (biological window BW-2) is optimal for deepest penetration of skin and tissue.[5] In the appropriate environment, Ni^{2+}, Cr^{4+} and Mn^{5+} ions are amongst the TM ions that emit in the desired window of transparency.[6–9]

Whilst the relative sensitivity, S_r, is generally seen as the most important figure of merit within luminescence thermometry, it is the uncertainty in measurement σ_r of the emission intensity that is paramount to practical performance. The temperature resolution δT of the thermometer is determined by σ_r / S_r (Equation 1.13).[10] The ideal luminescence thermometry phosphor should therefore have a high quantum yield (QY) and high extinction coefficients at λ_{Ex}, to ensure high brightness. NIR phosphors tend to suffer from low quantum yields due to the small energy gap between the excited state and the ground state, causing increased non-radiative decay through vibrational pathways, while Ln^{3+} ions have the disadvantage of low molar extinction coefficients. The d-d absorption bands of TM ions, conversely, have higher extinction coefficients (especially when tetrahedrally coordinated) – Molar absorption of f-f ions = 1-10 $dm^3\ mol^{-1}\ cm^{-1}$, octahedral d-d ions = 20-100 $dm^3\ mol^{-1}\ cm^{-1}$, and tetrahedral d-d ions = ~250 $dm^3\ mol^{-1}\ cm^{-1}$.[11]

Mixed metal oxides containing Mn^{5+} in tetrahedral coordination environments have been the subject of research interest for NIR laser applications based on the narrow $^1E \rightarrow {}^3A_2$ emission of this d^2 ion (Figure 5.1a).[12–14] In the pursuit of new blue and blue-green pigments, MnO_4^{3-} tetrahedra have been identified as potential chromophores owing to their absorption in the red-orange regions of the electromagnetic spectrum, $^3T_1(F) \leftarrow {}^3A_2$, and an increase in absorption at 450 nm, $^3T_1(P) \leftarrow {}^3A_2$, as Mn^{5+} content increases causing the shift to greener hues.[15,16] Efforts have recently been made to exploit this ion for luminescence thermometry via *LIR*, lifetime, and band-shift readout methods.[9,17–21]

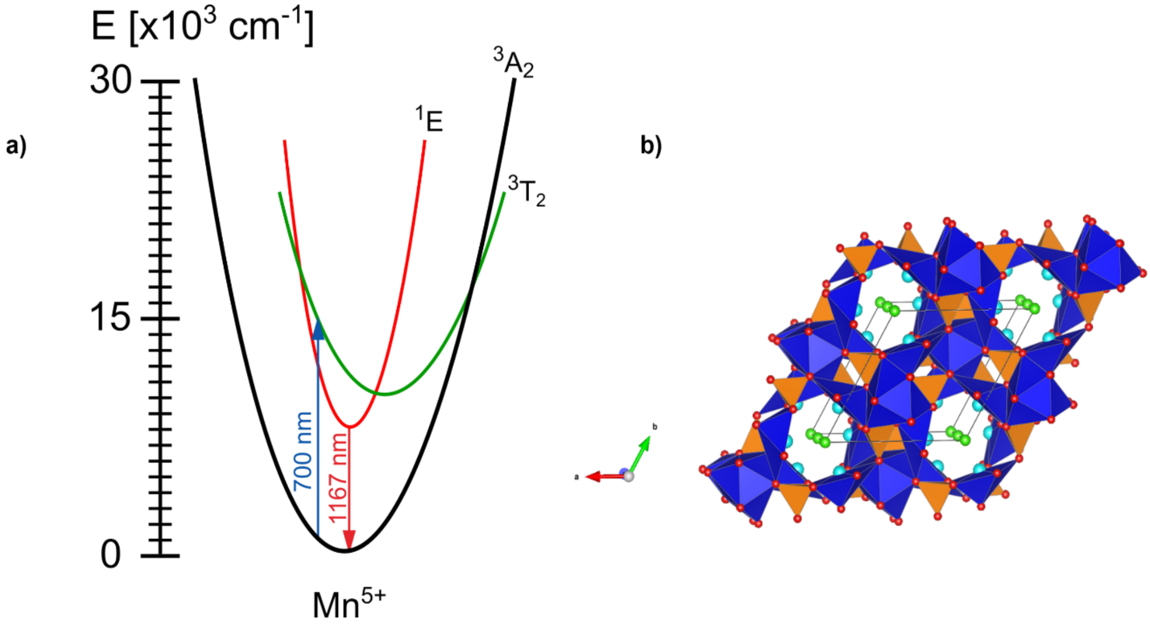

Figure 5.1: a) Configurational coordinate diagram of the energy levels of Mn^{5+}*; b) (a) View of the* $A_{10}(TO_4)_6X_2$ *apatite structure in (approximately) the (ab) plane. Dark blue polyhedra and light blue spheres represent two crystallographically unique A atoms; orange tetrahedra represent the* TO_4 *groups; green spheres represent X anions.*

The selection of a host material for the design and optimisation of Mn^{5+}-based luminescence thermometers must take into account several requirements: (1) The host material must be chemically and crystallographically suitable to stabilise Mn^{5+} ions in a tetrahedral environment. (2) Its bandgap must be sufficiently large to accommodate the Mn^{5+} energy levels associated with the key transitions. (3) It must be chemically and thermally stable under the conditions relevant to particular applications; for bioimaging and biothermal imaging, the probe should obviously be biocompatible, too. Apatite-type materials are ubiquitous both as natural biomaterials (*e.g.*, in bone and teeth) and as synthetic functional materials with a range of technological applications.[22–29] Owing to the compositional flexibility captured by the general formula $A_{10}(TO_4)_6X_{2\pm x}$ {where A = alkaline or rare earth metal; T = tetrahedrally-coordinated cation (e.g. P^{5+}, V^{5+}, Si^{4+}, Ge^{4+}); X = halide, O^{2-} or $[OH]^-$, and the corresponding crystallographic flexibility, the apatite structure provides a plethora of opportunities for the development of phosphors. The ideal apatite can be described as a framework in which columns of face-sharing AO_6 trigonal prisms share corners with TO_4 tetrahedra (dark blue and orange polyhedra, respectively, in Figure 5.1b), forming channels parallel to the crystallographic *c*-axis, in which some of the A cations and the X anions are located (light blue and green spheres in Figure 5.1b). The space group adopted is usually hexagonal $P6_3/m$, with two crystallographically inequivalent A sites and one unique T site. Low-symmetry apatites are less common, and typically crystallise in space group *P-1* with five unique A sites and two independent T sites, providing even more possibilities to fine-tune the properties of phosphors.[30,31] Vanadates give an excellent match between the ionic radii of V^{5+} and Mn^{5+} dopant (0.355 Å and 0.33 Å respectively), such that the incorporation of the activator Mn^{5+} ion into a vanadate host is likely to be successful.[32] An additional advantage of the apatite structure type is that it readily accommodates mixed anions. Whilst oxides are historically the most widely researched phosphor hosts, mixed anion oxyhalides are very attractive host materials and have been explored for lighting phosphors, laser materials, white light-emitting diodes (WLEDs) and luminescence thermometry, with performance improvements over purely oxide-based or purely halide-based materials.[33–42]

While the majority of luminescence thermometers reported in literature to date demonstrate a single readout method, there has been a rise in multi-modal, and multi-parametric luminescence thermometers being researched.[19,43–46] Multi-parametric thermometry has been explored to improve upon the sensitivities of multiple single-readout methods and upon temperature accuracies. One approach is multi-linear regression (MLR), a statistical technique whereby the linear correlation with temperature of a number of distinct readout methods can be used as variables for a singular experimental outcome. The use of MLR usually results in increased S_r and δT compared to the individual readout methods alone.[19,45]

The aims of this work were:

- To synthesise and characterise Mn^{5+}-doped apatite-type oxychloride materials as possible phosphors for NIR luminescence thermometry.
- To investigate the thermal expansion of selected materials, and their local environments using VT-PXRD and ^{51}V ssNMR respectively.
- To record room-temperature absorption and emission spectra, and QY for each phosphor.
- To acquire variable-temperature luminescence emission data for the $^3T_2$ and ^1E emissions in the temperature range 298–373 K for *LIR*, band-shift, bandwidth, and MLR luminescence thermometry.
- To compare the calculated figures of merit against luminescence thermometers in the current literature.

5.2. Experimental

5.2.1. Synthesis

A series of polycrystalline materials of general formula $A_5(V_{1-x}O_4)_3Cl:Mn^{5+}{}_x$, where A = Ca^{2+}, Sr^{2+}, Ba^{2+} and x = 0.00, 0.01, 0.03, 0.05, were initially synthesised by Mr Artemijs Krimovs using a conventional solid-state method.[47] Monitoring of the product purity by PXRD consistently showed the presence of a small amount (0.3(1)-5.4(1) wt%) of impurities – Ca_2MnO_3, $CaMnO_3$, $Sr_3(VO_4)_2$, and $Ba_3(VO_4)_2$ – for samples synthesised in this way, suggesting chloride loss during synthesis.[47–49]

The materials described in this chapter were therefore synthesised via a sol-gel method instead, in the presence of an excess of chloride ions.[50] $Sr(NO_3)_2$ (Sigma-Aldrich, ≥98%), $Ba(NO_3)_2$ (Sigma-Aldrich, 99.999%), NH_4VO_4 (Sigma-Aldrich, ≥99%), and Mn_2O_3 (Aldrich, 99%) were weighed stoichiometrically; NH_4Cl (Afra Aesar, 99.999%) was weighed in excess of 6-10 mol% of the stoichiometric amount. Citric acid (Sigma-Aldrich, >99.5%) was weighed out in a 2:1 ratio relative to the metal cations. The selected alkaline-earth nitrate, NH_4VO_4, NH_4Cl, and Mn_2O_3 (Table 5.1) were added to 100 ml of deionised water with the hot plate set to ~50°C, and stirring at ~500 rpm. Citric acid was then added to form a transparent yellow solution. NH_4OH (Fischer-Sci, 35%) was added dropwise until the solution pH was 7. The solution was heated with the hot plate set to 110°C with stirring until a viscous blue gel formed. The gel was left to stand for two days before being placed into a muffle furnace for a pre-calcination in an alumina crucible at 250°C for 2 h (0.1°C/min heating rate). The product was ground into a fine maroon-brown powder, pressed into 10 mm (o.d.) pellets via a pneumatic pellet press (5 tonnes), and heated to 750°C in alumina crucibles in 12-h intervals (1.0°C/min heating rate, materials required either one or two heating intervals) until phase purity was confirmed by powder X-ray diffraction.

Thermogravimetric analysis-mass spectrometry (TGA-MS) conducted by Mr William Carswell at Durham University showed that NH_4Cl and citrate volatilised from the material as CO, CO_2, NH_3, and H_2O.

Homogenous distribution of the Mn^{5+} activator ions was confirmed using chemical mapping via EDX using a JEOL 2100F FEG transmission electron microscope (TEM) with a single tilt holder. Sample powder was placed into a glass vial with isopropanol, homogenised using an ultrasound bath (10-minute cycle) and a single drop of suspended sample placed onto a lacey carbon film 200 copper mesh disk (Agar scientific). TEM images were captured via a

Gatan Orius CCD camera. Chemical mapping was done using an Oxford INCAx-sight Si(Li) detector for EDX, and software Aztec 5.1.

Table 5.4: Table of reagents for each material, added to 100 ml of water for sol-gel reaction.

Alkali earth cation (Mn^{5+} conc (%))	Reagent	Mass (g)
Sr^{2+} (3%)	$Sr(NO_3)_2$	2.5849
	NH_4VO_3	0.8316
	NH_4Cl	0.1437
	Mn_2O_3	0.0174
	Citric acid	4.7354
Ba^{2+} (0%)	$Ba(NO_3)_2$	2.4495
	NH_4VO_3	0.6579
	NH_4Cl	0.1063
	Citric acid	3.6015
Ba^{2+} (3%)	$Ba(NO_3)_2$	2.4487
	NH_4VO_3	0.6379
	NH_4Cl	0.1103
	Mn_2O_3	0.0133
	Citric acid	3.6327

5.2.2. Powder X-ray diffraction

Powder X-ray diffraction (PXRD) data were collected on a Bruker d8 AXS Advance diffractometer using CuKα radiation, a Lynx-Eye detector and a HTK1200 furnace. Routine diffraction patterns for monitoring the progress of syntheses were recorded at room-temperature in the range of $10° < 2\theta < 90°$ with a step size of 0.02° and a step time of 0.5 s/step. Variable-temperature data (25 measurements per material) were recorded at static temperatures between the temperatures 30°C to150°C with a ramp rate of 2°C/10 mins, in the range of $10° < 2\theta < 90°$ with a step size of 0.02° and a step time of 0.5 s/step. When PXRD patterns were analysed for routine phase identification purposes, the refined parameters included unit cell parameters, an overall isotropic atomic displacement parameter, scale factor, sample height displacement, pseudo-Voigt peak shape function terms and nine background polynomial terms. For detailed structural analysis, PXRD patterns were collected in the range of $10° < 2\theta < 120°$ with a step size of 0.02° and a step time of 6.5 s/step. Refined parameters included the sample height displacement, background polynomial terms, pseudo-Voigt peak shape function terms, unit cell parameters, atomic fractional coordinates, using bond valence sum restraints on the vanadium atoms, and individual isotropic atomic displacement parameters. All diffraction data were analysed in the TOPAS Academic v7 software by the Rietveld method.[51,52]

5.2.3. Solid-state nuclear magnetic resonance

^{51}V solid-state NMR (ssNMR) magic angle spinning measurements were conducted on a sample of the material (~0.2 g) contained within a 4 mm (o.d.) probe using a Bruker advance III HD spectrometer. Spectra were acquired at a spin rate of 12 kHz. All direct-excitation ^{51}V spectra were acquired with a 1 μs 30-degree solid pulse which was determined on the first sample. The spectra were acquired with a recycle delay of 0.4 s determined on the sample. For each temperature 3600 spectra were taken and averaged. Spectra were referenced to the ^{1}H resonance of neat tetramethylsilane and adjusting the frequency using the method described by Harris *et al*.[53] Variable-temperature ssNMR data were collected between 20°C and 100°C in 10°C increments. $Pb(NO_3)_2$ was used as a standard for temperature reference. Q_{iso} of the highest intensity peak for each spectrum was obtained by fitting in software DMFit.[54]

5.2.4. Photoluminescence spectroscopy

Room-temperature measurements were performed using a Horiba Jobin-Yvon Fluorolog-3 spectrometer with a xenon lamp excitation source in conjunction with a monochromator for excitation at 700 nm. A Hamamatsu NIR photomultiplier tube was utilised for detection. Samples were contained within quartz capillaries (3 mm o.d.) placed into the cuvette sample holder using a 3D printed holder. Long-pass filters (400 and 850 nm) were used to remove scattered light harmonics during the acquisition of excitation and emission spectra respectively. Diffuse reflectance spectroscopy (DRS) measurements were undertaken using a Shimadzu UV-2600 (Shimadzu corporation, Tokyo, Japan) spectrophotometer with an integrating sphere using $BaSO_4$ as a blank reference over the 220–1350 nm wavelength range. DRS data were transformed to absorption intensity data using the Kubelka-Munk function, $F(R) = (1-R)^2 / 2R$ where R is reflectance. Variable-temperature emission spectra were recorded (as 5 mm pressed pellets) over the temperature range 298–373 K, using an Ocean Insight FX NIR-Quest spectrometer with bifurcated fibre-optic cable and a custom-built heating stage.[55] An Ocean Insight LSM-365A LED was utilised as an 365 nm excitation source. The quantum yield (QY) was measured by the OMAS group at Vinča Nuclear

Institute, Belgrade, Serbia, using an Ocean Insight ISS-REF integrating sphere in combination with Ocean Insight LSM-635A LED at 635 nm as an excitation source and Ocean Insight OCEAN-FX-XR1-ES and NIR Quest+ as spectrometers. Ocean Insight WS-1 Diffuse Reflectance Standard was used as reference.

5.3. Results and discussion

5.3.1. Structural characterisation

Analysis of the PXRD patterns of $Sr_5(V_{0.97}O_4)_3Cl{:}Mn_{0.03}$ and $Ba_5(V_{0.97}O_4)_3Cl{:}Mn_{0.03}$ by Rietveld refinements was carried out using the structural models from the literature for $Sr_5(VO_4)_3Cl$ (ICSD code 171381) and $Ba_5(VO_4)_3Cl$ (ICSD code 171382).[56,57]. The agreement factors obtained were $R_{wp} = 3.20\%$ and $R_{wp} = 1.99\ \%$ for $Sr_5(V_{0.97}O_4)_3Cl{:}Mn_{0.03}$ and $Ba_5(V_{0.97}O_4)_3Cl{:}Mn_{0.03}$, respectively; the final Rietveld fits are shown in Figure 5.1. The unit cell parameters refined for the two compounds are $a = 10.20911(9)$ Å, $c = 7.30625(7)$ Å, $V = 659.48(1)$ Å^3, and $a = 10.55442(4)$ Å, $c = 7.75600(4)$ Å, $V = 748.234(7)$ Å^3. In $Sr_5(V_{0.97}O_4)_3Cl{:}Mn_{0.03}$, the average V–O bond length is 1.721(5) Å, while bond angles range from 105.4(5) to 113.0(5)°. In the Ba analogue, the average V–O bond length is 1.717(4) Å and bond angles range between 106.4(3) and 113.4(4)°. These bond lengths give V^{5+} bond valence sum values of 5.02(7) and 5.05(6) for $Sr_5(V_{0.97}O_4)_3Cl{:}Mn_{0.03}$ and $Ba_5(V_{0.97}O_4)_3Cl{:}Mn_{0.03}$, respectively.

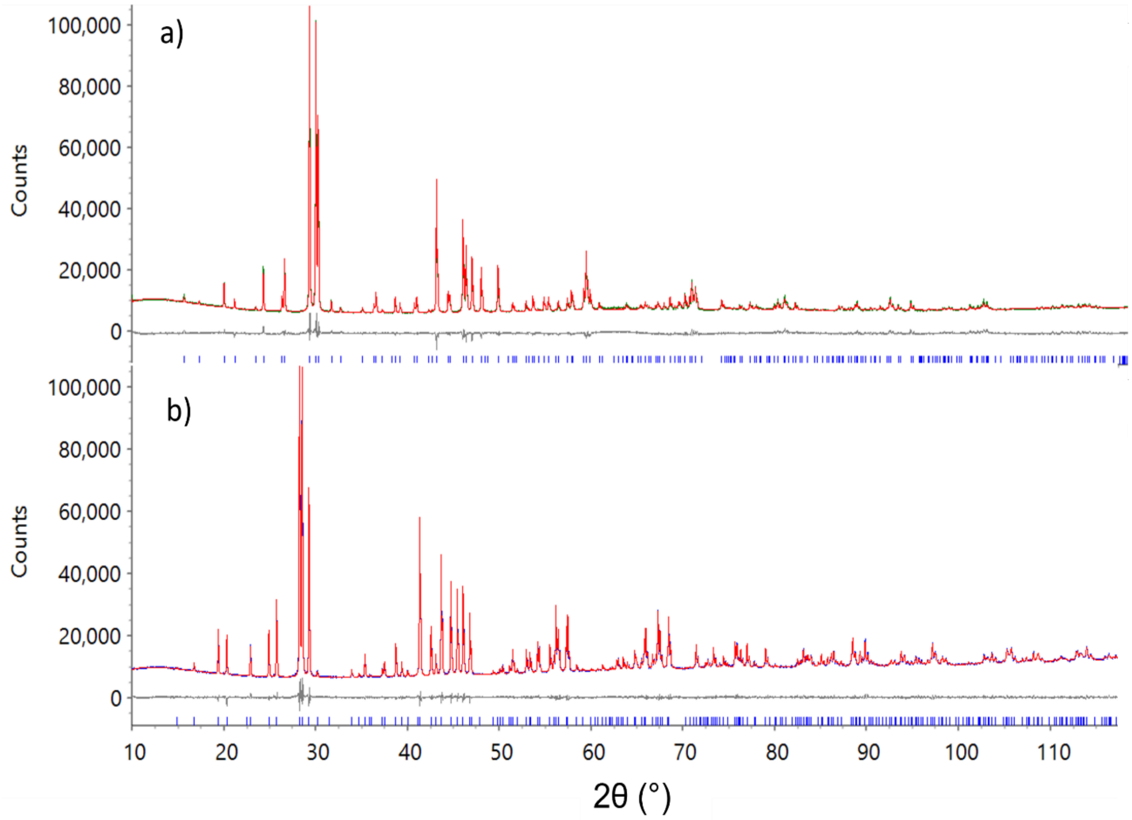

Figure 5.2: The final Rietveld fits for (a) $Sr_5(V_{0.97}O_4)_3Cl{:}Mn_{0.03}$ and (b) $Ba_5(V_{0.97}O_4)_3Cl{:}Mn_{0.03}$. The blue curves show the experimental data, the red curve shows the calculated patterns, and the difference between the experimental and calculated pattern is depicted as the grey curve. Tick-marks represent the Bragg peak positions.

Both materials crystallise in hexagonal space group $P6_3/m$ (Figure 5.1b), with the Mn^{5+} dopant ions replacing V^{5+} on the 6h Wyckoff site with local symmetry C_s (centres of the orange tetrahedra in Figure 5.1b). The key structural difference between $A^{2+} = Ca^{2+}$, Sr^{2+}, Ba^{2+} compounds is that, while the Sr- and Ba-based phases are fully ordered, the Ca-based materials contain Cl^{-} ions disordered over partially occupied crystallographic sites in the channels parallel to the *c*-axis (Figures 5.3a and 5.3b respectively).[57] In addition to being observable in the average structure probed by XRD, anion disorder in the channels of $Ca_5(VO_4)_3Cl$-based materials affects the local environment of the ions occupying tetrahedral sites, as evidenced by solid-state NMR; it also affects their luminescence properties (discussed in Section 5.3.3).[47]

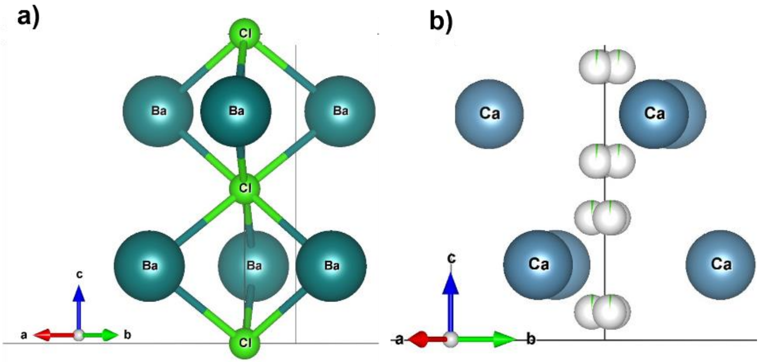

Figure 5.3: a) Crystallographically ordered distribution of Cl$^-$ ions (light green spheres) in Ba- and Sr-containing materials. b) Disordered distribution of Cl$^-$ ions (grey spheres with some light green, indicating partial occupancy) in Ca-containing materials.[57]

Variable-temperature PXRD (VT-PXRD) data were collected on $Sr_5(V_{0.97}O_4)_3Cl:Mn^{5+}_{0.03}$ and $Ba_5(V_{0.97}O_4)_3Cl:Mn^{5+}_{0.03}$ on heating and cooling between 30°C and 150° (Figure 5.4a,b). The data show smooth thermal expansion trends, demonstrating thermal stability over this range, and the absence of structural phase transitions in the temperature range of interest. Unit cell parameters extracted from Rietveld refinements (Figures 5.4c and 5.4d) were used to calculate the thermal expansion coefficients using the relationship:

$$\alpha_V = \left(\frac{1}{V}\frac{\partial V}{\partial T}\right) \tag{5.1}$$

where V is the unit cell volume in Å^3, and T is the temperature in K. For both samples, the volume expansion coefficient is ~4.0×10^{-5} K^{-1}, comparable to values reported for similar apatite-type materials.[28,58,59]

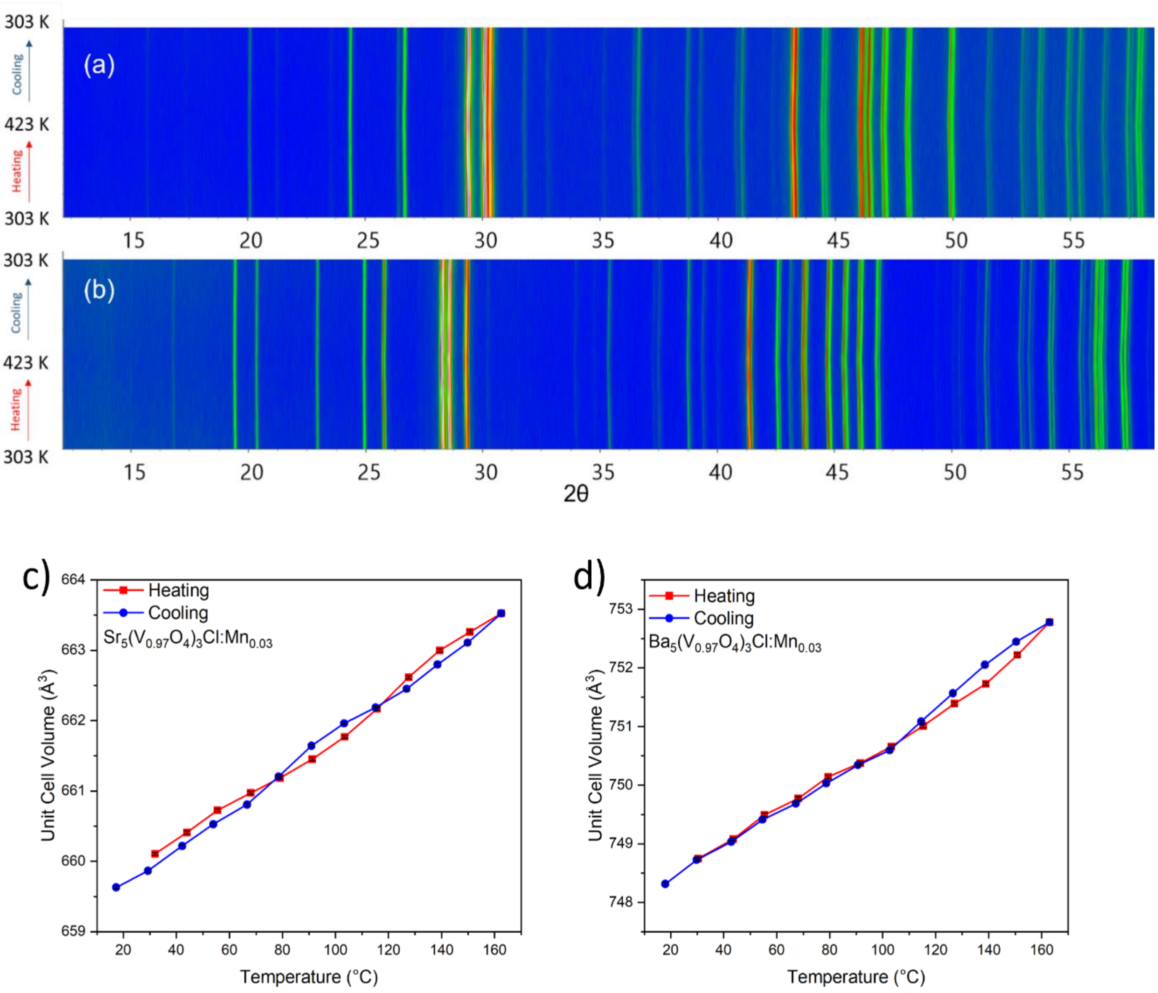

Figure 5.4: Variable-temperature PXRD data for a) $Sr_5(V_{0.97}O_4)_3Cl:Mn^{5+}_{0.03}$ and b) $Ba_5(V_{0.97}O_4)_3Cl:Mn^{5+}_{0.03}$ upon heating and cooling. Unit cell volume vs temperature of c) $Sr_5(V_{0.97}O_4)_3Cl:Mn^{5+}_{0.03}$ and d) $Ba_5(V_{0.97}O_4)_3Cl:Mn^{5+}_{0.03}$.

Figure 5.5a and Figure 5.5b show the homogeneous distribution of Mn^{5+} (indicated by light blue dots) in $Sr_5(V_{0.97}O_4)_3Cl:Mn_{0.03}$ and $Ba_5(V_{0.97}O_4)_3Cl:Mn_{0.03}$ samples, respectively.

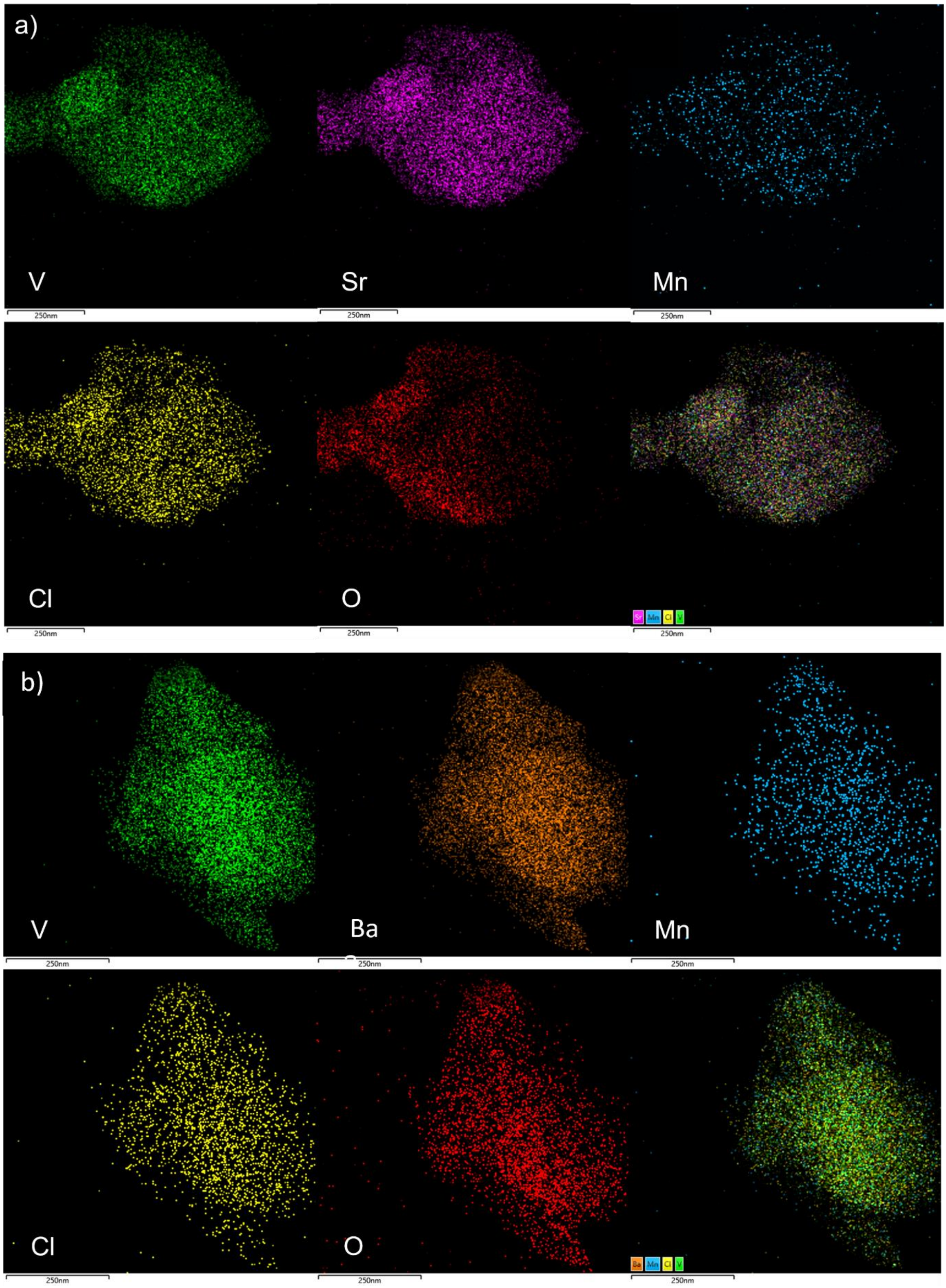

Figure 5.5: EDX chemical maps of singular grains of a) $Sr_5(V_{0.97}O_4)_3Cl:Mn_{0.03}$*, and b)* $Ba_5(V_{0.97}O_4)_3Cl:Mn_{0.03}$.

5.3.2. Investigation of local structure by ^{51}V solid-state NMR

To probe the geometry of tetrahedral crystallographic sites in the apatite-type materials in more detail, VT ^{51}V ssNMR experiments were performed using ^{51}V as a proxy for the local environments of the Mn^{5+} ions.

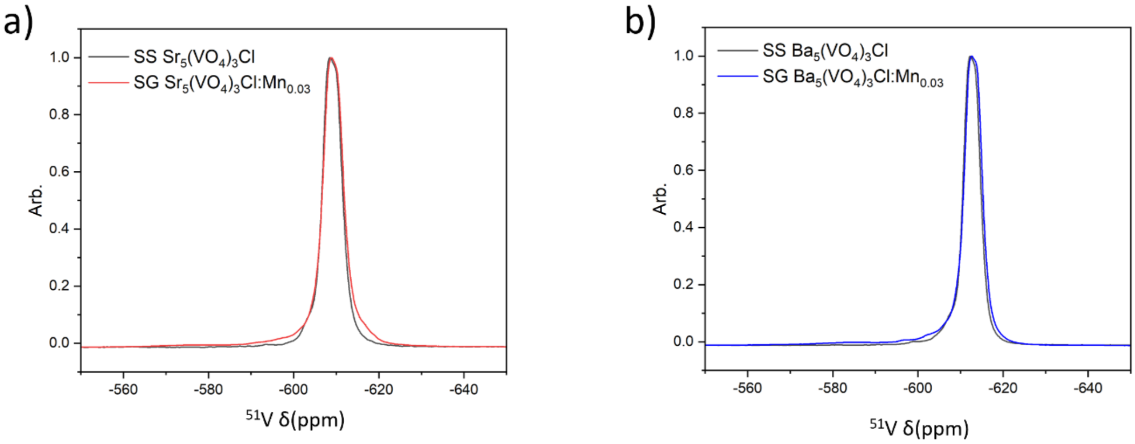

Figure 5.6: Room temperature ^{51}V ssNMR spectra of solid-state synthesised host, and sol-gel synthesised a) $Sr_5(V_{0.97}O_4)_3Cl:Mn_{0.03}$ and b) $Ba_5(V_{0.97}O_4)_3Cl:Mn_{0.03}$.[46]

Undoped $Sr_5(VO_4)_3Cl$ and $Ba_5(VO_4)_3Cl$ each showed a single ^{51}V environment at -608.6 and -612.3 ppm, respectively (Figures 5.6a and 5.6b, black curves), characteristic of tetrahedral ^{51}V coordination environments, each with a weak satellite to the left of the central transitions (-596.8 and -596.4 ppm), consistent with ^{51}V being a quadrupolar nucleus.[47,60] The $Sr_5(V_{0.97}O_4)_3Cl$: $Mn_{0.03}$ and $Ba_5(V_{0.97}O_4)_3Cl$: $Mn_{0.03}$ materials, apart from the same ^{51}V environment at similar shifts of -608.8 and -612.6 ppm respectively, contain very low intensity peaks at -573.7 and -584.5 ppm respectively, when compared to the undoped $Sr_5(VO_4)_3Cl$ and $Ba_5(VO_4)_3Cl$ (Figures 5.6a, red curve, and 5.6b, blue curve). The additional resonances were compared to the ^{51}V ssNMR spectra of $Sr_3(VO_4)_2$ and $Ba_3(VO_4)_2$, which showed resonances at chemical shift values of -611 ppm and -605.0 ppm, respectively.[47] Therefore, additional weak resonances observed for $Sr_5(V_{0.97}O_4)_3Cl$: $Mn_{0.03}$ and $Ba_5(V_{0.97}O_4)_3Cl$: $Mn_{0.03}$ do not belong to any impurity phases that were undetected by PXRD. Instead, they represent a small fraction of the V^{5+} environments distorted by the proximity of Mn^{5+} dopant ions.

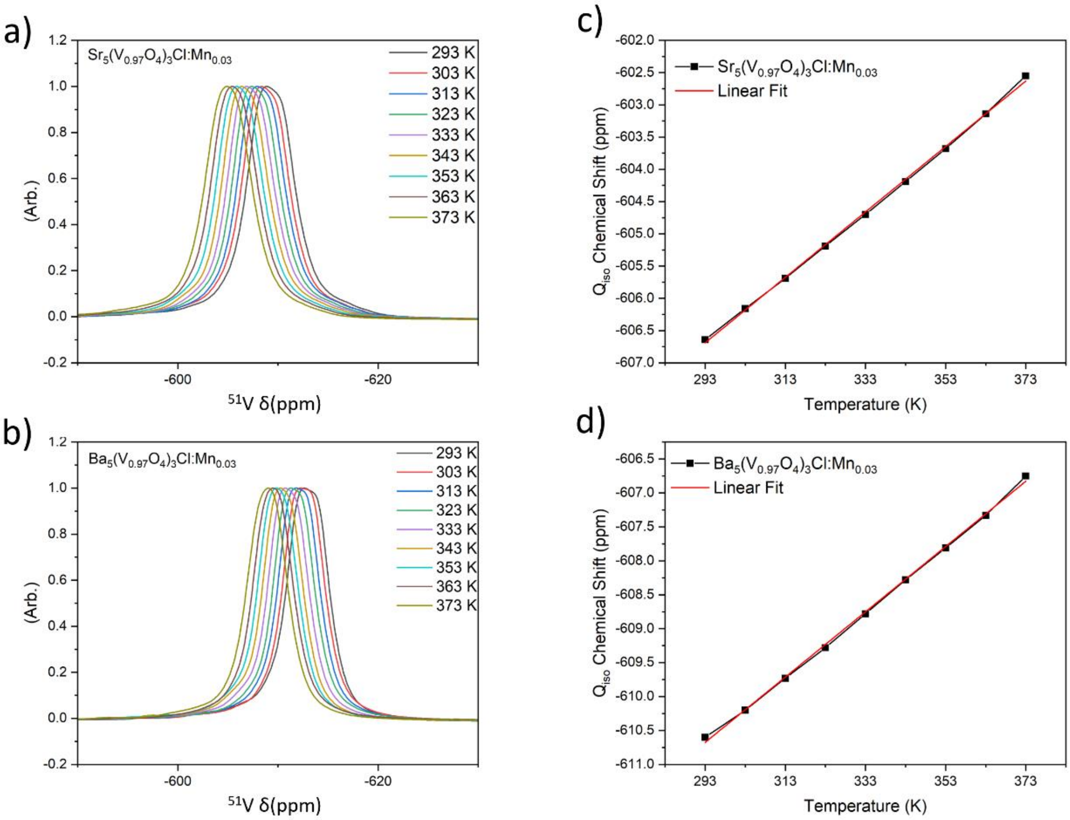

Figure 5.7: Solid-state ^{51}*V NMR spectra collected between 20 and 100°C on (a)* $Sr_5(V_{0.97}O_4)_3Cl:Mn_{0.03}$ *and (b)* $Ba_5(V_{0.97}O_4)_3Cl:Mn_{0.03}$. ^{51}*V ssNMR* Q_{iso} *chemical shift (ppm) vs Temperature of c)* $Sr_5(V_{0.97}O_4)_3Cl:Mn_{0.03}$ *and d)* $Ba_5(V_{0.97}O_4)_3Cl:Mn_{0.03}$.

Variable-temperature ^{51}V ssNMR spectra collected on $Sr_5(V_{0.97}O_4)_3Cl: Mn_{0.03}$ and $Ba_5(V_{0.97}O_4)_3Cl: Mn_{0.03}$ between 20°C and 100°C are shown in Figures 5.7a and 5.7b. In both cases, there is a gradual up-field shift of the main resonances amounting to about 5 ppm, consistent with the thermal expansion of the materials and the absence of significant or abrupt local structure changes, thus demonstrating the stability of the local coordination environments of the Mn^{5+} ions over this temperature range.

Temperature can also be calculated from the change in a peak's chemical shift, a branch of temperature sensing called NMR thermometry.[61] Using linear-least squares fitting, the slopes were calculated from Q_{iso} chemical shift values versus temperature (Figures 5.7c and 5.7d) as 0.0507(6) ppm K^{-1} for $Sr_5(VO_4)_3Cl:Mn_{0.03}$ ($R^2 = 0.9989$), and 0.0481(6) ppm K^{-1} for $Ba_5(VO_4)_3Cl:Mn_{0.03}$ ($R^2 = 0.9987$).

5.3.3. Room-temperature photoluminescence

Preliminary room-temperature emission spectra acquired on the solid-state synthesised materials found that the emission intensity of the $^1E \rightarrow ^3A_2$ transition was much weaker for the Ca apatite materials than the Sr and Ba analogues, at all Mn^{5+} doping levels.[47] The low emission intensity is potentially due to the disordered Cl^- anions introducing defects into the materials' structures causing quenching of emission intensity. The highest emission intensity amongst the solid-state synthesised materials was found for $Ba_5(V_{0.97}O_4)_3Cl:Mn_{0.03}$. Consequently, for sol-gel materials synthesis, $x = 0.03$ was selected as the Mn^{5+} dopant concentration to allow for comparison between $Sr_5(V_{0.97}O_4)_3Cl:Mn_{0.03}$ and $Ba_5(V_{0.97}O_4)_3Cl:Mn_{0.03}$.[47]

The room-temperature emission spectra of $Sr_5(V_{0.97}O_4)_3Cl:Mn_{0.03}$ and $Ba_5(V_{0.97}O_4)_3Cl:Mn_{0.03}$ obtained on excitation at 700 nm are shown in Figures 5.9c and 5.9d.[47] Both samples show the split, narrow ^1E spin-forbidden emission, a low intensity broad $^3T_2$ emission band, alongside two Mn–O vibronic sidebands. All peak maxima, including the vibrational bands, are red-shifted in the Sr-containing material relative to the Ba-analogue. The peaks at ~1225 and ~1280 nm are assigned to the O–Mn–O bending and Mn–O stretching vibrations, respectively.[62] The low intensity of the broad $^3T_2$ emission (~1025 nm) is due to the low thermally activated population of this state at room-temperature. The main ^1E emission peak maxima are at 1167 nm (8600 cm^{-1}) and 1176 nm (8500 cm^{-1}) for $Sr_5(V_{0.97}O_4)_3Cl:Mn_{0.03}$ and $Ba_5(V_{0.97}O_4)_3Cl:Mn_{0.03}$, respectively. A similar red-shifting of the ^1E emission peak is observed for Mn^{5+} doped in $Ba_3(PO_4)_2$ hosts compared to $Sr_3(PO_4)_2$ analogue.[20]

The Tanabe–Sugano diagram for the d^2 electron configuration in the tetrahedral crystal field (Figure 5.8) shows that the energy gap between the ground state $^3A_2$ and the first excited state ^1E is essentially independent of the crystal field strength as the singlet state originates from the same e^2 electron configuration as the ground state.[63–65]. The gap is close to that between the ^3F and the ^1D states of the free ion, which is determined by the Racah parameters, B and C. Variations in the energy of the ^1E state are caused by the nephelauxetic effect influencing the Racah parameter B and C.

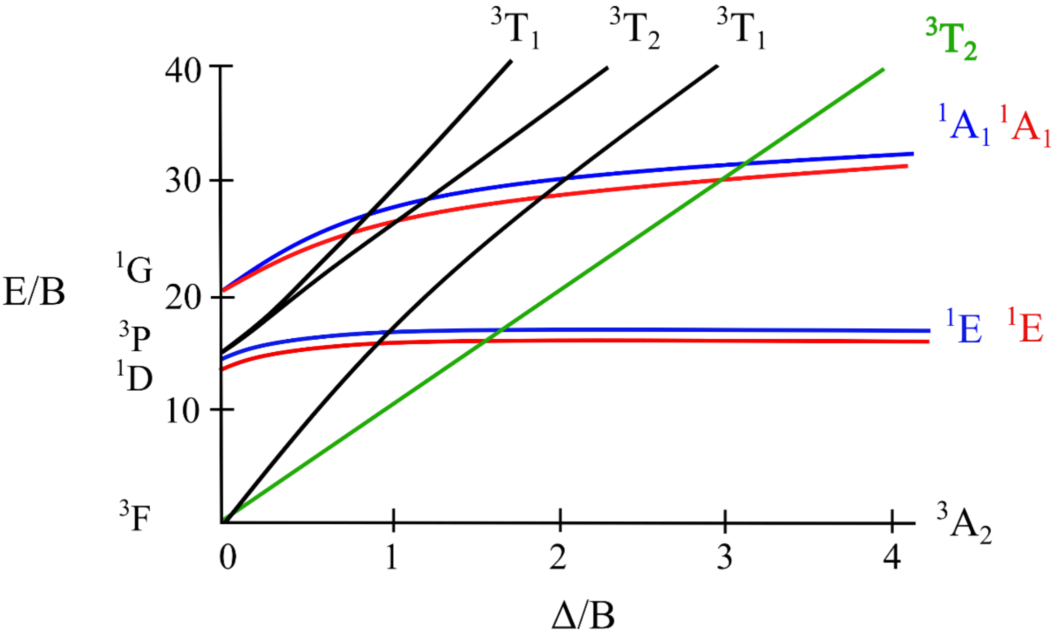

Figure 5.8: Tanabe-Sugano diagram of for a d^2 ion in an octahedral environment. The red and blue colours of the singlet states indicate the Ba- and Sr-analogues of the apatite emission energy respectively. [65]

As has been shown in the literature by isostructural Mn^{5+}-doped fluorophosphate apatites, the Racah *B* value of Mn^{5+} in Ba^{2+} apatite is lower than that of Sr^{2+} apatite, supporting an increase in covalency when $A^{2+} = Ba^{2+}$.[66] In both host materials the first coordination sphere of the A^{2+} cations is comprised of oxide ions, with a number of them subsequently bonded to the isolated tetrahedral Mn^{5+} cations. Changes in the covalency of the A–O bond will affect the covalency of the Mn–O bond and, in turn, the energy of the ^1E peak maxima.[66] The electronegativity of Ba^{2+} is lower than that of Sr^{2+} which increases the electron density of the oxygen ligands of Ba–O bonds. The increased electron density around the oxygen when it is bound to Ba^{2+} allows for more a covalent bond.

Both Figure 5.9c and 5.9d show that the ^{1}E emission, due to the Mn^{5+} ion in MnO_4^{3-}, is split into >1 band. The Mn^{5+} ions are not in a perfect tetrahedral environment, but rather are in distorted tetrahedra with C_s local symmetry, such that the ^{1}E splits into non-degenerate ^{1}A' and ^{1}A'' states. The magnitude of the splitting is 11 nm (82 cm^{-1}) for $Sr_5(V_{0.97}O_4)_3Cl:Mn_{0.03}$ and 5 nm (36 cm^{-1}) for $Ba_5(V_{0.97}O_4)_3Cl:Mn_{0.03}$. This splitting is commonly seen in isostructural apatites with different *B* cations and *X* anions, and structures such as spodiosites.[9,67,68]

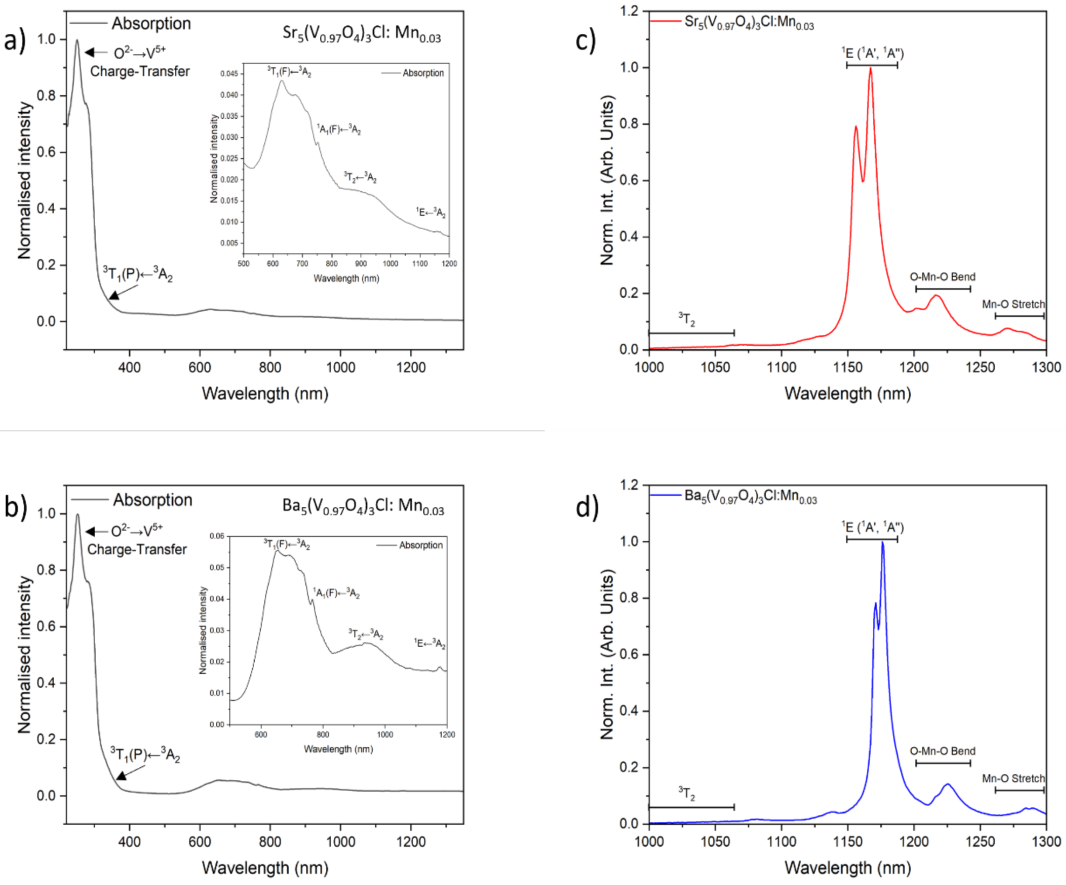

Figure 5.9: Normalised room-temperature absorption (obtained from diffuse reflectance) and (inset) expansion of the 500-1200 nm region of the pseudo-absorption spectrum of a) $Sr_5(V_{0.97}O_4)_3Cl:Mn_{0.03}$ and b) $Ba_5(V_{0.97}O_4)_3Cl:Mn_{0.03}$. Normalised room-temperature emission spectrum of c) $Sr_5(V_{0.97}O_4)_3Cl:Mn_{0.03}$, and d) $Ba_5(V_{0.97}O_4)_3Cl:Mn_{0.03}$.

The absorption spectra, obtained by applying the Kubelka-Munk function to diffuse reflectance data (Figures 5.9a and 5.9b) show a broad, intense absorption band arising from the charge transfer transition from the p-orbitals of the oxide ligands to vacant d-orbitals of the V^{5+} ions. The inset spectra of Figures 5.9a and 5.9b show the broad absorption bands of the Mn^{5+} ions belonging to the $^3T_1(F) \leftarrow {}^3A_2$, $^3T_1(P) \leftarrow {}^3A_2$, and $^3T_2 \leftarrow {}^3A_2$ transitions, alongside the sharper peaks of the spin-forbidden $^1A_1 \leftarrow ^3A_2$ and $^1E \leftarrow ^3A_2$ transitions. For both $Sr_5(V_{0.97}O_4)_3Cl:Mn_{0.03}$ and $Ba_5(V_{0.97}O_4)_3Cl:Mn_{0.03}$, the $^3T_1(F) \leftarrow ^3A_2$ transition is made up of three individual peaks, due to the lowing of the MnO_4^{3-} symmetry from the ideal T_d to C_s causing a loss of degeneracy of the $^3T_1(^3F)$ state. This affects the broadness of the absorption band and therefore influences the colour of the material.[66]

The quantum yields (QY) determined for $Sr_5(V_{0.97}O_4)_3Cl:Mn_{0.03}$ and $Ba_5(V_{0.97}O_4)_3Cl:Mn_{0.03}$ are 47% and 51%, respectively. These are markedly high values, particularly for NIR emitters. Coupled with the large extinction coefficients, both $Sr_5(V_{0.97}O_4)_3Cl:Mn_{0.03}$ and $Ba_5(V_{0.97}O_4)_3Cl:Mn_{0.03}$ thus offer high brightness. Table 5.2 presents current Mn^{5+} luminescence thermometry phosphors. Both $Sr_5(V_{0.97}O_4)_3Cl:Mn_{0.03}$ and $Ba_5(V_{0.97}O_4)_3Cl:Mn_{0.03}$ offer two of the highest values of QY for Mn^{5+}-doped phosphors.

Table 5.2: Comparison table of Mn^{5+}-doped phosphor QY. Parenthesis indicate errors of own samples derived from a single measurement and MATLAB code.

Materials	**Dopant**	**Maximum QY (%)**	**Ref**
$Sr_5(VO_4)_3Cl$	Mn^{5+}	47(2)	This work
$Ba_5(VO_4)_3Cl$	Mn^{5+}	51(2)	This work
$Ba_3(PO_4)_2$	Mn^{5+}	34	[27]
$Ba_3(PO_4)_2$	Mn^{5+}	40	[80]
$Ba_3(VO_4)_2$	Mn^{5+}	51	[18]
$Ca_6Ba(PO_4)_4O$	Mn^{5+}	38	[17]
$Ca_{14}Zn_6Ga_{10-x}Mn_xO_{35}$	Mn^{5+}/ Mn^{4+}	32	[69]

5.3.4. LIR luminescence thermometry

$Sr_5(V_{0.97}O_4)_3Cl:Mn_{0.03}$ and $Ba_5(V_{0.97}O_4)_3Cl:Mn_{0.03}$ were first investigated for luminescence thermometry at physiologically relevant temperatures by *LIR*. Figures 5.10 and 5.11 show the thermometry data for the two materials (note that a logarithmic scale is used in Figures 5.10a and 5.11a). For both materials, the main ^1E narrow emission intensity peak decreases relative to the weaker and broader $^3T_2$ peak, with increasing temperature, due to thermal population of the latter from the former.

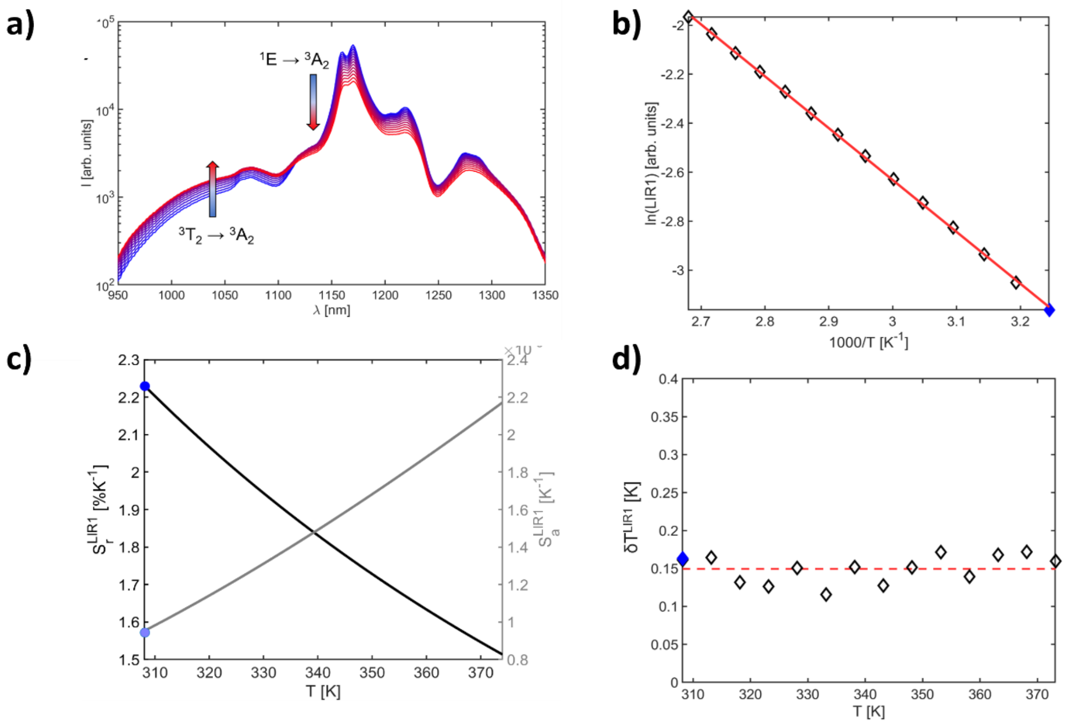

Figure 5.10: $Sr_5(V_{0.97}O_4)_3Cl:Mn_{0.03}$ variable-temperature data; a) The logarithmic scaled version of the variable-temperature emission intensity highlighting the changes in intensity of the $^3T_2$ and ^1E bands as temperature increases from 35°C to 100°C; b) The linear Boltzmann equation, fitting the LIR data (diamond markers – average of 75 scans); c) A plot of the experimentally obtained sensitivities – relative (black line, left axis) and absolute (grey line, right axis); d) δT of each experimental measurement – the filled blue diamond represents 308 K.

At each temperature, 75 readings were recorded and averaged to give *LIR* values shown in Figures 5.10c and 5.11c. To obtain the *LIR* values, for $Sr_5(V_{0.97}O_4)_3Cl:Mn_{0.03}$ the $^3T_2$ band intensity was integrated between 950 and 1050 nm and the ^1E peak between 1140 and 1200 nm; for $Ba_5(V_{0.97}O_4)_3Cl:Mn_{0.03}$, the $^3T_2$ band intensity was integrated between 950 and 1067 nm and the ^1E doublet between 1152 and 1208 nm. From Equation 1.20, a linear dependence can be observed (Figures 5.10b and 5.11b), from the gradient of which the energy gap between the two investigated thermally coupled states was determined to be 1471 cm^{-1} for

$Sr_5(V_{0.97}O_4)_3Cl:Mn_{0.03}$, and 1360 cm^{-1} for $Ba_5(V_{0.97}O_4)_3Cl:Mn_{0.03}$. The temperature-invariant constant, *B*, was calculated from the y-intercept of the linear fit and found to be 41.21 for $Sr_5(V_{0.97}O_4)_3Cl:Mn_{0.03}$ and 31.82 for $Ba_5(V_{0.97}O_4)_3Cl:Mn_{0.03}$. The Boltzmann *LIR* equation was fitted to the *LIR* values (red line in Figures 5.10b and 5.11b), giving good fits with $R^2 = 0.9996$ and $R^2 = 0.9999$ respectively. From this energy difference, the absolute, S_a, and relative, S_r, sensitivities of the thermometers were calculated from Equations 1.21 and 1.22.

The obtained S_a values for $Sr_5(V_{0.97}O_4)_3Cl:Mn_{0.03}$ and $Ba_5(V_{0.97}O_4)_3Cl:Mn_{0.03}$ at 373 K are

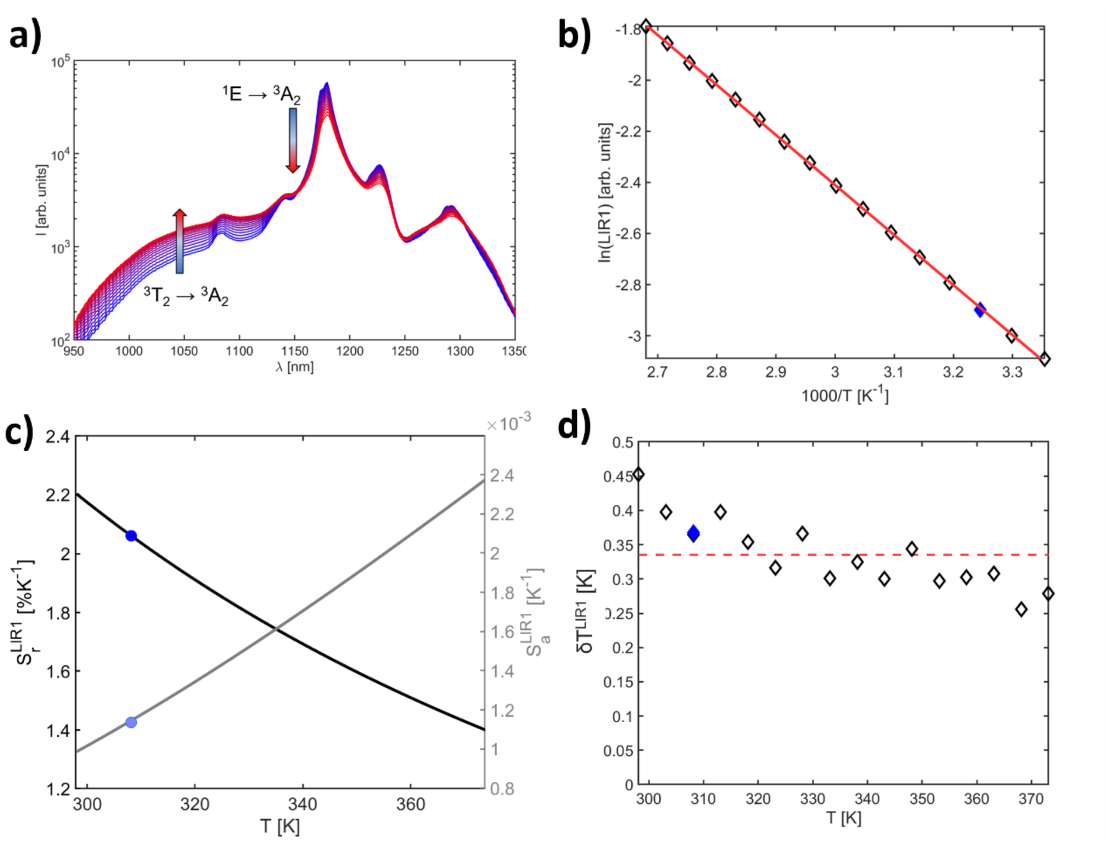

Figure 5.11: $Ba_5(V_{0.97}O_4)_3Cl:Mn_{0.03}$ variable-temperature data; a) The logarithmic scaled version of the variable-temperature emission intensity highlighting the changes to intensity of the $^3T_2$ and ^1E bands as temperature increases between 35°C and 100°C; b) The linear Boltzmann equation, fitting the LIR data (diamond markers – average of 75 scans); c) A plot of the experimentally obtained sensitivities – relative (black, left) and absolute (grey, right); d) δT of each experimental measurement – the filled blue diamond represents 308 K.

2.2 x 10^{-3} K and 2.4 x 10^{-3} K, respectively (Figures 5.10c and 5.11c). In terms of S_r, the best performance observed for $Sr_5(V_{0.97}O_4)_3Cl$: $Mn_{0.03}$ is 2.23% K^{-1} at 308 K. $Ba_5(VO_4)_3Cl$: $Mn_{0.03}$ is similar, with a S_r of 2.20% K^{-1} at 298 K (and 2.06% K^{-1} at 308 K).

The δT, was calculated using Equation 1.13 where σ_r was the relative uncertainty estimated from 75 consecutive measurement at a given temperature. As shown in Figures 5.10d and 5.11d, on average across the temperature range, the δT for $Sr_5(V_{0.97}O_4)_3Cl{:}Mn_{0.03}$ is 0.15 K, and for $Ba_5(V_{0.97}O_4)_3Cl{:}Mn_{0.03\ it}$ is 0.34 K (indicated by the red dashed lines in Figures 5.10d and 5.11d). For physiological temperature (35°C, 308 K) the δT is 0.15 K and 0.34 K for $Sr_5(V_{0.97}O_4)_3Cl{:}Mn_{0.03}$ and $Ba_5(V_{0.97}O_4)_3Cl{:}Mn_{0.03}$, respectively.

5.3.5. Band-shift luminescence thermometry

Band-shift luminescence thermometry is based on the change in the position of the maximum intensity of the peak centroid either as wavelength (nm) or converted to energy across a measured temperature range. In this work, the position of the highest intensity emission peak was found at each temperature and converted to wavenumber (cm^{-1}). The experimental peak-shift data for $Sr_5(V_{0.97}O_4)_3Cl{:}Mn_{0.03}$ were fitted using a 2nd order polynormal function, Equation 5.2:

$$E_{MAX}^{Av}(T) = a.T^2 + \ b.T + \ c \tag{5.2}$$

with fitting parameters $Sr_5(V_{0.97}O_4)_3Cl{:}Mn_{0.03}$ are $a = 3.57 \text{ x } 10^{-4}\ K^{-2}\ cm^{-1}$, $b = -3.00 \text{ x } 10^{-1}\ K^{-1}\ cm^{-}1$ and $c = 8605.62\ cm^{-1}$, ($R^2 = 0.9996$).

Similarly, $Ba_5(V_{0.97}O_4)_3Cl{:}Mn_{0.03}$ VT-emission data were fitted using a 3rd order polynomial function, Equation 5.3:

$$E_{MAX}^{Av}(T) = e.T^3 + \ f.T^2 + \ g.T + h \tag{5.3}$$

with fitting parameters $Sr_5(V_{0.97}O_4)_3Cl{:}Mn_{0.03}$ found to be $e = 2.53 \text{ x } 10^{-6}\ K^{-3}\ cm^{-1}$, $f = 1.95 \text{ x } 10^{-3}\ K^{-2}\ cm^{-1}$, $g = -4.95 \text{ x } 10^{-1}\ K^{-1}\ cm^{-1}$, and $h = 8522.80\ cm^{-1}$ ($R^2 = 0.9999$).

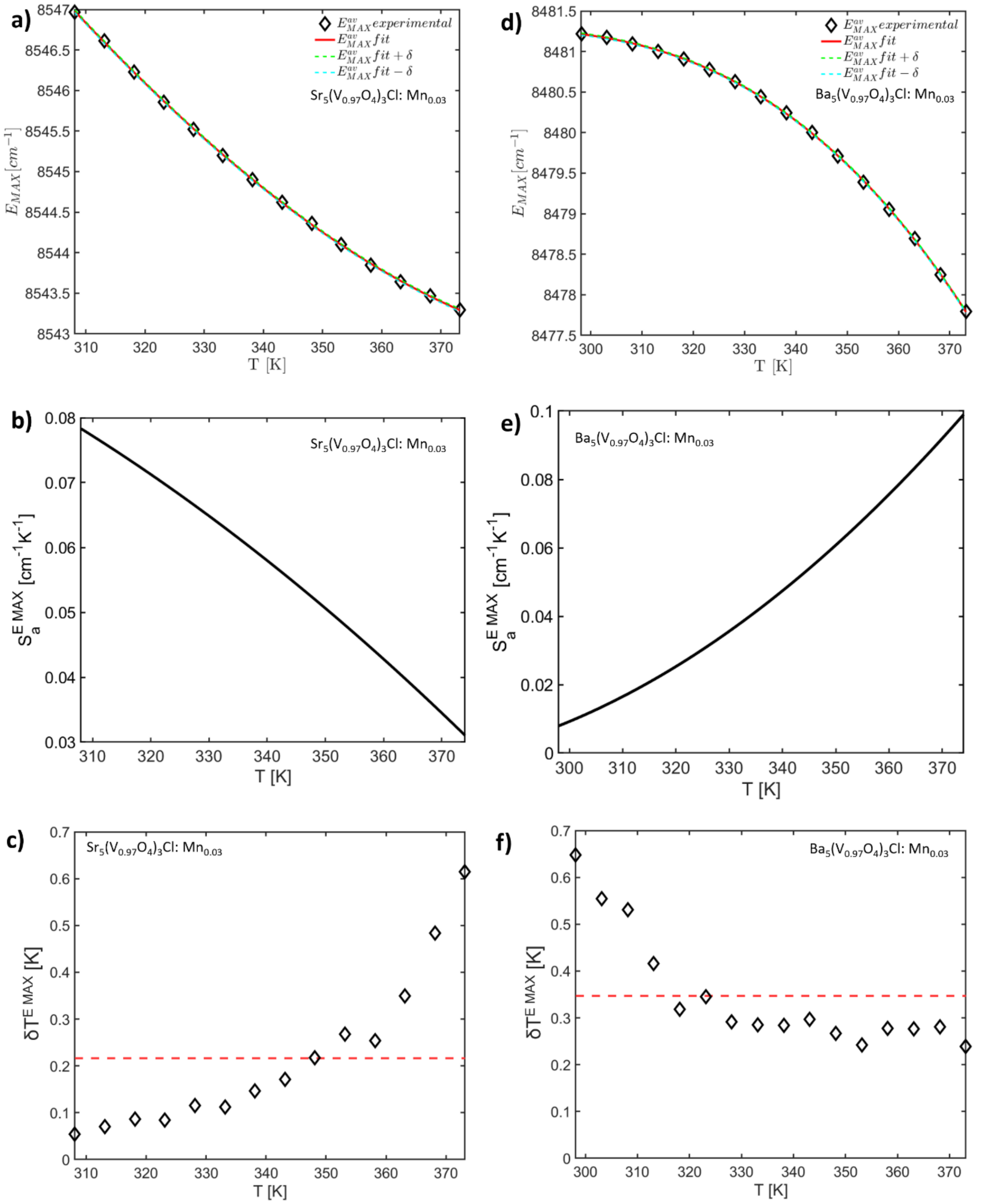

Figure 5.12: Band-shift thermometry data of materials $Sr_5(V_{0.97}O_4)_3Cl: Mn_{0.03}$ (a, b, c) and $Ba_5(V_{0.97}O_4)_3Cl: Mn_{0.03}$ (d, e, f); a,d) Fitted sample peak maxima data as absolute energy (cm^{-1}) with dashed lines showing a 95% confidence interval; b, e) absolute sensitivity, S_a; c, f) δT with average over the temperature range shown by the dashed red line.

Figures 5.12a and 5.12d show the experimental data fit dependence on temperature for $Sr_5(V_{0.97}O_4)_3Cl$: $Mn_{0.03}$ and $Ba_5(V_{0.97}O_4)_3Cl:Mn_{0.03}$ respectively with a red-shifting of the ^1E peak maximum energy as temperature increases from 308 K to 373 K. $Sr_5(V_{0.97}O_4)_3Cl$: $Mn_{0.03}$ demonstrates a maximum S_a of 0.08 cm^{-1} K^{-1} at 308 K (35°C) that decreases as temperature increases (Figure 5.12b). Inversely $Ba_5(V_{0.97}O_4)_3Cl:Mn_{0.03}$ gives a maximum S_a value of 0.1 cm^{-1} K^{-1} at 373 K (100°C), decreasing with decreasing temperature (Figure 5.12e) with a S_a of 0.015 cm^{-1} K^{-1} at 308 K (35°C). The average δT indicated by the dashed red line, for $Sr_5(V_{0.97}O_4)_3Cl$: $Mn_{0.03}$ in Figure 5.12c was found to be ~0.2 K, with a specific δT of ~0.05K at 308 K (35°C), and ~0.35 K with a δT of ~0.52 K at 308 K (35°C) for $Ba_5(V_{0.97}O_4)_3Cl:Mn_{0.03}$ (Figure 5.12f).

5.3.6 Bandwidth (FWHM) luminescence thermometry

Band-width thermometry measures the change in width (in units of cm^{-1}) at half the maximum intensity of a selected peak as a function of temperature. For both materials the FWHM experimental data were fitted using a second-order polynomial, Equation 5.4:

$$FWHM(T) = i.T^2 + j.T + k \tag{5.4}$$

Fitting parameters for $Sr_5(V_{0.97}O_4)_3Cl$: $Mn_{0.03}$ were $i = 2.00 \times 10^{-3}$ K^{-2} cm^{-1}, $j = 8.32 \times 10^{-1}$ K^{-1} cm^{-1}, $k = 219.35$ cm^{-1} ($R^2 = 0.9999$); and for $Ba_5(V_{0.97}O_4)_3Cl$: $Mn_{0.03}$ were $i = 1.70 \times 10^{-3}$ K^{-2} cm^{-1}, $j = 7.18 \times 10^{-1}$ K^{-1} cm^{-1}, $k = 165.43$ cm^{-1} ($R^2 = 0.9999$).

Figures 5.13a and 5.13d show the FWHM experimental data fit which indicate a broadening of the ^1E peak of both $Sr_5(V_{0.97}O_4)_3Cl:Mn_{0.03}$ from 153 to 187 cm^{-1}, and $Ba_5(V_{0.97}O_4)_3Cl$: $Mn_{0.03}$ from 103 to 135 cm^{-1} as temperature increases from 308 to 373 K. $Sr_5(V_{0.97}O_4)_3Cl:Mn_{0.03}$ and $Ba_5(V_{0.97}O_4)_3Cl$: $Mn_{0.03}$ demonstrate maximum S_a values of 0.66 cm^{-1} K^{-1} (Figure 5.13b) and 0.55 cm^{-1} K^{-1} (Figure 5.13e) at 373 K respectively. The maximum S_r of $Sr_5(V_{0.97}O_4)_3Cl:Mn_{0.03}$ was calculated as ~0.35 % K^{-1}, with a S_r of 0.26 % K^{-1} (Figure 5.13b) at 308 K (35°C), similarly for $Ba_5(V_{0.97}O_4)_3Cl$: $Mn_{0.03}$, maximum S_r was 0.41 % K^{-1} at 373 K (100°C), with 0.29 % K^{-1} at 308 K (35°C) (Figure 5.13e). The average δT (dashed red line), and δT at 308 K for $Sr_5(V_{0.97}O_4)_3Cl:Mn_{0.03}$ were ~0.08 K (Figure 5.13c), and ~0.04 K respectively, and for $Ba_5(V_{0.97}O_4)_3Cl$: $Mn_{0.03}$ were ~0.07 K and ~0.05 K (Figure 5.13f) respectively.

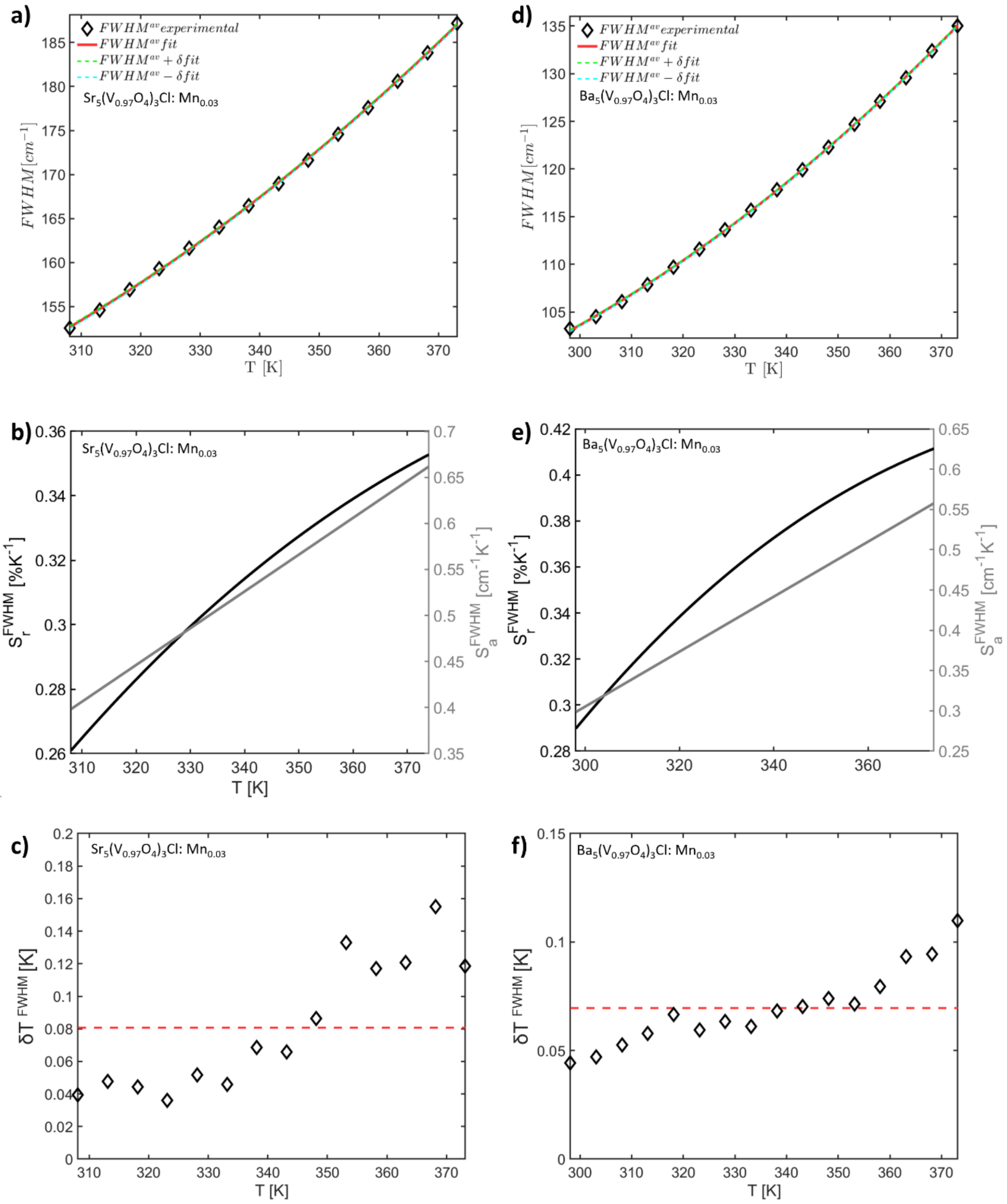

Figure 5.13: Bandwidth (FWHM) thermometry data of materials $Sr_5(V_{0.97}O_4)_3Cl:Mn_{0.03}$ (a, b, c) and $Ba_5(V_{0.97}O_4)_3Cl:Mn_{0.03}$ (d, e, f); a,d) Fitted peak width data as absolute energy (cm^{-1}) with dashed lines showing a 95% confidence interval; b, e) absolute sensitivity, S_a, and relative sensitivity, S_r, parameters; c, f) δT with average over the temperature range shown by the dashed red line.

5.3.7. Multiparametric luminescence thermometry and its comparison with single-parameter thermometry

It is possible to combine the luminescent thermometry parameters of *LIR*, band-shift and bandwidth by using multiparametric linear regression (MLR) - a statistical method that uses two or more explanatory variables to determine the outcome of a response variable. In concise terms, MLR is a multidimensional extension of the least-squares regression.

Here, *LIR*, E_{max} and FWHM are the desirable independent explanatory variables and temperature is the response variable. The prerequisite for using MLR, however, is that there be a linear relationship between the dependent variables and the independent variables and that the independent variables are not too highly correlated with each other. While *LIR*, E_{max} and FWHM are indeed not highly correlated with each other, none of them has a linear relationship with *T* in the observed temperature range. Nevertheless, there have been successful applications of MLR demonstrated over the limited temperature range wherein the linearity can be assumed.[45,46] In addition, although not strictly required, the values of independent variables should be of the same magnitude due to the nature of the fitting procedure that favours variables with larger values.

To overcome the non-linearity and the magnitude problem here, thermometric parameters Δ_i (independent variables) that are simply temperature readouts obtained from single-parameter readouts were introduced:[19]

$$\Delta_1 = T_{LIR} = \frac{\Delta E}{k[\log(B) - \log(LIR)]} \tag{5.5}$$

$$\Delta_2 = T_{E_{max}} = \frac{-b - \sqrt{b^2 - 4a(c - E_{max})}}{2a} \tag{5.6}$$

$$\Delta_3 = T_{FWHM} = \frac{-i - \sqrt{i^2 - 4h(j - FWHM)}}{2h} \tag{5.7}$$

Parameters of ΔE, B, a, b, c, h, i, and j for $Sr_5(V_{0.97}O_4)_3Cl:Mn_{0.03}$ are obtained by fitting experimental results to the Equations 5.5, 5.6 and 5.7 (from data given in Sections 5.3.4, 5.3.5, and 5.3.6). Using MLR, one can represent the linear relationship between these parameters and the thermometric temperature (*i.e.*, the dependent variable) such that:

$$T_{MLR} = \beta_0 + \beta_1\Delta_1 + \beta_2\Delta_2 + \beta_3\Delta_3 \tag{5.8}$$

where β_0 is the constant term and β_1, β_2, and β_3 are the slope coefficients for each of three explanatory variables. One should notice that in this representation β_1, β_2, and β_3 have a role of significance coefficients for each of the three temperature readouts Δ_1, Δ_2 and Δ_3 respectively ($\beta_1 + \beta_2 + \beta_3 \approx 1$). Also note that β_0 is a measure of accuracy correction since, if all Δ_i parameters show the same temperature readout, then β_0 represents T_{MLR} offset from that value.

The comparison of the performance between three single-parameter thermometry methods and the multiparametric method was done experimentally by acquiring 75 spectroscopic measurements at each temperature. Values of β_i obtained after applying MLR on the whole parameter dataset are presented in Table 5.3.

Table 5.3: Values of β_i obtained as a result of MLR application on the acquired dataset.

$\boldsymbol{\beta_0}$ $[\boldsymbol{K}]$	$\boldsymbol{\beta_1}$ [%]	$\boldsymbol{\beta_2}$ [%]	$\boldsymbol{\beta_3}$ [%]
-0.050	*11.03*	*30.19*	*58.80*

Based on these β values and according to the following reference,[45] the relative error of the MLR method can be calculated as:

$$S_r^{MLR}[\%K^{-1}] = 100\% \sqrt{\frac{1}{(\beta_1\Delta_1)^2} + \frac{1}{(\beta_2\Delta_2)^2} + \frac{1}{(\beta_3\Delta_3)^2}} \tag{5.9}$$

The temperature dependence of the relative sensitivity is presented in Figure 5.14a, exhibiting the highest value at 308.15 K of 3.14 % K^{-1}. As the temperature increases the relative sensitivity decreases reaching the lowest value of 2.59 % K^{-1} at 373.15 K. Likewise the accuracy (the extent of agreement between a measured temperature value and the nominal temperature, Figure 5.14b) and precision (the standard deviation of repeated temperature measurements, Figure 5.14c) for each method and temperature are calculated. Figure 5.14 also shows the distributions of calculated temperatures at the nominal temperature of 313.15 K, for single-parameter methods based on *LIR* (d), band-shift (e) and FWHM (f), as well as for the multiparametric method that utilises these three thermometric indicators (g).

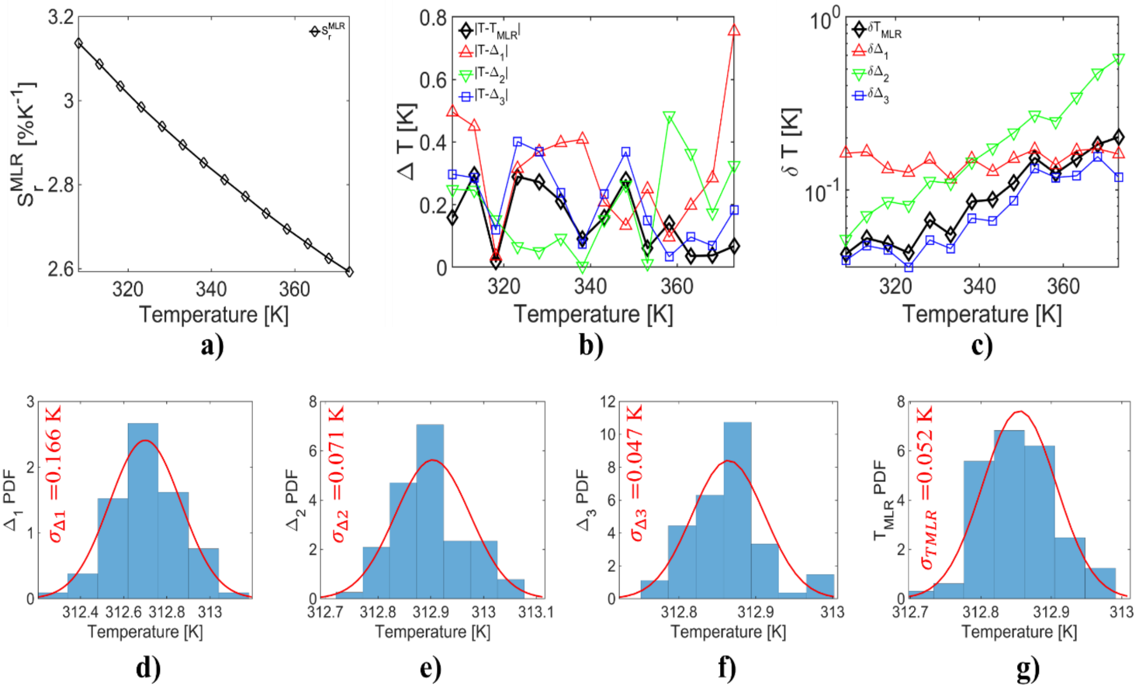

a) **b)** **c)**

d) **e)** **f)** **g)**

Figure 5.14: (a) The relative error of MLR, (b) the accuracy (ΔT) and (c) the precision (δT) of single-parametric (LIR—red Δ symbol and line, ^{1}E peak maximum energy—green D symbol and line, and ^{1}E peak FWHM—blue □ symbol and line) and multiparametric (black ◊ symbol and line) temperature readings from the near-infrared emission of $Sr_5(V_{0.97}O_4)_3Cl:Mn_{0.03}$ at different temperatures; (d–g) distributions of temperatures measured by single-parametric (LIR, ^{1}E peak maximum, and ^{1}E peak FWHM) and multiparametric thermometry, respectively (nominal temperature 313.15 K); temperature distributions were fitted to the normal distribution (red line) with obtained standard deviations indicated on each graph.

Based on these data, and considering the entire investigated temperature range, the temperature determined by MLR (T_{MLR}) has the best accuracy while at the same time sustaining precision similar to the most precise single parametric method used (in this case, that based on FWHM). This observation is in agreement with previously observed characteristics of MLR thermometry.[19]

5.4. Discussion and comparison of selected NIR luminescence thermometers

It is important to compare and contrast our materials' synthetic route, physical stability, and thermometric performance to the known phosphors. Tables 5.4 and 5.5 summarise a number of Mn^{5+}-containing thermometers reported in the literature, and selected luminescence thermometers that emit within at least one of the three biological windows of transparency.

5.4.1. Comparison with other Mn^{5+} luminescence thermometers

Table 5.4: Comparison table of Mn^{5+} luminescence thermometers, their readout methods, and their figures of merit. Orange cells denote materials reported in this chapter.

Entry	Material	Dopant	Synthesis route (Temp, °C)	Readout	Max S_r (% K^{-1})	Temp. res (K)	Temp (K)	Ref
1	$Sr_5(VO_4)_3Cl$	Mn^{5+}	Sol-gel, 750	LIR	2.23	0.16	308	This work
				Band-shift	S_a = 0.08 cm^{-1} K^{-1}	0.05	308	
				Bandwidth	0.35	0.04	373	
				MLR	3.14	0.042	308	
2	$Ba_5(VO_4)_3Cl$	Mn^{5+}	Sol-gel, 750	LIR	2.20	0.34	298	This work
				Band-shift	S_a = 0.10 cm^{-1} K^{-1}	0.35	373	
				Bandwidth	0.41	0.07	373	
3	$Ca_6BaP_4O_{17}$	Mn^{5+}	Solid-state, 1280	LIR	2.05	0.21	293	[17]
4	$Ca_6BaP_4O_{17}$	Mn^{5+}	Solid-state, 1200	LIR	2.0	0.22	298	[19]
				LIR	0.3	2.82	298	
				Band-shift	S_a = 0.21 cm^{-1} K^{-1}	0.16	298	
5	$Ba_3(PO_4)_2$	Mn^{5+}	Flame aerosol, 800	Single Int.	0.26	<1	283 - 343	[9]
				LIR	0.43	<1	283 - 343	
				Band-shift	S_a =0.022 nm C^{-1}	<1	283 - 343	
6	$Ba_5(PO_4)_3OH$	Mn^{5+}	Flame aerosol, 800	Single Int.	0.81	N/A	283 - 343	[9]
				LIR	0.34	N/A	283 - 343	
				Band-shift	0.51 % C^{-1}	N/A	283 - 343	
7	$Ba_3(VO_4)_2$	Mn^{5+}, Er^{3+}	Pechini, 1000	Lifetime	1.19	0.026	443	[18]
8	$Ba_3(VO_4)_2$	Mn^{5+}, Nd^{3+}	Pechini, 1000	LIR	0.94	N/A	453	[21]
9	$Ba_3(PO_4)_2$	Mn^{5+}	Solid-state, 1200	Lifetime	0.93	N/A	469	[20]
10	$Sr_3(PO_4)_2$	Mn^{5+}	Solid-state, 1200	Lifetime	1.00	N/A	443	[20]

$Ca_6BaP_4O_{17}$:0.5%Mn^{5+} (Entry 3) demonstrated a S_r of 2.05% K^{-1} at 293 K and 1.92% K^{-1} at 303 K for *LIR* thermometry using the $^3T_2$ and ^1E emission peaks, with an average δT of 0.21 K.[17] Compared to Entries 1 and 2, the $Ca_6BaP_4O_{17}$:0.5%Mn^{5+} thermometer gave a *LIR* S_r with a slightly lower value at physiological temperature, although the δT of $Ca_6BaP_4O_{17}$:0.5% Mn^{5+} for *LIR* thermometry was better than that of Entry 2 (0.34 K at 308 K).

$Ca_6Ba(PO_4)_4O$: 0.75% Mn^{5+} (Entry 4) gave a *LIR* S_r of ~2.0% K^{-1}. *LIR* of the Stokes and anti-Stokes vibrations of the O–Mn–O bend coupled to the ^1E excited state gave an S_r of 0.3% K^{-1}, and the peak shift had a S_a of 0.21 cm^{-1} K^{-1}, all at 298 K.[19] The average δT of all three single readouts were 0.22 K, 2.82 K, and 0.16 K respectively. Using the three single readouts as variables for a MLR thermometry, the resultant δT was 0.22 K. Compared to Entries 1 and 2, *LIR* of the $^3T_2$ and ^1E states for $Ca_6Ba(PO_4)_4O$: 0.75% Mn^{5+} has a similar S_r value at physiological temperatures, whilst the S_a of the ^1E band-shift for Entry 4 was over double that of the $Sr_5(V_{0.97}O_4)_3Cl:Mn_{0.03}$ and $Ba_5(V_{0.97}O_4)_3Cl:Mn_{0.03}$ thermometers. All the readout methods for $Sr_5(V_{0.97}O_4)_3Cl:Mn_{0.03}$ gave lower values (thus higher δT) than $Ca_6Ba(PO_4)_4O$: 0.75% Mn^{5+}, as did all but the *LIR* δT for $Ba_5(V_{0.97}O_4)_3Cl:Mn_{0.03}$.

Mn^{5+}-doped $Ba_3(PO_4)_2$ (Entry 5) gives an S_r of 0.26% K^{-1} using total intensity of the ^1E emission (with a δT of <1 K), *LIR* of the ^1E emission and Mn–O vibrational peak gave a S_r of 0.43% K^{-1}, and a ^1E peak shift S_a of 0.022 nm °C^{-1}.[9] Compared to Entries 1 and 2, the single intensity and *LIR* readout methods between 10 to 70°C have S_r values far lower than the S_r values of both $Sr_5(V_{0.97}O_4)_3Cl:Mn_{0.03}$ and $Ba_5(V_{0.97}O_4)_3Cl:Mn_{0.03}$ at similar physiological temperatures. Additionally, the δT of the apatite thermometers readout methods is lower than that of the reported δT from the total intensity of the ^1E emission of Mn^{5+} doped $Ba_3(PO_4)_2$.

$Ba_5(PO_4)_3OH$: Mn^{5+} (Entry 6) has a single emission intensity S_r of 0.81% K^{-1}, an *LIR* S_r of the ^1E emission and Mn–O vibrational peak of 0.34% K^{-1}, and a band-shift S_r of 0.51% K^{-1}.[9] However, the temperature of maximal S_r was not noted, and δT was not calculated for any readout method. Compared to isostructural Entries 1 and 2, the *LIR* and single emission intensity readout methods gave S_r values lower than that of $Sr_5(V_{0.97}O_4)_3Cl:Mn_{0.03}$ and $Ba_5(V_{0.97}O_4)_3Cl:Mn_{0.03}$. The band-shift value was reported as S_r, which due to its arbitrary nature, cannot be correctly compared unlike S_a for band-shift data. Both the low value of the single emission intensity S_r and the *LIR* S_r may be due to only part of the split ^1E peak being integrated for sensitivity calculations.

A series of 1.0% Mn^{5+}, *x*% Er^{3+}-doped $Ba_3(VO_4)_2$ (x = 0.1, 0.2, 0.5, 1.0, 1.2) phosphors (Entry 7) were studied as lifetime thermometers monitoring the lifetime of the ^1E state of Mn^{5+}.[18] The best S_r (for x = 0.5) was 1.19% K^{-1} at 443 K with a biologically relevant S_r of 0.5% K^{-1} alongside a δT of 0.026 K at 303 K. The best performing phosphor – 1.0% Mn^{5+}, 0.5% Er^{3+}-doped $Ba_3(VO_4)_2$ – gave an S_r value approximately a quarter of that of $Sr_5(V_{0.97}O_4)_3Cl{:}Mn_{0.03}$ and $Ba_5(V_{0.97}O_4)_3Cl{:}Mn_{0.03}$ at physiological temperatures. However, the δT of the lifetime measurement was the lowest of any Mn^{5+}-doped luminescence thermometer in the literature at physiological temperature, and lower than all the readout δT of both Entries 1 and 2, with only bandwidth and MLR readouts of $Sr_5(V_{0.97}O_4)_3Cl{:}Mn_{0.03}$ having slightly higher values.

A range of 1.0% Mn^{5+}, *x*% Nd^{3+} dual-doped $Ba_3(VO_4)_2$ phosphors (x = 0.1, 0.2, 0.5, 1.0, 2.0, 5.0) (Entry 8) were investigated as *LIR* thermometers using the Mn^{5+} $^1E \rightarrow {}^3A_2$ and Nd^{3+} $^4F_{3/2} \rightarrow {}^4I_{11/2}$ transitions (Figure 18).[21] The maximum S_r value for $Ba_3(VO_4)_2$:0.1 Mn^{5+}, 0.5 Nd^{3+} was 0.94% K^{-1} at 453 K, with $Ba_3(VO_4)_2$:0.1 Mn^{5+}, 0.2% Nd^{3+} giving the best S_r at physiological temperature of 0.69% K^{-1}. When compared to Entries 1 and 2, the S_r at physiological temperatures of the best performing phosphor is one-third the value of both $Sr_5(V_{0.97}O_4)_3Cl{:}Mn_{0.03}$ and $Ba_5(V_{0.97}O_4)_3Cl{:}Mn_{0.03}$ *LIR* S_r.

The luminescence lifetime thermometers $Sr_3(VO_4)_2$ (Entry 9) and $Ba_3(VO_4)_2$ (Entry 10), doped with 0.01% Mn^{5+} gave ^1E state lifetime S_r values of 1.00% K^{-1} at 443 K and 0.93% K^{-1} at 469 K respectively, and S_r values of 0.5% K^{-1} and 0.4% K^{-1} at 310 K, respectively.[20] When compared to Entries 1 and 2, the maximum S_r of the $Sr_3(VO_4)_2$ and $Ba_3(VO_4)_2$ lifetime thermometers are approximately half that of the $Sr_5(V_{0.97}O_4)_3Cl{:}Mn_{0.03}$ and $Ba_5(V_{0.97}O_4)_3Cl{:}Mn_{0.03}$ *LIR* thermometers, whilst occurring at above physiological temperatures. At physiological temperature, the S_r values of the $Sr_3(VO_4)_2$ and $Ba_3(VO_4)_2$ phosphors are approximately a quarter of those given by Entries 1 and 2.

To compare, the materials presented (Entries 1 and 2) were synthesised via sol-gel reaction requiring one pre-calcination step at 250°C and a single heating at 750°C. This low temperature heating compared to the heating temperatures used in the other synthetic methods (Table 5.4) is advantageous for energy saving, suppressing the loss of volatile Cl^- reagent, and reducing agglomeration of crystallites into larger particle sizes caused by multiple high temperature heatings. Both $Sr_5(V_{0.97}O_4)_3Cl:Mn_{0.03}$ and $Ba_5(V_{0.97}O_4)_3Cl:Mn_{0.03}$ materials demonstrated a *LIR* S_r using the $^3T_2$ and ^1E emission peaks of over 2.00% K^{-1} at 308 K, with an MLR S_r of 3.14% K^{-1} for $Sr_5(V_{0.97}O_4)_3Cl:Mn_{0.03}$, alongside all readout parameters giving $\delta T < 0.65$ K across their investigated temperature ranges. At the time of writing, the new materials presented in this chapter show the largest *LIR* and MLR S_r values among the reported Mn^{5+}-containing luminescence thermometers within the biologically relevant temperature range emitting in BW-2.

5.4.2. Comparison with other luminescence thermometers emitting in the biological windows

Table 5.5: Comparison table of BW-1-3 luminescence thermometers, their readout methods, and their figures of merit. Orange cells denote materials reported in this chapter.

Entry	**Material**	**Dopant**	**Synthesis route (Temp, °C)**	**Readout**	**Max Sr (% K^{-1})**	**Temp. Res (K)**	**Temp (K)**	**Ref**
1	$Sr_5(VO_4)_3Cl$	Mn^{5+}	Sol-gel, 750	LIR	2.23	0.16	308	This Work
				Band-shift	$S_a = 0.08\ cm^{-1}\ K^{-1}$	0.05	308	
				Bandwidth	0.35	0.04	373	
				MLR	3.14	0.042	308	
2	$Ba_5(VO_4)_3Cl$	Mn^{5+}	Sol-gel, 750	LIR	2.20	0.34	298	This Work
				Band-shift	$S_a = 0.10\ cm^{-1}\ K^{-1}$	0.35	373	
				Bandwidth	0.41	0.07	373	
3	YAG	Yb^{3+}, Er^{3+}	Pechini, 1100	LIR	1.0	N/A	163	70
				LIR	0.73	N/A	83	
				Band-shift	$S_a = 0.09\ cm^{-1}\ K^{-1}$	N/A	575	
				Bandwidth	0.40	N/A	249	
				Lifetime	0.73	N/A	154	
4	YAG	Yb^{3+}, Er^{3+}	Pechini, 1100	LIR	1.0	N/A	163	70
				LIR	0.80	N/A	83	
				Band-shift	$S_a = 0.08\ cm^{-1}\ K^{-1}$	N/A	575	
				Bandwidth	0.46	N/A	201	
				Lifetime	0.86	N/A	156	
5	LaF_3	Nd^{3+}	Co-precipitation, RT	LIR	0.1	2	283 - 343	71
				Band-shift	$S_a = 0.10\ cm^{-1}\ K^{-1}$	2	283 - 343	
6	YVO_4	Nd^{3+}	Pechini, 950	LIR	0.54	0.1	303	72
				Band-shift	$S_a = 0.75\ cm^{-1}\ K^{-1}$	17	303	
				Bandwidth	0.14	3	298	
7	$CaAl_2O_4$	Co^{3+}, Nd^{3+}	Pechini, 850-1100	LIR	1.43	~0.1	303	73
				Lifetime	2.36	N/A	349	
8	Ag_2S	N/A	Not provided	Single Int.	5.0	N/A	298	46
				LIR	1.4	N/A	298	
				Band-shift	$S_a = 1.65\ nm\ C^{-1}$	N/A	298	

Yttrium aluminium garnet (YAG) doped with Yb^{3+} and Er^{3+} was investigated with 10%Yb^{3+} each, and 1%Er^{3+} (Entry 3) and 2% Er^{3+} (Entry 4) respectively.[70] Two different *LIR* readouts – the Stark sublevels for $^4I_{13/2}$ and $^4I_{15/2}$ of Er^{3+}, and between the $^2F_{5/2} \rightarrow {}^2F_{7/2}$ transition of Yb^{3+} and $^4I_{13/2} \rightarrow {}^4I_{15/2}$ transition of Er^{3+}– were investigated, alongside band-shift, FWHM and lifetime of the Nd^{3+} transition. Figure 5.15 shows the relevant transitions for both dopants. For all five readout methods reported, no δT values were given.

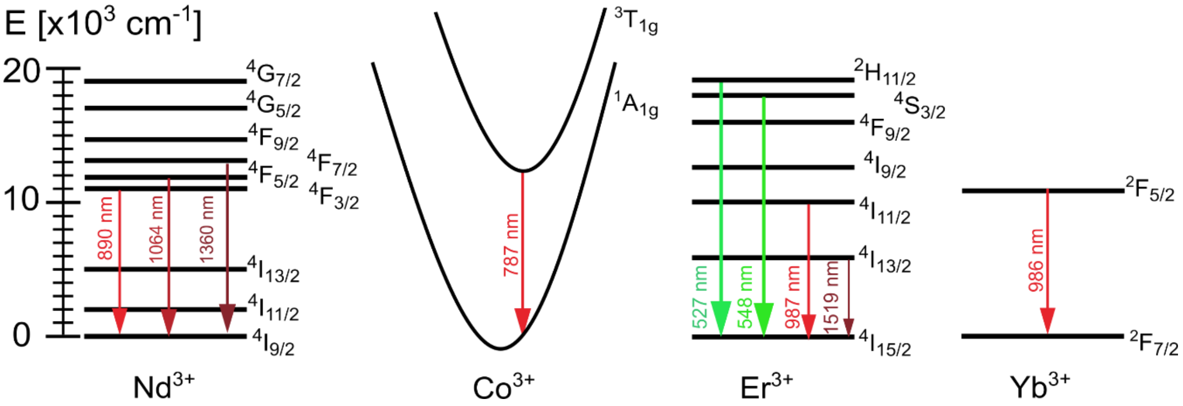

Figure 5.15: Energy level and coordinate configuration diagrams for Ln^{3+} and TM ions of luminescence thermometer dopants reported in Table 5.5.

For YAG:10%Yb^{3+}, 1%Er^{3+} (Entry 3), the *LIR* Sr values were of 1.0% K^{-1} at 163 K (0.3% K^{-1} at physiological temperature), and 0.73% K^{-1} at 83 K respectively. The S_r of the band-shift, FWHM and lifetime of the Nd^{3+} transition were S_a = 0.09 cm^{-1} K^{-1} at 575 K, 0.40% K^{-1} at 249 K, and 0.73% K^{-1} at 154 K respectively. The S_r value of both *LIR* readouts, the bandwidth and lifetime for YAG:10%Yb^{3+}, 1%Er^{3+} all show lower values than those of the readout methods for both $Sr_5(V_{0.97}O_4)_3Cl:Mn_{0.03}$ and $Ba_5(V_{0.97}O_4)_3Cl:Mn_{0.03}$ with their maximum values also only occurring at below physiological temperatures. Whilst the S_a of the band-shift is comparable to both Entries 1 and 2, this only occurred for YAG:10%Yb^{3+}, 1%Er^{3+} at non-physiological temperatures.

For YAG:10%Yb^{3+}, 2%Er^{3+} (Entry 4), the *LIR* S_r were 1.0% K^{-1} at 163 K (0.3% K^{-1} at physiological temperature), and 0.80% K^{-1} at 83 K respectively. The S_r of the band-shift, FWHM, and luminescence lifetime were 0.08 cm^{-1} K^{-1} at 575 K, 0.86% K^{-1} at 210 K, and 0.46% K^{-1} at 156 K respectively. Similar to Entry 3, the S_r value of both *LIR* readouts, the bandwidth and lifetime for YAG:10%Yb^{3+}, 2%Er^{3+} all show lower values than those of the readout methods for both $Sr_5(V_{0.97}O_4)_3Cl:Mn_{0.03}$ and $Ba_5(V_{0.97}O_4)_3Cl:Mn_{0.03}$ with their maximum values also only occurring at below physiological temperatures. Whilst the S_a of the band-shift is comparable to both Entries 1 and 2, this only occurred for YAG:10%Yb^{3+}, 1%Er^{3+} at non-physiological temperatures.

LaF_3:Nd^{3+} core-shell nanoparticles (Entry 5) gave a low LIR S_r of 0.1% K^{-1} using the ratio of the Stark splitting of the $^4F_{3/2}$ to $^4I_{9/2}$ transition band (emission peaks at 863 nm and 885 nm), and a band-shift of the 863 nm peak of S_a of 0.10 cm^{-1} K^{-1} in the physiological temperature range.[71] Both readouts gave low δT of 2 K. Whilst the *LIR* and MLR S_r values of both Entries 1 and 2 are greater than that of LaF_3:Nd^{3+}, the band-shift S_a is comparable to both $Sr_5(V_{0.97}O_4)_3Cl$:$Mn_{0.03}$ and $Ba_5(V_{0.97}O_4)_3Cl$:$Mn_{0.03}$ thermometers. δT values for both the LaF_3:Nd^{3+} readout methods were markedly high in comparison to both $Sr_5(V_{0.97}O_4)_3Cl$:$Mn_{0.03}$ and $Ba_5(V_{0.97}O_4)_3Cl$:$Mn_{0.03}$, indicating poor δT.

YVO_4:Nd^{3+} (Entry 6) used the Nd^{3+} $^4F_{3/2}$ to $^4I_{11/2}$ transition (Figure 5.15) for *LIR* of the 1063.9 nm and 1065.3 nm emission lines, band-shift, and FWHM.[72,74] Maximum S_r values were 0.54% K^{-1} at 303 K, 0.75% K^{-1} at 303 K, and 0.14% K^{-1} at 298 K. δT was given for 313 K as 0.1 K, 17 K, and 3 K respectively. When compared to Entries 1 and 2, all S_r values were lower than S_r values reported by the $Sr_5(V_{0.97}O_4)_3Cl$:$Mn_{0.03}$ and $Ba_5(V_{0.97}O_4)_3Cl$:$Mn_{0.03}$ thermometers. Additionally, only the *LIR* δT reported for YVO_4:Nd^{3+} had a similar value to those of the $Sr_5(V_{0.97}O_4)_3Cl$:$Mn_{0.03}$ readout methods, and the $Ba_5(V_{0.97}O_4)_3Cl$:$Mn_{0.03}$ band-shift and bandwidth readout methods.

$CaAl_2O_4$: 0.02% Co^{3+}, 5% Nd^{3+} (Entry 7) gave a maximum *LIR* S_r for the 1000°C annealed sample using the $^3T_{1g} \rightarrow {}^1A_{1g}$ transition of Co^{3+} and the $^4F_{3/2} \rightarrow {}^4I_{9/2}$ transition of Nd^{3+} (Figure 5.15) of 1.43 % K^{-1} at 303 K with a δT of under 0.1 K. Maximum lifetime S_r was calculated for the 1100°C annealed sample with S_r = 2.36 % K^{-1} at 349 K. Whilst the *LIR* S_r of 1000°C synthesised $CaAl_2O_4$: 0.02% Co^{3+}, 5% Nd^{3+} was lower than the S_r values reported for all readout methods for $Sr_5(V_{0.97}O_4)_3Cl$:$Mn_{0.03}$ and $Ba_5(V_{0.97}O_4)_3Cl$:$Mn_{0.03}$, the maximum lifetime S_r for 1100°C synthesised $CaAl_2O_4$: 0.02% Co^{3+}, 5% Nd^{3+} was higher than the *LIR* S_r of both $Sr_5(V_{0.97}O_4)_3Cl$:$Mn_{0.03}$ and $Ba_5(V_{0.97}O_4)_3Cl$:$Mn_{0.03}$, with only $Sr_5(V_{0.97}O_4)_3Cl$:$Mn_{0.03}$ S_r for MLR thermometry being greater. The maximum S_r for the lifetime readout was also only achieved above physiological temperatures, unlike both $Sr_5(V_{0.97}O_4)_3Cl$:$Mn_{0.03}$ and $Ba_5(V_{0.97}O_4)_3Cl$:$Mn_{0.03}$.

Ag_2S-PEG nanoparticles (Entry 8) demonstrated single emission intensity S_r of the broadband centred at 1225 nm of ~5% K^{-1}, the LIR of peaks 1225 nm and 1175 nm of 1.4% K^{-1}, and the band-shift of the broadband gave a S_a of 1.65 nm $°C^{-1}$. No δT were presented for any Ag_2S-PEG readout method. When compared to Entries 1 and 2, the single emission intensity S_r is markedly higher than both apatite materials' *LIR* S_r values and the S_r value of $Sr_5(V_{0.97}O_4)_3Cl:Mn_{0.03}$ MLR readout method. The S_r of the *LIR* readout method, however, is lower than all S_r values for all $Sr_5(V_{0.97}O_4)_3Cl:Mn_{0.03}$ and $Ba_5(V_{0.97}O_4)_3Cl:Mn_{0.03}$ readout methods. Comparison of the S_a for band-shift was given as both wavelength (1.65 nm $°C^{-1}$) and energy (-1.3 meV $°C^{-1}$) which when converted to wavenumber gives a value of 10.5 cm^{-1} $°C^{-1}$, a near 100-fold increase on the band-shift S_a of both Entries 1 and 2.

For a general comparison against the selected BW-1-3 thermometers, only the core-shell co-precipitation method had a lower synthesis temperature (room temperature) than the apatite sol-gel synthetic route of 750°C. Both $Sr_5(V_{0.97}O_4)_3Cl:Mn_{0.03}$ and $Ba_5(V_{0.97}O_4)_3Cl:Mn_{0.03}$ materials (Entries 1 and 2) demonstrated a *LIR* S_r of over 2% K^{-1} at 308 K, with all three readout parameters giving $\delta T < 0.65$ K across their investigated temperature range. When compared to the multiparametric thermometers in Table 5.4, only the *LIR* S_r of Ag_2S is higher than both $Sr_5(V_{0.97}O_4)_3Cl:Mn_{0.03}$ and $Ba_5(V_{0.97}O_4)_3Cl:Mn_{0.03}$ *LIR* S_r and $Sr_5(V_{0.97}O_4)_3Cl:Mn_{0.03}$ MLR S_r, whilst the highest lifetime S_r of $CaAl_2O_4$: Co^{3+}, Nd^{3+} has a similar value around physiological temperature. $Sr_5(V_{0.97}O_4)_3Cl:Mn_{0.03}$ showed a particularly high δT (below 0.16 K) across all three readout methods. Whilst both $Sr_5(V_{0.97}O_4)_3Cl:Mn_{0.03}$ and $Ba_5(V_{0.97}O_4)_3Cl:Mn_{0.03}$ showed low bandwidth S_r values when compared to bandwidth readouts of the multiparametric thermometers in Table 5.4, the bandwidth δT is the highest across all readout methods particularly at physiological temperatures. Similarly, whilst the band-shift S_a of $Sr_5(V_{0.97}O_4)_3Cl:Mn_{0.03}$ is small compared to the multi-readout comparisons, it shows an excellent δT of 0.05 K at 308 K. The ability to use multiple readouts allows for increased reliability by self-calibration and increased precision in measurement, which is particularly important for potential bio-thermometry application, giving the presented Mn^{5+}-based apatite thermometers increased appeal.[46]

5.5. Conclusion and future work

$Sr_5(V_{0.97}O_4)_3Cl:Mn_{0.03}$ and $Ba_5(V_{0.97}O_4)_3Cl:Mn_{0.03}$ have been successfully synthesised by sol-gel synthesis and characterised by PXRD. The chlorapatite host materials were proven to be thermally stable between the temperatures of 30 and 150°C through VT-PXRD. Local structure probed by ^{51}V ssNMR revealed the influence of the Mn^{5+} ions on the V^{5+} tetrahedral environment. The Mn^{5+}-doped phosphors were shown to be excitable between 500 and 1000 nm, allowing for a wide choice of excitation wavelengths across BW-1 and BW-2 as well as a narrow BW-2 emission, particularly useful for deeper skin penetration. The high QY value of 47% and 51% coupled with the wide absorption bands of the Mn^{5+} ions make both $Sr_5(V_{0.97}O_4)_3Cl:Mn_{0.03}$ and $Ba_5(V_{0.97}O_4)_3Cl:Mn_{0.03}$ bright NIR phosphors. *LIR*, band-shift, and bandwidth, luminescence thermometry were explored for both $Sr_5(V_{0.97}O_4)_3Cl:Mn_{0.03}$ and $Ba_5(V_{0.97}O_4)_3Cl:Mn_{0.03}$ with S_r values of 2.23% K^{-1}, S_a = 0.08 cm^{-1} K^{-1}, and 0.35% K^{-1} at 308 K obtained for $Sr_5(V_{0.97}O_4)_3Cl:Mn_{0.03}$, and 2.06% K^{-1}, S_a = 0.01 cm^{-1} K^{-1} and 0.29% K^{-1} for $Ba_5(V_{0.97}O_4)_3Cl:Mn_{0.03}$ respectively. Most importantly, the δT values for the readout methods were calculated to be 0.15 K, 0.05 K, and 0.04 K for $Sr_5(V_{0.97}O_4)_3Cl:Mn_{0.03}$, and 0.34 K, 0.35 K, and 0.07 K for $Ba_5(V_{0.97}O_4)_3Cl:Mn_{0.03}$ respectively. Multiparametric luminescence thermometry using MLR was carried out using $Sr_5(V_{0.97}O_4)_3Cl:Mn_{0.03}$ and gave an excellent S_r of 3.14% K^{-1} at 308 K, alongside a great δT of 0.042 K. The high quantum yield, excellent S_r values of the *LIR* and MLR readout methods, and high δT of the band-shift, bandwidth, and MLR readouts demonstrate that both materials have great potential as NIR luminescence thermometers operating within a range of physiological temperatures.

Further improvement to these materials may be possible by preparing these materials in nanoparticle form, and comparing their performance to other nanoparticle luminescence thermometers. [6,75,76] Co-synthesising a Mn^{5+}-containing phosphor with Bi_2O_3, or by substituting Bi^{3+} at the A cation site for improved brightness through increasing emission intensity and biocompatibility has been previously explored in literature through stabilisation of the Mn^{5+} ion increasing the absorption of NIR excitation light, but has yet to be investigated for improvements to a Mn^{5+}-doped luminescence thermometer.[77] Co-synthesis of $Sr_5(V_{0.97}O_4)_3Cl:Mn_{0.03}$ with Bi_2O_3 may further enhance the already excellent brightness of the phosphor through the stabilisation of the Mn^{5+} ion, further increasing the QY of the $Sr_5(V_{0.97}O_4)_3Cl:Mn_{0.03}$ phosphor. Doping the apatite A site with a Ln^{3+} ion for dual-emission *LIR* thermometry could be investigated, as similar research has been undertaken using the Mn^{5+}-doped host material $Ba_3(VO_4)_2$ and Nd^{3+}.[21] The small splitting of the narrow ^1E emission peak of Mn^{5+} could be investigated for cryogenic *LIR* thermometry, as similarly small energy gaps for split TM emission peaks such as the R-lines of Cr^{3+} have been investigated and found to give high S_r values at such low temperature.[78,79] As mentioned in the introduction, Mn^{5+} doped materials have recently been extensively studied as potential green-blue pigments. All solid-state and sol-gel synthesised materials mentioned in this chapter showed varying shades of blue, depending on their synthetic route, the identity of A^{2+} cation (A^{2+} = Sr^{2+} or Ba^{2+}), and Mn^{5+} doping concentration. Applications as a pigment could allow for further investigation into how the identity of the T cation and X anion of the apatite material affects its colour when doped with Mn^{5+}.

Additional Mn^{5+}-doped materials can be pursued using hosts such as isostructural $A_5(PO_4)_3Cl$ phosphate apatites, or spodiosite-type materials with formula $A_2(VO_4)Cl$. The spodiosite structure in orthorhombic space group *Pbcm*, contains isolated tetrahedral sites able to stabilise Mn^{5+} and has been previously investigated as a NIR laser material, and as a host for solid-state lighting.[38,80,81] Of note is the sigmoidal lifetime dependence of the Mn^{5+} ^1E state in $Ca_2(VO_4)Cl$ between the temperatures of 10 K (0.41 ms) and 300 K (~0.04 ms).[62] Such a large decline in the excited states lifetime with increasing temperature makes Mn^{5+} doped $Ca_2(VO_4)Cl$ a candidate for lifetime thermometry with the potential of a high S_r value. Additionally, a Mn^{5+}-doped spodiosite host could be investigated for *LIR*, band-shift, and bandwidth thermometry allowing for MLR to be an optional readout method should linear dependencies be found or able to be inferred across the selected temperature range. Spodiosite Mn^{5+} emission also shows a larger splitting of the ^1E emission than that of apatite materials due to the tetrahedral distortion being C_2, not C_s like apatite, allowing for the possibility of using the split ^1E peak for *LIR* thermometry to be investigated, with high S_r at non-ambient and non-cryogenic temperatures.[38]

5.6. References

1 E. C. Ximendes, W. Q. Santos, U. Rocha, U. K. Kagola, F. Sanz-Rodríguez, N. Fernández, A. da S. Gouveia-Neto, D. Bravo, A. M. Domingo, B. del Rosal, C. D. S. Brites, L. D. Carlos, D. Jaque and C. Jacinto, *Nano Lett.*, 2016, **16**, 1695–1703.

2 L. Aigouy, G. Tessier, M. Mortier and B. Charlot, *Appl. Phys. Lett.*, 2005, **87**, 184105.

3 R. G. Geitenbeek, J. C. Vollenbroek, H. M. H. Weijgertze, C. B. M. Tregouet, A.-E. Nieuwelink, C. L. Kennedy, B. M. Weckhuysen, D. Lohse, A. van Blaaderen, A. van den Berg, M. Odijk and A. Meijerink, *Lab. Chip*, 2019, **19**, 1236–1246.

4 R. R. Anderson and J. A. Parrish, *J. Invest. Dermatol.*, 1981, **77**, 13–19.

5 A. N. Bashkatov, E. A. Genina, V. I. Kochubey and V. V. Tuchin, *J. Phys. Appl. Phys.*, 2005, **38**, 2543–2555.

6 C. Matuszewska and L. Marciniak, *J. Lumin.*, 2020, **223**, 117221.

7 C. Matuszewska, K. Elzbieciak-Piecka and L. Marciniak, *J. Phys. Chem. C*, 2019, **123**, 18646–18653.

8 X. Chen, S. Liu, K. Huang, J. Nie, R. Kang, X. Tian, S. Zhang, Y. Li and J. Qiu, *Chem. Eng. J.*, 2020, **396**, 125201.

9 P. M. Gschwend, D. Niedbalka, L. R. H. Gerken, I. K. Herrmann and S. E. Pratsinis, *Adv. Sci.*, 2020, **7**, 2000370.

10 M. Dramicanin, *Luminescence Thermometry: Methods, Materials, and Applications*, Elsevier Science & Technology, Duxford, United Kingdom, 2018.

11 M. Weller, T. Overton, J. Rourke and F. Armstrong, Oxford University Press, 6th edn., 2014, pp. 542–543.

12 L. D. Merkle, A. Pinto, H. R. Verdún and B. McIntosh, *Appl. Phys. Lett.*, 1992, **61**, 2386–2388.

13 L. D. Merkle, Y. Guyot and B. H. T. Chai, *J. Appl. Phys.*, 1995, **77**, 474–480.

14 M. A. Scott, D. L. Russell, B. Henderson, T. P. J. Han and H. G. Gallagher, *J. Cryst. Growth*, 1998, **183**, 366–376.

15 S. Laha, S. Tamilarasan, S. Natarajan and J. Gopalakrishnan, *Inorg. Chem.*, 2016, **55**, 3508–3514.

16 S. Laha, R. Sharma, S. V. Bhat, M. L. P. Reddy, J. Gopalakrishnan and S. Natarajan, *Bull. Mater. Sci.*, 2011, **34**, 1257–1262.

17 M. D. Dramićanin, Ł. Marciniak, S. Kuzman, W. Piotrowski, Z. Ristić, J. Periša, I. Evans, J. Mitrić, V. Đorđević, N. Romčević, M. G. Brik and C.-G. Ma, *Light Sci. Appl.*, 2022, **11**, 279.

18 W. M. Piotrowski, R. Marin, M. Szymczak, E. Martín Rodríguez, D. H. Ortgies, P. Rodríguez-Sevilla, M. D. Dramićanin, D. Jaque and L. Marciniak, *Adv. Opt. Mater.*, 2022, **11**, 2202366.

19 T. A. Alrebdi, A. N. Alodhayb, Z. Ristić and M. D. Dramićanin, *Sensors*, 2023, **23**, 3839.

20 Z. Ristić, W. Piotrowski, M. Medić, J. Periša, Ž. M. Antić, L. Marciniak and M. D. Dramićanin, *ACS Appl. Electron. Mater.*, 2022, **4**, 1057–1062.

21 W. M. Piotrowski, R. Marin, M. Szymczak, E. M. Rodríguez, D. H. Ortgies, P. Rodríguez-Sevilla, P. Bolek, M. D. Dramićanin, D. Jaque and L. Marciniak, *J. Mater. Chem. C*, 2023, **11**, 6713–6723.

22 S. Von Euw, Y. Wang, G. Laurent, C. Drouet, F. Babonneau, N. Nassif and T. Azaïs, *Sci. Rep.*, 2019, **9**, 8456.

23 L. Mei, H. Liu, L. Liao, Y. Zhang and R. V. Kumar, *Sci. Rep.*, 2017, **7**, 15171.

24 M. M. Rodríguez-García, J. A. G. Williams and I. R. Evans, *J. Mater. Chem. C*, 2019, **7**, 7779–7787.

25 E. Kendrick, M. S. Islam and P. R. Slater, *J. Mater. Chem.*, 2007, **17**, 3104–3111.

26 P. M. Panchmatia, A. Orera, G. J. Rees, M. E. Smith, J. V. Hanna, P. R. Slater and M. S. Islam, *Angew. Chem. Int. Ed.*, 2011, **50**, 9328–9333.

27 M. L. Tate, D. A. Blom, M. Avdeev, H. E. A. Brand, G. J. McIntyre, T. Vogt and I. R. Evans, *Adv. Funct. Mater.*, 2017, **27**, 1605625.

28 M. S. Chambers, P. A. Chater, I. R. Evans and J. S. O. Evans, *Inorg. Chem.*, 2019, **58**, 14853–14862.

29 C. A. Fuller, M. J. Gutmann, C. D. Ling, C.-H. Wang, W. Zhang, P. S. Halasyamani, I. R. Evans and J. S. O. Evans, *J. Mater. Chem. A*, 2022, **10**, 14576–14584.

30 T. J. White and D. ZhiLi, *Acta Crystallogr. B*, 2003, **59**, 1–16.

31 S. S. Pramana, T. J. White, M. K. Schreyer, C. Ferraris, P. R. Slater, A. Orera, T. J. Bastow, S. Mangold, S. Doyle, T. Liu, A. Fajar, M. Srinivasan and T. Baikie, *Dalton Trans.*, 2009, 8280–8291.

32 R. D. Shannon, *Acta Cryst. A*, 1976, **32**, 751–767.

33 G. Gouget, M. Pellerin, L. Pautrot-D’Alençon, T. L. Mercier and C. B. Murray, *Chem. Commun.*, 2020, **56**, 3429–3432.

34 T. Konishi, M. Shimizu, Y. Kameyama and K. Soga, *J. Mater. Sci. Mater. Electron.*, 2007, **18**, 183–186.

35 C. Renero-Lecuna, A. Herrero, D. Jimenez de Aberasturi, M. Martínez-Flórez, R. Valiente, M. Mychinko, S. Bals and L. M. Liz-Marzán, *J. Phys. Chem. C*, 2021, **125**, 19887–19896.

36 X. Zhang, F. Zhou, J. Shi and M. Gong, *Mater. Lett.*, 2009, **63**, 852–854.

37 P.-P. Dai, C. Li, X.-T. Zhang, J. Xu, X. Chen, X.-L. Wang, Y. Jia, X. Wang and Y.-C. Liu, *Light Sci. Appl.*, 2016, **5**, e16024.

38 J. A. Capobianco, G. Cormier, R. Moncorgé, H. Manaa and M. Bettinelli, *Appl. Phys. Lett.*, 1992, **60**, 163–165.

39 P. Li, Z. Wang, Z. Yang and Q. Guo, *Opt. Commun.*, 2014, **332**, 83–88.

40 D. Gao, X. Zhang and J. Zhang, *CrystEngComm*, 2014, **16**, 11115–11121.

41 M. Pokhrel, S. K. Gupta, A. Perez, B. Modak, P. Modak, L. A. Lewis and Y. Mao, *ACS Appl. Nano Mater.*, 2021, **4**, 13562–13572.

42 H. Suo, C. Guo, J. Zheng, B. Zhou, C. Ma, X. Zhao, T. Li, P. Guo and E. M. Goldys, *ACS Appl. Mater. Interfaces*, 2016, **8**, 30312–30319.

43 V. Mykhaylyk, H. Kraus, Y. Zhydachevskyy, V. Tsiumra, A. Luchechko, A. Wagner and A. Suchocki, *Sensors*, 2020, **20**, 5259.

44 Z. Cai, S. Kang, X. Huang, X. Song, X. Xiao, J. Qiu and G. Dong, *J. Mater. Chem. C*, 2018, **6**, 9932–9940.

45 F. E. Maturi, C. D. S. Brites, E. C. Ximendes, C. Mills, B. Olsen, D. Jaque, S. J. L. Ribeiro and L. D. Carlos, *Laser Photonics Rev.*, 2021, **15**, 2100301.

46 Y. Shen, H. D. A. Santos, E. C. Ximendes, J. Lifante, A. Sanz-Portilla, L. Monge, N. Fernández, I. Chaves-Coira, C. Jacinto, C. D. S. Brites, L. D. Carlos, A. Benayas, M. C. Iglesias-de la Cruz and D. Jaque, *Adv. Funct. Mater.*, 2020, **30**, 2002730.

47 A. Krimovs, Masters Thesis, Durham University, 2022.

48 M. Azdouz, B. Manoun, R. Essehli, M. Azrour, L. Bih, S. Benmokhtar, A. A. Hou and P. Lazor, *J. Alloys Compd.*, 2010, **498**, 42–51.

49 M. E. Leonowicz, K. R. Poeppelmeier and J. M. Longo, *J. Solid State Chem.*, 1985, **59**, 71–80.

50 E. A. Medina, J. Li, J. K. Stalick and M. A. Subramanian, *Solid State Sci.*, 2016, **52**, 97–105.

51 A. A. Coelho, J. Evans, I. Evans, A. Kern and S. Parsons, *Powder Diffr.*, 2011, **26**, S22–S25.

52 H. M. Rietveld, *J. Appl. Crystallogr.*, 1969, **2**, 65–71.

53 R. K. Harris, E. D. Becker, S. M. Cabral De Menezes, P. Granger, R. E. Hoffman and K. W. Zilm, *Solid State Nucl. Magn. Reson.*, 2008, **33**, 41–56.

54 D. Massiot, F. Fayon, M. Capron, I. King, S. Le Calvé, B. Alonso, J.-O. Durand, B. Bujoli, Z. Gan and G. Hoatson, *Magn. Reson. Chem.*, 2002, **40**, 70–76.

55 A. Ćirić, S. Stojadinović and M. D. Dramićanin, *Meas. Sci. Technol.*, 2019, **30**, 045001.

56 D. Zagorac, H. Müller, S. Ruehl, J. Zagorac and S. Rehme, *J. Appl. Crystallogr.*, 2019, **52**, 918–925.

57 H. P. Beck, M. Douiheche, R. Haberkorn and H. Kohlmann, *Solid State Sci.*, 2006, **8**, 64–70.

58 A. V. Knyazev, N. G. Chernorukov and E. N. Bulanov, *Mater. Chem. Phys.*, 2012, **132**, 773–781.

59 M. M. Rodríguez-García, A. Ciric, Z. Ristic, J. A. G. Williams, M. D. Dramićanin and I. R. Evans, *J. Mater. Chem. C,* 2021, **9**, 7474–7484.

60 Y. Fang, S. J. Page, G. J. Rees, M. Avdeev, J. V. Hanna and T. J. White, *Inorg. Chem.*, 2018, **57**, 9122–9132.

61 A. Bielecki and D. P. Burum, *J. Magn. Reson. A*, 1995, **116**, 215–220.

62 M. Herren, H. U. Guedel, C. Albrecht and D. Reinen, *Chem. Phys. Lett.*, 1991, **183**, 98–102.

63 Y. Tanabe and S. Sugano, *J. Phys. Soc. Jpn.*, 1954, **9**, 766–779.

64 Y. Tanabe and S. Sugano, *J. Phys. Soc. Jpn.*, 1954, **9**, 753–766.

65 Tanabe-Sugano Diagrams, https://chem.libretexts.org/Bookshelves/Inorganic_Chemistry/Supplemental_Modules_and_Websites_(Inorganic_Chemistry)/Crystal_Field_Theory/Tanabe-Sugano_Diagrams, (accessed 30 June 2021).

66 K. Dardenne, D. Vivien and D. Huguenin, *J. Solid State Chem.*, 1999, **146**, 464–472.

67 X. Zhang, J. Nie, S. Liu and J. Qiu, *J. Mater. Sci. Mater. Electron.*, 2018, **29**, 6419–6427.

68 U. Oetliker, M. Herren, H. U. Güdel, U. Kesper, C. Albrecht and D. Reinen, *J. Chem. Phys.*, 1994, **100**, 8656–8665.

69 V. Rajendran, K.-C. Chen, W.-T. Huang, N. Majewska, T. Leśniewski, M. Grzegorczyk, S. Mahlik, G. Leniec, S. M. Kaczmarek, W. K. Pang, V. K. Peterson, K.-M. Lu, H. Chang and R.-S. Liu, *ACS Energy Lett.*, 2023, **1**, 289–295.

70 J. Periša, Z. Ristić, W. Piotrowski, Ž. Antić, L. Marciniak and M. D. Dramićanin, *RSC Adv.*, 2021, **11**, 15933–15942.

71 U. Rocha, C. Jacinto da Silva, W. Ferreira Silva, I. Guedes, A. Benayas, L. Martínez Maestro, M. Acosta Elias, E. Bovero, F. C. J. M. van Veggel, J. A. García Solé and D. Jaque, *ACS Nano*, 2013, **7**, 1188–1199.

72 I. E. Kolesnikov, A. A. Kalinichev, M. A. Kurochkin, E. V. Golyeva, E. Y. Kolesnikov, A. V. Kurochkin, E. Lähderanta and M. D. Mikhailov, *Sci. Rep.*, 2017, **7**, 18002.

73 K. Kniec, A. Kochanowska, L. Li, M. Suta and L. Marciniak, *J. Mater. Chem. C*, 2022, **10**, 9278–9286.

74 I. E. Kolesnikov, E. V. Golyeva, A. A. Kalinichev, M. A. Kurochkin, E. Lähderanta and M. D. Mikhailov, *Sens. Actuators B Chem.*, 2017, **243**, 338–345.

75 H. D. A. Santos, D. Ruiz, G. Lifante, C. Jacinto, B. H. Juarez and D. Jaque, *Nanoscale*, 2017, **9**, 2505–2513.

76 E. C. Ximendes, U. Rocha, T. O. Sales, N. Fernández, F. Sanz-Rodríguez, I. R. Martín, C. Jacinto and D. Jaque, *Adv. Funct. Mater.*, 2017, **27**, 1702249.

77 P. M. Gschwend, K. Keevend, M. Aellen, A. Gogos, F. Krumeich, I. K. Herrmann and S. E. Pratsinis, *J. Mater. Chem. B*, 2021, **9**, 3038–3046.

78 A. Ćirić, S. Stojadinović, Z. Ristić, Ž. Antić and M. D. Dramićanin, *Sens. Actuators Phys.*, 2021, **331**, 112987.

79 M. Back, J. Ueda, J. Xu, K. Asami, M. G. Brik and S. Tanabe, *Adv. Opt. Mater.*, 2020, **8**, 2000124.

80 V. R. Panse, A. shukla and S. J. Dhoble, *Optik*, 2017, **130**, 539–542.

81 A. Meijerink and G. Blasse, *J. Phys. Condens. Matter*, 1990, **2**, 3619–3628.

6. Conclusion and future work

This chapter summarises the work undertaken on perovskite-type $LaGaO_3$ and apatite-type $A_5(VO_4)_3Cl$ hosts doped with Cr^{3+}, Nd^{3+}, and Mn^{5+} and their characterisation as potential luminescence thermometers compatible with two biological windows.

A series of Cr^{3+}-doped $LaGa_{1-x}O_3:Cr_x$ phosphors (where $x = 0.0, 0.02, 0.05, 0.01, 0.02, 0.04$) were synthesised by the solid-state method and characterised by PXRD and Rietveld refinement. At room-temperature, all the samples emit from the ^2E state with Cr^{3+}-dependent N-lines, and Stokes and anti-Stokes peaks. Analysis of the excitation spectrum of $LaGa_{0.99}O_3:Cr_{0.01}$ indicated that the Cr^{3+} cation experiences a strong crystal field in the perovskite structure, of $Dq/B = 2.6$, agreeing with only the ^2E emission being observed at room temperature. The quantum yields of the materials were calculated and $LaGa_{0.99}O_3:Cr_{0.01}$ gave the highest value of 8%. Variable-temperature analysis of $LaGa_{0.99}O_3:Cr_{0.01}$ between 300 and 650 K was undertaken, using the lower-lying ^2E state and the higher-lying $^4T_2$ state as the *LIR* intensities. Deconvolution of the overlapping Cr^{3+} emissions allowed the ^2E emission and $^4T_2$ emission to be monitored with increasing temperature. Fitting the linearised *LIR* equation to the calculated *LIR* points gave a ΔE of 1509 cm^{-1}. S_r was calculated from the ΔE as 2.5% K^{-1} at 300 K, with a temperature resolution of 0.05 K.

Further work in this area should focus on increasing the crystal field strength experienced by the Cr^{3+} ion either by:

- using a perovskite such as $LaAlO_3$; or
- systematically doping the $LaGaO_3$ host material with a smaller cation, for instance Al^{3+}, to reduce the Cr–O distance.

Increasing the crystal field strength will increase the energy gap between the ^2E and $^4T_2$ states allowing for a higher S_r value when using Cr^{3+} emissions for a single-centre *LIR* thermometer. Secondary dopants such as Ln^{3+} ions can be introduced to allow for dual-centre LIR to be investigated. Further work on $LaGa_{0.99}O_3:Cr_{0.01}$ specifically could involve calculating figure of merit for a larger range of readout methods, such as LIR of the two R-lines for cryogenic thermometry due to their small energy gap; lifetime, band-shift, and bandwidth thermometry of the R-lines and LIR of the ^2E state with the N-lines of the Cr-Cr pairs. MLR thermometry could also be applied to multiple readout methods from $LaGa_{0.99}O_3:Cr_{0.01}$.

A series of Nd^{3+}-doped $La_{x\text{-}1}Ga_{0.99}O_3{:}Cr_{0.01}$, Nd_x phosphors (where $x = 0.05$, 0.1, and 0.2) were synthesised by the solid-state method and characterised by PXRD and Rietveld refinement. Room-temperature luminescence showed that a single wavelength of light could lead to the simultaneous emission of both the Cr^{3+} and Nd^{3+} ions. Excitation spectra of all three materials showed Nd^{3+} excitation peaks present when monitoring the ^2E Cr^{3+} emission, and broad Cr^{3+} bands when monitoring Nd^{3+} emissions – indicating energy transfer between the Cr^{3+} and Nd^{3+} ions in both directions. Lifetime studies of the materials showed a decrease in the Cr^{3+} lifetime as Nd^{3+} concentration increased from 4.2 ms ($x = 0.0$) to 2.6 ms ($x = 0.02$), and a $Cr^{3+} \rightarrow Nd^{3+}$ energy transfer efficiency of ~40%. The variable-temperature investigation of the $La_{x\ 1}Ga_{0.99}O_3{:}Cr_{0.01}{,}Nd_x$ (where $x = 0.05$, 0.1, and 0.2) revealed tha $x = 0.02$ was optimal for further investigation due to both the Cr^{3+} and the Nd^{3+} emissions having similar intensities. For $La_{0.98}Ga_{0.99}O_3{:}Cr_{0.01}{,}Nd_{0.02}$, it was found that the integrated Cr^{3+} emission (including the ^2E, $^4T_2$, Stokes, anti-Stokes, and N-lines emissions) decreases in intensity more slowly than that of the Nd^{3+} $^4F_{3/2} \rightarrow {}^4I_{9/2}$ emission band. The slower Cr^{3+} emission quenching is due to the increasing temperature promoting the Cr^{3+} ions from the ^2E state to the $^4T_2$ higher-lying state, allowing the broad $^4T_2$ band to emit but keeping the Cr^{3+} emission from quenching quickly compared to the Nd^{3+} emission. Fitting the linearised *LIR* equation to the calculated *LIR* points at each temperature, gave the ΔE as 1170 cm^{-1}, and thus the S_r was found to be 2.0% K^{-1} at 300 K with a temperature resolution of 0.04 K.

Future work on this material could involve further increasing the concentration of Nd^{3+} ions in the material until an optimum is found where Nd^{3+} emission is highest, allowing for comparison with the $x = 2.0\%$ material. As dual-emission *LIR* thermometry requires one emission that quenches rapidly with increasing temperature, the host material can be modified to increase the quenching rate of the Cr^{3+} ion by lowering the crystal field strength affecting the activator. The use of a host material such as $LaInO_3$ would lead to longer Cr–O bond lengths and thus decrease the crystal field and lower the energy barrier for thermal deactivation at the intersection of the Cr^{3+} $^4T_2$ state and the $^4A_2$ ground state. Additional readout methods could be investigated using the Cr^{3+} and Nd^{3+} emissions such as:

- *LIR* between the Cr^{3+} emission and longer wavelength $^4F_{3/2}$ to $^4I_{11/2}$ emissions for improved skin penetration for biological applications.
- band-shift of the narrow ^2E Cr^{3+} peak or $^4F_{3/2} \rightarrow {}^4I_{11/2}$ Nd^{3+} peaks.

- using the smaller energy gaps between the ^2E R-lines or the Stark splitting of the Nd^{3+} emission for cryogenic thermometry; and a combination of additional readouts for MLR thermometry.

Following exploratory solid-state synthesis of $A_5(V_{x\text{-}1}O_4)_3Cl{:}Mn_x$ (A = Ca^{2+}, Sr^{2+}, Ba^{2+}, where x = 0.00, 0.01, 0.03, 0.05), two materials – $Sr_5(V_{0.97}O_4)_3Cl{:}Mn_{0.03}$ and $Ba_5(V_{0.97}O_4)_3Cl{:}Mn_{0.03}$ – were synthesised by sol-gel synthesis and characterised by PXRD. Variable-temperature PXRD between 30 and 150°C indicated that both materials were thermally stable with no abrupt changes to unit cell parameters that would denote a phase change across the investigated temperature range. Short-range order was probed by ssNMR using ^{51}V as a proxy for the doped Mn^{5+} ions on the tetrahedral site. The ^{51}V spectra for both materials showed an additional peak not belonging to an impurity phase, posited to belong to the Mn^{5+} interacting with the V^{5+} ions. Room-temperature luminescence showed the typical Mn^{5+} absorption spectra for both materials featuring the $^3T_1(F) \leftarrow {}^3A_2$, $^3T_1(P) \leftarrow {}^3A_2$, $^3T_2 \leftarrow {}^3A_2$, $^1A_1 \leftarrow {}^3A_2$, and $^1E \leftarrow {}^3A_2$ transitions. The emission spectra for both materials showed a high intensity split ^1E emission, a low intensity $^3T_2$ emission and two distinct Mn–O vibrational peaks. The split ^1E emissions and additional peaks on the absorption band of the $^3T_1(F) \leftarrow {}^3A_2$ transition indicated a lowering of symmetry from T_d to C_S for the Mn^{5+} site. The slight red-shifting of the $Ba_5(V_{0.97}O_4)_3Cl{:}Mn_{0.03}$ emissions compared to the $Sr_5(V_{0.97}O_4)_3Cl{:}Mn_{0.03}$ was due to the increased covalency of the barium apatite compared to the strontium apatite, lowering the energy of the $Ba_5(V_{0.97}O_4)_3Cl{:}Mn_{0.03}$ ^1E state. The quantum yields of $Sr_5(V_{0.97}O_4)_3Cl{:}Mn_{0.03}$ and $Ba_5(V_{0.97}O_4)_3Cl{:}Mn_{0.03}$ were calculated as 47% and 51% respectively. Variable-temperature investigation was undertaken on both samples between 298 and 373 K in 10 K steps, with 75 spectra per step taken and averaged. *LIR* of the higher-lying ^1E emission and $^3T_2$ lower-lying gave a ΔE of 1216 cm^{-1} and 1306 cm^{-1} for $Sr_5(V_{0.97}O_4)_3Cl{:}Mn_{0.03}$ and $Ba_5(V_{0.97}O_4)_3Cl{:}Mn_{0.03}$ respectively.

S_r values for *LIR*, band-shift of the ^1E emission, and bandwidth of the ^1E emission at 308 K were:

- 2.23% K^{-1}, S_a = 0.08 cm^{-1} K^{-1}, and 0.26% K^{-1} for $Sr_5(V_{0.97}O_4)_3Cl{:}Mn_{0.03}$.
- 2.06% K^{-1}, S_a = 0.015 cm^{-1} K^{-1}, and 0.31% K^{-1} for $Ba_5(V_{0.97}O_4)_3Cl{:}Mn_{0.03}$.

Temperature resolutions were calculated as:

- 0.16 K, 0.05 K, and 0.04 K for $Sr_5(V_{0.97}O_4)_3Cl{:}Mn_{0.03}$.

- 0.36 K, 0.52 K, and 0.05 K for $Ba_5(V_{0.97}O_4)_3Cl:Mn_{0.03}$.

MLR luminescence thermometry from $Sr_5(V_{0.97}O_4)_3Cl:Mn_{0.03}$ using the three readout methods as variables gave an S_r of 3.14% K^{-1} at 308 K, with a temperature resolution of 0.042 K.

Future work for these materials would be to co-synthesise the apatite with Bi_2O_3 to improve the quantum yield further through increased stabilisation of the Mn^{5+} ion. Addition of a second luminescent dopant such as a Ln^{3+} ion or a second tetrahedral TM ion could allow for dual-emission *LIR* thermometry to be explored. Further *LIR* readouts, such as with the split ^1E peak may be useful for cryogenic thermometry due to the small ΔE between the non-degenerate ^1E emissions; or the ^1E peak, and the vibrational bands at longer wavelength can be explored. Materials such as alkaline earth phosphate-chlorapatite, spodiosite (A_2MO_4Cl, where A = Ca^{2+}, Sr^{2+} and M = V^{5+} or P^{5+}), Li_3MO_4, $BaBPO_7$, $Ba_3Al_2O_6$, $BaAl_2O_4$, and $Ba_7Al_2O_{10}$ have been explored as Mn^{5+} phosphors or lasing materials but they have not been investigated as luminescence thermometers. Synthesising these materials would allow for a suite of new Mn^{5+} luminescence thermometers to be examined.

Across Chapters 3–5, four luminescence thermometers have been successfully characterised which demonstrated high S_r and temperature resolution values. Solid-state synthesis of the perovskite materials offered a simpler method, but a higher heating temperature (1200°C) was required compared to the sol-gel method (850°C) used for the apatite materials. $Ba_5(V_{0.97}O_4)_3Cl:Mn_{0.03}$ gave the highest quantum yield of 51%, $Sr_5(V_{0.97}O_4)_3Cl:Mn_{0.03}$ 47%, and $LaGa_{0.99}O_3:Cr_{0.01}$ 8%. Comparing and contrasting the luminescence thermometry figures of merit of the four thermometers, the highest S_r was found for $Sr_5(V_{0.97}O_4)_3Cl:Mn_{0.03}$ with the MLR readout of 3.14% K^{-1} at 308 K. For the *LIR* readout method that was investigated for all four materials, $LaGa_{0.99}O_3:Cr_{0.01}$ gave the highest S_r of 2.5% K^{-1} at 300 K. The best temperature resolution was produced by both the $La_{0.98}Ga_{0.99}O_3:Cr_{0.01},Nd_{0.02}$ *LIR* readout and $Sr_5(V_{0.97}O_4)_3Cl:Mn_{0.03}$ bandwidth method at 0.04 K at 300 K and 308 K, respectively. For band-shift thermometry, the $Ba_5(V_{0.97}O_4)_3Cl:Mn_{0.03}$ material had the highest S_a value at 0.10 K^{-1} at 373 K. Similarly for bandwidth thermometry, the highest S_r value was found for the $Ba_5(V_{0.97}O_4)_3Cl:Mn_{0.03}$ material at 0.42 % K^{-1} at 373 K.

Recent research in the field of luminescence thermometry has aimed to improve and optimise the S_r of novel and known luminescence thermometers. Some successful methods include:

- Investigating Ln^{3+}-TM dual-doped *LIR* luminescence thermometers as they are able to produce S_r values higher than those of thermally-coupled energy level-dependent Ln^{3+} single-doped *LIR* luminescence thermometers.
- Adjusting factors including activator ion concentration, the crystal field strength affecting the activator through systematic substitution of the host cations, phonon energy through host choice, and synthetic procedure.
- Using the MLR readout method which has produced higher S_r values compared to the S_r values of the individual variables used for the readout's calculation.

The incidence of Mn^{5+} as an activator ion for luminescence thermometry has increased owing to the ion's emission in BW-2, and large range of excitation wavelengths in BW-1, ideal for biological temperature sensing. The lack of previous exploration into this activator ion for luminescence thermometry is most likely due to the need for materials with tetrahedral sites able to stabilise the Mn^{5+} ion. With an increase in the number of Mn^{5+} phosphors reported in the literature, there can potentially be a new selection of Mn^{5+} thermometers to explore for BW-2 luminescence thermometry.